

**INTEGRATED ON-BOARD BATTERY CHARGERS FOR  
EVS BASED ON MULTIPHASE MACHINES AND  
POWER ELECTRONICS**

**IVAN SUBOTIĆ**

**A thesis submitted in partial fulfilment of the requirements of  
Liverpool John Moores University for the degree of  
Doctor of Philosophy**

**May 2015**

## ABSTRACT

The concept of integration of an electric vehicle (EV) drivetrain's components into the charging process is not novel. It has been considered over the years in both industry and academia, which resulted in a number of published papers and patents in this area. Possibilities of charging from single-phase and three-phase mains were both considered. In the former group the charging power rating cannot exceed the limit set by the single-phase mains. Therefore, the topologies are characterised with low charging powers, leading to a long duration of the charging process. Although the topologies supplied from three-phase mains are capable of achieving fast charging, they were considered to a much lesser extent. The main reason is the undesirable torque production in machines integrated into the charging process during the battery charging, which is unavoidable when a three-phase machine of either synchronous or induction type is used.

The thesis investigates integrated on-board battery chargers for electric vehicles (EVs) based on multiphase machines and multiphase power electronics. At present, EVs rely on three-phase systems for machine propulsion. However, recent advances in multiphase drive technology have firmly established their potential advantages over their three-phase counterparts for this application. One of the most notable features of multiphase drive systems is their excellent fault tolerance, which is highly desirable in EVs since it enables realisation of the requirement for "limp-home" operation in the propulsion mode, in case of a fault. The thesis demonstrates that multiphase drives have an additional major advantage over three-phase systems in vehicular applications, which is related to the aspect of battery charging. It shows a clear superiority of multiphase over three-phase systems in designing integrated charging topologies for EVs. In order to support the statement, the thesis provides a multitude of novel charging solutions that incorporate multiphase machines and multiphase power electronics into the charging process. The developed solutions could contribute to achieve significantly faster and cost-free (or at a minimum additional cost) on-board chargers in the near future.

The thesis demonstrates how additional degrees of freedom that exist in multiphase systems can be conveniently utilised to achieve torque-free charging operation. Therefore, although three-phase currents flow through machines' stator windings, they are not capable of producing a torque; thus the machines do not have to be mechanically locked. The principal advantage is that either very few or no new elements are required in order to realise the charging process. Thus savings are made with regard to cost and weight, and available spare space in the vehicle is increased.

The novel integrated charging solutions, developed in the thesis, are based on primarily five-phase, asymmetrical and symmetrical six-phase, and asymmetrical and symmetrical nine-phase systems. Solutions with other phase numbers are also considered. Thus, in essence, all the possible phase numbers are encompassed by the research and the solutions are valid for both induction and synchronous machines. A common attribute of all discussed topologies is that they do not require a charger as a separate device since the charging function is performed by the drivetrain elements, predominantly a multiphase machine and an inverter. Further, each topology is capable of operating in both charging and vehicle-to-grid (V2G) mode.

Three types of voltage sources are considered as a power supply for the charging process, namely single-phase, three-phase, and multiphase. For each supply type, and each phase number, viability of torque-free charging operation is theoretically assessed. Mathematical models of multiphase rectifiers are developed. For each topology equivalent scheme in the charging/V2G mode of operation is constructed. A control scheme, which aims at achieving unity power factor operation and complete suppression of the low order grid current harmonics, is designed for each solution. Finally, the validity of theoretical considerations and control algorithms for the developed solutions is experimentally assessed in charging, V2G, and propulsion mode of operation. Experimental performances of all discussed topologies are compared, and advantages and shortcomings of each solution are identified and discussed.

## ACKNOWLEDGEMENT

I would like to express my sincere gratitude to several people who have helped me during my PhD studies.

First of all, my deepest gratitude goes to my Director of Studies, Prof. Emil Levi, for his professional mentoring, permanent support, encouragement and guidance. He was everything that I could ever hope for from a supervisor and much more. He has been a great support and inspiration. With his vast knowledge and top expertise and, at the same time, incredible modesty, he made hard work a joy and a completely stress-less experience, for which I am particularly grateful. I consider people like him extremely rare, and I feel enormously lucky to have had opportunity to work with him.

I would also like to acknowledge the help from my second supervisor Dr. Martin Jones in form of numerous technical discussions.

Next, I would like to acknowledge the Engineering and Physical Sciences Research Council (EPSRC) for supporting the Vehicle Electrical Systems Integration (VESI) project (EP/I038543/1) and hence my PhD studies financially.

I would like to thank Dr. Nandor Bodo, who was working on the same project as Postdoctoral Research Associate, for a substantial help that he provided to me during all performed experiments.

My huge gratitude goes to Dr. Obrad Đorđević. He has been an enormous support, always ready to unselfishly share his time and expertise. Moreover, he has been a great friend and in numerous cases a role model. His influence on me was invaluable, and I cannot even imagine how my time spent during doctoral studies would have looked like without him.

I would like to thank Milan Darijević, Ivan Zorić, Dr. Hang Seng Che, Dr. Lim Che Shen, Michal Rolak, Dr. Wahyu N. Satiawan, Dr. Fazli Patkar, and Engku Ariff Engku Ahmad Rafiqi. Their friendship and willingness for discussion were indispensable for me during my studies.

Finally, I would like to thank my family for all their love and support.

## CONTENTS

<b>ABSTRACT</b> .....	i
<b>ACKNOWLEDGEMENT</b> .....	ii
<b>CONTENTS</b> .....	iii
<b>CHAPTER 1: INTRODUCTION</b> .....	1
1.1 Preliminary considerations .....	1
1.2 An overview of integrated chargers for EVs .....	2
1.3 Novelty and originality of the thesis .....	4
1.4 Organisation of the thesis .....	4
<b>CHAPTER 2: STATE-OF-THE-ART IN BATTERY CHARGERS FOR ELECTRICAL VEHICLES</b> .....	6
2.1 Introduction .....	6
2.2 Off-board battery charging systems .....	6
2.2.1 Ac-dc converter .....	6
2.2.2 Dc-dc converter .....	9
2.2.3 Inductive (wireless) chargers .....	11
2.3 On-board battery charging systems .....	11
2.3.1 Standard (non-integrated) solutions .....	11
2.3.2 Solutions with only inverter integration .....	12
2.3.3 Single-phase chargers with integrated inverter and motor .....	13
2.3.4 Three-phase chargers with integrated inverter and motor .....	16
2.3.5 Comparison of solutions .....	18
2.4 Conclusion .....	19
<b>CHAPTER 3: TOPOLOGIES OF MULTIPHASE MACHINES AND SUPPLY FOR INTEGRATED PROPULSION MOTOR/ON-BOARD BATTERY CHARGER</b> .....	20
3.1 Introduction .....	20
3.2 Multiphase supply .....	20
3.3 Single-phase supply .....	26
3.4 Three-phase supply .....	32
3.5 Conclusion .....	37
<b>CHAPTER 4: MULTIPHASE VOLTAGE SOURCE RECTIFIERS</b> .....	39
4.1 Introduction .....	39
4.2 Principle of operation .....	39
4.3 Mathematical modelling of multiphase VSRs .....	40
4.3.1 Model in terms of phase variables .....	40
4.3.2 Model after application of the decoupling transformation .....	41
4.3.3 Model in the rotating reference frame .....	43
4.3.5 Closed loop transfer function .....	45
4.4 Conclusion .....	46
<b>CHAPTER 5: CHARGING AND V2G MODES OF OPERATION</b> .....	47
5.1 Introduction .....	47
5.2 Control .....	47
5.2.1 Multiphase supply .....	47
5.2.1.1 Topologies without field production in the rotor .....	50
5.2.1.2 Topologies with pulsating field in the rotor .....	52
5.2.2 Single-phase supply .....	52
5.2.2.1 Topologies without field production in the rotor .....	54
5.2.2.2 Topologies with the pulsating field in the rotor .....	54
5.2.3 Three-phase supply .....	55
5.2.3.1 Topologies without the field in the rotor .....	55
5.2.3.2 Topologies with the pulsating field in the rotor .....	57
5.3 Experimental results .....	58
5.3.1 Multiphase supply .....	59
5.3.1.1 Topologies without the field in the rotor .....	59
5.3.1.2 Topologies with the pulsating field in the rotor .....	61
5.3.2 Single-phase supply .....	64

- 5.3.3 Three-phase supply .....69
  - 5.3.3.1 Topologies without the field in the rotor .....69
  - 5.3.3.2 Topologies with the pulsating field in the rotor.....73
- 5.4 Conclusion.....79
- CHAPTER 6: PROPULSION MODE OF OPERATION .....80**
  - 6.1 Introduction .....80
  - 6.2 Control.....80
  - 6.3 Experimental results .....82
  - 6.4 Conclusion.....86
- CHAPTER 7: CONCLUSIONS AND FUTURE WORK .....87**
  - 7.1 Conclusions .....87
  - 7.2 Future work .....88
- REFERENCES .....89**
- APPENDIX A: EXPERIMENTAL RIG DATA .....94**
- APPENDIX B: PUBLICATIONS FROM THE THESIS .....95**

## CHAPTER 1: INTRODUCTION

### 1.1 Preliminary considerations

Due to fossil fuel shortage and the global warming-related problems, internal combustion engine (ICE) vehicles will be replaced in the near future at a faster rate with electric vehicles (EVs). Some countries have already adopted action plans for this transition. In the US the forecast was for one million EVs by 2015 [Saber and Venayagamoorthy (2009)], while in the Netherlands the same number is anticipated until 2025 [Harikumar et al (2012)]. In order to accomplish this changeover, some of the main goals that need to be achieved are an increase in the battery capacity, and development of suitable, preferably on-board, battery chargers, capable of realising fast battery charging that complies with grid standards [Electromagnetic compatibility EMC (1995), SAE international standards (2011)]. However, these two problems can be considered completely separately. Thus, in what follows, the focus is on the second problem, namely on on-board battery charging solutions.

Fast battery chargers are mandatory for a wider use of EVs. There are two basic types of battery chargers, off-board and on-board, and for both types many configurations have been proposed [Yilmaz and Krein (2011)]. However, only on-board chargers liberate their users from the need to search for charging stations, and allow them a freedom of charging their vehicles from almost any single-phase or three-phase (as appropriate) power socket. Also, on-board chargers in combination with EVs' batteries are seen as a possible solution for the mass energy storage problem, which is currently one of the main concerns in the electric energy sector. EVs are for most of the time parked; hence, if integrated into the smart grid, they can accumulate the energy from the grid when the demand for the energy is low, and supply the grid with the energy when the demand is high (vehicle to grid, V2G concept) [Pillai and Bak-Jensen (2011), Kisacikoglu et al (2010)]. This requires a bidirectional on-board battery charger. It can be concluded that even in a futuristic scenario where off-board charging stations might be widely spread, on-board chargers will still be very desirable.

On-board battery chargers typically have, in addition to advantages, also a few drawbacks. If made like a separate unit, which is currently the case with many EVs, they increase the cost of the vehicle by introducing new power electronics elements. Depending on the model the additional cost can be up to \$ 3,000 [Tesla Roadster Specifications (2009)]. Their installation requires additional space and increases the weight. However, all these drawbacks can be overcome by integrating the existing propulsion motor and power electronics into the charging process [Hagbin et al (2013)].

It is to be noted that during the battery charging process most of the propulsion power electronics components are in an idle state. Moreover it can be observed that power electronics components of separate chargers have a great similarity with the existing components. The major part of a charger, a voltage source rectifier (VSR) that converts the ac voltage of the grid into the dc voltage capable of charging the battery is by hardware the same element as a voltage source inverter (VSI) which already exists in the powertrain. The second important part of a charger is a filter consisting of bulky inductive elements. However, propulsion machine windings are already of inductive nature. Thus if the existing power electronics components and the propulsion motor can be somehow integrated into the charging process instead of installing the new elements with the same capabilities, remarkable savings can be achieved.

The main obstacle to a straightforward integration is that ac currents flowing through a machine can provide unwanted torque in the machine during the charging process. If that happens the motor has to be mechanically locked, or separated from the transmission system causing a decrease of its lifetime, audible noise, and increased cost of a system. However, three-phase ac currents flowing through a three-phase machine will always produce a rotating field. This is the main reason why in the beginning only single-phase integrated chargers were researched. Single-phase current flowing through the machine windings will result in either field absence or a pulsating field which is incapable of producing the average torque. Although they found their place in electric scooter industry, single-phase chargers are still very slow, and limited by the power of a single-phase source. While they may be very desirable as an additional asset to a fast (three-phase) charger, they are not capable of providing fast charging.

Since a three-phase machine cannot be fully and conveniently integrated into the fast charging process, different types of machines started to be considered for this purpose. This resulted in the shift of the focus toward multiphase machines. In very recent past the first proposals for configurations integrating this type of machines were made, and one of these configurations will most likely be used in industry by Valeo [Sandulescu et al (2013)].

Multiphase drives are mainly used in high power applications. Their two main advantages over three-phase systems are reduced current (power) rating of the semiconductor switches and excellent fault-tolerant operation features [Levi et al (2007), Levi (2008)]. In general, multiphase machines are characterised with existence of additional degrees of freedom with regard to the control. This brings in an added advantage over their three-phase counterparts in applications related to the integrated on-board charging of EVs. These additional degrees of freedom can be used for both fast and slow battery charging without any torque production.

A majority of EVs at present use a machine of induction type for propulsion [de Santiago et al (2012)], although permanent magnet (PM) synchronous machines are also a common choice, especially outside US. Nevertheless, currently only four integrated on-board solutions allow fast (three-phase) charging incorporating these types of machines.

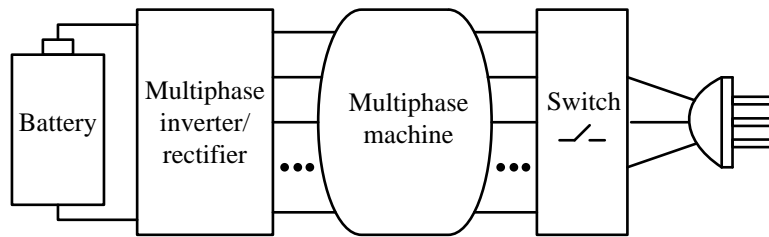


**Fig. 1.1:** Basic structure of an on-board integrated multiphase battery charging system.

The aim of this research is to investigate the benefits of integration of multiphase machines into the charging process, and to try to produce new charging configurations. The focus will be on induction and PM machines, as these are, as noted, the two most common types of propulsion machines used in EVs. The basic configuration of an on-board integrated charger incorporating a multiphase machine into the charging process is given in Fig. 1.1.

Although multiphase machines have a great potential for integration into the charging process, they have not been sufficiently investigated for these applications. Their additional advantage in EV applications is a very good fault tolerance, since they can continue to operate normally (although with a decreased maximal torque) as long as there are at least three healthy phases. This brings an important benefit to a drive in cases when possibility of the uninterrupted motion is specified, as the case is in the most of the modern electric vehicles ('limp-home' mode).

A final industrial standard for integrated on-board chargers is far from being set; thus every new configuration has a potential of being used in industry. Even the configurations that are presently employed in some industrial areas are applicable only for single-phase charging and have many downsides and the scope for improvements. Multiphase machines have not been yet used in industry for integrated charging, but are seen as a potential competitor to standard three-phase machines for these applications. Considering the growing need for EVs and predicted benefits of multiphase machine integration into the charging process, the research in this area is with a potentially high impact.

In the following section a brief overview of the state-of-the-art in battery chargers for EVs, with emphasis placed on on-board integrated solutions, is given.

## 1.2 An overview of integrated chargers for EVs

At present, research on integrated chargers for EVs is gaining on importance, as they combine multiple advantages. Some of these are:

- Reduced cost (extra cost of new elements is avoided);
- More space and better packaging (saved space which new elements would require);
- Lighter system (this also means higher speed and lower power consumption).

There is a great incentive for this research since there is a huge market where the solutions could potentially penetrate. EV market is growing daily and the impact of this research will be seen in the years to come as new models enter the market. The research gathered momentum only in the last few years; however, the initial interest in this area is three decades old.

The first powertrain elements, considered for possible integration into the charging process, were switches of the inverter. In 1985 an idea of integrating single inverter switch into the dc-dc converter for single-phase charging process was patented [Slicker (1985)]. Five years later, the idea of integrating a whole inverter leg was presented in [Rippel (1990)], where it was used to operate the converter like a boost-regulated battery charger. The supply in both cases was from a single-phase diode bridge rectifier. A topology with two integrated inverter legs was presented in [Surada and Khaligh (2010)]. The supply was again from a single-phase source, but now a bidirectional operation was possible. The motor had to be disconnected from the inverter during the charging process.

A reactive power compensation study using a dc-link capacitor of an integrated inverter is reported in [Kisacikoglu et al (2010)]. It is shown that a reactive power control does not cause a degradation of the battery life, and that is why reactive power compensation instead of V2G operation is considered.

The integration of a multilevel converter into the charging process was presented in [Josefsson et al (2010)]. It is proposed to disconnect the motor during the charging mode, and to use a converter for the bidirectional charging with excellent fault-tolerant performance. The converter was made from multiple H-bridge cells. The main advantage of the multilevel converters is that the input is spread across several units; thus, due to reduced voltage of each unit, various semiconductor technologies can be employed. Still, it is not yet clear if this multilevel technology can be introduced in a vehicle operation due to a lack of research on the energy utilisation and the efficiency optimisation with these types of converters.

As stated above, inverter integration has some advantages. However, in most cases, during the charging process, the machine needs to be disconnected from the inverter, which includes additional cost of the hardware reconfiguration. A better idea is therefore to try to integrate both the inverter and the propulsion motor. Not only that the reconfiguration cost could be reduced in this manner, but also the machine windings could play an important role as voltage harmonic filters for the charging process.

The initial solutions for both inverter and motor integration, presented in 1985 [Slicker (1985), Thimmesh (1985)], were characterised with limited integration and had many drawbacks. The first remarkable integrated solution in this area was reported in [Rippel and Cocconi (1992)]. The idea was to use isolated neutral points of two motors as connecting points for a single-phase supply. There was no torque developed in the machines during charging, since the same currents were flowing through the windings, and the stator leakage inductance was used for filtering. Moreover, the solution is bidirectional and it does not require a hardware reconfiguration between the propulsion and charging mode. In the same document a configuration that uses a single motor with two isolated sets of windings instead of two separate motors is proposed. The operating principle remained the same.

The idea of using a machine's neutral point for connecting the voltage source was later investigated to a larger extent. A solution utilising four neutral points of four motors is presented in [Sang Joon and Seung Ki (1994)]. The first two motors are used in the same manner as in the previous solution and the remaining two motors with their converters were used as a part of two buck-type converters. The solution has a limited application potential because it is applicable only for vehicles with four propulsion motors. Another configuration employing the same idea is presented in [Solero (2001)]. This configuration now has the advantage of containing a single motor. Output from a diode bridge rectifier is used as a voltage source. The configuration found place in a prototype of an electric scooter aimed for Far-East markets. A shortcoming of the solution is that it is not bidirectional.

In 2009 an additional advantage of configurations using the isolated neutral point of a machine was established. Until then all inverter legs attached to a single machine were operated simultaneously to ensure a torque-free operation. In [Pellegrino et al (2009a)] it is shown how the switching of inverter legs can be spread over the switching period to improve the efficiency of the previous configuration. Although all the legs still have the same turn-on time, their carriers are shifted by  $120^\circ$ . A significant current ripple reduction was reported for the same switching frequency because of the ripple cancellation among the phases. A year later, in [Gui-Jia and Lixin (2010)], the same idea was applied to a two-motor drive of [Rippel and Cocconi (1992)], with a very similar conclusion. It is noted that a grid phase current ripple frequency is three times higher than the ripple frequency of the individual phase currents flowing through the machine. In [Dong-Gyun et al (2011)] an interleaving solution with two machines is found to be superior to the one with a single machine. The comparison was based on the grid current ripple as a figure of merit.

A completely different integration idea, which now does not include access to the machine's neutral point, is presented in [Cocconi and Calif (1994)]. The solution employs a three-phase machine and an inverter. In the charging mode an inverter leg is disconnected from its corresponding machine phase and a single-phase supply is inserted between them. The system in the charging mode operates like a boost switching regulator and a bidirectional and near-unity power factor operation can be achieved. There is only a pulsating field developed in the machine, thus an average torque is not generated during the process. The configuration is presently employed in industry.

All of the previously considered configurations use a single-phase voltage source. Although it is widely available, it is inferior to a three-phase voltage source for battery charging applications in a vehicle. Single-phase systems require one conductor less than the three-phase systems, but have three times smaller power for the same per-phase voltage and current rating. Even bigger limitation for single-phase systems is the small current (power) that can be taken out of a socket, resulting in a slow charging. For fast charging three-phase systems have to be utilised.

As noted, induction and PM synchronous machines are the two most common types of propulsion machines in EVs [de Santiago et al (2012)]. However, only four integrated on-board solutions [Kinoshita (1997), Lacressonniere and Cassoret (2005), Haghbin et al (2011), De Sousa et al (2010)] have been reported so far as being capable of performing fast (three-phase) battery charging incorporating these types of machines.

In [Kinoshita (1997)] the simplest connection of three-phase voltage source to a three-phase machine is investigated. In the charging mode, the neutral point of the machine's winding is opened leaving the machine in open-end winding configuration. Phase windings retain their connections to the inverter, while their other terminal is now attached to a three-phase grid. During the charging mode a rotating field like the one in the propulsion mode is developed. Thus, in order to prevent rotation, the rotor has to be mechanically locked, which represents a severe drawback.

In [Lacressonniere and Cassoret (2005)], an isolated topology is proposed. Isolation takes place in the machine, which is operated like a transformer during the charging mode. However, this solution increases the cost of the drive system since it requires a wound rotor, so that the isolation advantage is completely overshadowed.

Another isolated solution is presented in [Haghbin et al (2011)]. It avoids the additional cost of wound rotor by using an asymmetrical six phase machine with two isolated neutral points. This type of machine has two sets of three-phase windings spatially shifted by  $30^\circ$ . In the charging mode one set is connected to the inverter and plays a role of a secondary transformer winding set while the other set is connected to the grid and plays the role of a primary transformer winding set. In contrast to the previous two, this one has an industrial potential.

Finally, only the solution of [De Sousa et al (2010)] has an advantage of no torque development in the machine during the charging. It uses a configuration with a three-phase machine in which, during the charging mode, three-phase grid connections are attached to the three middle points of the machine windings. Hence the machine operates as a three-phase in propulsion mode, while it is an equivalent of a symmetrical six-phase machine in the charging mode; the half-windings of each phase in spatial opposition are paralleled for the charging and are thus supplied with the same

currents, causing cancellation of the rotating field. The solution is currently being considered for use in future EVs by Valeo [Sandulescu et al (2013)]. Moreover, it currently presents the only on-board integrated fast (three-phase) charging configuration in general without the requirement of hardware reconfiguration between the charging and propulsion mode of operation.

### 1.3 Novelty and originality of the thesis

The aim of this research has been development of alternative charging configurations that could potentially be utilised in conjunction with induction and PM machines and it has focused on multiphase machines. The basic idea that has been used throughout the research is a transfer of the excitation from the flux/torque producing  $\alpha\text{-}\beta$  plane to non-flux/torque producing plane(s). Depending on the considered topology, the transfer of the excitation may be complete (i.e. no currents in the flux/torque producing  $\alpha\text{-}\beta$  plane during charging) or partial (some current remains to flow in the  $\alpha\text{-}\beta$  plane, but its nature is such that rotating field is not developed). In this manner the excitation of the machine will not lead to the average torque production; hence, the machine will stay at standstill, and it will be used as a simple inductive-resistive element. During the charging mode the same principles of multiphase machine analysis are applicable as in the propulsion mode.

The transfer of the machine's excitation, be it complete or partial, can be accomplished in various ways. One of these is the change of the order in which phases of a supply are connected to a machine and this typically requires some sort of a hardware reconfiguration. Another possibility is utilisation of multiple neutral points in the machine's stator winding for connection of the single-phase or three-phase supply, in which case hardware reconfiguration will typically not be needed. The research has focused on achieving the excitation transfer with as little reconfiguration as possible, due to the fact that every additional contactor or a switch increases the total cost of the system and, by doing so, diminishes the effect of the integration.

The main objectives of the conducted research can be summarised as follows:

1. To develop new integrated charging topologies employing multiphase machines with various phase numbers. The topologies are considered in conjunction with single-phase, three-phase and multiphase voltage source regarded as being available at the charging station.
2. To perform theoretical investigation of machines' behaviour during charging mode of operation. The major task of the analysis is an assessment of whether a torque is produced in a machine during the process.
3. To develop suitable control algorithms for the developed topologies. The aim is to achieve unity power factor operation at the grid side, with good suppression of low-order harmonics in grid currents.
4. To develop experimental rig for various integrated charging topologies.
5. To perform experimental testing of dynamic and steady state operation in both charging and propulsion mode of operation for selected configurations.
6. To consolidate experimental results and perform detailed comparative analysis of all experimental results for the analysed configurations.

The original research results, obtained during the work on this thesis, have been published in eight conference papers [Subotic et al (2013a), Subotic et al (2013b), Subotic et al (2013c), Subotic et al (2014a), Subotic et al (2014b), Subotic et al (2014c), Bodo et al (2014), Subotic et al (2015d)] and three journal papers [Subotic et al (2015a), Subotic et al (2015b), Subotic et al (2015c)] (Appendix B). Results that are currently in preparation for publication relate to topologies employing six-phase machines with direct grid connection, as well as single-phase charging solutions for the studied topologies.

### 1.4 Organisation of the thesis

The thesis is divided into 7 chapters.

Chapter 1 contains a brief overview of the existing battery charging systems for EVs. It starts with non-integrated chargers, and a transition from low towards higher levels of integration is explained in logical steps. Advantages of on-board and integrated systems are detailed, and their applications in industry are addressed. The need for the research on fast charging solutions incorporating multiphase machines into the charging process is thus identified. Research aim and objectives are set forth at the end of the chapter.

Chapter 2 contains a literature review of the state-of-the-art in battery chargers for electrical vehicles. The starting point are the off-board charging solutions. Non-integrated on-board solutions are then explained and compared with off-board solutions. The focus is placed on integrated on-board charging solutions, where each configuration is elaborated and its advantages and drawbacks identified. All the on-board charging solutions are quantitatively compared in the tabular format at the end of the chapter.

Chapter 3 presents new charging configurations with multiphase machines, which have been studied at a theoretical level within the work on this project. Three possible types of the grid supply are considered as a voltage source: single-phase, three-phase, and multiphase. For a multiphase source, all sources with an odd number of phases are covered, and for the even phase numbers only the asymmetrical and symmetrical six-phase cases are included. All the configurations in this chapter have an advantage of no average torque production during the charging mode, and

some of them also do not need reconfiguration between the propulsion and the charging mode of operation. A great majority of configurations is characterised with the absence of the magnetic field generation in the air-gap of the machine.

Chapter 4 discusses principle of operation of multiphase voltage source rectifiers. Basic principles of operation are given and operating limits are discussed. A general mathematical model of the voltage source rectifier (VSR), applicable not only for three-phase systems, but also for multiphase systems, is derived.

Chapter 5 considers the control for the configurations detailed in Chapter 3 in charging mode of operation. As in Chapter 3, configurations are grouped into three major categories: those with multiphase supply, with single-phase supply, and with three-phase supply. Complete voltage oriented control (VOC) algorithms, capable of controlling the considered systems in the charging mode, are given. Experiments are performed in order to provide validation of both theoretical considerations from Chapter 3, and the proposed control from this chapter. It should be noted that experimental results confirm the performance predicted by simulations. Although the simulation results are not included in the thesis, they can be found in publications [Subotic et al (2013a), Subotic et al (2013b), Subotic et al (2013c), Subotic et al (2014a), Subotic et al (2014b), Subotic et al (2014c), Bodo et al (2014), Subotic et al (2015c)]. The decision to omit them from the thesis is justified by the fact that they would not contribute with any new information. They would however introduce unnecessary repetition, which would be substantial considering the number of developed and assessed topologies.

Chapter 6 discusses propulsion mode of operation of the proposed integrated topologies. Well-known control algorithms for multiphase machines are briefly elaborated. Experiments in propulsion mode of operation are performed using a five-phase, an asymmetrical and symmetrical six-phase, and an asymmetrical nine-phase machine (all of induction motor type). Performance and current harmonic suppression are assessed in both steady state and in transient.

Chapter 7 gives a summary of the completed work. Main conclusions are given and directions for further course of investigation are detailed.

Chapter 7 is followed by the list of references used in the Thesis.

Finally, Appendix A contains experimental rig data, while the list of publications that have resulted from the thesis is provided in Appendix B.

## CHAPTER 2: STATE-OF-THE-ART IN BATTERY CHARGERS FOR ELECTRICAL VEHICLES

### 2.1 Introduction

As noted in section 1.1, due to fossil fuel shortage and the global warming-related problems, in the near future internal combustion engine (ICE) vehicles will be replaced at a faster rate with electric vehicles (EVs). In order to accomplish this transition, two main goals need to be achieved: the battery capacity must be increased and suitable, preferably on-board, battery chargers must be developed, capable of realising fast battery charging. Batteries and on-board chargers for EVs are also seen as a possible solution for the mass energy storage problem, which is currently one of the main concerns in the electric energy sector. EVs are for most of the time parked; hence, if integrated into the smart grid, they can accumulate the energy from the grid when the demand for the energy is low, and supply the grid with the energy when the demand is high (vehicle-to-grid, V2G concept). This requires a bidirectional on-board battery charger. On the other hand, since V2G technology is still very far from mature and widely spread, the chargers without bidirectional capability will still be needed in the foreseeable future. Final industrial standard for on-board battery chargers has not been introduced yet, and numerous new solutions have been reported in recent times. In this chapter, a review of different battery charging topologies for EVs is reported and comprehensive quantitative comparison of the described on-board topologies is made, which identifies the advantages and shortcomings of each solution.

### 2.2 Off-board battery charging systems

The main purpose of an off-board charger is to provide a fast (level 3) charging which complies with the grid rules. Fast charging, as a term, is not strictly defined. One of the most frequently utilised classifications of chargers for electrical vehicles defines three charging levels [Rawson and Kateley (1998)]: level 1 charging is up to 120 V and 15 A, level 2 is up to 240 V and 60 A, and level 3 charging is charging rated at more than 14.4 kW.

Li-type batteries are widely regarded as the best choice for EVs and almost every modern EV has a Li battery [de Santiago et al (2012)]. The common energy storages are from 10 to 85 kWh, and the ranges are between 100 and 480 km. There are various techniques of controlling the charging process for energy optimization, especially if temperature is not constant. However, when the temperature is constant, it has been proven that the CC/CV (constant current/constant voltage) method is near optimal for minimal energy losses [Inoa and Jin (2011)].

There is currently a variety of off-board charging configurations for EVs. However, the great majority of them fit into a few groups of basic configurations, which are discussed in the following subsections.

#### 2.2.1 Ac-dc converter

One of the best known ac-dc converters is a single-phase boost PFC (power factor correction) rectifier, which is shown in Fig. 2.1. The inductor on the dc-side of the rectifier allows operation like a boost chopper. The current taken from the grid can be almost sinusoidal and in phase with the grid voltage.

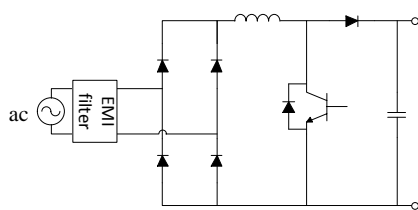


Fig. 2.1: Single-phase boost PFC rectifier.

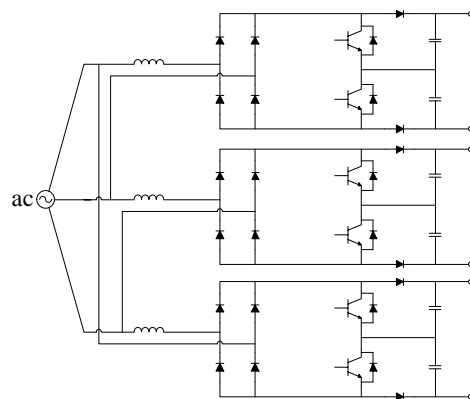


Fig. 2.2: Phase-modular delta rectifier

When the configuration and the mode of operation of the single-phase PFC rectifier are applied to three-phase systems, new configurations called phase-modular rectifiers are created. There are two types of phase-modular rectifiers: phase-modular star rectifiers [Greul et al (2003)] (when single-phase PFC rectifiers are connected in star connection), and phase-modular delta rectifiers [Greul et al (2006)] (when single-phase PFC rectifiers are connected in delta connection – Fig. 2.2). Phase-modular delta rectifiers have a number of advantages over phase-modular star rectifiers, which therefore have minor industrial potential. The major advantage of the phase-modular delta rectifiers is that the three single-phase subsystems are decoupled and each subsystem can be controlled independently. At the output stage three individual dc voltages are obtained, thus there is the necessity for three isolated dc-dc converters to connect these to a single dc output. The fact that a line voltage is applied to each subsystem can be considered to be a drawback

as well as an advantage. This means that a higher voltage is provided at the output of the modules, or if a reduced voltage is required, power semiconductors with higher voltage blocking capability have to be used. On the other hand, if diodes in the front end of each subsystem are replaced with three-phase transistor bridges connected to each mains phase, then even with the failure of a mains phase fully rated post-fault operation can be achieved, which is a great advantage of the system.

Another way to apply the configuration of a single-phase PFC rectifier to three-phase systems is to insert an additional diode leg in the input. As a result, each phase would have its own diode leg [Prasad et al (1991)]. This direct application of single-phase configuration to three-phase systems results in a rectifier with poor efficiency. Although the output voltage is controllable, the current THD is around 30%, which is way beyond the permitted limit for EV chargers. A similar version of this system is obtainable if boost inductor is moved from the dc to the ac side and spread over the phases. However, this cannot significantly decrease the current THD.

The only way to improve the current quality is to insert additional fully controllable semiconductors to the system, for enhancing the control. One such system with improved controllability is presented in Fig. 2.3. The idea is to achieve sinusoidal currents with unity power factor by independently controlling currents in the positive and negative dc-bus. Currents in the positive and negative dc-bus rails should be controlled to be proportional to the voltages that are applied to the dc-buses, which are two phase voltages with the greatest absolute value in that particular instant. The difference between currents in the positive and negative dc-bus rails should then be injected into the idle phase [Salmon (1994)]. The injection is realised through a configuration of six switches. In each instant only a single switch is turned on, the one that is allowing a connection to the idle mains phase. If the system is symmetrical, the difference of two currents that will be injected in idle mains phase will be proportional to that idle phase voltage. Thus, in each instant three-phase currents and three-phase voltages will be proportional. Transistor  $T_+$  is controlling the current in the positive dc-bus rail, and  $T_-$  is controlling the current in the negative dc-bus rail, thus the ratio between phase voltages and currents can be controlled. The six switches that are allowing current injection cannot be used for controlling this ratio because their mode of operation is completely determined by mains voltages. Frequency of the current that flows through injection line is three times higher than the mains frequency, but during the period ( $360^\circ$ ) only two segments (each of  $60^\circ$  duration) of this current are injected into a single phase. However, the term “third harmonic injection rectifier” is customarily used in accordance with the complete injected current.

The system is capable of fault-tolerant operation in case of a mains phase failure. In this case, it would operate at a lower power but still with sinusoidal currents. The fault-tolerant operation is achievable by turning off permanently all six switches for current injection, and by simultaneously controlling the transistors  $T_+$  and  $T_-$ . This manner of operation would transform the system into a single-phase PFC rectifier. The only difference with regard to the standard one would be that the system is now operating with a line instead of a phase-to-neutral voltage at the input.

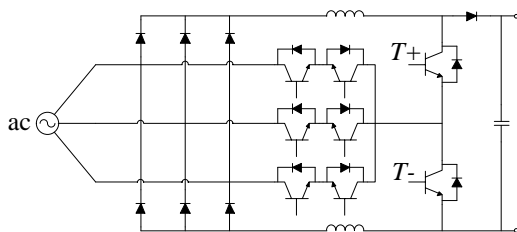


**Fig. 2.3:** Conventional hybrid third-harmonic injection rectifier.

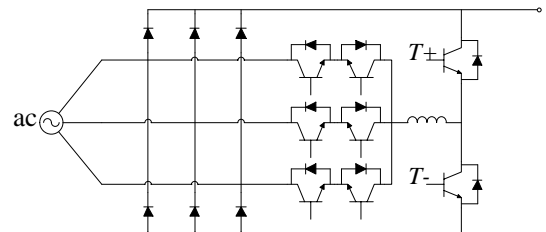


**Fig. 2.4:** Modified hybrid third harmonic injection rectifier.

A somewhat similar system is presented in Fig. 2.4. Two inductors in the dc-bus rails are replaced with one inductor in the injection branch, and the diode in the dc-bus is removed. The smoothing capacitance is removed from the output stage of the rectifier. The dc-bus voltage of this system is the direct output of the diode bridge, thus it is only dependent on mains voltages and cannot be regulated. This presents the major drawback of the system. However, if a dc-dc converter is connected to this rectifier, the output voltage is controllable, input currents can be sinusoidal, and a unity power factor can be achieved [Kolar and Friedli (2011)]. Thus, the application value of this rectifier should be assessed only by considering the whole configuration (including a specific dc-dc converter).

As can be seen from the scheme, if the transistors  $T_+$  and  $T_-$  are switched on at the same time this would cause a short circuit between the two mains phases that have the biggest absolute values of voltages at that instant. Control algorithm should include precautions such that this state cannot be obtained. Except for this difference, the principle of operation of the conventional hybrid third-harmonic injection filter can be used for obtaining sinusoidal voltages.

A configuration in which diode bridge commutates at the switching frequency is shown in Fig. 2.5 [Soeiro et al (2011)]. Switches are connected in delta, and thus the name: delta-switch rectifier. Switches are able to fully control conduction state of the diode bridge; thus they are able to control the output voltage, which is determined only by the conduction state of the diode bridge. The voltage is controlled using PWM method. Reference values for voltages are obtained by phase current controllers after star-delta transformation. This topology is capable of not just providing a unity power factor, but also of providing any angle lower than  $\pm 30^\circ$  between currents and voltages. This might be useful

for grid reactive power compensation, but due to the regulations for permitted power factor, this possibility is unlikely to find application in the charging process.

Fault-tolerant operation is possible in case of a failure of one mains phase. In that case four switches that connect that phase to the other two must be kept in the off state. The remaining two switches should be controlled simultaneously. This would lead to the well-known single-phase PFC rectifier, which operates with line voltages and sinusoidal mains currents.

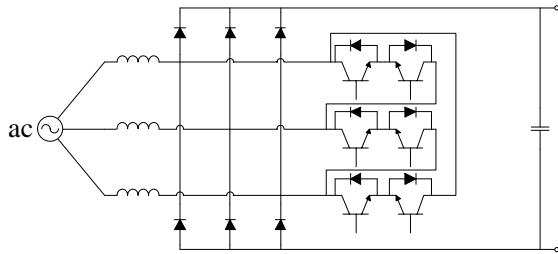


**Fig. 2.5:** Delta-switch rectifier.

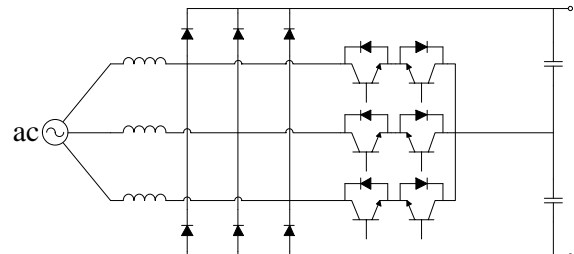


**Fig. 2.6:** Vienna rectifier.

The previous configuration does not have physical mid-point of the output voltage. One somewhat different configuration, with the physical mid-point, is the Vienna rectifier depicted in Fig. 2.6. The switches are in star connection and star point is connected to the newly formed mid-point of the output voltage, obtained using two identical capacitors in series. The advantage of having a physical mid-point is an additional degree of freedom in terms of the diode bridge input voltage. Now, a phase voltage can be connected to the output voltage mid-point in addition to the connection to the positive and negative dc-bus. This is why this configuration is a three-level converter, which introduces numerous advantages [Ming et al (2012)]. One of them is that the voltage blocking capability of transistors can be reduced because voltage applied to them is twice smaller than before. In addition to that, the voltage drop on inductances is lower, thus the mains current ripple is reduced and lower rated boost inductors can be used. EMI noise is reduced due to the switching of reduced voltages. The existence of the output voltage mid-point introduces the need for balancing of the two output voltages. One of the techniques for achieving this is to add an offset to the phase current reference values, which can provide the system with ability of charging the lower or upper capacitor.

A configuration which is widely used in industry is the six-switch converter, presented in Fig. 2.7 [Capece et al (2003)]. Unlike the other configurations discussed so far, this one is bidirectional. It can work like an inverter if the power needs to be supplied back to the grid. In the rectifying mode it can control the voltages of each phase independently of the input currents. This configuration is a two-level converter, because only two voltage levels (positive and negative) can be applied with reference to the virtual mid-point of the dc-bus. The system is capable of fault-tolerant operation in case of a mains phase failure.

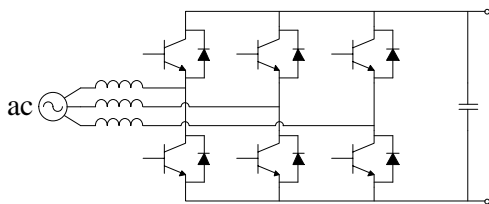


**Fig. 2.7:** Fully-controlled active three-phase ac-dc bridge.

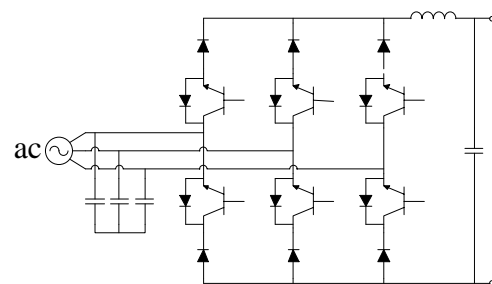


**Fig. 2.8:** Active six-switch buck PFC rectifier.

A unidirectional buck-type converter is presented in Fig. 2.8 [Stupar et al (2011)]. A buck converter with uncontrollable three-phase diode bridge is not capable of providing sinusoidal currents, thus switches have to be added to the system to improve the controllability by blocking the voltages and stopping the current flow. A current will flow only in the path where two transistors are turned on, thus the output current can be switched between phases in a manner that will provide sinusoidal mains currents. Output voltage can be regulated by controlling the freewheeling state, which occurs when two transistors in the same leg are turned on. Conduction losses in the freewheeling state can be reduced by adding a freewheeling diode.

Unlike boost PFC rectifiers, buck type PFC rectifiers do not use information on controlled dc current values, which results in inability to correct variations of dc currents and parasitic timing errors. This is why the boost PFC rectifiers generally have better mains current quality than the buck type.

A buck converter that uses current injection, known as Swiss rectifier, is shown in Fig. 2.9 [Soeiro et al (2012)]. Unlike in a previously considered configuration, commutation of the diode bridge is not performed at the switching frequency. In contrast to the boost third-harmonic injection rectifier, inductor is now placed at the right hand side, creating a boost rectifier. The current injection is performed in a similar way like in the third-harmonic current

injection boost rectifier. Current injection is applied to the phase which has the smallest absolute value of the voltage at that particular instant. The system is only capable of operation with zero phase shift between the input voltages and currents.

Dimensioning of the input capacitors is dependent on the manner of control. The PWM modulation of switches in the dc-bus rails can be performed in phase or in counter-phase. If the switches work in phase one with the other, the current in the injection branch is minimized. If they work in counter-phase, the output dc current ripple will be minimized, but the current ripple in the injection branch will be increased, and larger capacitances will be required at the front of the rectifier.

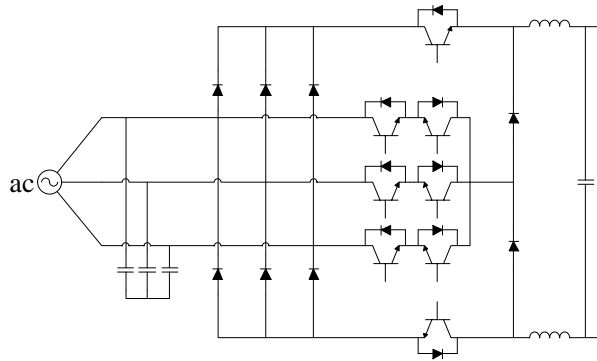


**Fig. 2.9:** Swiss rectifier.

A similar buck converter can be designed using a third-harmonic injection PFC rectifier in combination with a dc-dc buck converter [Kolar and Friedli (2011)] (Fig. 2.10). The dc-dc buck converter can ensure constant power consumption, which can be independent of the output voltage. This configuration has the advantage of low conduction losses, which is due to the fact that only one semiconductor switches the full current. This also means that only that transistor has to be fully rated. The advantage of the configuration is a reduced number of the power semiconductors and the lack of high frequency variations of the output common mode (CM) voltage.

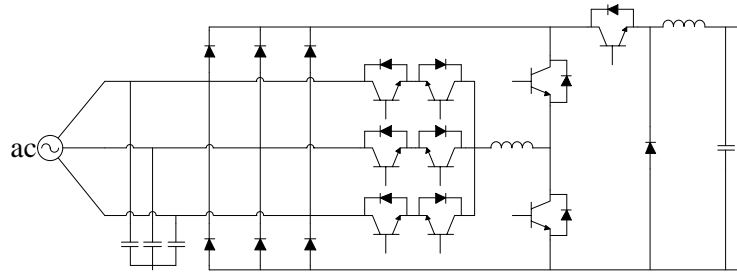


**Fig. 2.10:** Combination of the active filter third-harmonic injection rectifier and the dc-dc buck converter.

Configurations described so far cover the most of the ac-dc stages of off-board chargers. There are also some atypical solutions, like the one presented in [Kuperman et al (2010)], where the ac-dc stage uses three-phase diode bridge rectifier and an active power filter. The configuration results in uncontrolled dc stage which is then routed to six interleaved groups of two dc-dc converters which are able of controlling the output voltage or current. These atypical solutions cannot be classified into neat groups, and have to be considered individually. Since they are typically of minor importance here, more detailed review of these topologies is beyond the scope.

### 2.2.2 Dc-dc converter

Off-board chargers require a galvanic isolation between a vehicle and the grid. This is in most cases accomplished by using a high frequency transformer integrated into a dc-dc converter. Solutions employing a low frequency transformer on the grid side and non-isolated dc-dc converters are possible [Yu et al (2010)], but not typical. One of the most commonly used dc-dc converters for off-board chargers that provides galvanic isolation is the phase-shifted zero voltage transition (ZVT) full-bridge converter [Yu-Kang et al (2011)] (Fig. 2.11). ZVT means that every switch is turned on while current passes through its anti-parallel diode, which significantly reduces turn-on switching losses.

Operating principle of the presented phase-shifted converter differs from the conventional (without phase shift) full bridge dc-dc converter by shapes of the switching signals that are applied to the switches. In the conventional full bridge converter transistors T1 and T4 are operated simultaneously, and when they are turned on a positive square voltage is applied to the primary winding of the transformer for some required time. Transistors T2 and T3 are also operated simultaneously but they are turned on 180° after transistors T1 and T4, applying a negative square voltage to the primary winding. Thus, over a control period, a high frequency ac voltage is applied to the transformer. Downside

of this (conventional) topology is the existence of high frequency oscillations between parasitic capacitances and the leakage inductance.

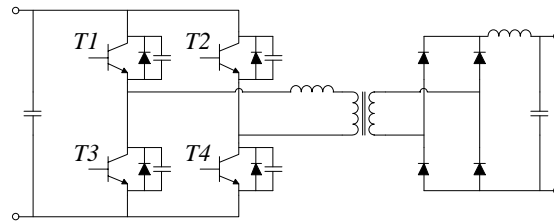


**Fig. 2.11:** Phase-shifted ZVT full-bridge dc-dc converter.

In the phase-shifted ZVT full bridge dc-dc converter switches T1 and T4 are not operated simultaneously. First, T1 is turned on and after a phase shift switch T4 is turned on. Transistors T2 and T3 are turned on after a  $180^\circ$  delay from the turning on instants of the transistors T1 and T4, respectively. This phase shift between switching the transistors T1 and T4 allows a ZVT operation by adding necessary dead time. This topology can achieve higher efficiency than a conventional full bridge topology due to the use of undesired parasitic elements of the semiconductors and the transformer leakage inductance to make the resonant transitions. This topology has the advantage of PWM control, reduced switching losses, and high efficiency under high input voltage. However, the resonance is load-current dependent, thus ZVT operation can be utilised only during a corresponding power level. Converter parameters should be designed with respect to this fact so that high charging currents (which are present more than 80% of the time) for fast charging can be obtained under ZVT, even if that means that with low currents operation cannot be in the same (ZVT) mode.

Another representative dc-dc topology with isolation on the dc-dc side is a half-bridge LLC converter [Gopiyani et al (2010)] (Fig. 2.12). Here  $L_m$  is the magnetising inductor, which is present due to the nature of a transformer, and  $L_r$  and  $C_r$  are the resonant inductor and the resonant capacitor. Losses at the output side are reduced by soft commutation of diodes in a centre-tapped rectifier, and the size is reduced due to the absence of a bulky inductor. Between control signals for the switches T1 and T2 there is a phase shift of  $180^\circ$ . When a square voltage is applied to the resonant LC circuit, it will only allow the fundamental voltage to pass, and a sinusoidal waveform for soft switching will result. There are two different resonant frequencies between  $L_r/C_r$  and  $(L_m+L_r)/C_r$ . Operating mode of the converter is dependent on these two frequencies, thus the converter can operate in a zero current switching (ZCS) or a zero voltage switching (ZVS) mode. Generally, for electric vehicle off-board chargers, ZVS is a better option because at the high input voltages for the ZCS efficiency is remarkably reduced, and switching frequency is limited due to the turn-on losses.

Compared to the other resonant topologies this topology has the advantage of high efficiency at high input voltage, can operate under ZVS mode with a wide range of loads, and has low voltage stress on the output diodes. The major drawback of this topology is that the output voltage is adjusted by changing the switching frequency, which can increase the design complexity of the filter and transformer.

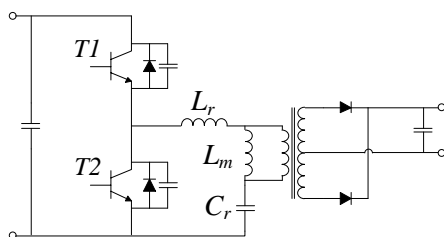


**Fig. 2.12:** Half-bridge LLC dc-dc converter.

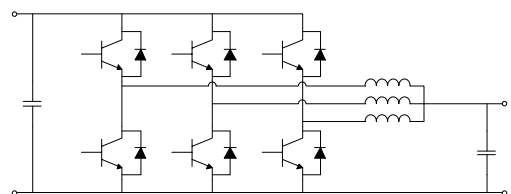


**Fig. 2.13:** Three-phase interleaved dc-dc converter.

If isolation is provided on the ac side of the converter, than interleaved buck converter can be used for the energy efficient dc-dc conversion [Garcia et al (2006)] (Fig. 2.13). In contrast to the traditional buck converter, interleaved buck converters do not need a bulky inductor. Instead of using a configuration with single bulky inductor, multi-phase interleaved converters are used. The system has a higher frequency, which is equal to the fundamental frequency multiplied by the number of phases, resulting current ripple cancelation and an increased efficiency. Output current ripples are mainly compensated because they oppose each other, thus the output filter is not needed. Due to the use of multiple inductors, the current sharing makes possible utilization of lower rated inductors. Control of the converter is phase-shifted PWM control, where phase shift between the phases equals  $360^\circ$  divided by the number of phases. It is shown that using more than three (e.g. 16 or 36) parallel stages could be very beneficial in vehicular applications.

In [Dusmez et al (2011)] the topologies discussed in this subsection are compared and it is shown that a phase-shifted full bridge converter has the lowest efficiency, while a half bridge LLC dc-dc converter has the highest

efficiency under ZVS mode. Interleaved buck converter is shown to be probably the best solution if isolation is not required, due to its low current ripple which can significantly extend the battery cycle life.

Moreover, if a charging station with multiple off-board chargers is considered, additional storage element on the dc-bus of the station system could be used to provide additional energy if the demand in certain instants exceeds the capability of the grid tie. It is shown that this solution can be used for elimination of the dc-side ripple and ac-side harmonics [Bai and Lukic (2011)].

It should be noted that the off-board configurations discussed so far can be used for on-board chargers; thus in many cases the configurations are designated as on-board chargers, e.g. [Gallardo-Lozano et al (2011), Tae-Hoon et al (2011)]. However, these solutions do not have anything that differentiates them from off-board chargers. The charger is simply physically moved from the charging station to the vehicle, enabling now battery charging through an ac connection (three-phase or single-phase), rather than dc connection of the vehicle to the charging station.

### 2.2.3 Inductive (wireless) chargers

To complete a review of off-board chargers it is necessary to address inductive chargers. Inductive (contactless) chargers, in addition to drawbacks, have some advantages over conventional (contact) chargers. Conventional, plug-in chargers have increased risk of electrocution in a wet environment. When the temperature is low connectors on the vehicle may freeze. In addition to that, cables of the plug-in chargers contribute to poor aesthetics of the system, and may impose a trip hazard. None of the mentioned downsides exists in inductive chargers.

The idea is that a vehicle can be charged wirelessly while standing in a place where a primary pad is installed. Principle of operation is as follows: initially the primary pad gets supplied by high frequency ac currents. Then the power gets inductively transferred to the receiver pad (coil), and gets rectified by power electronics finally allowing the dc charging of the battery [Chang-Yu et al (2009)]. The coupling between a transmitter and a receiver pad is usually loose, thus resonance and high frequency are mandatory for a proper charging operation.

Unlike plug-in charging, inductive charging introduces some potential health related problems. The magnetic field that runs through human body is not harmless and must be restricted to low levels. An organization that is dealing with standards in that area is ICNIRP (International Committee on Non-Ionizing Radiation Protection). It defines the maximum value of  $6.25\mu\text{T}$  for the average magnetic field that human body can be exposed to for the frequencies that are used for inductive charging (10 – 150 kHz).

Another downside of inductive chargers is that a V2G operation is hardly economically viable due to the low system efficiency and the reduction of the battery life made by the discharge-charge process.

Recently reported average efficiencies of inductive chargers are around 85% and the heights are around 25cm [Wu et al (2011)]. Some researchers report maximum efficiencies over 95% [Nagatsuka et al (2010)], but this should not be used as a representative value, due to the high dependence of efficiency on the output power [Neves et al (2011)].

One of possible additional applications for inductive charging is the electrified roadway concept. The idea is to charge a vehicle while it is in motion over a special electrified road which is capable of creating a magnetic field. This would decrease the cost of the EVs mainly due to the reduced cost of the battery, which can be dozens times smaller. If the current average battery price of 700\$/kWh is considered, than the cost reduction can be impressive. However, this cost reduction should be compared with the expected increase of the road taxes, which is inevitable in order to recover the initial investment in such a road. By using an electrified roadway the range for EVs would be practically unlimited and dependent only on the road infrastructure. For improved efficiency it is necessary to perform the current vehicle position detection and to power up only the part of the road that is below the vehicle.

## 2.3 On-board battery charging systems

As discussed in section 1.1, fast on-board battery chargers are mandatory for a wider use of EVs because they liberate their users from the need to search for charging stations, and allow them a freedom of charging their vehicles from almost any single-phase or three-phase power socket. This section attempts to review and assess different on-board battery charging topologies and is organised as follows. The starting point are the non-integrated solutions. This is followed by solutions with integrated inverter, and single-phase solutions with integrated inverter and the motor. Finally, the three-phase charging solutions, in which both the inverter and a motor are integrated, are surveyed. A comparison of the on-board chargers discussed in this section, is given in the last subsection.

### 2.3.1 Standard (non-integrated) solutions

There are many different non-integrated on-board charging solutions, which cannot be easily classified into specific groupings. The most of them are however closely related to a few basic configurations, which are presented in this subsection.

The most basic configurations for single-phase chargers are a half-bridge and a full bridge PWM rectifier (Fig. 2.14). They provide bidirectional charging with a simple, inexpensive configuration. During the charging mode transistors are in the off state, and one (for the half-bridge) or two (for the full bridge) diodes conduct in each half-period. During the battery discharging mode (V2G mode), the transistors are in the PWM regime.

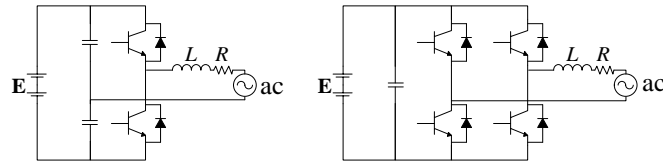


**Fig. 2.14:** Single-phase half-bridge (left) and full bridge (right) PWM rectifiers.

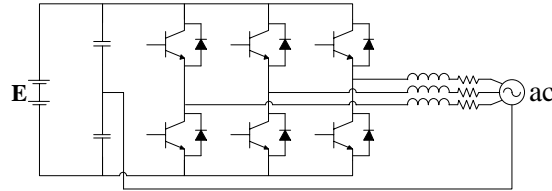


**Fig. 2.15:** Three-phase bridge PWM rectifier with neutral connected to the capacitor mid-point.

A basic topology, for widely-used single-phase chargers, which can be on-board as well, has been presented in Fig. 2.1. This topology differs from the PWM rectifier because the inductor is now located on the dc-side of the bridge and the additional components work like a boost chopper [Erb et al (2010)]. The current taken from the grid can be almost sinusoidal and in phase with the grid voltage; hence the name, “power factor correction (PFC) rectifier”. There are alternative versions of this topology, which use transistors in the bridge, thus allowing a bidirectional operation.

Three-phase chargers are today very popular because they can provide fast charging [Jinrong and Lee (2000)]. A typical three-phase non-integrated on-board charging configuration is shown in Fig. 2.15. The manner of operation during the charging mode is similar to the single-phase half-bridge charger. During the discharging mode (V2G operation), the circuit operates like three independently controlled single-phase circuits that share the same dc supply. Different three-phase solutions that vary very little from the presented solution are possible, like a bridge PWM rectifier with neutral connected to the fourth leg, a three-level PWM rectifier, or the same chargers with various dc-dc converters inserted between the capacitors and the battery.

Standard chargers need bulky inductors and other power electronics components, which occupy the space and increase the cost and the weight of a vehicle. A possibly advantageous solution is therefore to use existing power electronic components and to integrate them into the charging system. Integrated chargers are presented in the following subsections.

### 2.3.2 Solutions with only inverter integration

The idea of integrating a propulsion inverter into the on-board charging power electronics of a vehicle is practically three decades old. A patent [Slicker (1985)] describes an integrated charger in which during the charging mode a control circuit disables all but one of the electronic switches in the inverter. The remaining electronic switch of the inverter is a part of a fly-back dc-dc converter circuit for charging the battery. Charging was from a single-phase source and a diode bridge rectifier was used for rectifying the ac voltage.

Another integrated inverter based solution is presented in [Rippel (1990)]. A three-phase bridge inverter in the propulsion mode is used for controlling an ac traction motor. In the charging mode it is used as a part of a regulated battery charger, without any need for circuit reconfiguration and with a low number of additional components. The integrated apparatus includes the three-phase bridge inverter, a capacitor, a line filter, a line rectifier, and a control circuit (Fig. 2.16). Elements contained within one phase leg of the inverter are used to operate it as a boost-regulated battery charger with the unity power factor operation. During the charging mode, all other power switches, except of one phase leg, are kept off at all times by the control circuit. It is not necessary to disconnect the motor during the charging process, because there is no return path for the current flow through the motor. Current flow to the filter on the ac side during the propulsion mode is prevented by diodes of the bridge rectifier.

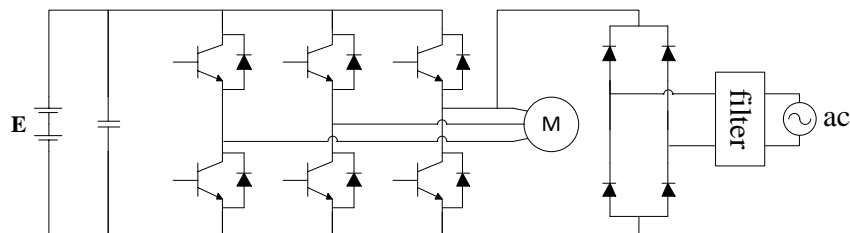


**Fig. 2.16:** Integrated battery charger using a single inverter leg.

A single-phase integrated charging solution, which uses two inverter legs and is capable of V2G and charging operation, is elaborated in [Surada and Khaligh (2010)]. The system utilises a three-phase inverter and a bidirectional dc-dc converter (Fig. 2.17). The motor needs to be disconnected from the system during the charging operation. It is

shown that the system efficiency is not lower than in non-integrated on-board solutions. The main drawback of the solution is that it is obtained by using a number of elements for system reconfiguration, while only two inverter legs are integrated into the on-board charger.

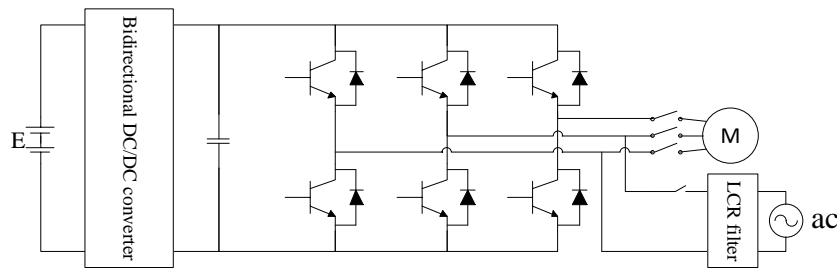


**Fig. 2.17:** Integrated battery charger using two legs of the inverter.

A reactive power compensation study using a dc-link capacitor of an integrated inverter is reported in [Kisacikoglu et al (2010)]. The compensation happens during the charging process. Active power V2G transfer was not considered for a number of reasons: it might not be accepted by customers due to safety concerns, it can decrease a battery lifetime and customer would have a reduced available energy of the battery. It is shown that a reactive power control does not cause a degradation of the battery life. This is because the dc-link capacitor is sufficient for supplying full reactive power for level 1 (up to 1.8 kW) charging, so that the battery is not engaged in the reactive power transfer.

A multilevel converter for battery charging is described in [Josefsson et al (2010)]. Here, it is proposed to integrate power electronics with the battery system, and to use a switch for disconnecting the motor and connecting the ac power supply to the converter system. The converter system is made of multiple dc sources, each connected in H-bridge configuration. Hence, the multilevel converter system made of “N” H-bridges with equal voltage sources can provide “ $2N+1$ ” voltage levels. One phase of the system is depicted in Fig. 2.18. In a common vehicle application the IGBT technology is commonly used due to the battery voltage level, which is kept at several hundred volts in order to reduce the current level. Using the multilevel converter, the energy source is split into several sources, therefore, thanks to the reduced voltage, other semiconductor technologies, like the MOSFET technology, can be used. The multilevel converter consisting of 12 H-bridge boards, which is designed and built for the purpose of the verification of the proposed solution, shows that at low loads and low currents, the MOSFET power losses are low, and at higher loads the losses increase with the square of the current. With an increased number of levels, the total loss increases. Also, it is shown that it could be beneficial to mix energy optimized dc sources with power optimized ones. That is because during the charging mode, a current through the dynamic resistance of the battery (power losses) will slowly increase in the power optimized battery, while the dynamics are much faster in the energy optimized battery. It even might be beneficial to mix super capacitors and battery sources. A new control algorithm is needed to control the converter. It is possible to increase the expected lifetime of the energy source by making the battery temperature distribution uniform along its length by moving the losses to more desirable parts of the battery stack. A fault-tolerant operation is also possible. In addition to the advantages, there are many drawbacks, first of which is a much higher number of semiconductors than the standard 3-level H-bridge configuration. This increases the cost of the solution. There has been little or no work done on the energy utilization or the efficiency optimization using multilevel converters, so it is not yet clear if this multilevel technology can be introduced in a vehicle operation.

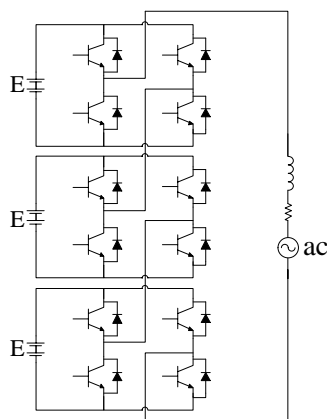


**Fig. 2.18:** One phase of a multilevel integrated charger.

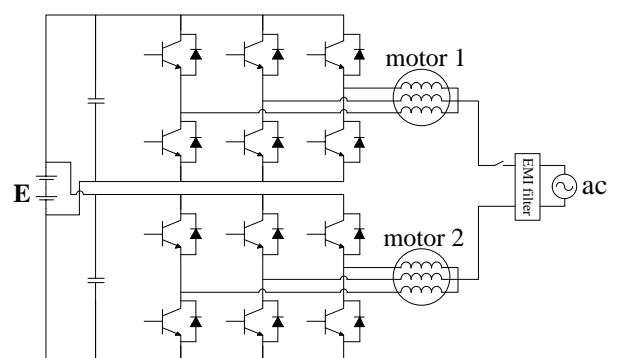


**Fig. 2.19:** Charger based on use of neutral points of the two motors.

### 2.3.3 Single-phase chargers with integrated inverter and motor

One of the first solutions for using motor windings for charging purposes was presented as an additional aspect in the patent [Slicker (1985)], which has already been discussed in the previous subsection.

An integral-type battery charger using the propulsion inverter was reported in [Thimmesch (1985)]. It was implemented using thyristors. The reported charger efficiency was 86%, with the power factor of 0.95. The circuit included four circuit breakers that had to be operated manually.

In the solution described in [Rippel and Cocconi (1992)] the drive and charging system included a bidirectional dc power source, two voltage-fed inverters, two induction motors, and a control unit (Fig. 2.19). In the propulsion mode, each inverter is controlled in such a manner that equal torques are produced by the two motors. This way of control is independent of the motor speed, thus the need for a mechanical differential is eliminated. In the charging mode, a single-phase power is applied through the two neutral points of the two motors. This solution is bidirectional, thus, a battery power can be transferred to the grid. In the same patent an alternative scheme is also presented, which operates using exactly the same principle and with a single motor having two sets of windings.

A similar topology is discussed in [Lixin and Gui-Jia (2009)]: two inverters designed to drive the main and auxiliary motors were used as an ac-dc converter, while two three-phase motors were used as inductors for the converter with their neutral points connected to the grid for charging the battery. The auxiliary motor is proposed to be a three phase air compressor drive motor, water pump motor or even a generator. Control is achieved by switching the three legs of either inverter on and off at the same time. An improved solution for control is presented in [Gui-Jia and Lixin (2010), Lixin and Gui-Jia (2010)], where an interleaved PWM scheme is used to increase the effective frequency of the grid current's ripple. It is shown that the amplitude of the grid current ripple is much smaller than the individual phase current ripple because of the cancellation, while its frequency is three times higher than the one of the individual phase current ripple.

In the solution given in [Cocconi and Calif (1994)] a powertrain employs a conventional three-phase inverter and a motor, in addition to some relays for disconnecting the third phase winding of the motor from the inverter and connecting it to the grid (Fig. 2.20). In the charging mode inverter operates as a boost switching regulator and near-unity power factor operation can be achieved. This solution is bidirectional. The main drawback is the necessity for three relays for the mode changeover. This solution is currently used in industry.

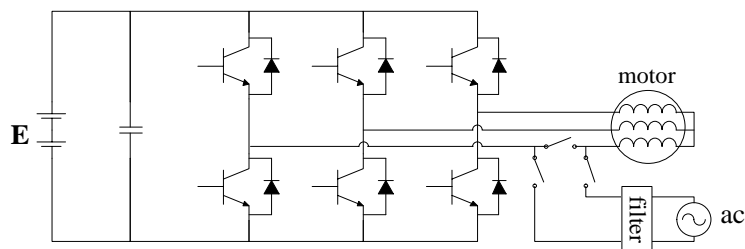


**Fig. 2.20:** Charger using all three phase windings of the motor.

Charging solution presented in [Sang Joon and Seung Ki (1994), Seung-Ki and Sang-Joon (1995)] uses a mechanical transfer switch, four inverters, four motors, and a battery (Fig. 2.21). In the traction mode motors operate in the standard manner. In the charging mode a single-phase ac source is connected between the two neutral points of two motors. The other two motors are employed during the charging process as a part of two buck-type converters. During the charging process electromagnetic torque is not developed in any of the motors because the same currents flow through each of the three phases. The upper three IGBTs and the lower three IGBTs of each inverter are turned on and off simultaneously, as a single power switch. In this case the motor can be represented only with the stator leakage inductance and the stator resistance. The effect of the stator resistance can be neglected without much error. This solution is very expensive and only applicable for vehicles with four propulsion motors.

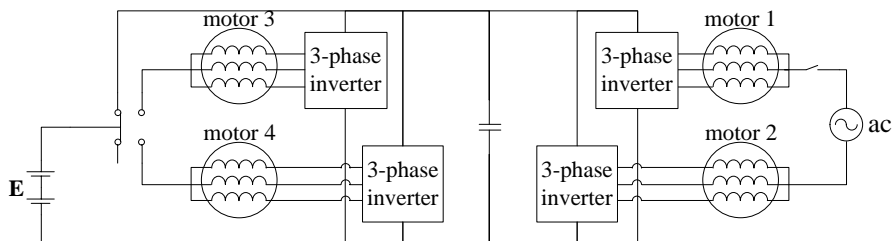


**Fig. 2.21:** Charger based on use of neutral point connection and four propulsion motors.

A single-motor charging solution is elaborated in [Solero (2001)]. As noted already, the charger was installed on-board an electric scooter prototype. The current control of the charging process is achieved by simultaneously switching the negative dc-bus rail connected IGBTs, while keeping the positive-bus IGBTs continuously in the off state. The use of the three paralleled IGBTs results in a reduction of the conduction loss and increased efficiency in comparison to the case when a single IGBT is used. The motor windings in unipolar configuration are used as the inverter input inductance. The only power devices added to the original motor drive arrangement are the mains rectifier and a line-frequency LC filter. The charger configuration is presented in Fig. 2.22.

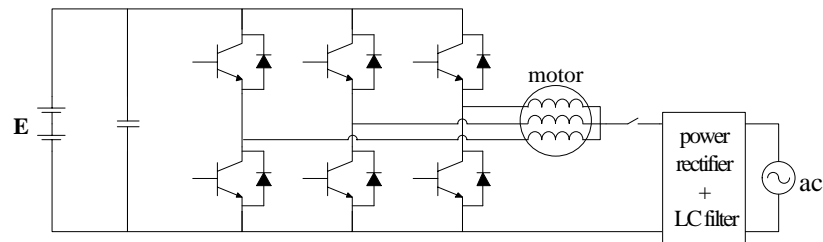


**Fig. 2.22:** Charger connected to the neutral point of a single motor.

A similar solution to the previous one was described recently in [Pellegrino et al (2009a), Pellegrino et al (2009b), Pellegrino et al (2010)]. A dc-dc converter stage was added to the system. It consists now of an induction motor drive plus a dc-dc bidirectional stage, and extra hardware components like single-phase rectifier bridge with a mechanical switch, small capacitor, an EMI filter, and the device for measuring the rectified voltage. In the charging mode, in contrast to the previous solution, the inverter is used as an interleaved PFC boost rectifier. The input current is regulated by controlling the common-mode voltage of the inverter. Multiphase interleaved converters with coupled inductors have been shown to have very low current ripple and high dynamics and they are particularly suited for use as single phase PFC rectifiers.

A comparison of few on-board and off-board solutions is presented in [Lisheng et al (2008)]. It compares solutions using two motors and two inverters with solutions using single motor and inverter, and concludes that the single-motor option is preferable due to the easier control.

In [Dong-Gyun et al (2011)] some integrated solutions are compared. First, the series type of a conversion system of HEVs is compared with the parallel type. It is shown that series type is preferable because the vehicle operates in a high efficiency area for longer time regardless of the speed, and in the pure electrical mode it does not need to overcome the engine load (friction). Then, topologies with one or two integrated inverters, with zero vector control method or interleaving control method, are assessed. The manner of operation of the zero vector control method is that the three bottom switches of each inverter are controlled simultaneously. Therefore, the same currents flow in all three inverters legs. In the interleaving method, PWM signals for the bottom switches of the inverters are shifted by 120 degrees, so that each phase current waveform is also shifted by 120 degrees. The solution which uses one inverter has a diode rectifier, which is a big disadvantage. It is concluded that the solution with two integrated inverters using the interleaving method is the one with the lowest input current ripple. Finally a buck-PFC topology with a bi-directional dc-dc converter is compared with the previous four, and it is shown that although it can eliminate switching losses due to the inverters, it has higher input current THD, which is around 21%, and higher ripple of the battery voltage, so it is an inferior solution in comparison to the previously assessed ones.

An electric air conditioner system with an on-board charger for plug-in hybrid EV (PHEV) is presented in [Jianing et al (2011)]. A novel switched reluctance motor (SRM) converter topology with integrated driving and charging function is proposed. In addition to the standard propulsion power electronics components it uses a line filter, a rectifier, one transistor and three diodes which connect power supply to the motor windings. In the charging mode, the phase windings which are used as energy storage element form a buck-boost converter to satisfy the charging characteristics and the power quality requirements of the grid. When the voltage of the battery is higher than the peak value of the input voltage, the converter operates in the boost mode, and when the voltage of the battery is lower than the peak value of the input voltage, it operates in the buck mode. All three windings are used during charging process.

An integrated battery-powered SRM drive with voltage-boosting and on-board PFC charging is presented in [Hung-Chun and Chang-Ming (2009)] and [Hung-Chun and Chang-Ming (2011)]. The dc-dc boost converter is used in the propulsion mode, but not during the charging (Fig. 2.23). A switch is used to reconfigure the system from charging mode to traction mode and vice versa. In the charging mode two motor windings are used as input filters for Graetz rectifier, and the third motor winding is employed as the energy storage component of the buck-boost converter. The fourth motor winding is not used during charging.

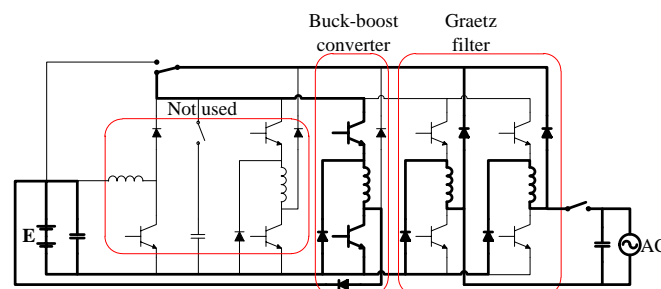


**Fig. 2.23:** Charger integrated with SRM drive.

### 2.3.4 Three-phase chargers with integrated inverter and motor

Probably the first solution which uses windings of a single machine for the three-phase charging is the one described in [Kinoshita (1997)] (Fig. 2.24). A very similar idea has also been published much more recently in [Stancu et al (2004)]. In the charging mode motor three-phase windings are in an open-end winding configuration. At one side they are connected to the three legs of the inverter, while the other three winding terminals at the other side are connected to a three-phase grid. In the propulsion mode the windings are connected to the three legs of the inverter in the same manner, but they are short-circuited at the other side, making the star connection with isolated neutral point. Leakage inductances of the motor windings can be used in this way as a voltage filter during the charging process. In order to prevent an electric shock to a human during the charging operation, the body of the electric vehicle, which one may touch during the charging operation, is grounded so that the body is kept at the ground potential. Although providing probably the first solution for the 3-phase charging process using one motor, like every pioneering solution, this one has some major drawbacks. They include the need for switches in order to change the mode of operation, the necessity for a high current relay to connect the ac grid to the electrical machine's windings, and, worst of all, development of the rotating field during the charging mode, so that the motor must be mechanically locked during the charging process.

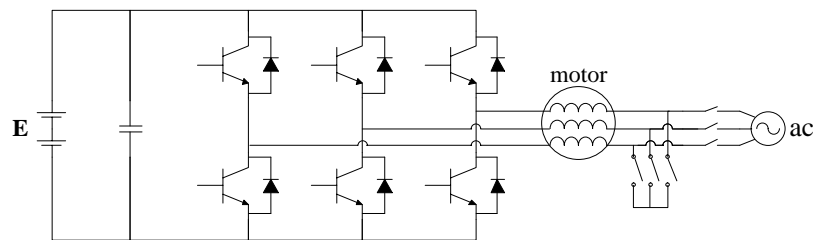


**Fig. 2.24:** Non-isolated three-phase charging solution.

An isolated solution for three-phase charging is presented in [Lacressonniere and Cassoret (2005)] (Fig. 2.25). In order to provide a galvanic isolation, an induction machine is used like a transformer in the battery charging mode of operation. For this purpose, a special wound rotor is required. The rotor winding is connected to a contactor which connects it to the grid in the charging mode and into the star connection in the propulsion mode. Stator windings are continuously connected to an inverter, which is operating as a PWM rectifier in the charging mode. The rotor has to be mechanically locked during the charging mode, because the motor creates a torque which is capable of moving the rotor. Although this configuration has few advantages due to the galvanic isolation and a low harmonic distortion of a current, it still has major drawbacks in terms of an extra cost of a wound rotor and the need for contactors.

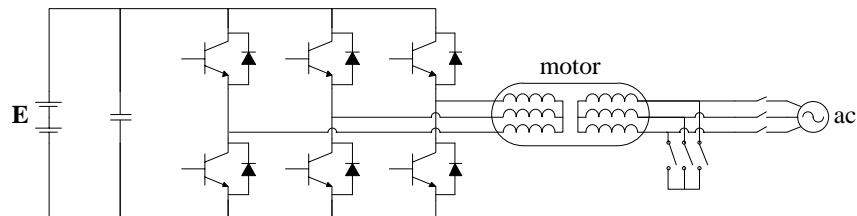


**Fig. 2.25:** Isolated three-phase charging solution.

In 2010, two major solutions were presented, one by Saeid Haghbin and the other by Luis De Sousa. Both are protected by patents. Haghbin's is covered by a Swedish and a European patent [Haghbin and Alakula (2010), Haghbin (2011)] which are currently being extended into a US patent, and De Sousa's is covered by two international patents [De Sousa and Bouchez (2010b), De Sousa and Bouchez (2010a)]. Because of the importance of these two leading solutions and a number of papers that derived from them, each solution will be separately discussed to a greater extent below.

Haghbin has proposed an interesting isolated solution for three-phase charging [Haghbin et al (2011)]. It is based on a special configuration of the stator windings (Fig. 2.26). The solution is applicable for different machine types, but all of them have to have the same stator configuration. That is why in this paragraph the focus will be only on the stator configuration, and the rotor configuration will be discussed in the next paragraph. Stator has two sets of three-phase windings (Fig. 2.26), which are shifted spatially by 30 degrees (split-phase or asymmetrical six-phase configuration). Hence, for a two-pole machine there are six windings shifted symmetrically around the stator periphery. In the traction mode each pair of phases of the two three-phase windings that has spatial shift of 30 degrees is connected in series to constitute a single three-phase winding set. The motor is powered from a battery through an inverter. For the charging mode the system requires reconfiguration. The first set of three-phase windings is connected to the inverter on one side, and into the star on the other side, while the second set is connected into delta on one side, and to the grid at the other side. In this manner the inverter is still able, if needed, to control the machine as a classical motor using one

set of windings. A relay-based device is used for winding reconnection, and a contactor is used for connection to the grid. The inverter-side windings pick up the induced voltage due to the developed flux inside the machine. The inverter uses this isolated voltage source to charge the battery. To have a proper boost converter operation, a dc-bus voltage should be higher than the peak of ac line voltage. To obtain this, the star-delta connection for the sets of windings is chosen (star connection is on the set that is connected to the inverter), instead of an additional dc-dc converter. This solution has bidirectional capability so it is possible to feed the battery power back to the grid. A unity power factor operation is feasible.

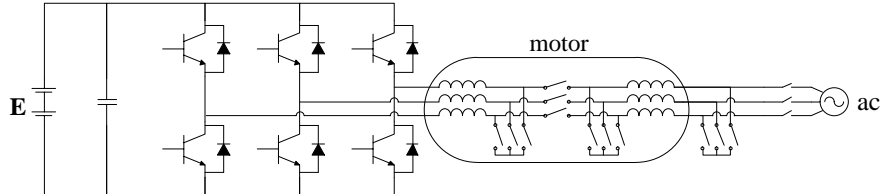


**Fig. 2.26:** Isolated three-phase charging solution with two sets of three-phase stator windings.

A few rotor configurations are possible for Haghbin's solution, thus making the use of an induction, permanent magnet (PM) synchronous, or PM assisted synchronous reluctance machine feasible (PMASynRM) [Khan et al (2010), Shuang et al (2011)]. If the rotor has permanent magnets, then, because of the torque development, it will rotate at a synchronous speed. This is a disadvantage because of the audible noise, increased wear, and the need for a clutch to disconnect the motor-generator system from the power system during charging. During the rotor rotation at synchronous speed, the magnets will induce voltages in the inverter-side windings that emulate an isolated PM ac generator for the inverter. The inverter-side windings will pick up the induced voltage due to the developed flux inside the machine. The inverter can use this isolated voltage source to charge the battery by means of the machine inductances as a converter energy storage component (yielding a three-phase boost converter). Synchronization of the machine to the grid is needed, so inverter has to drive the motor from its side while the grid side windings are opened. At this point voltage measurement is needed to see if the induced voltage has synchronized with the grid, thus additional measurement device must be used [Haghbin et al (2011)]. After the synchronization, the grid side windings are closed and the inverter controls the inverter side winding voltages to charge the battery. It is shown in [Haghbin et al (2010a)] that it is possible to have a unity power factor operation, and the current and torque control. In [Haghbin et al (2010b)] it is shown that the same solution can be used for charging from the single-phase grid supply. In every solution the charging power is limited by the motor thermal limit, the inverter power limit and the limit of the supply. Therefore, the charging power is restricted to the half of the traction power (because of the motor thermal limit), and this is the major drawback.

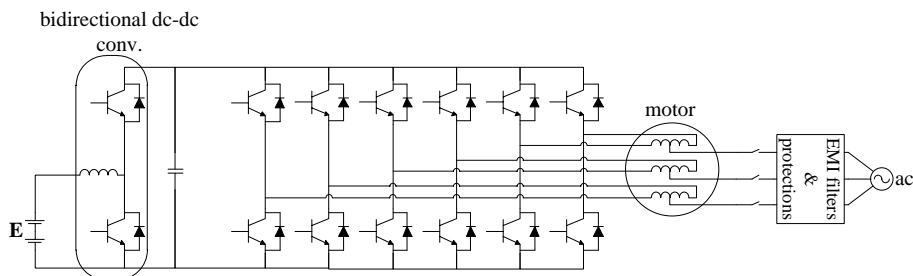


**Fig. 2.27:** Three-phase charger with access to the mid-point of each phase.

De Sousa proposed a completely different charger topology. The solution uses mid-points of each of the three windings of a three-phase machine to connect them to a three-phase ac grid during charging (Fig. 2.27). There is no need for hardware reconnections for changing the mode of operation (propulsion-charging). Terminals of the machine windings are connected to three H-bridge inverters with common dc link. In this manner a full magnetic decoupling between the rotor and the stator during the charging process is obtained. The grid connection is made through small EMI filters and other protections, therefore no relay is necessary. The ac socket and the filters do not disturb the system during propulsion mode. On the whole stator, the magnetomotive force (MMF) is cancelled because the current of one split-phase coil cancels the effect of the other one. Hence, no rotation of the rotor is possible even if permanent magnets are mounted. Some slight vibrations due to an unbalanced rotor mass or an unbalanced current sharing may take place [De Sousa et al (2010)]. In the charging mode, the inverter is used like a PFC boost rectifier. The addition of a step-up front end converter (FEC) between the battery and the inverter globally reduces the Silicone Surface Ratio (SSR), up to 39% in comparison to the topology which uses a bridgeless inverter directly fed by a battery. The dc link voltage is set to a much higher value than the maximum battery voltage, and can be adjusted according to the back-EMF of the electrical machine. It is shown that a significant switching loss reduction is possible at low speeds if the dc-bus value decreases for this regime (which is possible only if the adjustable dc link voltage is used). A special winding arrangement is necessary because if the MMF is locally cancelled, in the same slot for example, the apparent inductance

in the charging mode is similar to the leakage inductance, which is too low for a proper charger operation. The main drawback of the proposed topology is related to the control. The stator of the machine has to be designed with an acceptable zero-sequence inductance. A special care regarding the zero-sequence current is needed [Bruyère et al (2010), De Sousa and Dogan (2011)]. A special space-vector approach for controlling the 6-leg VSI is proposed in [Sandulescu et al (2011)]. It is implemented on FPGA chips in order to preserve the parallelism of the algorithm and fulfil execution time constraints. It is shown in [Lacroix et al (2010)] that the same topology can be used for the single-phase battery charging, where only two H-bridges of the inverter and two phases of the motor are used for the charging process.

### 2.3.5 Comparison of solutions

Various solutions, surveyed so far, have very differing characteristics. An attempt is made here to provide a comparative insight into main advantages and shortcoming of each configuration. The summary is provided in Table 2.1.

**Table 2.1:** Main characteristics of the surveyed battery chargers for EVs.

	<b>Three-phase charging</b>	<b>V2G</b>	<b>No rotating field</b>	<b>High efficiency</b>	<b>Low cost</b>	<b>No connection changeover</b>
1. Single-phase half-bridge and full bridge PWM rectifiers (Fig. 2.14)	✗	✓	not applicable	✓	✗	✓
These are the most basic configurations for single-phase chargers. Although they have very simple and inexpensive configuration, they do not take advantage of using the existing propulsion power electronics for charging, and thus cannot be assessed as being a low cost charging solutions.						
2. Single-phase PFC rectifier (Fig. 2.1)	✗	✗	not applicable	✓	✗	✓
There are many similar configurations which use two or four transistors in the bridge. They lose the simplicity of the solution, but gain possibility of more control and the V2G operation.						
3. Three-phase bridge PWM rectifier with neutral connected to the capacitor mid-point (Fig. 2.15)	✓	✓	not applicable	✓	✗	✓
This is a basic configuration for three-phase on-board non-integrated chargers. Many different three-phase solutions that vary very little from the presented solution are possible, like a bridge PWM rectifier with neutral connected to the fourth leg, a three-level PWM rectifier, or the same chargers with various dc-dc converters inserted between the capacitors and the battery.						
4. Integrated battery charger using a single inverter leg (Fig. 2.16)	✗	✗	not applicable	✓	✗	✓
This solution does not need system reconfiguration between the propulsion and the charging mode. However, it uses additional elements like a diode bridge and a filter and does not use existing windings of the propulsion motor as input inductance.						
5. Integrated battery charger using two legs of the inverter (Fig. 2.17)	✗	✓	not applicable	✓	✗	✗
In the charging mode, this solution acts like a full bridge PWM rectifier, and it allows V2G operation. However, switching elements must be used to completely disconnect the motor during the charging mode of operation, and an additional winding must be used to filter the current.						
6. Multilevel integrated charger (Fig. 2.18)	✓	✓	not applicable	✓	✗	✗
Instead of one high voltage source, several sources are providing reduced voltage, and thus other semiconductor technologies (e.g. MOSFET) can be used. This solution has a possibility of fault-tolerant operation in addition to a possibility of mixing different kinds of power sources, which can be beneficial to the system efficiency. The main drawback is the necessity for a high number of semiconductors. It is at present not clear whether this topology will find a place in the vehicle industry.						
7. Charger based on use of neutral points of the two motors (Fig. 2.19)	✗	✓	✓	✓	✗	✓
During the charging process a rotating field is not developed in any of the motors because the same current flows through each of the three phases. A mechanical differential is not necessary because in the drive mode two motors are controlled to provide the same torques. However, this solution demands two inverters and two motors.						

8. Charger using all three phase windings of the motor (Fig. 2.20)	✗	✓	✓	✓	✓	✗
	With this configuration bidirectional operation with near unity power factor operation can be achieved, and rotating field is not developed during the charging. This solution is currently used in the car industry.					
9. Charger based on use of neutral point connection and four propulsion motors (Fig. 2.21)	✗	✓	✓	✓	✗	✗
	This solution is very expensive and can be used only for very specific drives which have four motors (four-wheel drives), which is currently not the case in the EV car industry.					
10. Charger connected to the neutral point of a single motor (Fig. 2.22)	✗	✗	✓	✓	✓	✓
	This topology allows only slow charging because three motor winding are in the parallel configuration resulting in a small value of the input inductance.					
11. Charger integrated with SRM drive (Fig. 2.23)	✗	✓	✗	✓	✓	✗
	This solution is providing high charging performance with almost unity power factor and low current THD.					
12. Non-isolated three-phase charging solution (Fig. 2.24)	✓	✓	✗	✗	✓	✗
	This solution does not take care of the developed rotating flux during the charging mode. Thus it is necessary to mechanically lock the motor during this mode of operation. Rotating field is also causing low system efficiency due to the induced rotor currents.					
13. Isolated three-phase charging solution (Fig. 2.25)	✓	✓	✗	✗	✗	✗
	This solution, although providing isolated charging, is still very expensive due to the increased cost of the wound rotor in comparison to the squirrel cage rotor.					
14. Isolated three-phase charging solution with two sets of three-phase stator windings (Fig. 2.26)	✓	✓	✗	✗	✓	✗
	This solution provides low cost isolated charging and thus might be interesting for the car industry. Efficiency can be improved, but then machine would have to rotate during the charging mode, causing the audible noise, increased wear, and the need for a clutch to disconnect the motor from the transmission system during charging.					
15. Three-phase charger with access to the mid-point of each phase (Fig. 2.27)	✓	✓	✓	✓	✓	✓
	Split-phase windings cancel each other's field. Thus no field is developed in the machine during charging mode. Moreover, the same configuration is used for traction and charging. This solution has a potential to be used in the car industry.					

Finally, power levels of chargers from this chapter should be addressed. While non-integrated chargers have charging power levels (some of them classified in [Yilmaz and Krein (2011)]) independent of propulsion power, this is not the case with integrated chargers. Currents that flow through a machine during integrated charging process cannot exceed their ratings for propulsion mode. Thus, if voltage levels for propulsion and charging mode of operation are taken as similar, the similarity manifests through similarity between their power ratings. Therefore, integrated chargers can achieve high charging powers, and they do not require any modification of power rating of propulsion drivetrain.

Single-phase integrated chargers have charging powers lower than those for propulsion. The reason originates in difference between single-phase and three-phase energy transfer process. On the other hand this difference is irrelevant since the main limitation comes from power rating of a single-phase voltage source. Three-phase integrated chargers do not have this problem, and their charging powers are similar to those for propulsion. The exception is the solution from Fig. 2.26 (no. 14 in Table 2.1), with charging power that cannot exceed one half of the propulsion power, as explained above.

## 2.4 Conclusion

The literature review, provided in this chapter, has surveyed the state-of-the-art in battery chargers for electrical vehicles. Both off-board and on-board battery chargers have been discussed. Additionally, a comprehensive quantitative comparison of the described on-board topologies is made, which identifies the advantages and shortcomings of each solution.

## CHAPTER 3: TOPOLOGIES OF MULTIPHASE MACHINES AND SUPPLY FOR INTEGRATED PROPULSION MOTOR/ON-BOARD BATTERY CHARGER

### 3.1 Introduction

On the basis of the literature survey of the available topologies for the integrated propulsion motor/on-board battery charger, reported in Chapter 2, it is obvious that there is at present a single topology that in essence uses a multiphase (symmetrical six-phase) machine in conjunction with a three-phase mains supply in the charging mode. The purpose of this chapter is to propose other possible configurations, based on the multiphase drive system topology, which can be used in an integrated battery charger/propulsion motor system. All the considerations of this chapter are purely theoretical and are based on the analysis of the multiphase machine current flow in the charging configuration for any selected topology. In essence, the starting point is in all cases the decoupling transformation matrix for a multiphase ( $n$ -phase) system, which is given for any symmetrical multiphase machine (i.e. a machine with equidistant spatial distribution of phases, such that any two consecutive phases are shifted by  $\alpha = 2\pi/n$ ) with [Levi et al (2007)]

$$[C] = \sqrt{\frac{2}{n}} \begin{bmatrix} \alpha & 1 & \cos \alpha & \cos 2\alpha & \cos 3\alpha & \dots & \cos 3\alpha & \cos 2\alpha & \cos \alpha \\ \beta & 0 & \sin \alpha & \sin 2\alpha & \sin 3\alpha & \dots & -\sin 3\alpha & -\sin 2\alpha & -\sin \alpha \\ x_1 & 1 & \cos 2\alpha & \cos 4\alpha & \cos 6\alpha & \dots & \cos 6\alpha & \cos 4\alpha & \cos 2\alpha \\ y_1 & 0 & \sin 2\alpha & \sin 4\alpha & \sin 6\alpha & \dots & -\sin 6\alpha & -\sin 4\alpha & -\sin 2\alpha \\ x_2 & 1 & \cos 3\alpha & \cos 6\alpha & \cos 9\alpha & \dots & \cos 9\alpha & \cos 6\alpha & \cos 3\alpha \\ y_2 & 0 & \sin 3\alpha & \sin 6\alpha & \sin 9\alpha & \dots & -\sin 9\alpha & -\sin 6\alpha & -\sin 3\alpha \\ \dots & \dots \\ x_{\frac{n-4}{2}} & 1 & \cos\left(\frac{n-2}{2}\alpha\right) & \cos 2\left(\frac{n-2}{2}\alpha\right) & \cos 3\left(\frac{n-2}{2}\alpha\right) & \dots & \cos 3\left(\frac{n-2}{2}\alpha\right) & \cos 2\left(\frac{n-2}{2}\alpha\right) & \cos\left(\frac{n-2}{2}\alpha\right) \\ y_{\frac{n-4}{2}} & 0 & \sin\left(\frac{n-2}{2}\alpha\right) & \sin 2\left(\frac{n-2}{2}\alpha\right) & \sin 3\left(\frac{n-2}{2}\alpha\right) & \dots & -\sin 3\left(\frac{n-2}{2}\alpha\right) & -\sin 2\left(\frac{n-2}{2}\alpha\right) & -\sin\left(\frac{n-2}{2}\alpha\right) \\ 0_+ & 1/\sqrt{2} & 1/\sqrt{2} & 1/\sqrt{2} & 1/\sqrt{2} & \dots & 1/\sqrt{2} & 1/\sqrt{2} & 1/\sqrt{2} \\ 0_- & 1/\sqrt{2} & -1/\sqrt{2} & 1/\sqrt{2} & -1/\sqrt{2} & \dots & -1/\sqrt{2} & 1/\sqrt{2} & -1/\sqrt{2} \end{bmatrix} \quad (3.1)$$

If the machine under consideration is not with a symmetrical disposition of stator phases, transformation matrix (3.1) has to be modified. In such a case a universal transformation matrix representation, for all phase numbers with which an asymmetrical winding can be designed, is not possible. Hence transformation matrix will be given separately for each asymmetrical winding phase number (e.g. six, nine, etc.) at the point of first discussion in this chapter.

Three generic cases from the point of view of the ac source supply topology, available for the charging mode, are considered in what follows. These are the multiphase sinusoidal supply (more than three-phases available as the sinusoidal or near-sinusoidal source), single-phase mains supply, and three-phase mains supply. In all considered topologies it is required that the motor does not develop torque during charging, so that the machine naturally stays at standstill and its stator winding leakage inductances are utilised for filtering during the charging process.

### 3.2 Multiphase supply

At present charging takes place with either single-phase or three-phase mains supply and these two possibilities will be analysed in the next two sections. In this section it is assumed that the charging station is equipped with a multiphase supply system ( $n > 3$ ) and this is a scenario that is currently futuristic but may become realistic some time in future.

A multiphase supply in the charging station can be obtained in different ways. The simplest one would be based on a three-phase to  $n$ -phase transformer. Such transformer configurations are currently known for, for example, three-phase to five-phase transformers [Iqbal et al (2010)] and three-phase to seven-phase transformers [Moinoddin et al (2012)]. The alternative solutions would be based on power electronic converters, and would require output voltage filtering. One could use either a three-phase to  $n$ -phase matrix converter [Ahmed et al (2011a), Ahmed et al (2011b), Iqbal et al (2012)] or a two-stage converter with an  $n$ -phase inverter as the output stage. In what follows it is assumed that, whatever the source of the multiphase supply is, the voltages can be regarded as sinusoidal and symmetrical.

The first considered topology is a five-phase propulsion motor, which is star-connected with isolated neutral point in the normal driving cycle. For charging purposes the neutral point of the motor is opened and the phases are connected to the sinusoidal five-phase source. However, instead of connecting the motor phases  $a$  to  $e$  directly to  $a$  to  $e$  phases of the supply, the principle of phase transposition [Levi et al (2004)] is applied. The resulting connection diagram for the charging mode is as shown in Fig. 3.1a. The basic idea here is that in a five-phase machine with sinusoidal spatial magneto-motive force distribution current flow according to Fig. 3.1a connection will not result in the rotating field (and hence there will be no torque developed), since the currents of the supply will map into the non-flux/torque producing plane [Levi et al (2004)]. Basically, the flux/torque producing  $\alpha$ - $\beta$  plane will not be excited, as shown next.

The transformation matrix (3.1) is for a five-phase system given in power invariant form with  $(\alpha = 2\pi/5)$

$$[C] = \sqrt{\frac{2}{5}} \begin{bmatrix} \alpha & 1 & \cos(2\pi/5) & \cos(4\pi/5) & \cos(6\pi/5) & \cos(8\pi/5) \\ \beta & 0 & \sin(2\pi/5) & \sin(4\pi/5) & \sin(6\pi/5) & \sin(8\pi/5) \\ x & 1 & \cos(4\pi/5) & \cos(8\pi/5) & \cos(12\pi/5) & \cos(16\pi/5) \\ y & 0 & \sin(4\pi/5) & \sin(8\pi/5) & \sin(12\pi/5) & \sin(16\pi/5) \\ 0 & 1/\sqrt{2} & 1/\sqrt{2} & 1/\sqrt{2} & 1/\sqrt{2} & 1/\sqrt{2} \end{bmatrix} \quad (3.2)$$

For further considerations, it is convenient to combine the first two rows and the subsequent two rows into space vectors of the two planes, according to ( $f$  stands for any variable that is being transformed, e.g. current, voltage, etc.):

$$\begin{aligned} \underline{f}_{\alpha\beta} &= f_\alpha + jf_\beta = \sqrt{2/5} (f_a + \underline{a}f_b + \underline{a}^2 f_c + \underline{a}^3 f_d + \underline{a}^4 f_e) \\ \underline{f}_{xy} &= f_x + jf_y = \sqrt{2/5} (f_a + \underline{a}^2 f_b + \underline{a}^4 f_c + \underline{a}^6 f_d + \underline{a}^8 f_e) \end{aligned} \quad (3.3)$$

Here  $\underline{a} = \exp(j\alpha) = \cos \alpha + j \sin \alpha$ , where once more  $\alpha = 2\pi/5$ .

For the sake of simplicity, sinusoidal quantities  $f$  are taken further on as currents, and they can be given as

$$\begin{aligned} i_{ag} &= \sqrt{2}I \cos(\omega t) \\ i_{bg} &= \sqrt{2}I \cos(\omega t - 2\pi/5) \\ i_{cg} &= \sqrt{2}I \cos(\omega t - 4\pi/5) \\ i_{dg} &= \sqrt{2}I \cos(\omega t - 6\pi/5) \\ i_{eg} &= \sqrt{2}I \cos(\omega t - 8\pi/5) \end{aligned} \quad (3.4)$$

where  $\omega$  is the angular frequency of the supply and index  $g$  denotes the multiphase currents of the assumed five-phase grid. Substitution of (3.4) into (3.3) and use of the simple relationship  $\cos \delta = (\exp(j\delta) + \exp(-j\delta))/2$ , while having in mind that due to the phase transposition machine currents are related to the grid currents according to

$$i_a = i_{ag} \quad i_b = i_{cg} \quad i_c = i_{eg} \quad i_d = i_{bg} \quad i_e = i_{dg} \quad (3.5)$$

leads to the following space vectors in the two planes of the five-phase system:

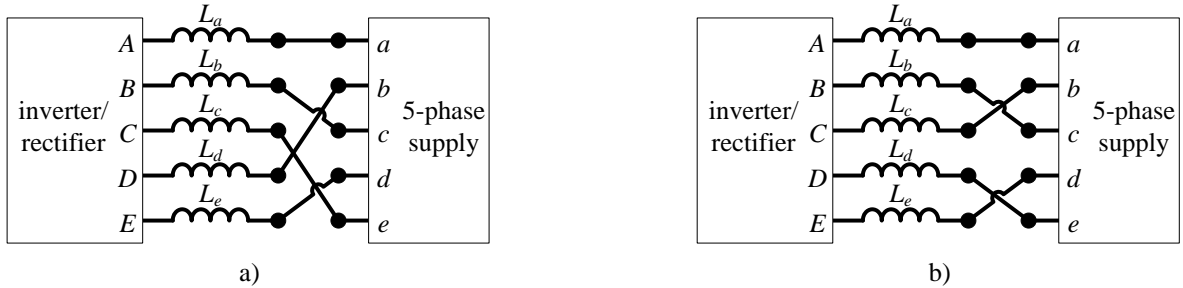


**Fig. 3.1:** a) Supply-to-machine connection according to the phase transposition rule (no field produced in the  $\alpha$ - $\beta$  plane, b) Configuration of connection with pulsating field in the  $\alpha$ - $\beta$  plane.

$$\begin{aligned} i_{\alpha\beta} &= \sqrt{2/5} (1/2) \sqrt{2}I ((\exp(j\omega t) + \exp(-j\omega t)) + \exp(j\alpha)[\exp(j(\omega t - 2\alpha)) + \exp(-j(\omega t - 2\alpha))] + \exp(j2\alpha)[\exp(j(\omega t - 4\alpha)) + \exp(-j(\omega t - 4\alpha))] + \exp(j3\alpha)[\exp(j(\omega t - \alpha)) + \exp(-j(\omega t - \alpha))] + \exp(j4\alpha)[\exp(j(\omega t - 3\alpha)) + \exp(-j(\omega t - 3\alpha))]) \\ i_{\alpha\beta} &= 0 \end{aligned} \quad (3.6)$$

$$\begin{aligned} i_{xy} &= \sqrt{2/5} (1/2) \sqrt{2}I ((\exp(j\omega t) + \exp(-j\omega t)) + \exp(j2\alpha)[\exp(j(\omega t - 2\alpha)) + \exp(-j(\omega t - 2\alpha))] + \exp(j4\alpha)[\exp(j(\omega t - 4\alpha)) + \exp(-j(\omega t - 4\alpha))] + \exp(j6\alpha)[\exp(j(\omega t - \alpha)) + \exp(-j(\omega t - \alpha))] + \exp(j8\alpha)[\exp(j(\omega t - 3\alpha)) + \exp(-j(\omega t - 3\alpha))]) \\ i_{xy} &= \sqrt{2/5} (1/2) \sqrt{2}I (5\exp(j\omega t)) = \sqrt{5}I \exp(j\omega t) \end{aligned} \quad (3.7)$$

Hence it follows from (3.6)-(3.7) that the phase transposition connection of Fig. 3.1a maps grid phase currents into non-flux/torque producing ( $x$ - $y$ ) plane of the machine, while the flux/torque producing currents ( $\alpha$ - $\beta$ ) are identically equal to zero at all times. The machine will therefore remain at standstill if connection of Fig. 3.1a is used.

Zero-sequence component of (3.2) is of course identically equal to zero.

An alternative connection, which does not follow the phase transposition rule, is shown in Fig. 3.1b. It may be also, at least in theory, used. Such a connection produces pulsating field in the first plane, as shown next. The machine  $a$  to  $e$  phases are now supplied with a phase sequence  $a, c, b, e, d$ . The space vectors (3.3) now become

$$\begin{aligned} i_{\alpha\beta} &= \sqrt{2/5}(1/2)\sqrt{2}I((\exp(j\omega t) + \exp(-j\omega t) + \exp(j\alpha))(\exp(j(\omega t - 2\alpha)) + \exp(-j(\omega t - 2\alpha))) + \exp(j2\alpha)(\exp(j(\omega t - \alpha)) + \exp(-j(\omega t - \alpha))) + \exp(j3\alpha)(\exp(j(\omega t - 4\alpha)) + \exp(-j(\omega t - 4\alpha))) + \exp(j4\alpha)(\exp(j(\omega t - 3\alpha)) + \exp(-j(\omega t - 3\alpha)))) \\ i_{\alpha\beta} &= \sqrt{1/5}I\{\exp(j\omega t)[1 + 2\exp(-j\alpha) + 2\exp(j\alpha)] + \exp(-j\omega t)[1 + 2\exp(j3\alpha) + 2\exp(j2\alpha)]\} \\ i_{\alpha\beta} &= \sqrt{1/5}I[\exp(j\omega t)(1 + 4\cos\alpha) + \exp(-j\omega t)(1 + 4\cos 2\alpha)] = \sqrt{1/5}I[\sqrt{5}\exp(j\omega t) - \sqrt{5}\exp(-j\omega t)] \\ i_{\alpha\beta} &= j2I\sin\omega t \end{aligned} \quad (3.8)$$

$$\begin{aligned} i_{xy} &= \sqrt{2/5}(1/2)\sqrt{2}I((\exp(j\omega t) + \exp(-j\omega t) + \exp(j2\alpha))(\exp(j(\omega t - 2\alpha)) + \exp(-j(\omega t - 2\alpha))) + \exp(j4\alpha)(\exp(j(\omega t - \alpha)) + \exp(-j(\omega t - \alpha))) + \exp(j6\alpha)(\exp(j(\omega t - 4\alpha)) + \exp(-j(\omega t - 4\alpha))) + \exp(j8\alpha)(\exp(j(\omega t - 3\alpha)) + \exp(-j(\omega t - 3\alpha)))) \\ i_{xy} &= \sqrt{1/5}I\{\exp(j\omega t)[1 + 1 + \exp(j3\alpha) + \exp(j2\alpha) + 1] + \exp(-j\omega t)[1 + \exp(j4\alpha) + 1 + 1 + \exp(j\alpha)]\} \\ i_{xy} &= \sqrt{1/5}I[\exp(j\omega t)(3 + \exp(j2\alpha) + \exp(j3\alpha)) + \exp(-j\omega t)(3 + \exp(j\alpha) + \exp(j4\alpha))] \\ i_{xy} &= \sqrt{1/5}I[\exp(j\omega t)(3 + 2\cos 2\alpha) + \exp(-j\omega t)(3 + 2\cos\alpha)] = \sqrt{1/5}I[1.3819\exp(j\omega t) + 3.618\exp(-j\omega t)] \\ i_{xy} &= \sqrt{1/5}I[5\cos\omega t - j\sqrt{5}\sin\omega t] = I(\sqrt{5}\cos\omega t - j\sin\omega t) \end{aligned} \quad (3.9)$$

It follows from (3.8)-(3.9) that in the topology of Fig. 3.1b only one axis of the first plane is excited, so that a pulsating field is produced. In the second plane the components are now not of the same magnitude. However, since the second plane does not give torque production and the pulsating field in the first plane cannot produce an average torque, the machine stays at standstill during the charging process. Trajectories described with (3.8)-(3.9) in the two planes are illustrated in Fig. 3.2, taking the current rms value as equal to 1 per unit and grid frequency as 50 Hz.

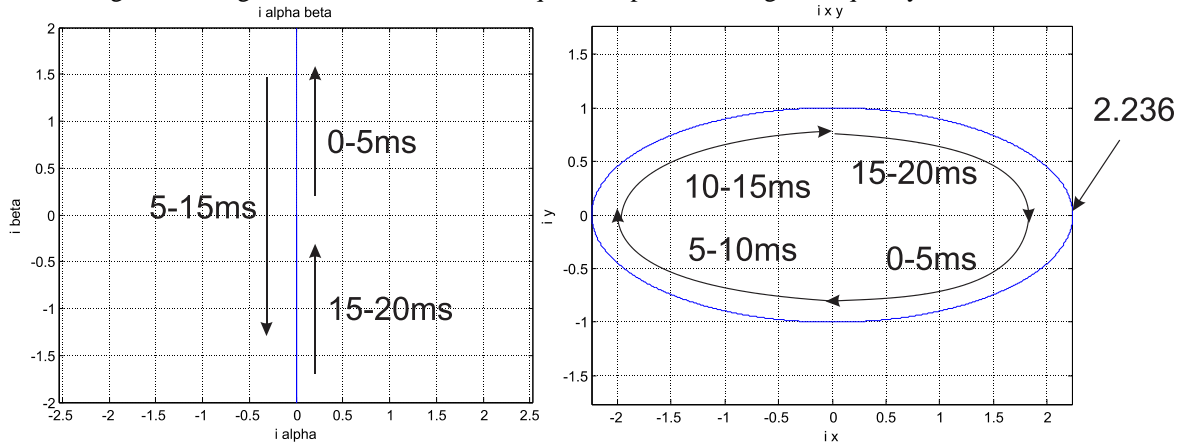


**Fig. 3.2:** Trajectories described with (3.8)-(3.9) in the charging mode of operation, according to Fig. 3.1b.

Consider next a seven-phase machine. Only the situation with phase transposition is now considered, since it is believed to be better suited for potential real-world applications. The configurations for the charging mode are shown in Fig. 3.3. The difference, compared to the five-phase case, is that there are two  $x$ - $y$  planes rather than one (labelled with additional indices 1 and 2). Hence two connections to the grid are possible in charging mode. Once again, charging mode requires opening of the machine's neutral and connection of motor phases to the grid phases, according to the schemes given in Fig. 3.3.

The starting point is again general transformation matrix (3.1), this time for a seven-phase system. The equivalent space vector representation in the form of (3.3) is now given with

$$\begin{aligned} \underline{f}_{\alpha\beta} &= \sqrt{2/7}(f_a + \underline{a}f_b + \underline{a}^2f_c + \underline{a}^3f_d + \underline{a}^4f_e + \underline{a}^5f_f + \underline{a}^6f_g) \\ \underline{f}_{x_1y_1} &= \sqrt{2/7}(f_a + \underline{a}^2f_b + \underline{a}^4f_c + \underline{a}^6f_d + \underline{a}^8f_e + \underline{a}^{10}f_f + \underline{a}^{12}f_g) \\ \underline{f}_{x_2y_2} &= \sqrt{2/7}(f_a + \underline{a}^3f_b + \underline{a}^6f_c + \underline{a}^9f_d + \underline{a}^{12}f_e + \underline{a}^{15}f_f + \underline{a}^{18}f_g) \end{aligned} \quad (3.10)$$

where  $\underline{a} = \exp(j\alpha) = \cos\alpha + j\sin\alpha$  and  $\alpha = 2\pi/7$ . The grid currents are given with

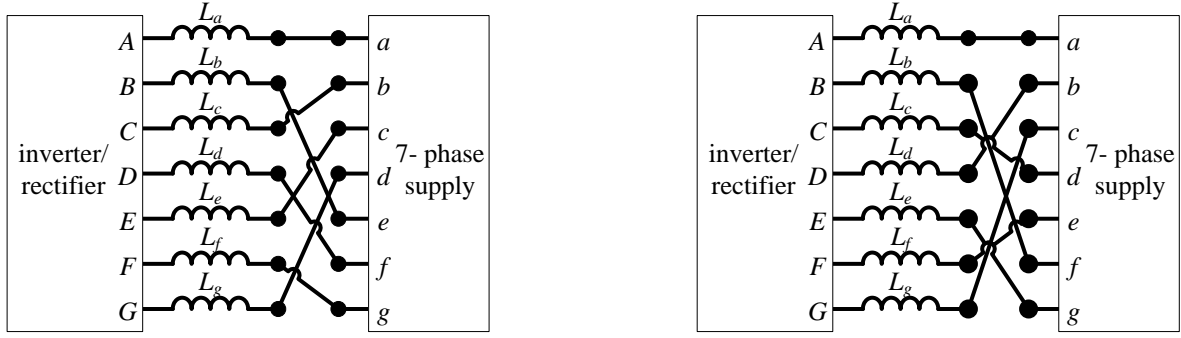


**Fig. 3.3:** Possible connections of a seven-phase machine to the seven-phase supply in charging mode.

$$\begin{aligned}
 i_{ag} &= \sqrt{2}I \cos(\omega t) \\
 i_{bg} &= \sqrt{2}I \cos(\omega t - 2\pi/7) = \sqrt{2}I \cos(\omega t - \alpha) \\
 i_{cg} &= \sqrt{2}I \cos(\omega t - 4\pi/7) = \sqrt{2}I \cos(\omega t - 2\alpha) \\
 i_{dg} &= \sqrt{2}I \cos(\omega t - 6\pi/7) = \sqrt{2}I \cos(\omega t - 3\alpha) \\
 i_{eg} &= \sqrt{2}I \cos(\omega t - 8\pi/7) = \sqrt{2}I \cos(\omega t - 4\alpha) \\
 i_{fg} &= \sqrt{2}I \cos(\omega t - 10\pi/7) = \sqrt{2}I \cos(\omega t - 5\alpha) \\
 i_{gg} &= \sqrt{2}I \cos(\omega t - 12\pi/7) = \sqrt{2}I \cos(\omega t - 6\alpha)
 \end{aligned} \tag{3.11}$$

For the connection diagrams of Fig. 3.3 the correlation between machine phase currents and grid currents is given with

$$i_a = i_{ag} \quad i_b = i_{eg} \quad i_c = i_{bg} \quad i_d = i_{fg} \quad i_e = i_{cg} \quad i_f = i_{gg} \quad i_g = i_{dg} \tag{3.12}$$

and

$$i_a = i_{ag} \quad i_b = i_{fg} \quad i_c = i_{dg} \quad i_d = i_{bg} \quad i_e = i_{gg} \quad i_f = i_{eg} \quad i_g = i_{cg} \tag{3.13}$$

respectively. Substitution of (3.12) into (3.10) gives the following space vectors in the three planes for the first connection of Fig. 3.3:

$$\begin{aligned}
 i_{\alpha\beta} &= \sqrt{2/7} (1/2) \sqrt{2}I \{ \exp(j\omega t) + \exp(-j\omega t) + \exp(j\alpha)[\exp(j(\omega t - 4\alpha)) + \exp(-j(\omega t - 4\alpha))] + \exp(j2\alpha)[\exp(j(\omega t - \alpha)) + \exp(-j(\omega t - \alpha))] \\
 &\quad + \exp(j3\alpha)[\exp(j(\omega t - 5\alpha)) + \exp(-j(\omega t - 5\alpha))] + \exp(j4\alpha)[\exp(j(\omega t - 2\alpha)) + \exp(-j(\omega t - 2\alpha))] + \\
 &\quad + \exp(j5\alpha)[\exp(j(\omega t - 6\alpha)) + \exp(-j(\omega t - 6\alpha))] + \exp(j6\alpha)[\exp(j(\omega t - 3\alpha)) + \exp(-j(\omega t - 3\alpha))] \} \\
 i_{\alpha\beta} &= 0
 \end{aligned} \tag{3.14}$$

$$\begin{aligned}
 i_{x1y1} &= \sqrt{2/7} (1/2) \sqrt{2}I \{ \exp(j\omega t) + \exp(-j\omega t) + \exp(j2\alpha)[\exp(j(\omega t - 4\alpha)) + \exp(-j(\omega t - 4\alpha))] + \exp(j4\alpha)[\exp(j(\omega t - \alpha)) + \exp(-j(\omega t - \alpha))] \\
 &\quad + \exp(j6\alpha)[\exp(j(\omega t - 5\alpha)) + \exp(-j(\omega t - 5\alpha))] + \exp(j\alpha)[\exp(j(\omega t - 2\alpha)) + \exp(-j(\omega t - 2\alpha))] + \\
 &\quad + \exp(j3\alpha)[\exp(j(\omega t - 6\alpha)) + \exp(-j(\omega t - 6\alpha))] + \exp(j5\alpha)[\exp(j(\omega t - 3\alpha)) + \exp(-j(\omega t - 3\alpha))] \} \\
 i_{x1y1} &= 0
 \end{aligned} \tag{3.15}$$

$$\begin{aligned}
 i_{x2y2} &= \sqrt{2/7} (1/2) \sqrt{2}I \{ \exp(j\omega t) + \exp(-j\omega t) + \exp(j3\alpha)[\exp(j(\omega t - 4\alpha)) + \exp(-j(\omega t - 4\alpha))] + \exp(j6\alpha)[\exp(j(\omega t - \alpha)) + \exp(-j(\omega t - \alpha))] \\
 &\quad + \exp(j2\alpha)[\exp(j(\omega t - 5\alpha)) + \exp(-j(\omega t - 5\alpha))] + \exp(j5\alpha)[\exp(j(\omega t - 2\alpha)) + \exp(-j(\omega t - 2\alpha))] + \\
 &\quad + \exp(j\alpha)[\exp(j(\omega t - 6\alpha)) + \exp(-j(\omega t - 6\alpha))] + \exp(j4\alpha)[\exp(j(\omega t - 3\alpha)) + \exp(-j(\omega t - 3\alpha))] \} \\
 i_{x2y2} &= \sqrt{1/7}I \{ \exp(j\omega t)[1 + \exp(j(\omega t - \alpha)) + \exp(j(\omega t - 2\alpha)) + \exp(j(\omega t - 3\alpha)) + \exp(j(\omega t - 4\alpha)) + \exp(j(\omega t - 5\alpha)) + \\
 &\quad + \exp(j(\omega t - 6\alpha))] + \exp(-j\omega t)(1 + 1 + 1 + 1 + 1 + 1) = \sqrt{7}I \exp(-j\omega t)
 \end{aligned} \tag{3.16}$$

On the other hand, for the second connection diagram in Fig. 3.3 the following space vectors are obtained:

$$\begin{aligned}
 i_{\alpha\beta} &= \sqrt{2/7} (1/2) \sqrt{2}I \{ \exp(j\omega t) + \exp(-j\omega t) + \exp(j\alpha)[\exp(j(\omega t - 5\alpha)) + \exp(-j(\omega t - 5\alpha))] + \exp(j2\alpha)[\exp(j(\omega t - 3\alpha)) + \exp(-j(\omega t - 3\alpha))] \\
 &\quad + \exp(j3\alpha)[\exp(j(\omega t - \alpha)) + \exp(-j(\omega t - \alpha))] + \exp(j4\alpha)[\exp(j(\omega t - 6\alpha)) + \exp(-j(\omega t - 6\alpha))] + \\
 &\quad + \exp(j5\alpha)[\exp(j(\omega t - 4\alpha)) + \exp(-j(\omega t - 4\alpha))] + \exp(j6\alpha)[\exp(j(\omega t - 2\alpha)) + \exp(-j(\omega t - 2\alpha))] \} \\
 i_{\alpha\beta} &= 0
 \end{aligned} \tag{3.17}$$

$$i_{x1y1} = \sqrt{2/7} (1/2) \sqrt{2} I \{ \exp(j\omega t) + \exp(-j\omega t) + \exp(j2\alpha)[\exp(j(\omega t - 5\alpha)) + \exp(-j(\omega t - 5\alpha))] + \exp(j4\alpha)[\exp(j(\omega t - 3\alpha)) + \exp(-j(\omega t - 3\alpha))] + \exp(j6\alpha)[\exp(j(\omega t - \alpha)) + \exp(-j(\omega t - \alpha))] + \exp(j\alpha)[\exp(j(\omega t - 6\alpha)) + \exp(-j(\omega t - 6\alpha))] + \exp(j3\alpha)[\exp(j(\omega t - 4\alpha)) + \exp(-j(\omega t - 4\alpha))] + \exp(j5\alpha)[\exp(j(\omega t - 2\alpha)) + \exp(-j(\omega t - 2\alpha))] \} \quad (3.18)$$

$$i_{x1y1} = \sqrt{1/7} I \{ \exp(j\omega t)[1 + \exp(j(\omega t - 3\alpha)) + \exp(j(\omega t - 6\alpha)) + \exp(j(\omega t - 2\alpha)) + \exp(j(\omega t - 5\alpha)) + \exp(j(\omega t - \alpha)) + \exp(j(\omega t - 4\alpha))] + \exp(-j\omega t)(1 + 1 + 1 + 1 + 1 + 1) = \sqrt{7} I \exp(-j\omega t) \}$$

$$i_{x2y2} = \sqrt{2/7} (1/2) \sqrt{2} I \{ \exp(j\omega t) + \exp(-j\omega t) + \exp(j3\alpha)[\exp(j(\omega t - 5\alpha)) + \exp(-j(\omega t - 5\alpha))] + \exp(j6\alpha)[\exp(j(\omega t - 3\alpha)) + \exp(-j(\omega t - 3\alpha))] + \exp(j2\alpha)[\exp(j(\omega t - \alpha)) + \exp(-j(\omega t - \alpha))] + \exp(j5\alpha)[\exp(j(\omega t - 6\alpha)) + \exp(-j(\omega t - 6\alpha))] + \exp(j\alpha)[\exp(j(\omega t - 4\alpha)) + \exp(-j(\omega t - 4\alpha))] + \exp(j4\alpha)[\exp(j(\omega t - 2\alpha)) + \exp(-j(\omega t - 2\alpha))] \} \quad (3.19)$$

$$i_{x2y2} = 0$$

As is obvious from (3.14)-(3.16) and (3.17)-(3.19), each of the two possible connection diagrams means that the charging process will utilise one of the two  $x$ - $y$  planes.

The procedure, illustrated here for a five-phase and a seven-phase machine, can be extended in the same manner to any other higher phase number. Only one more case is therefore considered. It is the utilisation of an asymmetrical six-phase machine with two three-phase windings shifted spatially by 30 degrees. The machine is configured with two isolated neutral points in propulsion mode. In the charging mode it is again necessary to open the neutral points and connect the six-phase grid supply. The main difference, compared to the previous two cases, is that the asymmetrical six-phase supply is readily obtainable from the three-phase grid without the use of any sophisticated power electronic converters or transformers. It is only necessary to use a three-phase transformer with dual secondary windings. By connecting the two secondary windings in star and delta, respectively, required phase shift between two three-phase winding supplies of 30 degrees is achieved (the voltage levels are made the same by proper selection of the turn numbers for the secondaries). Hence the situation discussed here is realistic rather than futuristic, as in the previous two cases.

The principle of the machine-to-grid connection is again the same and follows the phase transposition rule [Levi et al (2005)]. It is illustrated in Fig. 3.4a. As noted, neutral points have to be opened in order to connect the grid supply for the charging mode.

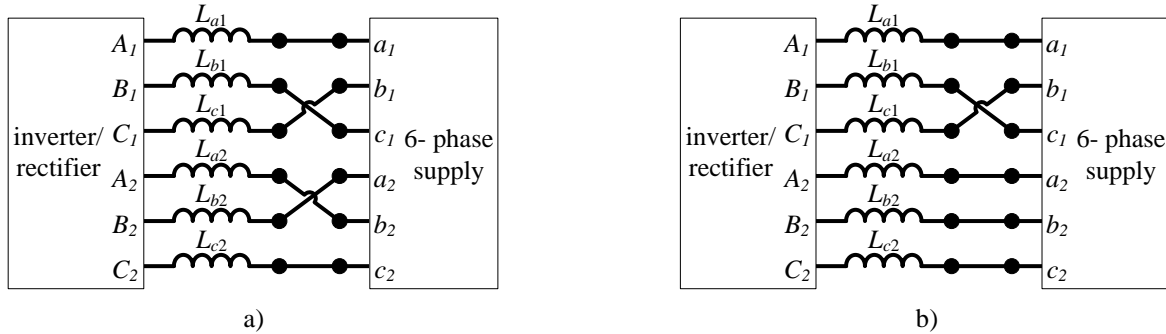


**Fig. 3.4:** Connection for the charging mode of operation of: a) an asymmetrical six-phase machine to the asymmetrical six-phase voltage source (no field production in the rotor), b) a symmetrical six-phase machine to the symmetrical six-phase source (a pulsating field exists in the rotor).

Transformation matrix of an asymmetrical six-phase machine does not follow from (3.1) directly. However, it can be shown that its form is [Levi et al (2007)]

$$[C] = \begin{bmatrix} a_1 & b_1 & c_1 & a_2 & b_2 & c_2 \\ \alpha & \begin{bmatrix} 1 & \cos 2\pi/3 & \cos 4\pi/3 & \cos \pi/6 & \cos 5\pi/6 & \cos 9\pi/6 \\ \beta & \begin{bmatrix} 0 & \sin 2\pi/3 & \sin 4\pi/3 & \sin \pi/6 & \sin 5\pi/6 & \sin 9\pi/6 \\ x & \begin{bmatrix} 1 & \cos 4\pi/3 & \cos 8\pi/3 & \cos 5\pi/6 & \cos \pi/6 & \cos 9\pi/6 \\ y & \begin{bmatrix} 0 & \sin 4\pi/3 & \sin 8\pi/3 & \sin 5\pi/6 & \sin \pi/6 & \sin 9\pi/6 \\ 0_+ & \begin{bmatrix} 1 & 1 & 1 & 0 & 0 & 0 \\ 0_- & \begin{bmatrix} 0 & 0 & 0 & 1 & 1 & 1 \end{bmatrix} \end{bmatrix} \end{bmatrix} \end{bmatrix} \end{bmatrix} \end{bmatrix} \quad (3.20)$$

Hence the space vectors are given with

$$\underline{f}_{-\alpha\beta} = \sqrt{2/6} (f_{a_1} + \underline{a}^4 f_{b_1} + \underline{a}^8 f_{c_1} + \underline{a} f_{a_2} + \underline{a}^5 f_{b_2} + \underline{a}^9 f_{c_2})$$

$$\underline{f}_{-xy} = \sqrt{2/6} (f_{a_1} + \underline{a}^8 f_{b_1} + \underline{a}^{16} f_{c_1} + \underline{a}^5 f_{a_2} + \underline{a} f_{b_2} + \underline{a}^9 f_{c_2}) \quad (3.21)$$

where  $\underline{a} = \exp(j\alpha) = \cos \alpha + j \sin \alpha$  and  $\alpha = \pi/6$ .

The grid currents can now be written as

$$\begin{aligned} i_{a_1g} &= \sqrt{2}I \cos(\omega t) & i_{b_1g} &= \sqrt{2}I \cos(\omega t - 4\pi/6) & i_{c_1g} &= \sqrt{2}I \cos(\omega t - 8\pi/6) \\ i_{a_2g} &= \sqrt{2}I \cos(\omega t - \pi/6) & i_{b_2g} &= \sqrt{2}I \cos(\omega t - 5\pi/6) & i_{c_2g} &= \sqrt{2}I \cos(\omega t - 9\pi/6) \end{aligned} \quad (3.22)$$

while the relationship between machine and grid phase currents is, according to Fig. 3.4a, given with

$$i_{a_1} = i_{a_1g} \quad i_{b_1} = i_{c_1g} \quad i_{c_1} = i_{b_1g} \quad i_{a_2} = i_{b_2g} \quad i_{b_2} = i_{a_2g} \quad i_{c_2} = i_{c_2g} \quad (3.23)$$

Using (3.23) in conjunction with (3.21), the following two space vectors are obtained:

$$\begin{aligned} \underline{i}_{\alpha\beta} &= \sqrt{2/6} (1/2) \sqrt{2}I \{ \exp(j\omega t) + \exp(-j\omega t) + \exp(j4\alpha)[\exp(j(\omega t - 8\alpha)) + \exp(-j(\omega t - 8\alpha))] + \\ &\quad \exp(j8\alpha)[\exp(j(\omega t - 4\alpha)) + \exp(-j(\omega t - 4\alpha))] + \exp(j\alpha)[\exp(j(\omega t - 5\alpha)) + \exp(-j(\omega t - 5\alpha))] + \\ &\quad \exp(j5\alpha)[\exp(j(\omega t - \alpha)) + \exp(-j(\omega t - \alpha))] + \exp(j9\alpha)[\exp(j(\omega t - 9\alpha)) + \exp(-j(\omega t - 9\alpha))] \} \end{aligned} \quad (3.24)$$

$$\underline{i}_{\alpha\beta} = 0$$

$$\begin{aligned} \underline{i}_{xy} &= \sqrt{2/6} (1/2) \sqrt{2}I \{ \exp(j\omega t) + \exp(-j\omega t) + \exp(j8\alpha)[\exp(j(\omega t - 8\alpha)) + \exp(-j(\omega t - 8\alpha))] + \\ &\quad \exp(j16\alpha)[\exp(j(\omega t - 4\alpha)) + \exp(-j(\omega t - 4\alpha))] + \exp(j5\alpha)[\exp(j(\omega t - 5\alpha)) + \exp(-j(\omega t - 5\alpha))] + \\ &\quad \exp(j\alpha)[\exp(j(\omega t - \alpha)) + \exp(-j(\omega t - \alpha))] + \exp(j9\alpha)[\exp(j(\omega t - 9\alpha)) + \exp(-j(\omega t - 9\alpha))] \} \end{aligned} \quad (3.25)$$

$$\begin{aligned} \underline{i}_{xy} &= \sqrt{1/6} I \{ \exp(j\omega t)(1+1+1+1+1+1) + \exp(-j\omega t)(1 + \exp(j4\alpha) + \exp(j8\alpha) + \exp(j10\alpha) + \exp(j2\alpha) + \\ &\quad \exp(j6\alpha)) \} = \sqrt{6}I \exp(j\omega t) \end{aligned}$$

Clearly, the flux/torque producing plane is again not excited and the grid currents flow through the  $x$ - $y$  plane, so that the machine stays at standstill. Zero-sequence components of (3.20) are both equal to zero.

Finally, a somewhat different topology utilizing a symmetrical six-phase machine and a symmetrical six-phase voltage source is presented in Fig. 3.4b. Again the six-phase voltage source can be obtained by means of a transformer with two secondary winding sets. Now both sets on secondary should be in star connection, and have the same number of turns. In this case a decoupling matrix follows directly from (3.1) and is given with:

$$\begin{aligned} \underline{f}_{\alpha\beta} &= \sqrt{2/6} (f_a + \underline{a}f_b + \underline{a}^2f_c + \underline{a}^3f_d + \underline{a}^4f_e + \underline{a}^5f_f) \\ \underline{f}_{xy} &= \sqrt{2/6} (f_a + \underline{a}^2f_b + \underline{a}^4f_c + \underline{a}^6f_d + \underline{a}^8f_e + \underline{a}^{10}f_f) \end{aligned} \quad (3.26)$$

where  $\underline{a} = \exp(j\alpha) = \cos \alpha + j \sin \alpha$  and  $\alpha = 2\pi/6$ .

The grid currents are governed with:

$$\begin{aligned} i_{a_1g} &= \sqrt{2}I \cos(\omega t) & i_{b_1g} &= \sqrt{2}I \cos(\omega t - 2\pi/3) & i_{c_1g} &= \sqrt{2}I \cos(\omega t - 4\pi/3) \\ i_{a_2g} &= \sqrt{2}I \cos(\omega t - \pi/3) & i_{b_2g} &= \sqrt{2}I \cos(\omega t - 3\pi/3) & i_{c_2g} &= \sqrt{2}I \cos(\omega t - 5\pi/3) \end{aligned} \quad (3.27)$$

while the relationship between machine and grid phase currents is, according to Fig. 3.4b, given with

$$i_{a_1} = i_{a_1g} \quad i_{b_1} = i_{c_1g} \quad i_{c_1} = i_{b_1g} \quad i_{a_2} = i_{a_2g} \quad i_{b_2} = i_{b_2g} \quad i_{c_2} = i_{c_2g} \quad (3.28)$$

Using (3.28) in conjunction with (3.26), the following two space vectors are obtained:

$$\begin{aligned} \underline{i}_{\alpha\beta} &= \sqrt{2/6} (1/2) \sqrt{2}I \{ \exp(j\omega t) + \exp(-j\omega t) + \exp(j\alpha)[\exp(j(\omega t - 1\alpha)) + \exp(-j(\omega t - 1\alpha))] + \\ &\quad \exp(j2\alpha)[\exp(j(\omega t - 4\alpha)) + \exp(-j(\omega t - 4\alpha))] + \exp(j3\alpha)[\exp(j(\omega t - 3\alpha)) + \exp(-j(\omega t - 3\alpha))] + \\ &\quad \exp(j4\alpha)[\exp(j(\omega t - 2\alpha)) + \exp(-j(\omega t - 2\alpha))] + \exp(j5\alpha)[\exp(j(\omega t - 5\alpha)) + \exp(-j(\omega t - 5\alpha))] \} \end{aligned} \quad (3.29)$$

$$\underline{i}_{\alpha\beta} = \sqrt{6}I \cos(\omega t)$$

$$\begin{aligned} \underline{i}_{xy} &= \sqrt{2/6} (1/2) \sqrt{2}I \{ \exp(j\omega t) + \exp(-j\omega t) + \exp(j2\alpha)[\exp(j(\omega t - 1\alpha)) + \exp(-j(\omega t - 1\alpha))] + \\ &\quad \exp(j4\alpha)[\exp(j(\omega t - 4\alpha)) + \exp(-j(\omega t - 4\alpha))] + \exp(j6\alpha)[\exp(j(\omega t - 3\alpha)) + \exp(-j(\omega t - 3\alpha))] + \\ &\quad \exp(j8\alpha)[\exp(j(\omega t - 2\alpha)) + \exp(-j(\omega t - 2\alpha))] + \exp(j10\alpha)[\exp(j(\omega t - 5\alpha)) + \exp(-j(\omega t - 5\alpha))] \} \end{aligned} \quad (3.30)$$

$$\underline{i}_{xy} = j\sqrt{6}I \sin(\omega t)$$

It is obvious that unlike in the previous case, there is now excitation in the first plane. However, it can be seen that the excitation is along only one axis, i.e.  $\alpha$ . Therefore, the situation is similar to the one of Fig. 3.1b, and this topology will not cause torque production since the other current component of the first plane ( $i_{\beta}$ ) is equal to zero. Thus, the symmetrical six-phase machine in this topology can remain at standstill without being mechanically locked.

### 3.3 Single-phase supply

Consider at first an  $n$ -phase machine, where  $n = ak$ . Here  $a$  stands for the number of sub-windings, each of which is with  $k$  phases. A typical example is the asymmetrical six-phase machine already discussed in section 3.2, where  $a = 2$  and  $k = 3$ . In propulsion mode the machine operates with  $a$  isolated neutral points. The particularly convenient phase numbers for the case of the single-phase grid supply in charging mode are those where  $a = 2$ , while  $k$  could be any number. For simplicity, only the topologies with  $k = 3$  and  $k = 5$  are covered here. In addition to  $a = 2$ , the situation with  $a = 3$  (for  $k = 3$ ) is also covered. The particular advantage of all the configurations with the phase number equal to  $n = ak$ , considered in this section, is that no hardware reconfiguration is necessary (i.e. there is no need to open the neutral points of the windings). This is in contrast with solutions discussed in section 3.2 and is also in contrast to the remaining topology discussed in this section.

An exception from this desirable situation, discussed as the last possibility in this section, is a topology employing a five-phase machine. In this case it is also possible to realise single-phase charging in a rather simple manner, but hardware reconfiguration becomes a necessity. The concept shown for the five-phase machine can be extended to any other prime phase number in a rather straightforward manner.

For the battery charging purposes the single-phase grid supply is connected between two neutral points. The connection can be of plug-in type, since nothing else needs to be done except the supply connection, for the battery charging to take place.

If a symmetrical six-phase machine with two isolated neutral points is supplied from a single-phase source connected between two neutral points of the three-phase windings, then  $\alpha\text{-}\beta$  plane will not be excited. The connection is shown in Fig. 3.5 and is further analysed using the same approach as in section 3.2. Note that the connection shown in Fig. 3.5 is simultaneously valid for an asymmetrical six-phase machine as well. The only difference is that the two three-phase windings are spatially shifted by 60 and 30 degrees in the former and the latter case, respectively. Note also that a symmetrical six-phase machine could also be supplied from a three-phase transformer, using again a transformer with two secondary windings. However, in contrast to the asymmetrical six-phase machine, both secondary windings would now be connected in star and be such that the phase shift of the two three-phase systems of voltages is  $180^\circ$ .

Consider at first the symmetrical six-phase machine. General transformation matrix (3.1), when applied to six-phase system and written in space vector representation, yields (3.26).

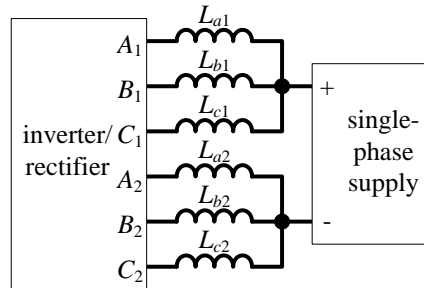


**Fig. 3.5:** Configuration for single-phase charging through a symmetrical or asymmetrical six-phase machine with two isolated neutral points.

In charging mode one also has to consider the zero-sequence components, since the two neutral points, isolated in the propulsion mode, are now connected through the single-phase grid supply and the zero-sequence current can flow. Hence the machine behaves as having two neutral points, connected through the source. From (3.1) the relevant zero-sequence components are given with

$$f_{0+} = \sqrt{1/6} (f_{a1} + f_{a2} + f_{b1} + f_{b2} + f_{c1} + f_{c2}) \quad (3.31)$$

$$f_{0-} = \sqrt{1/6} (f_{a1} - f_{a2} + f_{b1} - f_{b2} + f_{c1} - f_{c2})$$

The grid currents are now given with

$$i_{+g} = \sqrt{2} I \cos(\omega t) \quad (3.32)$$

$$i_{-g} = -\sqrt{2} I \cos(\omega t)$$

and their form will be the same for all the configurations that will be discussed in this section. Fig. 3.5 gives the following correlations between machine phase currents and grid currents:

$$i_{a1} = i_{b1} = i_{c1} = i_{+g} / 3 \quad i_{a2} = i_{b2} = i_{c2} = i_{-g} / 3 \quad (3.33)$$

The space vectors in the two planes can be obtained by substituting (3.33) into (3.26), which yields the following

$$\begin{aligned} i_{\alpha\beta} = & \sqrt{2/6} (1/2) \sqrt{2} (I/3) \{ \exp(j\omega t) + \exp(-j\omega t) + \exp(j\alpha) [ -\exp(j\omega t) - \exp(-j\omega t) ] + \exp(j2\alpha) [ \exp(j\omega t) + \\ & \exp(-j\omega t) ] + \exp(j3\alpha) [ -\exp(j\omega t) - \exp(-j\omega t) ] + \exp(j4\alpha) [ \exp(j\omega t) + \exp(-j\omega t) ] \} + \\ & \exp(j5\alpha) [ -\exp(j\omega t) - \exp(-j\omega t) ] \} \end{aligned} \quad (3.34)$$

$$i_{\alpha\beta} = 0$$

$$\begin{aligned} i_{xy} = & \sqrt{2/6} (1/2) \sqrt{2} (I/3) \{ \exp(j\omega t) + \exp(-j\omega t) + \exp(j2\alpha) [ -\exp(j\omega t) - \exp(-j\omega t) ] + \exp(j4\alpha) [ \exp(j\omega t) + \\ & \exp(-j\omega t) ] + \exp(j6\alpha) [ -\exp(j\omega t) - \exp(-j\omega t) ] + \exp(j8\alpha) [ \exp(j\omega t) + \exp(-j\omega t) ] \} + \\ & \exp(j10\alpha) [ -\exp(j\omega t) - \exp(-j\omega t) ] \} \end{aligned} \quad (3.35)$$

$$i_{xy} = 0$$

The 0<sub>-</sub> component has, using (3.31), the value of

$$\begin{aligned} i_{0-} = & \sqrt{2/6} (1/2) \sqrt{2} (I/3) \{ \exp(j\omega t) + \exp(-j\omega t) - [ -\exp(j\omega t) - \exp(-j\omega t) ] + [ \exp(j\omega t) + \exp(-j\omega t) ] - \\ & [ -\exp(j\omega t) - \exp(-j\omega t) ] + [ \exp(j\omega t) + \exp(-j\omega t) ] - [ -\exp(j\omega t) - \exp(-j\omega t) ] \} \end{aligned} \quad (3.36)$$

$$i_{0-} = (\sqrt{12}/3) I \cos(\omega t)$$

while the 0<sub>+</sub> component is of course equal to zero. It can be seen from (3.34)-(3.36) that only the 0<sub>-</sub> component will be utilised in the charging process, leaving the  $\alpha$ - $\beta$  plane without excitation. Thus torque will not be produced, and the machine will not rotate during the charging process.

The same charging principle can be applied to an asymmetrical six-phase machine with two isolated neutral points in propulsion mode. Again the single-phase supply connections for charging mode will be attached between the two isolated neutral points (Fig. 3.5), and reconfiguration between the propulsion and charging mode will not be necessary. Decoupling matrix for this type of machine is given with (3.20), and the equivalent space vector representation is governed with (3.21), which are repeated here for the sake of convenience:

$$\begin{aligned} \underline{f}_{\alpha\beta} = & \sqrt{2/6} ( \underline{f}_{a_1} + \underline{a}^4 \underline{f}_{b_1} + \underline{a}^8 \underline{f}_{c_1} + \underline{a} \underline{f}_{a_2} + \underline{a}^5 \underline{f}_{b_2} + \underline{a}^9 \underline{f}_{c_2} ) \\ \underline{f}_{xy} = & \sqrt{2/6} ( \underline{f}_{a_1} + \underline{a}^8 \underline{f}_{b_1} + \underline{a}^{16} \underline{f}_{c_1} + \underline{a}^5 \underline{f}_{a_2} + \underline{a} \underline{f}_{b_2} + \underline{a}^9 \underline{f}_{c_2} ) \end{aligned} \quad (3.37)$$

where  $\underline{a} = \exp(j\alpha) = \cos \alpha + j \sin \alpha$  and  $\alpha = \pi/6$ . The grid currents and the correlation between machine phase currents and grid currents remain to be given with (3.32) and (3.33), respectively. Equation (3.33), when substituted into (3.37), gives the following space vectors in the two planes:

$$\begin{aligned} i_{\alpha\beta} = & \sqrt{2/6} (1/2) \sqrt{2} (I/3) \{ \exp(j\omega t) + \exp(-j\omega t) + \exp(j4\alpha) [ \exp(j\omega t) + \exp(-j\omega t) ] + \exp(j8\alpha) [ \exp(j\omega t) + \\ & \exp(-j\omega t) ] + \exp(j\alpha) [ -\exp(j\omega t) - \exp(-j\omega t) ] + \exp(j5\alpha) [ -\exp(j\omega t) - \exp(-j\omega t) ] \} + \\ & \exp(j9\alpha) [ -\exp(j\omega t) - \exp(-j\omega t) ] \} \end{aligned} \quad (3.38)$$

$$i_{\alpha\beta} = 0$$

$$\begin{aligned} i_{xy} = & \sqrt{2/6} (1/2) \sqrt{2} (I/3) \{ \exp(j\omega t) + \exp(-j\omega t) + \exp(j8\alpha) [ \exp(j\omega t) + \exp(-j\omega t) ] + \exp(j16\alpha) [ \exp(j\omega t) + \\ & \exp(-j\omega t) ] + \exp(j5\alpha) [ -\exp(j\omega t) - \exp(-j\omega t) ] + \exp(j\alpha) [ -\exp(j\omega t) - \exp(-j\omega t) ] \} + \\ & \exp(j9\alpha) [ -\exp(j\omega t) - \exp(-j\omega t) ] \} \end{aligned} \quad (3.39)$$

$$i_{xy} = 0$$

Zero-sequence components of the two three-phase windings are governed with the last two rows of (3.20), which are the same regardless of whether there is a single neutral or two isolated neutral points. Hence

$$\begin{aligned} i_{0+} = & \sqrt{2/6} (1/2) \sqrt{2} (I/3) \{ \exp(j\omega t) + \exp(-j\omega t) + \exp(j\omega t) + \exp(-j\omega t) + \exp(j\omega t) + \exp(-j\omega t) \} \\ i_{0+} = & \sqrt{6} (I/3) \cos \omega t \end{aligned} \quad (3.40)$$

$$i_{0-} = \sqrt{2/6} (1/2) \sqrt{2} (I/3) \{ [ -\exp(j\omega t) - \exp(-j\omega t) ] + [ -\exp(j\omega t) - \exp(-j\omega t) ] + [ -\exp(j\omega t) - \exp(-j\omega t) ] \}$$

$$i_{0-} = -\sqrt{6} (I/3) \cos \omega t$$

It can be seen that both zero-sequence components exist. They have opposite signs, since the currents through the two three-phase windings flow in opposite directions (and are the same in all phases of any of the two three-phase windings). Total sum of zero-sequence components is zero. The first plane is still without excitation, thus the machine will stay at standstill.

It has been shown that single-phase charging is applicable for both symmetrical and asymmetrical multiphase machines. This manner of charging is inferior to the three-phase charging, mainly due to the reduced maximum charging power when compared to the three-phase system, which prolongs the charging process. However, if a vehicle has already a three-phase or a multiphase charger, it is desirable that it also has an integrated single-phase charger. It can provide its user with additional charging options, considering that the single-phase sockets are much more widely

spread than the three-phase (and multiphase) ones. One example of this would be combination of the single-phase charging solution for an asymmetrical six-phase machine with the multiphase solution for the same machine discussed in section 3.2.

Consider next  $n$ -phase machines, where  $n = ak$ , such that  $a = 3$ . A typical representative of this type of machine is an asymmetrical nine-phase machine with three isolated neutral points ( $a = 3, k = 3$ ). There are multiple options for connecting a single-phase supply to a machine with a number of isolated neutral points  $a$  greater than two, because now it can be chosen whether to connect a conductor from the supply to a single or to multiple neutral points. If one wants to connect each supply conductor to multiple neutral points, hardware reconfiguration becomes necessary (assuming that in propulsion mode operation is with isolated neutral points). Hence the best solution, which does not require hardware reconfiguration, is to utilise only two neutral points of the multiphase windings with  $a \geq 3$  for connecting the single-phase grid in the charging mode, while leaving the other neutral points unconnected. It should be noted that the possible connection of each of the two grid conductors to multiple neutral points is only sensible if the number of neutral points is an even number. This would, in addition to the requirement for hardware reconfiguration, also result in the reduction of the equivalent inductance (equivalent leakage inductance of the machine) used to filter the charging current, since more than the minimum number of phases would be paralleled, although it would potentially be able to increase the charging power (which is however anyway limited by the grid single-phase outlet and is therefore always likely to be less than what the machine could take in).

When the number of isolated neutral points is three, one isolated neutral point is left without connection to the single-phase supply. This case is shown in Fig. 3.6a for a representative of this group, which is an asymmetrical nine-phase machine. It should be noted that the same figure is valid also for the symmetrical nine-phase machine. Connection as in Fig. 3.6a results in charging mode that does not excite the first plane. As noted, hardware reconfiguration between propulsion and charging mode is not required.

If a symmetrical nine-phase machine is considered first, the starting point is again the general transformation matrix (3.1) for a nine-phase system. In propulsion mode there are three isolated neutral points, while in the charging mode there are two neutral points that are connected through the grid supply, while the third one is isolated from the rest of the system. The matrix can be written in the space vector form as

$$\begin{aligned} \underline{f}_{\alpha\beta} &= \sqrt{2/9} (f_{a1} + \underline{a} f_{a2} + \underline{a}^2 f_{a3} + \underline{a}^3 f_{b1} + \underline{a}^4 f_{b2} + \underline{a}^5 f_{b3} + \underline{a}^6 f_{c1} + \underline{a}^7 f_{c2} + \underline{a}^8 f_{c3}) \\ \underline{f}_{x1y1} &= \sqrt{2/9} (f_{a1} + \underline{a}^2 f_{a2} + \underline{a}^4 f_{a3} + \underline{a}^6 f_{b1} + \underline{a}^8 f_{b2} + \underline{a}^{10} f_{b3} + \underline{a}^{12} f_{c1} + \underline{a}^{14} f_{c2} + \underline{a}^{16} f_{c3}) \\ \underline{f}_{x2y2} &= \sqrt{2/9} (f_{a1} + \underline{a}^3 f_{a2} + \underline{a}^6 f_{a3} + \underline{a}^9 f_{b1} + \underline{a}^{12} f_{b2} + \underline{a}^{15} f_{b3} + \underline{a}^{18} f_{c1} + \underline{a}^{21} f_{c2} + \underline{a}^{24} f_{c3}) \\ \underline{f}_{x3y3} &= \sqrt{2/9} (f_{a1} + \underline{a}^4 f_{a2} + \underline{a}^8 f_{a3} + \underline{a}^{12} f_{b1} + \underline{a}^{16} f_{b2} + \underline{a}^{20} f_{b3} + \underline{a}^{24} f_{c1} + \underline{a}^{28} f_{c2} + \underline{a}^{32} f_{c3}) \end{aligned} \quad (3.41)$$

where  $\underline{a} = \exp(j\alpha) = \cos \alpha + j \sin \alpha$  and  $\alpha = 2\pi/9$ . The grid currents are one more time given with (3.32), but now the correlation between machine phase currents and grid currents is given with

$$i_{a1} = i_{b1} = i_{c1} = i_{+g}/3 \quad i_{a2} = i_{b2} = i_{c2} = i_{-g}/3 \quad i_{a3} = i_{b3} = i_{c3} = 0 \quad (3.42)$$

Substitution of (3.42) into (3.41) gives the following space vectors in the four planes:

$$\begin{aligned} i_{\alpha\beta} &= \sqrt{2/9} (1/2)\sqrt{2} (I/3) \{ \exp(j\omega t) + \exp(-j\omega t) + \exp(j\alpha) [-\exp(j\omega t) - \exp(-j\omega t)] + \exp(j2\alpha) 0 + \\ &\quad \exp(j3\alpha) [\exp(j\omega t) + \exp(-j\omega t)] + \exp(j4\alpha) [-\exp(j\omega t) - \exp(-j\omega t)] + \exp(j5\alpha) 0 + \\ &\quad \exp(j6\alpha) [\exp(j\omega t) + \exp(-j\omega t)] + \exp(j7\alpha) [-\exp(j\omega t) - \exp(-j\omega t)] + \exp(j8\alpha) 0 \} \end{aligned} \quad (3.43)$$

$$i_{\alpha\beta} = 0$$

$$\begin{aligned} i_{x1y1} &= \sqrt{2/9} (1/2)\sqrt{2} (I/3) \{ \exp(j\omega t) + \exp(-j\omega t) + \exp(j2\alpha) [-\exp(j\omega t) - \exp(-j\omega t)] + \exp(j4\alpha) 0 + \\ &\quad \exp(j6\alpha) [\exp(j\omega t) + \exp(-j\omega t)] + \exp(j8\alpha) [-\exp(j\omega t) - \exp(-j\omega t)] + \exp(j10\alpha) 0 + \\ &\quad \exp(j12\alpha) [\exp(j\omega t) + \exp(-j\omega t)] + \exp(j14\alpha) [-\exp(j\omega t) - \exp(-j\omega t)] + \exp(j16\alpha) 0 \} \end{aligned} \quad (3.44)$$

$$i_{x1y1} = 0$$

$$\begin{aligned} i_{x2y2} &= \sqrt{2/9} (1/2)\sqrt{2} (I/3) \{ \exp(j\omega t) + \exp(-j\omega t) + \exp(j3\alpha) [-\exp(j\omega t) - \exp(-j\omega t)] + \exp(j6\alpha) 0 + \\ &\quad \exp(j9\alpha) [\exp(j\omega t) + \exp(-j\omega t)] + \exp(j12\alpha) [-\exp(j\omega t) - \exp(-j\omega t)] + \exp(j15\alpha) 0 + \\ &\quad \exp(j18\alpha) [\exp(j\omega t) + \exp(-j\omega t)] + \exp(j21\alpha) [-\exp(j\omega t) - \exp(-j\omega t)] + \exp(j24\alpha) 0 \} \end{aligned} \quad (3.45)$$

$$i_{x2y2} = \sqrt{1/9} (I/3) \{ 3[\exp(j\omega t) + \exp(-j\omega t)] + 3\exp(j3\alpha) [-\exp(j\omega t) - \exp(-j\omega t)] \} = I(1 - j0.577) \cos(\omega t)$$

$$\begin{aligned} i_{x3y3} &= \sqrt{2/9} (1/2)\sqrt{2} (I/3) \{ \exp(j\omega t) + \exp(-j\omega t) + \exp(j4\alpha) [-\exp(j\omega t) - \exp(-j\omega t)] + \exp(j8\alpha) 0 + \\ &\quad \exp(j12\alpha) [\exp(j\omega t) + \exp(-j\omega t)] + \exp(j16\alpha) [-\exp(j\omega t) - \exp(-j\omega t)] + \exp(j20\alpha) 0 + \\ &\quad \exp(j24\alpha) [\exp(j\omega t) + \exp(-j\omega t)] + \exp(j28\alpha) [-\exp(j\omega t) - \exp(-j\omega t)] + \exp(j32\alpha) 0 \} \end{aligned} \quad (3.46)$$

$$i_{x3y3} = 0$$

while the zero-sequence component is equal to zero. It can be concluded from equations above that the charging process will utilise only the  $x_2$ - $y_2$  plane, thus leaving the machine without excitation capable of providing torque.

If an asymmetrical nine-phase machine with three isolated neutral points is considered, the general decoupling matrix format of (3.1) can no longer be used. However, it can be shown [Rockhill and Lipo, 2010] that the decoupling matrix form is, for the machine with a single neutral point, given with

$$[C] = \sqrt{\frac{2}{9}} \begin{bmatrix} a_1 & a_2 & a_3 & b_1 & b_2 & b_3 & c_1 & c_2 & c_3 \\ \alpha & \begin{bmatrix} 1 & \cos(\alpha) & \cos(2\alpha) & \cos(6\alpha) & \cos(7\alpha) & \cos(8\alpha) & \cos(12\alpha) & \cos(13\alpha) & \cos(14\alpha) \end{bmatrix} \\ \beta & \begin{bmatrix} 0 & \sin(\alpha) & \sin(2\alpha) & \sin(6\alpha) & \sin(7\alpha) & \sin(8\alpha) & \sin(12\alpha) & \sin(13\alpha) & \sin(14\alpha) \end{bmatrix} \\ x_1 & \begin{bmatrix} 1 & \cos(3\alpha) & \cos(6\alpha) & 1 & \cos(3\alpha) & \cos(6\alpha) & 1 & \cos(3\alpha) & \cos(6\alpha) \end{bmatrix} \\ y_1 & \begin{bmatrix} 0 & \sin(3\alpha) & \sin(6\alpha) & 0 & \sin(3\alpha) & \sin(6\alpha) & 0 & \sin(3\alpha) & \sin(6\alpha) \end{bmatrix} \\ x_2 & \begin{bmatrix} 1 & \cos(5\alpha) & \cos(10\alpha) & \cos(12\alpha) & \cos(17\alpha) & \cos(4\alpha) & \cos(6\alpha) & \cos(11\alpha) & \cos(16\alpha) \end{bmatrix} \\ y_2 & \begin{bmatrix} 0 & \sin(5\alpha) & \sin(10\alpha) & \sin(12\alpha) & \sin(17\alpha) & \sin(4\alpha) & \sin(6\alpha) & \sin(11\alpha) & \sin(16\alpha) \end{bmatrix} \\ x_3 & \begin{bmatrix} 1 & \cos(7\alpha) & \cos(14\alpha) & \cos(6\alpha) & \cos(13\alpha) & \cos(2\alpha) & \cos(12\alpha) & \cos(\alpha) & \cos(8\alpha) \end{bmatrix} \\ y_3 & \begin{bmatrix} 0 & \sin(7\alpha) & \sin(14\alpha) & \sin(6\alpha) & \sin(13\alpha) & \sin(2\alpha) & \sin(12\alpha) & \sin(\alpha) & \sin(8\alpha) \end{bmatrix} \\ 0 & \begin{bmatrix} 1/\sqrt{2} & -1/\sqrt{2} & 1/\sqrt{2} & 1/\sqrt{2} & -1/\sqrt{2} & 1/\sqrt{2} & 1/\sqrt{2} & -1/\sqrt{2} & 1/\sqrt{2} \end{bmatrix} \end{bmatrix} \quad (3.47)$$

The equivalent space vector representation of (3.47) is:

$$\begin{aligned} \underline{f}_{\alpha\beta} &= \sqrt{2/9} ( \underline{a} f_{a1} + \underline{a} f_{a2} + \underline{a}^2 f_{a3} + \underline{a}^6 f_{b1} + \underline{a}^7 f_{b2} + \underline{a}^8 f_{b3} + \underline{a}^{12} f_{c1} + \underline{a}^{13} f_{c2} + \underline{a}^{14} f_{c3} ) \\ \underline{f}_{x_1 y_1} &= \sqrt{2/9} ( f_{a1} + \underline{a}^3 f_{a2} + \underline{a}^6 f_{a3} + \underline{a}^0 f_{b1} + \underline{a}^3 f_{b2} + \underline{a}^6 f_{b3} + \underline{a}^0 f_{c1} + \underline{a}^3 f_{c2} + \underline{a}^6 f_{c3} ) \\ \underline{f}_{x_2 y_2} &= \sqrt{2/9} ( f_{a1} + \underline{a}^5 f_{a2} + \underline{a}^{10} f_{a3} + \underline{a}^{12} f_{b1} + \underline{a}^{17} f_{b2} + \underline{a}^4 f_{b3} + \underline{a}^6 f_{c1} + \underline{a}^{11} f_{c2} + \underline{a}^{16} f_{c3} ) \\ \underline{f}_{x_3 y_3} &= \sqrt{2/9} ( f_{a1} + \underline{a}^7 f_{a2} + \underline{a}^{14} f_{a3} + \underline{a}^6 f_{b1} + \underline{a}^{13} f_{b2} + \underline{a}^2 f_{b3} + \underline{a}^{12} f_{c1} + \underline{a} f_{c2} + \underline{a}^8 f_{c3} ) \end{aligned} \quad (3.48)$$

where  $\underline{a} = \exp(j\alpha) = \cos \alpha + j \sin \alpha$  and  $\alpha = \pi/9$ . The correlation between machine phase currents and grid currents is given with (3.42), which, when substituted into (3.48), gives the following space vectors in the four planes:

$$\begin{aligned} \underline{i}_{\alpha\beta} &= \sqrt{2/9} (1/2) \sqrt{2} (I/3) \{ \exp(j\omega t) + \exp(-j\omega t) + \exp(j\alpha) [ -\exp(j\omega t) - \exp(-j\omega t) ] + \exp(j2\alpha) 0 + \\ &\quad \exp(j6\alpha) [ \exp(j\omega t) + \exp(-j\omega t) ] + \exp(j7\alpha) [ -\exp(j\omega t) - \exp(-j\omega t) ] + \exp(j8\alpha) 0 + \\ &\quad \exp(j12\alpha) [ \exp(j\omega t) + \exp(-j\omega t) ] + \exp(j13\alpha) [ -\exp(j\omega t) - \exp(-j\omega t) ] + \exp(j14\alpha) 0 \} \\ \underline{i}_{x_1 y_1} &= 0 \end{aligned} \quad (3.49)$$

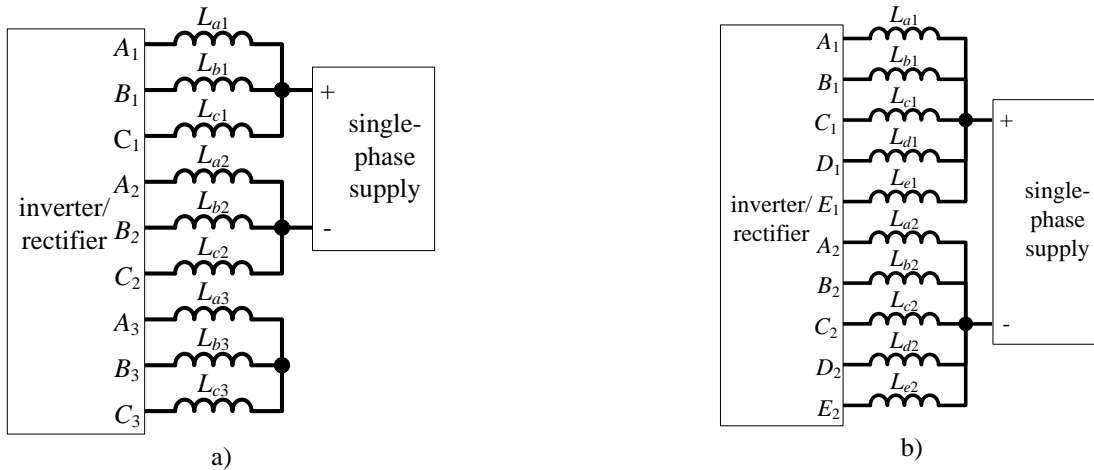


**Fig. 3.6:** Configuration for single-phase charging through: a) a symmetrical or asymmetrical nine-phase machine with three isolated neutral points, b) a symmetrical or asymmetrical ten-phase machine with two isolated neutral points.

$$\begin{aligned} \underline{i}_{x_1 y_1} &= \sqrt{2/9} (1/2) \sqrt{2} (I/3) \{ \exp(j\omega t) + \exp(-j\omega t) + \exp(j3\alpha) [ -\exp(j\omega t) - \exp(-j\omega t) ] + \exp(j6\alpha) 0 + \\ &\quad \exp(j0\alpha) [ \exp(j\omega t) + \exp(-j\omega t) ] + \exp(j3\alpha) [ -\exp(j\omega t) - \exp(-j\omega t) ] + \exp(j6\alpha) 0 + \\ &\quad \exp(j0\alpha) [ \exp(j\omega t) + \exp(-j\omega t) ] + \exp(j3\alpha) [ -\exp(j\omega t) - \exp(-j\omega t) ] + \exp(j6\alpha) 0 \} \end{aligned} \quad (3.50)$$

$$\underline{i}_{x_1 y_1} = \sqrt{1/9} (I/3) \{ 3[\exp(j\omega t) + \exp(-j\omega t)] + 3\exp(j3\alpha) [ -\exp(j\omega t) - \exp(-j\omega t) ] \} = I(0.33 - j0.577) \cos(\omega t)$$

$$\begin{aligned}
 i_{x_2y_2} &= \sqrt{2/9} (1/2) \sqrt{2} (I/3) \{ \exp(j\omega t) + \exp(-j\omega t) + \exp(j5\alpha) [-\exp(j\omega t) - \exp(-j\omega t)] + \exp(j10\alpha) 0 + \\
 &\quad \exp(j12\alpha) [\exp(j\omega t) + \exp(-j\omega t)] + \exp(j17\alpha) [-\exp(j\omega t) - \exp(-j\omega t)] + \exp(j4\alpha) 0 + \\
 &\quad \exp(j6\alpha) [\exp(j\omega t) + \exp(-j\omega t)] + \exp(j11\alpha) [-\exp(j\omega t) - \exp(-j\omega t)] + \exp(j16\alpha) 0 \}
 \end{aligned} \quad (3.51)$$

$$i_{x_2y_2} = 0$$

$$\begin{aligned}
 i_{x_3y_3} &= \sqrt{2/9} (1/2) \sqrt{2} (I/3) \{ \exp(j\omega t) + \exp(-j\omega t) + \exp(j7\alpha) [-\exp(j\omega t) - \exp(-j\omega t)] + \exp(j14\alpha) 0 + \\
 &\quad \exp(j6\alpha) [\exp(j\omega t) + \exp(-j\omega t)] + \exp(j13\alpha) [-\exp(j\omega t) - \exp(-j\omega t)] + \exp(j2\alpha) 0 + \\
 &\quad \exp(j12\alpha) [\exp(j\omega t) + \exp(-j\omega t)] + \exp(j\alpha) [-\exp(j\omega t) - \exp(-j\omega t)] + \exp(j8\alpha) 0 \}
 \end{aligned} \quad (3.52)$$

$$i_{x_3y_3} = 0$$

Unlike in the previous solution, the zero-sequence component now has the value of:

$$i_0 = \sqrt{2/9} (1/2) \sqrt{2} (I/3) [6\sqrt{0.5} (\exp(j\omega t) + \exp(-j\omega t))] = (\sqrt{8}/3) I \cos(\omega t) \quad (3.53)$$

The active plane currents in the case of an asymmetrical machine are smaller in magnitude, since they are complemented with the zero-sequence current of (3.53) to produce overall phase currents. The same conclusions follow again: the charging process will not excite  $\alpha$ - $\beta$  plane, and it will take place with the machine at standstill.

Let us consider next an  $n$ -phase machine, where  $n = ak$ , and  $a = 2$ ,  $k > 3$ . A representative of this type of machines is a symmetrical ten-phase machine with two isolated neutral points. Now conductors of the single-phase supply can be connected between two isolated neutral points (Fig. 3.6b) and, like in the previous configurations that were discussed in this section, there will be no excitation of the  $\alpha$ - $\beta$  plane, and thus no torque.

The decoupling matrix for the symmetrical ten-phase machine follows directly from (3.1), and its form in space vector representation is given with

$$\begin{aligned}
 \underline{f}_{\alpha\beta} &= \sqrt{2/10} \left( \underline{a}_{a1} + \underline{a}_{a2} + \underline{a}_{b1} + \underline{a}_{b2} + \underline{a}_{c1} + \underline{a}_{c2} + \underline{a}_{d1} + \underline{a}_{d2} + \underline{a}_{e1} + \underline{a}_{e2} \right) \\
 \underline{f}_{x_1y_1} &= \sqrt{2/10} \left( \underline{a}_{a1} + \underline{a}_{a2} + \underline{a}_{b1} + \underline{a}_{b2} + \underline{a}_{c1} + \underline{a}_{c2} + \underline{a}_{d1} + \underline{a}_{d2} + \underline{a}_{e1} + \underline{a}_{e2} \right) \\
 \underline{f}_{x_2y_2} &= \sqrt{2/10} \left( \underline{a}_{a1} + \underline{a}_{a2} + \underline{a}_{b1} + \underline{a}_{b2} + \underline{a}_{c1} + \underline{a}_{c2} + \underline{a}_{d1} + \underline{a}_{d2} + \underline{a}_{e1} + \underline{a}_{e2} \right) \\
 \underline{f}_{x_3y_3} &= \sqrt{2/10} \left( \underline{a}_{a1} + \underline{a}_{a2} + \underline{a}_{b1} + \underline{a}_{b2} + \underline{a}_{c1} + \underline{a}_{c2} + \underline{a}_{d1} + \underline{a}_{d2} + \underline{a}_{e1} + \underline{a}_{e2} \right)
 \end{aligned} \quad (3.54)$$

where  $\underline{a} = \exp(j\alpha) = \cos \alpha + j \sin \alpha$  and  $\alpha = 2\pi/10$ .

For the connection diagrams of Fig. 3.6b the correlation between machine phase currents and grid currents is given with

$$i_{a1} = i_{b1} = i_{c1} = i_{d1} = i_{e1} = i_{+g}/5 \quad i_{a2} = i_{b2} = i_{c2} = i_{d2} = i_{e2} = i_{-g}/5 \quad (3.55)$$

Substitution of (3.55) into (3.54) gives the following space vectors in the four planes:

$$\begin{aligned}
 \underline{i}_{\alpha\beta} &= \sqrt{2/10} (1/2) \sqrt{2} (I/5) \{ \exp(j\omega t) + \exp(-j\omega t) + \exp(j\alpha) [-\exp(j\omega t) - \exp(-j\omega t)] + \exp(j2\alpha) [\exp(j\omega t) + \exp(-j\omega t)] + \\
 &\quad \exp(j3\alpha) [-\exp(j\omega t) - \exp(-j\omega t)] + \exp(j4\alpha) [\exp(j\omega t) + \exp(-j\omega t)] + \exp(j5\alpha) [-\exp(j\omega t) - \exp(-j\omega t)] + \\
 &\quad \exp(j6\alpha) [\exp(j\omega t) + \exp(-j\omega t)] + \exp(j7\alpha) [-\exp(j\omega t) - \exp(-j\omega t)] + \exp(j8\alpha) [\exp(j\omega t) + \exp(-j\omega t)] + \\
 &\quad \exp(j9\alpha) [-\exp(j\omega t) - \exp(-j\omega t)] \}
 \end{aligned} \quad (3.56)$$

$$\underline{i}_{\alpha\beta} = 0$$

$$\begin{aligned}
 \underline{i}_{x_1y_1} &= \sqrt{2/10} (1/2) \sqrt{2} (I/5) \{ \exp(j\omega t) + \exp(-j\omega t) + \exp(j2\alpha) [-\exp(j\omega t) - \exp(-j\omega t)] + \exp(j4\alpha) [\exp(j\omega t) + \exp(-j\omega t)] + \\
 &\quad \exp(j6\alpha) [-\exp(j\omega t) - \exp(-j\omega t)] + \exp(j8\alpha) [\exp(j\omega t) + \exp(-j\omega t)] + \exp(j10\alpha) [-\exp(j\omega t) - \exp(-j\omega t)] + \\
 &\quad \exp(j12\alpha) [\exp(j\omega t) + \exp(-j\omega t)] + \exp(j14\alpha) [-\exp(j\omega t) - \exp(-j\omega t)] + \exp(j16\alpha) [\exp(j\omega t) + \exp(-j\omega t)] + \\
 &\quad \exp(j18\alpha) [-\exp(j\omega t) - \exp(-j\omega t)] \}
 \end{aligned} \quad (3.57)$$

$$\underline{i}_{x_1y_1} = 0$$

$$\begin{aligned}
 \underline{i}_{x_2y_2} &= \sqrt{2/10} (1/2) \sqrt{2} (I/5) \{ \exp(j\omega t) + \exp(-j\omega t) + \exp(j3\alpha) [-\exp(j\omega t) - \exp(-j\omega t)] + \exp(j6\alpha) [\exp(j\omega t) + \exp(-j\omega t)] + \\
 &\quad \exp(j9\alpha) [-\exp(j\omega t) - \exp(-j\omega t)] + \exp(j12\alpha) [\exp(j\omega t) + \exp(-j\omega t)] + \exp(j15\alpha) [-\exp(j\omega t) - \exp(-j\omega t)] + \\
 &\quad \exp(j18\alpha) [\exp(j\omega t) + \exp(-j\omega t)] + \exp(j21\alpha) [-\exp(j\omega t) - \exp(-j\omega t)] + \exp(j24\alpha) [\exp(j\omega t) + \exp(-j\omega t)] + \\
 &\quad \exp(j27\alpha) [-\exp(j\omega t) - \exp(-j\omega t)] \}
 \end{aligned} \quad (3.58)$$

$$\underline{i}_{x_2y_2} = 0$$

$$\begin{aligned} \underline{i}_{x3y3} = & \sqrt{2/10}(1/2)\sqrt{2}(I/5)\{\exp(j\omega t) + \exp(-j\omega t) + \exp(j4\alpha)[(-\exp(j\omega t) - \exp(-j\omega t)) + \exp(j8\alpha)[\exp(j\omega t) + \exp(-j\omega t)] + \\ & \exp(j12\alpha)[-\exp(j\omega t) - \exp(-j\omega t)] + \exp(j16\alpha)[\exp(j\omega t) + \exp(-j\omega t)] + \exp(j20\alpha)[-\exp(j\omega t) - \exp(-j\omega t)] + \\ & \exp(j24\alpha)[\exp(j\omega t) + \exp(-j\omega t)] + \exp(j28\alpha)[-\exp(j\omega t) - \exp(-j\omega t)] + \exp(j32\alpha)[\exp(j\omega t) + \exp(-j\omega t)] + \\ & \exp(j36\alpha)[-\exp(j\omega t) - \exp(-j\omega t)]\} \end{aligned} \quad (3.59)$$

$$\underline{i}_{x3y3} = 0$$

The two zero-sequence components are governed with the two last rows of (3.1) when there is a single neutral point. While  $0_+$  component is equal to zero,  $0_-$  component equals:

$$\underline{i}_{0_-} = \sqrt{2/10}(1/2)\sqrt{2}(I/5)[10\sqrt{0.5}(\exp(j\omega t) + \exp(-j\omega t))] = (\sqrt{20}/5)I \cos(\omega t) \quad (3.60)$$

Equations (3.56)-(3.60) show that only  $0_-$  component is used for the charging process, thus leaving the  $\alpha$ - $\beta$  and  $x$ - $y$  planes without excitation. Clearly there will be no torque development during the charging mode.

Finally, let us consider an asymmetrical ten-phase machine. The starting point is, similar to the case of the asymmetrical six-phase or nine-phase machine, not the general transformation matrix (3.1); however, transformation matrix can be derived from the transformation matrix of a symmetrical twenty-phase machine using certain rules which are beyond the scope here. The derived matrix is too big to be presented here, thus only its equivalent space vector representation is given

$$\begin{aligned} \underline{f}_{\alpha\beta} &= \sqrt{2/10} \left( f_{a1} + \underline{a} f_{a2} + \underline{a}^4 f_{b1} + \underline{a}^5 f_{b2} + \underline{a}^8 f_{c1} + \underline{a}^9 f_{c2} + \underline{a}^{12} f_{d1} + \underline{a}^{13} f_{d2} + \underline{a}^{16} f_{e1} + \underline{a}^{17} f_{e2} \right) \\ \underline{f}_{x1y1} &= \sqrt{2/10} \left( f_{a1} + \underline{a}^3 f_{a2} + \underline{a}^{12} f_{b1} + \underline{a}^{15} f_{b2} + \underline{a}^4 f_{c1} + \underline{a}^7 f_{c2} + \underline{a}^{16} f_{d1} + \underline{a}^{19} f_{d2} + \underline{a}^8 f_{e1} + \underline{a}^{11} f_{e2} \right) \\ \underline{f}_{x2y2} &= \sqrt{2/10} \left( f_{a1} + \underline{a}^7 f_{a2} + \underline{a}^8 f_{b1} + \underline{a}^{15} f_{b2} + \underline{a}^{16} f_{c1} + \underline{a}^3 f_{c2} + \underline{a}^4 f_{d1} + \underline{a}^{11} f_{d2} + \underline{a}^{12} f_{e1} + \underline{a}^{19} f_{e2} \right) \\ \underline{f}_{x3y3} &= \sqrt{2/10} \left( f_{a1} + \underline{a}^9 f_{a2} + \underline{a}^{16} f_{b1} + \underline{a}^5 f_{b2} + \underline{a}^{12} f_{c1} + \underline{a} f_{c2} + \underline{a}^8 f_{d1} + \underline{a}^{17} f_{d2} + \underline{a}^4 f_{e1} + \underline{a}^{13} f_{e2} \right) \end{aligned} \quad (3.61a)$$

where  $\underline{a} = \exp(j\alpha) = \cos \alpha + j \sin \alpha$  and  $\alpha = \pi/10$ . Zero-sequence components are determined with

$$\begin{aligned} \underline{i}_{0_+} &= \sqrt{2/10} (i_{a1} + i_{b1} + i_{c1} + i_{d1} + i_{e1}) \\ \underline{i}_{0_-} &= \sqrt{2/10} (i_{a2} + i_{b2} + i_{c2} + i_{d2} + i_{e2}) \end{aligned} \quad (3.61b)$$

Like for the symmetrical ten-phase machine, the grid currents and the correlation between machine phase currents and grid currents are given with (3.32) and (3.55), respectively. Substitution of (3.55) into (3.61) gives the following space vectors and zero-sequence components:

$$\begin{aligned} \underline{i}_{\alpha\beta} &= \sqrt{2/10}(1/2)\sqrt{2}(I/5)\{\exp(j\omega t) + \exp(-j\omega t)[1 + \exp(j4\alpha) + \exp(j8\alpha) + \exp(j12\alpha) + \exp(j16\alpha)] + \\ & [-\exp(j\omega t) - \exp(-j\omega t)][\exp(j\alpha) + \exp(j5\alpha) + \exp(j9\alpha) + \exp(j13\alpha) + \exp(j17\alpha)]\} \end{aligned} \quad (3.62)$$

$$\underline{i}_{\alpha\beta} = 0$$

$$\begin{aligned} \underline{i}_{x1y1} &= \sqrt{2/10}(1/2)\sqrt{2}(I/5)\{\exp(j\omega t) + \exp(-j\omega t)[1 + \exp(j12\alpha) + \exp(j4\alpha) + \exp(j16\alpha) + \exp(j8\alpha)] + \\ & [-\exp(j\omega t) - \exp(-j\omega t)][\exp(j3\alpha) + \exp(j15\alpha) + \exp(j7\alpha) + \exp(j19\alpha) + \exp(j11\alpha)]\} \end{aligned} \quad (3.63)$$

$$\underline{i}_{x1y1} = 0$$

$$\begin{aligned} \underline{i}_{x2y2} &= \sqrt{2/10}(1/2)\sqrt{2}(I/5)\{\exp(j\omega t) + \exp(-j\omega t)[1 + \exp(j8\alpha) + \exp(j16\alpha) + \exp(j4\alpha) + \exp(j12\alpha)] + \\ & [-\exp(j\omega t) - \exp(-j\omega t)][\exp(j7\alpha) + \exp(j15\alpha) + \exp(j3\alpha) + \exp(j11\alpha) + \exp(j19\alpha)]\} \end{aligned} \quad (3.64)$$

$$\underline{i}_{x2y2} = 0$$

$$\begin{aligned} \underline{i}_{x3y3} &= \sqrt{2/10}(1/2)\sqrt{2}(I/5)\{\exp(j\omega t) + \exp(-j\omega t)[1 + \exp(j16\alpha) + \exp(j12\alpha) + \exp(j8\alpha) + \exp(j4\alpha)] + \\ & [-\exp(j\omega t) - \exp(-j\omega t)][\exp(j9\alpha) + \exp(j5\alpha) + \exp(j\alpha) + \exp(j17\alpha) + \exp(j13\alpha)]\} \end{aligned} \quad (3.65)$$

$$\underline{i}_{x3y3} = 0$$

$$\underline{i}_{0_+} = \sqrt{2/10} (i_a + i_c + i_e + i_g + i_i) = \sqrt{1/10} (I/5)[5(\exp(j\omega t) + \exp(-j\omega t))] = \sqrt{10} (I/5) \cos(\omega t) \quad (3.66)$$

$$\underline{i}_{0_-} = \sqrt{2/10} (i_b + i_d + i_f + i_h + i_j) = \sqrt{1/10} (I/5)[-5(\exp(j\omega t) + \exp(-j\omega t))] = -\sqrt{10} (I/5) \cos(\omega t)$$

As is obvious from (3.62)-(3.66), the charging process will utilise only the  $0_+$  and  $0_-$  components, and the other planes will not be excited. Like in the previous cases the machine will stay at standstill during charging process.

A different charging topology, that does not utilise neutral points and requires hardware reconfiguration, is shown in Fig. 3.7. It employs a five-phase machine, and, as can be seen, requires a switch to disconnect neutral point of phases  $a$  and  $b$  from the neutral point of the remaining phases.

In this case the decoupling transformation is given with (3.3). While the grid currents remain to be given with (3.32), their relationship with machine currents is now:

$$i_a = i_b = i_{+g}/2 \quad i_c = i_d = i_e = i_{-g}/3 \quad (3.67)$$

Substitution of (3.67) into (3.3) gives the following space vectors:

$$\begin{aligned} i_{\alpha\beta} &= \sqrt{2/5} (1/2) I \sqrt{2} \{ 0.5 \cdot (\exp(j\omega t) + \exp(-j\omega t)) + 0.5 \cdot \exp(j\alpha) [(\exp(j\omega t) + \exp(-j\omega t)) + 0.33 \cdot \exp(j2\alpha) [-\exp(j\omega t) - \exp(-j\omega t)] + 0.33 \cdot \exp(j3\alpha) [-\exp(j\omega t) - \exp(-j\omega t)] + 0.33 \cdot \exp(j4\alpha) [-\exp(j\omega t) - \exp(-j\omega t)]] \\ i_{\alpha\beta} &= (0.9757 + 0.7089j) \cdot I \cdot \cos(\omega t) \end{aligned} \quad (3.68)$$

$$\begin{aligned} i_{xy} &= \sqrt{2/5} (1/2) I \sqrt{2} \{ 0.5 \cdot (\exp(j\omega t) + \exp(-j\omega t)) + 0.5 \cdot \exp(j2\alpha) [(\exp(j\omega t) + \exp(-j\omega t)) + 0.33 \cdot \exp(j4\alpha) [-\exp(j\omega t) - \exp(-j\omega t)] + 0.33 \cdot \exp(j6\alpha) [-\exp(j\omega t) - \exp(-j\omega t)] + 0.33 \cdot \exp(j8\alpha) [-\exp(j\omega t) - \exp(-j\omega t)]] \\ i_{xy} &= (0.1424 + 0.4381j) \cdot I \cdot \cos(\omega t) \end{aligned} \quad (3.69)$$

As is obvious, excitation in the first plane exists. However, it can be seen that  $\alpha$  and  $\beta$  current components are proportional to each other. Therefore, similarly as in topologies of Fig. 3.1b and Fig. 3.4b, the excitation is pulsating rather than rotating, not capable of producing a starting torque. As a consequence, the machine can operate at standstill during the charging mode without being mechanically locked.

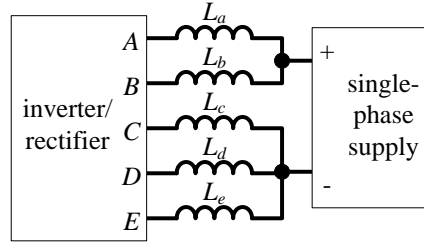


Fig. 3.7: Connection of a single-phase voltage supply to a five-phase machine.

This concludes the theoretical considerations of this section. It has been shown that a single-phase supply can be successfully used for charging the vehicle battery through the multiphase machines which have a multiple number of isolated neutral points, and that for this type of charging there is no need for connection changeover between propulsion and the charging mode.

An exception from this rule is a five-phase topology. Machines with single neutral point, with phase numbers other than five were not considered in this section, but a five-phase machine can be regarded as a representative case for all prime phase numbers. This is so since use of a single neutral point in the propulsion mode requires hardware reconfiguration (i.e. opening of the neutral point and formation of isolated neutral points for the single-phase supply connection) for all prime phase numbers. In essence, a single neutral point has to be split into two separate neutral points. If this hardware reconfiguration is performed, then all the analysis for the charging mode remains similar to the five-phase case for all the other prime phase numbers.

### 3.4 Three-phase supply

Depending on the machine's phase number and the number of neutral points, different methods can be devised to enable charging from the three-phase grid. The simplest possibility opens up if the machine has at least three isolated neutral points, so that the stator winding is nine-phase. This comes down to the fact that the principle, described in the previous section for the use of single-phase supply, can be extended to the use of three-phase supply in charging mode. Again, as in section 3.3 and in contrast to the solutions of section 3.2, hardware reconfiguration is not required. Since one needs to have at least three isolated neutral points, and given the phase number  $n = ak$ , the number of sub-windings needs to be  $a = 3$  (or more).

The concept, that is described next, can be extended in a straightforward manner to any machine with more than three neutral points (e.g. twelve-, fifteen- or eighteen-phase machine, for example, obtainable by using a multitude of three-phase windings with isolated neutral points). The number of phases of the sub-windings can be  $k = 3, 5, \dots$ . Since in the charging mode there will be  $k$  phases connected in parallel, this means that the equivalent leakage inductance available for the charging process will reduce more and more as the number of sub-winding phases  $k$  increases. It is for this reason that only the configurations with  $k = 3$  and  $a = 3$  are discussed further on. This in essence comes down to asymmetrical and symmetrical nine-phase machines with three isolated neutral points in the propulsion mode.

The second possibility of using the three-phase supply (in conjunction with multiphase machines) relates to the already available configuration of [De Sousa et al (2010a), 2010b)], where a three-phase machine with winding mid-points taken out from the machine and connected to three-phase supply for charging purposes was analysed. This

configuration in essence corresponds to a symmetrical six-phase machine and the solution with the use of the same idea for a symmetrical six-phase machine is therefore also covered in this section. Assuming that the six-phase machine operates in propulsion mode with either a single or with two neutral points, this possibility will require hardware reconfiguration since the neutral points will have to be opened. This is in contrast to the solution of [De Sousa et al (2010a, 2010b)]. Some other modified solutions, based on the use of six-phase machines and the three-phase supply, are also included towards the end of the section.

If a symmetrical nine-phase machine with three isolated neutral points is supplied from a three-phase source connected to the three neutral points of three-phase windings, where each set of three-phase windings remains as in normal propulsion mode of operation, as illustrated in Fig. 3.8, then the  $\alpha$ - $\beta$  plane will not be excited. The configuration of Fig. 3.8 simultaneously applies to an asymmetrical nine-phase machine with triple three-phase winding. For the purposes of proof, consider at first the symmetrical nine-phase machine.

The space vector representation of the decoupling matrix has already been given in (3.41), where again  $\underline{a} = \exp(j\alpha) = \cos \alpha + j \sin \alpha$  and  $\alpha = 2\pi/9$ . The grid currents are now different and they are given with:

$$\begin{aligned} i_{ag} &= \sqrt{2} I \cos(\omega t) \\ i_{bg} &= \sqrt{2} I \cos(\omega t - 2\pi/3) \\ i_{cg} &= \sqrt{2} I \cos(\omega t - 4\pi/3) \end{aligned} \quad (3.70)$$

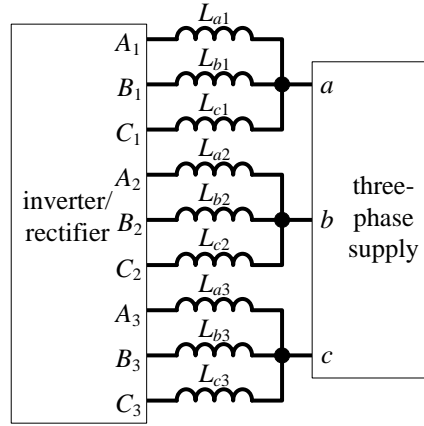


**Fig. 3.8:** Configuration for three-phase charging through a symmetrical or asymmetrical nine-phase machine with three isolated neutral points.

The same grid currents of the form of (3.70) will be used for all the configurations that will be discussed in this section. For the connection diagram of Fig. 3.8 the correlation between machine phase currents and grid currents is given with

$$i_{a1} = i_{b1} = i_{c1} = i_{ag}/3 \quad i_{a2} = i_{b2} = i_{c2} = i_{bg}/3 \quad i_{a3} = i_{b3} = i_{c3} = i_{cg}/3 \quad (3.71)$$

Following the same procedure like in the previous section, the following space vectors of the four planes can be obtained:

$$\begin{aligned} \underline{i}_{\alpha\beta} &= \sqrt{2/9} (1/2) \sqrt{2} (I/3) \{ [1 + \exp(j3\alpha) + \exp(j6\alpha)] [\exp(j\omega t) + \exp(-j\omega t)] + \\ &\quad [\exp(j\alpha) + \exp(j4\alpha) + \exp(j7\alpha)] [(\exp(j(\omega t - 2\pi/3)) + \exp(-j(\omega t - 2\pi/3)))] + \\ &\quad [\exp(j2\alpha) + \exp(j5\alpha) + \exp(j8\alpha)] [(\exp(j(\omega t - 4\pi/3)) + \exp(-j(\omega t - 4\pi/3)))] \} \end{aligned} \quad (3.72)$$

$$\underline{i}_{\alpha\beta} = 0$$

$$\begin{aligned} \underline{i}_{x_1 y_1} &= \sqrt{2/9} (1/2) \sqrt{2} (I/3) \{ [1 + \exp(j6\alpha) + \exp(j12\alpha)] [\exp(j\omega t) + \exp(-j\omega t)] + \\ &\quad [\exp(j2\alpha) + \exp(j8\alpha) + \exp(j14\alpha)] [(\exp(j(\omega t - 2\pi/3)) + \exp(-j(\omega t - 2\pi/3)))] + \\ &\quad [\exp(j4\alpha) + \exp(j10\alpha) + \exp(j16\alpha)] [(\exp(j(\omega t - 4\pi/3)) + \exp(-j(\omega t - 4\pi/3)))] \} \end{aligned} \quad (3.73)$$

$$\underline{i}_{x_1 y_1} = 0$$

$$\begin{aligned} \underline{i}_{x_2 y_2} &= \sqrt{2/9} (1/2) \sqrt{2} (I/3) \{ [1 + \exp(j9\alpha) + \exp(j18\alpha)] [\exp(j\omega t) + \exp(-j\omega t)] + \\ &\quad [\exp(j3\alpha) + \exp(j12\alpha) + \exp(j21\alpha)] [(\exp(j(\omega t - 2\pi/3)) + \exp(-j(\omega t - 2\pi/3)))] + \\ &\quad [\exp(j6\alpha) + \exp(j15\alpha) + \exp(j24\alpha)] [(\exp(j(\omega t - 4\pi/3)) + \exp(-j(\omega t - 4\pi/3)))] \} \end{aligned} \quad (3.74)$$

$$\begin{aligned} \underline{i}_{x_2 y_2} &= \sqrt{1/9} (I/3) \{ 3[\exp(j\omega t) + \exp(-j\omega t)] + 3\exp(j2\pi/3) [(\exp(j(\omega t - 2\pi/3)) + \exp(-j(\omega t - 2\pi/3)))] + \\ &\quad 3\exp(j4\pi/3) [(\exp(j(\omega t - 4\pi/3)) + \exp(-j(\omega t - 4\pi/3)))] \} = I \exp(j\omega t) \end{aligned}$$

$$\begin{aligned} \underline{i}_{x_3y_3} &= \sqrt{2/9} (1/2) \sqrt{2} (I/3) \{ [1 + \exp(j12\alpha) + \exp(j24\alpha)] [\exp(j\omega t) + \exp(-j\omega t)] + \\ &\quad [\exp(j4\alpha) + \exp(j16\alpha) + \exp(j28\alpha)] [\exp(j(\omega t - 2\pi/3)) + \exp(-j(\omega t - 2\pi/3))] + \\ &\quad [\exp(j8\alpha) + \exp(j20\alpha) + \exp(j32\alpha)] [\exp(j(\omega t - 4\pi/3)) + \exp(-j(\omega t - 4\pi/3))] \} \end{aligned} \quad (3.75)$$

$$\underline{i}_{x_3y_3} = 0$$

Naturally, the zero-sequence component is equal to zero. As is obvious from (3.72)-(3.75) the charging process, which is obtained without hardware reconfiguration, will utilise only the  $x_2$ - $y_2$  plane and the  $\alpha$ - $\beta$  plane will stay without excitation, thus the rotor will not move.

The same charging principle can be applied to an asymmetrical nine-phase machine. Transformation matrix of this type of machine is already given with (3.47), and its equivalent space vector representation with (3.48), where  $\underline{a} = \exp(j\alpha) = \cos \alpha + j \sin \alpha$  and  $\alpha = \pi/9$ . The grid currents and the correlation between machine phase currents and grid currents are again given with (3.70) and (3.71), respectively. Substitution of (3.71) into (3.48) gives the following space vectors:

$$\begin{aligned} \underline{i}_{\alpha\beta} &= \sqrt{2/9} (1/2) \sqrt{2} (I/3) \{ [1 + \exp(j6\alpha) + \exp(j12\alpha)] [\exp(j\omega t) + \exp(-j\omega t)] + \\ &\quad [\exp(j\alpha) + \exp(j7\alpha) + \exp(j13\alpha)] [\exp(j(\omega t - 2\pi/3)) + \exp(-j(\omega t - 2\pi/3))] + \\ &\quad [\exp(j2\alpha) + \exp(j8\alpha) + \exp(j14\alpha)] [\exp(j(\omega t - 4\pi/3)) + \exp(-j(\omega t - 4\pi/3))] \} \end{aligned} \quad (3.76)$$

$$\underline{i}_{\alpha\beta} = 0$$

$$\begin{aligned} \underline{i}_{x_1y_1} &= \sqrt{2/9} (1/2) \sqrt{2} (I/3) \{ [1 + 1 + 1] [\exp(j\omega t) + \exp(-j\omega t)] + \\ &\quad [\exp(j3\alpha) + \exp(j3\alpha) + \exp(j3\alpha)] [\exp(j(\omega t - 2\pi/3)) + \exp(-j(\omega t - 2\pi/3))] + \\ &\quad [\exp(j6\alpha) + \exp(j6\alpha) + \exp(j6\alpha)] [\exp(j(\omega t - 4\pi/3)) + \exp(-j(\omega t - 4\pi/3))] \} \end{aligned} \quad (3.77a)$$

$$\begin{aligned} \underline{i}_{x_1y_1} &= \sqrt{1/9} (I/3) \{ 3 [\exp(j\omega t) + \exp(-j\omega t)] + 3 \exp(j\pi/3) [\exp(j(\omega t - 2\pi/3)) + \exp(-j(\omega t - 2\pi/3))] + \\ &\quad 3 \exp(j2\pi/3) [\exp(j(\omega t - 4\pi/3)) + \exp(-j(\omega t - 4\pi/3))] \} = \sqrt{1/9} I \{ 3 \exp(j\omega t) (1 + \exp(-j\pi/3) + \\ &\quad \exp(-j2\pi/3)) + 3 \exp(-j\omega t) (1 + \exp(j\pi) + 1) \} = I \{ (2/3) \cos(\omega t) + (\sqrt{3}/3) \sin(\omega t) - j(\sqrt{3}/3) \cos(\omega t) \} \end{aligned} \quad (3.77b)$$

$$\begin{aligned} \underline{i}_{x_2y_2} &= \sqrt{2/9} (1/2) \sqrt{2} (I/3) \{ [1 + \exp(j12\alpha) + \exp(j6\alpha)] [\exp(j\omega t) + \exp(-j\omega t)] + \\ &\quad [\exp(j5\alpha) + \exp(j17\alpha) + \exp(j11\alpha)] [\exp(j(\omega t - 2\pi/3)) + \exp(-j(\omega t - 2\pi/3))] + \\ &\quad [\exp(j10\alpha) + \exp(j4\alpha) + \exp(j16\alpha)] [\exp(j(\omega t - 4\pi/3)) + \exp(-j(\omega t - 4\pi/3))] \} \end{aligned} \quad (3.78)$$

$$\underline{i}_{x_2y_2} = 0$$

$$\begin{aligned} \underline{i}_{x_3y_3} &= \sqrt{2/9} (1/2) \sqrt{2} (I/3) \{ [1 + \exp(j6\alpha) + \exp(j12\alpha)] [\exp(j\omega t) + \exp(-j\omega t)] + \\ &\quad [\exp(j7\alpha) + \exp(j13\alpha) + \exp(j\alpha)] [\exp(j(\omega t - 2\pi/3)) + \exp(-j(\omega t - 2\pi/3))] + \\ &\quad [\exp(j14\alpha) + \exp(j2\alpha) + \exp(j8\alpha)] [\exp(j(\omega t - 4\pi/3)) + \exp(-j(\omega t - 4\pi/3))] \} \end{aligned} \quad (3.79)$$

$$\underline{i}_{x_3y_3} = 0$$

The zero-sequence component has now the value of:

$$\begin{aligned} i_0 &= \sqrt{2/9} (1/2) \sqrt{2} (I/3) \{ [\sqrt{1/2} + \sqrt{1/2} + \sqrt{1/2}] [\exp(j\omega t) + \exp(-j\omega t)] + \\ &\quad [-\sqrt{1/2} - \sqrt{1/2} - \sqrt{1/2}] [\exp(j(\omega t - 2\pi/3)) + \exp(-j(\omega t - 2\pi/3))] + \\ &\quad [\sqrt{1/2} + \sqrt{1/2} + \sqrt{1/2}] [\exp(j(\omega t - 4\pi/3)) + \exp(-j(\omega t - 4\pi/3))] \} \end{aligned} \quad (3.80)$$

$$i_0 = I \{ -(\sqrt{8}/3) \cos(\omega t - 2\pi/3) \}$$

Hence once more the charging process will not utilise the  $\alpha$ - $\beta$  plane. Previous equations confirm that both symmetrical and asymmetrical nine-phase machines can be used for charging purposes without generation of the field in  $\alpha$ - $\beta$  plane in conjunction with both single-phase and three-phase supply.

Moreover, for these types of multiphase machines there is no need for any hardware reconfiguration as the grid connections can stay attached to the neutral points of each machine without interfering with the propulsion mode of operation. The solution of course requires a nine-phase machine with three isolated neutral points, but there are no requirements for contactors and intervention of any kind when transition from propulsion to charging mode takes place (of course, software for the control of the inverter/rectifier will change).

Until now, there was only a single solution available for three-phase charging without requirement for the hardware reconfiguration, based on a three-phase machine [De Sousa et al (2010a, 2010b)]. That solution requires taking out to the terminal box of the machine the mid-points of each of the individual phase windings, which is not really possible with standard off-the-shelf three-phase machines. Hence the solution of [De Sousa et al (2010a, 2010b)] has the same drawback as those covered in this section, namely a machine has to be specially manufactured for the purpose of use in both propulsion and charging mode, in order to avoid any hardware reconfiguration.

The idea presented in [De Sousa et al (2010a, 2010b)] is considered next, in conjunction with the symmetrical six-phase machine, Fig. 3.9a.

If a symmetrical six-phase machine is considered for the charging purposes, the equivalent space vector representation of the decoupling matrix is required, as given with (3.26), where again  $\underline{a} = \exp(j\alpha) = \cos \alpha + j \sin \alpha$  and  $\alpha = 2\pi/6$ . The grid currents are again given with (3.70). For the connection diagram of Fig. 3.9a the correlation between machine phase currents and grid currents is given with

$$i_{a1} = i_{b2} = i_{ag}/2 \quad i_{b1} = i_{c2} = i_{bg}/2 \quad i_{c1} = i_{a2} = i_{cg}/2 \quad (3.81)$$

Substitution of (3.81) into (3.26) gives the following space vectors in the two planes:

$$\begin{aligned} \underline{i}_{\alpha\beta} = & \sqrt{2/6} (1/2) \sqrt{2} (I/2) \{ (1 + \exp(j3\alpha)) [\exp(j\omega t) + \exp(-j\omega t)] + (\exp(j2\alpha) + \exp(j5\alpha)) [\exp(j(\omega t - 2\pi/3)) + \\ & \exp(-j(\omega t - 2\pi/3))] + (\exp(j4\alpha) + \exp(j\alpha)) [\exp(j(\omega t - 4\pi/3)) + \exp(-j(\omega t - 4\pi/3))] \} \end{aligned} \quad (3.82)$$

$$\underline{i}_{\alpha\beta} = 0$$

$$\begin{aligned} \underline{i}_{xy} = & \sqrt{2/6} (1/2) \sqrt{2} (I/2) \{ (1 + \exp(j6\alpha)) [\exp(j\omega t) + \exp(-j\omega t)] + (\exp(j4\alpha) + \exp(j10\alpha)) [\exp(j(\omega t - 2\pi/3)) + \\ & \exp(-j(\omega t - 2\pi/3))] + (\exp(j2\alpha) + \exp(j8\alpha)) [\exp(j(\omega t - 4\pi/3)) + \exp(-j(\omega t - 4\pi/3))] \} \end{aligned} \quad (3.83)$$

$$\underline{i}_{xy} = \sqrt{6} (I/2) \exp(-j\omega t)$$

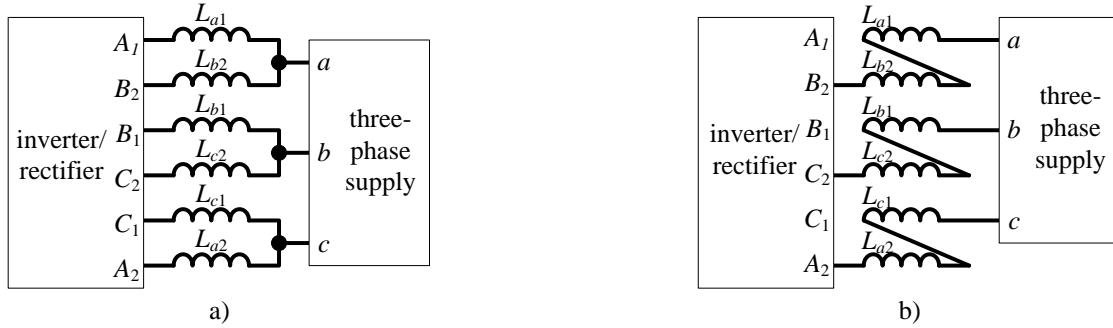


**Fig. 3.9:** Configuration for three-phase charging through: a) a symmetrical six-phase machine, b) a modified symmetrical six-phase machine.

The zero-sequence components are equal to zero.

As is obvious from (3.82)-(3.83) the charging process will utilise only the  $x$ - $y$  plane for charging. This solution confirms that the same charging operation like in the [De Sousa et al (2010a, 2010b)] can be obtained from a symmetrical six-phase machine. However, although both solutions require specially designed machines, which are not readily available, the solution of [De Sousa et al (2010a, 2010b)], based on a three-phase machine, has the advantage that hardware reconfiguration is not required. The solution of Fig. 3.9a requires hardware reconfiguration regardless of whether the symmetrical six-phase machine is operated in propulsion mode with a single or with two neutral points.

In the case of Fig. 3.9a the current in each pair of phases in spatial opposition is deliberately made the same, by connecting them in parallel. The previous configuration can be modified so that the phases in spatial opposition are connected in series, but in such a way that their currents are not in phase opposition (which would yield the three-phase machine configuration). This requires the following connection reconfiguration: the beginning of one phase winding is connected to the grid, while the end of the same phase winding is connected to the beginning of the phase winding in spatial opposition. The end of the phase winding in spatial opposition is connected to the inverter/rectifier leg. If that configuration, shown in Fig. 3.9b, is supplied from a three-phase source,  $\alpha$ - $\beta$  plane will not be excited. This solution will have an advantageous feature, in that that now the equivalent filter inductance will be four times greater than in the previous configuration. However, hardware reconfiguration is more involved since, in effect, only three phases remain connected to the inverter/rectifier in the charging mode.

For this solution the same space vector representation of decoupling model is valid as in the previous case, (3.26). The grid currents are again given with (3.70). Diagram from Fig. 3.9b yields the correlation between machine phase currents and grid currents

$$i_{a1} = i_{b2} = i_{ag} \quad i_{b1} = i_{c2} = i_{bg} \quad i_{c1} = i_{a2} = i_{cg} \quad (3.84)$$

It can be noticed that equation (3.84) has the same form as (3.81), but with two times larger motor phase currents. Thus, it can be concluded that  $\alpha$ - $\beta$  and zero-sequence components will not be excited during the charging process, and  $x$ - $y$  plane will have a space vector two times larger than in the previous case,  $\underline{i}_{xy} = \sqrt{6} I \exp(-j\omega t)$ .

Again there will be no torque and thus no rotor movement during the charging process. This solution has an advantage over the one of Fig. 3.9a if the equivalent filter inductance needs to be increased for the proper charging mode.

Let us consider next an alternative way of using a symmetrical six-phase machine for charging purposes. Most of the configurations discussed so far are without excitation of  $\alpha$ - $\beta$  plane, thus without generation of any field in rotor, which results in rotor staying at standstill during charging. However, if only single component of  $\alpha$ - $\beta$  plane is excited, there will be no rotational field in the rotor, and the rotor will remain at its position, as was the case in the configuration of Fig. 3.1b and Fig. 3.4b. This introduces additional degrees of freedom into charging process. Three such configurations that use these additional degrees of freedom are presented next.

A symmetrical six-phase machine is considered again, but now in the charging configuration depicted in Fig. 3.10. The same equations (3.26) and (3.70) apply again, but now the correlation between machine phase currents and grid currents is given with

$$i_{a1} = i_{a2} = i_{ag}/2 \quad i_{b1} = i_{c2} = i_{bg}/2 \quad i_{c1} = i_{b2} = i_{cg}/2 \quad (3.85)$$

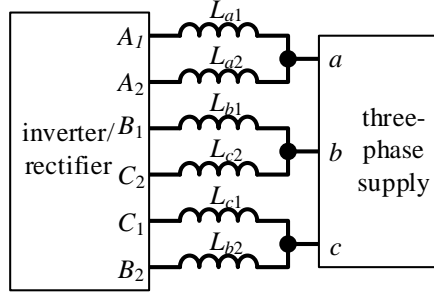


**Fig. 3.10:** Configuration for three-phase charging through a symmetrical or asymmetrical six-phase machine.

Substitution of (3.85) into (3.26) gives the following space vectors in the two planes:

$$\begin{aligned} \underline{i}_{\alpha\beta} &= \sqrt{2/6}(1/2)\sqrt{2}(I/2)\{(1 + \exp(j\alpha))[\exp(j\omega t) + \exp(-j\omega t)] + (\exp(j2\alpha) + \exp(j5\alpha))[(\exp(j(\omega t - 2\pi/3)) + \\ &\quad \exp(-j(\omega t - 2\pi/3))] + (\exp(j3\alpha) + \exp(j4\alpha))[(\exp(j(\omega t - 4\pi/3)) + \exp(-j(\omega t - 4\pi/3))]\} \\ \underline{i}_{\alpha\beta} &= \sqrt{2/6}(1/2)\sqrt{2}(I/2)\{\exp(j\omega t) \cdot [(1 + \exp(j\alpha)) + (\exp(-j(\omega t - 2\pi/3))(\exp(j2\alpha) + \exp(j5\alpha)) \\ &\quad + \exp(-j(\omega t - 4\pi/3))(\exp(j3\alpha) + \exp(j4\alpha)))] + \exp(-j\omega t)[(1 + \exp(j\alpha)) \\ &\quad + (\exp(j(\omega t - 2\pi/3))(\exp(j2\alpha) + \exp(j5\alpha)) + \exp(j(\omega t - 4\pi/3))(\exp(j3\alpha) + \exp(j4\alpha))]\} \\ \underline{i}_{\alpha\beta} &= \sqrt{1/6}(I/2)\{\exp(j\omega t) \cdot (3 + 0j) + \exp(-j\omega t) \cdot (1.5 + 2.5981j)\} \\ \underline{i}_{\alpha\beta} &= \sqrt{1/6}(3I/2)\{\exp(j\omega t) \cdot \exp(j0) + \exp(-j\omega t) \cdot (0.5 + 0.8660j)\} \\ \underline{i}_{\alpha\beta} &= \sqrt{1/6}(3I/2)\{\exp(j\omega t) \cdot \exp(j\pi/6) \cdot \exp(-j\pi/6) + \exp(-j\omega t) \cdot \exp(j\pi/6) \cdot \exp(j\pi/6)\} \\ \underline{i}_{\alpha\beta} &= \sqrt{1/6}(3I/2)\exp(j\pi/6) \cdot \{\exp(j(\omega t - \pi/6)) + \exp(-j(\omega t - \pi/6))\} \\ \underline{i}_{\alpha\beta} &= I\sqrt{3/2}\exp(j\pi/6) \cdot \cos(\omega t - \pi/6) = (1.0607 + 0.6124j) \cdot I \cdot \cos(\omega t - \pi/6) \\ \underline{i}_{xy} &= \sqrt{2/6}(1/2)\sqrt{2}(I/2)\{(1 + \exp(j2\alpha))[\exp(j\omega t) + \exp(-j\omega t)] + (\exp(j4\alpha) + \exp(j10\alpha))[(\exp(j(\omega t - 2\pi/3)) + \\ &\quad \exp(-j(\omega t - 2\pi/3))] + (\exp(j6\alpha) + \exp(j8\alpha))[(\exp(j(\omega t - 4\pi/3)) + \exp(-j(\omega t - 4\pi/3))]\} \\ \underline{i}_{xy} &= \sqrt{2/6}(1/2)\sqrt{2}(I/2)\{\exp(j\omega t) \cdot [(1 + \exp(j2\alpha)) + (\exp(-j(\omega t - 2\pi/3))(\exp(j4\alpha) + \exp(j10\alpha)) \\ &\quad + \exp(-j(\omega t - 4\pi/3))(\exp(j6\alpha) + \exp(j8\alpha)))] + \exp(-j\omega t)[(1 + \exp(j2\alpha)) + \\ &\quad + (\exp(j(\omega t - 2\pi/3))(\exp(j4\alpha) + \exp(j10\alpha)) + \exp(j(\omega t - 4\pi/3))(\exp(j6\alpha) + \exp(j8\alpha))]\} \\ \underline{i}_{xy} &= \sqrt{1/6}(I/2)\{\exp(j\omega t) \cdot (-1.5 + 2.5981j) + \exp(-j\omega t) \cdot (3 + 0j)\} \\ \underline{i}_{xy} &= \sqrt{1/6}(3I/2)\{\exp(j\omega t) \cdot (-0.5 + 0.8660j) + \exp(-j\omega t) \cdot \exp(j0)\} \\ \underline{i}_{xy} &= \sqrt{1/6}(3I/2)\{\exp(j\omega t) \cdot \exp(j\pi/3) \cdot \exp(j\pi/3) + \exp(-j\omega t) \cdot \exp(j\pi/3) \cdot \exp(-j\pi/3)\} \\ \underline{i}_{xy} &= \sqrt{1/6}(3I/2)\exp(j\pi/3) \cdot \{\exp(j(\omega t + \pi/3)) + \exp(-j(\omega t + \pi/3))\} \\ \underline{i}_{xy} &= I\sqrt{3/2}\exp(j\pi/3) \cdot \cos(\omega t + \pi/3) = (0.6124 + 1.0607j) \cdot I \cdot \cos(\omega t + \pi/3) \end{aligned} \quad (3.87)$$

Zero-sequence components are equal to zero. Unlike in the previously considered solution,  $\alpha$ - $\beta$  plane is now excited, and both components ( $\alpha$  and  $\beta$ ) are a sinusoidal function of time. However, excitation pulsates along a single direction, thus there is no generation of a rotating field. The pulsating field that will be present will not be able to move the rotor. Needless to say, hardware reconfiguration is required from propulsion to charging mode.

It can be concluded that charging without torque can take place even if components from the first plane are excited, as long as there is only pulsating field in the machine.

The same principle can be applied to an asymmetrical machine. The decoupling matrix in the space vector representation, and the correlation between machine phase currents and grid currents, are again given with (3.37) and (3.85), respectively. The two space vectors are now:

$$\underline{i}_{\alpha\beta} = \sqrt{2/6} (1/2) \sqrt{2} (I/2) \{ (1 + \exp(j\alpha)) [\exp(j\omega t) + \exp(-j\omega t)] + (\exp(j4\alpha) + \exp(j9\alpha)) [\exp(j(\omega t - 2\pi/3)) + \exp(-j(\omega t - 2\pi/3))] + (\exp(j8\alpha) + \exp(j5\alpha)) [\exp(j(\omega t - 4\pi/3)) + \exp(-j(\omega t - 4\pi/3))] \} \quad (3.88)$$

$$\underline{i}_{\alpha\beta} = I \sqrt{3/2} (0.966 + j0.259) \cos(\omega t - \pi/12)$$

$$\underline{i}_{xy} = \sqrt{2/6} (1/2) \sqrt{2} (I/2) \{ (1 + \exp(j5\alpha)) [\exp(j\omega t) + \exp(-j\omega t)] + (\exp(j8\alpha) + \exp(j9\alpha)) [\exp(j(\omega t - 2\pi/3)) + \exp(-j(\omega t - 2\pi/3))] + (\exp(j16\alpha) + \exp(j\alpha)) [\exp(j(\omega t - 4\pi/3)) + \exp(-j(\omega t - 4\pi/3))] \} \quad (3.89)$$

$$\underline{i}_{xy} = I \sqrt{3/2} (0.259 + j0.966) \cos(\omega t + 5\pi/12)$$

Zero-sequence components  $0_+$  and  $0_-$  are equal to zero. From equation (3.88) it can be seen that both components of the  $\alpha$ - $\beta$  plane are excited. However, the space vector  $\underline{i}_{\alpha\beta}$  will always have the same angle, similar as in (3.86), thus there will be no generation of a rotating field.

The final topology considered here is the one employing a five-phase machine. The connection scheme is given in Fig. 3.11. The decoupling matrix is given with (3.3), while the grid currents remain to be governed with (3.70). From Fig. 3.11 it can be seen that the relationship between grid and machine currents is the following:

$$i_a = i_{ag} \quad i_b = i_e = i_{bg}/2 \quad i_c = i_d = i_{cg}/2 \quad (3.90)$$

Substitution of (3.90) into (3.3) yields the following:

$$\underline{i}_{\alpha\beta} = \sqrt{2/6} (1/2) \sqrt{2} (I/2) \{ 2 \cdot [\exp(j\omega t) + \exp(-j\omega t)] + (\exp(j\alpha) + \exp(j4\alpha)) [\exp(j(\omega t - 2\pi/3)) + \exp(-j(\omega t - 2\pi/3))] + (\exp(j2\alpha) + \exp(j3\alpha)) [\exp(j(\omega t - 4\pi/3)) + \exp(-j(\omega t - 4\pi/3))] \} \quad (3.91)$$

$$\underline{i}_{\alpha\beta} = I \cdot \sqrt{2} \cos(\omega t - 0.659)$$

$$\underline{i}_{xy} = \sqrt{2/6} (1/2) \sqrt{2} (I/2) \{ 2 \cdot [\exp(j\omega t) + \exp(-j\omega t)] + (\exp(j2\alpha) + \exp(j8\alpha)) [\exp(j(\omega t - 2\pi/3)) + \exp(-j(\omega t - 2\pi/3))] + (\exp(j4\alpha) + \exp(j6\alpha)) [\exp(j(\omega t - 4\pi/3)) + \exp(-j(\omega t - 4\pi/3))] \} \quad (3.92)$$

$$\underline{i}_{xy} = I \cdot \sqrt{2} \cos(\omega t + 0.659)$$

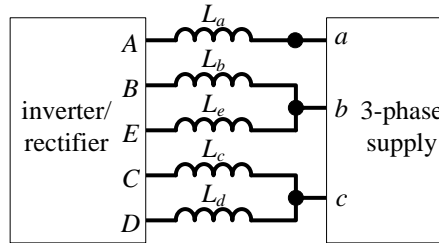


Fig. 3.11: Three-phase charging through a five-phase machine.

It is obvious that again only the pulsating field exists and in this case it is along  $\alpha$  axis. Since a pulsating field is incapable of producing a starting torque, the machine does not have to be mechanically locked during the charging process.

The concept used here for a five-phase machine can be extrapolated to other prime phase numbers in a simple manner. One possibility is to use only five phases of the machine in charging process regardless of the actual phase numbers; the other possibility is to parallel more and more phases of the machine to each grid phase as the machine's phase number increases.

### 3.5 Conclusion

In this chapter some of the possible configurations for the battery charging through multiphase machines have been introduced. At first the charging from a multiphase supply is considered and it is shown that machines with the same number of phases as a supply can be used like filters without the need to mechanically lock the rotor, as there will be no field in such machines during this process. Hardware reconfiguration would be required to open the neutral point of the winding.

Single-phase charging solutions with integrated multiphase machines are considered next. It is shown that for this type of charging there is no need for hardware reconnections between the propulsion and the charging mode as long as the machine has at least two isolated neutral points, since the supply connections are attached to isolated neutral

points of the machine and there is no interference with the propulsion mode. The other single-phase charging solutions, applicable to machines with a prime number of phases, do require hardware reconfiguration as illustrated for a five-phase winding.

Finally, the charging from a three-phase source is considered as, at present, the most important way of fast charging. Charging through a nine-phase machine with three isolated neutral points is presented as a solution with great potential, since it does not require hardware reconnections between the propulsion and the charging mode. The concept is directly extendable to machines with more than three neutral points and any phase number per sub-winding. Next, an already existing solution with a three-phase machine is further extended to a symmetrical six-phase machine, and a possible modification of this solution is presented.

In addition to the solutions which do not excite the first (flux/torque producing) plane at all, five charging solutions which produce pulsating field in the first plane are also introduced, three in conjunction with three-phase charging, one in conjunction with five-phase grid supply, and one in conjunction with single-phase grid supply.

## CHAPTER 4: MULTIPHASE VOLTAGE SOURCE RECTIFIERS

### 4.1 Introduction

Numerous possible on-board charging topologies, incorporating multiphase machines and multiphase voltage source converters, have been developed and analytically examined in the previous chapter. The common feature of all of them is that they require a multiphase voltage source rectifier (VSR) and an appropriate algorithm for its control. Basic operating principles of a VSR are therefore discussed in this chapter. Based on the theoretical results obtained in the Chapter 3, it is assumed that multiphase machines in the selected configurations will behave as a simple resistive-inductive passive circuit during the charging process. Thus in this chapter series connection of an inductance and a resistance will be used to represent the machine's equivalent phase disposition during the charging process. This simplifies the equivalent circuit model of the system, and facilitates development of its control.

Three-phase VSRs have been investigated extensively over the years [Neacsu (1999), Wang et al (2009), Zhang et al (2010), Gallardo-Lozano et al (2012)], mainly due to their ability of unity power factor operation, and are today regarded as well-known. Multiphase VSRs have not been covered in the literature, but the principle of operation and most parts of the control algorithm are the same as for a three-phase VSR. The main difference will be the existence of multiple planes in certain cases in the decoupled model, in contrast to a single  $\alpha$ - $\beta$  plane that exists in the three-phase VSR. These additional planes will in principle require multiple PI controller pairs.

Voltage source converters (VSCs) are particularly interesting in the area of EVs due to their ability to work in both rectifying and inverting mode with the same hardware. Rectifying mode corresponds to the charging mode of the vehicle's battery. Since only multiphase VSRs can be used in the configurations presented in the Chapter 3, only they will be considered in what follows.

Three main aspects of multiphase VSRs are elaborated. At first some of their main features are discussed. After that a mathematical model of the system is given. Finally, a complete control algorithm, suitable for multiphase VSRs, is presented.

### 4.2 Principle of operation

The ability to provide unity power factor rectification towards grid makes VSRs perfectly suitable for battery charging applications in EVs. Fig. 4.1 depicts the topology of a multiphase VSR system. In this section general information about this type of converter is given.

The principle of operation of a VSR is explained using Fig. 4.2, where equivalent circuit representation of the grid-side of VSR is given. The equivalent scheme is the same for multiphase and three-phase systems. The aim is to achieve current control with unity power factor for fundamental components towards grid. VSR's phase voltages ( $[v]$ ) are controlled to reduce the voltage ( $[v_g]-[v]$ ) that will be applied across the  $L_f$ - $R_f$  filter. If the inductive part of the filter ( $L_f$ ) were to be zero (which is never the case), individual phase voltage fundamentals would have the same waveform and phase as grid voltages, but a smaller amplitude. However, since inductive part always exists, converter phase voltage fundamentals should have different phases than grid voltages to be able to achieve unity power factor operation. In order to limit the grid currents one should introduce a lower limit on the converter's phase voltage fundamental amplitudes.

The filter between the grid and the converter is mandatory to separate them and, without it, the control would not be possible. It should be noted that converter phase voltages are not sinusoidal, as assumed in Fig. 4.2 and the discussion above, since there are harmonics associated with multiples of the switching frequency. Strict regulations govern the highest allowed THD of the rectifying systems in vehicular applications. Thus inductive part of the filter should be high enough to ensure proper filtering that will comply with standards.

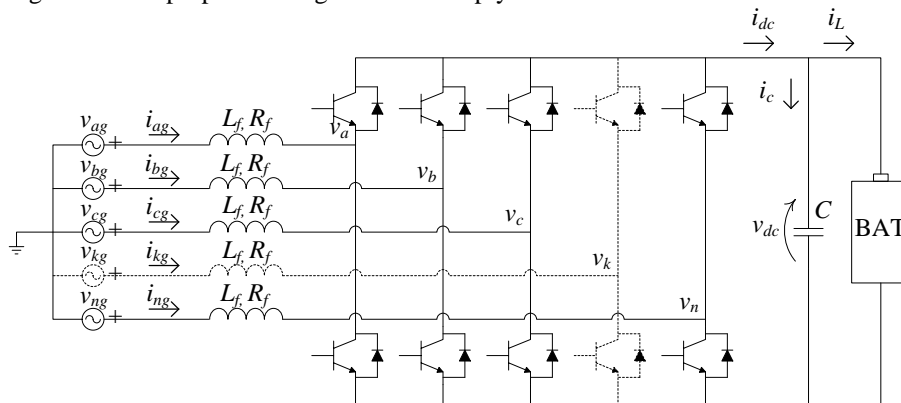
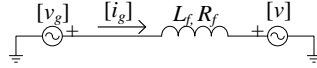


Fig. 4.1: Multiphase VSR system.



**Fig. 4.2:** Equivalent circuit representation of the grid-side of a multiphase VSR.

The inductive part of the filter has also an upper limit. This limit is well-known for three-phase systems [Malinowski (2001)] and has the form of (grid angular frequency, which was denoted simply as  $\omega$  in Chapter 3, is now labelled with  $\omega_g$  for the sake of consistency with other used symbols):

$$L_f \leq \frac{\sqrt{\frac{v_{dc}^2}{3} - V_{g \max}^2}}{\omega_g I_{g \max}}, \quad (4.1)$$

where  $V_{g \max}$  and  $I_{g \max}$  are the maximum values of grid voltages and grid currents, respectively. The upper limit for multiphase systems cannot be found in literature, but can be derived following the same rules as in [Malinowski (2001)] for three-phase systems. The expression for multiphase VSRs using zero-sequence injection is:

$$L_f \leq \frac{\sqrt{\left(\frac{M_{\max}}{2} v_{dc}\right)^2 - V_{g \max}^2}}{\omega_g I_{g \max}} \quad (4.2)$$

where  $M_{\max}$  is the maximum modulation index, which is different for each phase number of a multiphase machine. It can be shown that, as long as there is a single neutral point, its form is [Dujic et al (2010)]:

$$M_{\max} = \begin{cases} 1/\cos(\pi/2n) & \text{when } n \text{ is an odd number, or } n \text{ is an even number for asymmetrical systems} \\ 1 & \text{for symmetrical systems when } n \text{ is an even number} \end{cases} \quad (4.3)$$

It can be concluded that, having both the lower and upper limit, proper filter inductance should be carefully chosen. An inductance which is too high can unnecessarily restrict currents that can be taken from the grid, while a too low inductance can lead to insufficient filtering and hence high THD.

Battery-side of a VSR is not considered in this section because it is not important from the rectifier's point of view once the current references are created. This side is only important for obtaining the current references, which is usually achieved with a dc-bus voltage controller. However, this does not make any difference in the principle of operation of the VSR, due to the fact that it will still operate under current control.

### 4.3 Mathematical modelling of multiphase VSRs

Three-phase VSRs are widely employed in various applications. While nowadays they can be regarded as well-known and their mathematical model can be found in many papers [Jasinski et al (2011)], the situation is different for the case of multiphase VSRs, the main reason being the lack of real-world applications that demand this type of rectifier. With an increasing number of systems with multiphase inverters that might be used in automotive industry, multiphase VSRs are gaining in importance, mainly due to the fact that the same inverting hardware can be used also for rectification. Thus in this section a mathematical model of a multiphase VSR is derived.

#### 4.3.1 Model in terms of phase variables

With reference to Fig. 4.1 and its grid side, the following voltage equilibrium equation can be written:

$$[v_g] = [v_f] + [v] \quad (4.4)$$

where  $[v_g] = [v_{ag} \ v_{bg} \ v_{cg} \ \dots \ v_{ng}]^T$  is the grid phase voltage matrix,  $[v_f] = [v_{af} \ v_{bf} \ v_{cf} \ \dots \ v_{nf}]^T$  is the matrix of voltage drops on the filter, and  $[v] = [v_a \ v_b \ v_c \ \dots \ v_n]^T$  is the converter's phase voltage matrix. Voltage drops on the filter are equal to:

$$[v_f] = L_f \frac{d[i_g]}{dt} + R_f [i_g] \quad (4.5)$$

where  $[i_g] = [i_{ag} \ i_{bg} \ i_{cg} \ \dots \ i_{ng}]^T$ ,  $L_f = L_{fa} = L_{fb} = \dots = L_{fn}$ , and  $R_f = R_{fa} = R_{fb} = \dots = R_{fn}$ . Converter phase voltages depend on the dc-bus voltage and switching states  $[s]$  as follows:

$$[v] = v_{dc} \cdot \left( [s] - \frac{1}{n} \sum_{k=1}^n s_k \right) = v_{dc} \cdot \left( [I]_{n \times n} [s] - \frac{1}{n} [1]_{n \times n} [s] \right) = v_{dc} \cdot \left( [I]_{n \times n} - \frac{1}{n} [1]_{n \times n} \right) [s] \quad (4.6)$$

$$\text{where } [I]_{n \times n} = \begin{bmatrix} 1 & 0 & 0 & \dots & 0 \\ 0 & 1 & 0 & & 0 \\ 0 & 0 & 1 & & 0 \\ \vdots & & & \ddots & \vdots \\ 0 & 0 & 0 & \dots & 1 \end{bmatrix}_{n \times n}, [1]_{n \times n} = \begin{bmatrix} 1 & 1 & 1 & \dots & 1 \\ 1 & 1 & 1 & & 1 \\ 1 & 1 & 1 & & \vdots \\ \vdots & & & \ddots & 1 \\ 1 & 1 & 1 & \dots & 1 \end{bmatrix}_{n \times n}, \text{ and } [s] = \begin{bmatrix} s_1 \\ s_2 \\ s_3 \\ \vdots \\ s_n \end{bmatrix}.$$

In equation (4.6) the variable  $s_k$ , where  $k \in \{1 \ 2 \ 3 \ \dots \ n\}$ , represents switching state of the  $k^{\text{th}}$  leg of the converter, and can take the value of “1” (if the upper switch is turned on) or “0” (if the lower switch is turned on). By substituting (4.5) and (4.6) into (4.4) one further has:

$$[v_g] = L_f \frac{d[i_g]}{dt} + R_f [i_g] + v_{dc} \cdot \left( [I]_{n \times n} - \frac{1}{n} [1]_{n \times n} \right) [s]. \tag{4.7}$$

By inspecting the right-hand part of Fig. 4.1, it can be seen that:

$$C \frac{dv_{dc}}{dt} = i_{dc} - i_L \tag{4.8}$$

where  $i_{dc} = [s]^T \cdot [i_g]$ . Hence:

$$C \frac{dv_{dc}}{dt} = [s]^T \cdot [i_g] - i_L \tag{4.9}$$

Equations (4.7) and (4.9) represent the complete model of the system. Block diagram of the system is shown in Fig. 4.3. This block diagram can be represented in matrix form (Fig. 4.4). Matrix multiplication is represented with the block containing “x” symbol and a product with a scalar is represented with a sign “\*” in front of a matrix. Model expressed in terms of phase variables is useful only in simulations to substitute a real VSR with corresponding signals. However, for control purposes the model has to be in the same reference frame in which current control is performed, which is the synchronously rotating reference frame. Thus, in what follows, models obtained after decoupling transformation and subsequent application of the rotational transformation are derived.

### 4.3.2 Model after application of the decoupling transformation

Multiplying (4.7) from the left with the universal multiphase decoupling transformation matrix (3.1) yields the following:

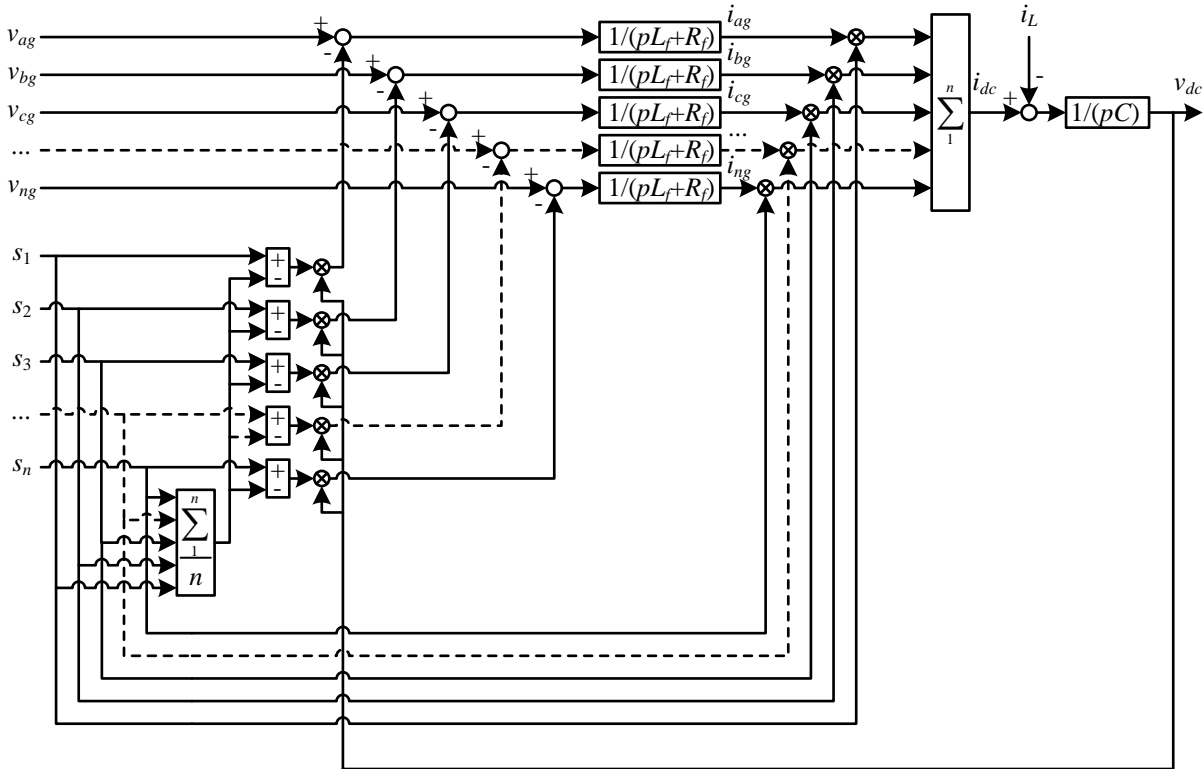


Fig. 4.3: Block diagram of the multiphase VSR in terms of phase variables ( $p$  stands for the differentiation operator).

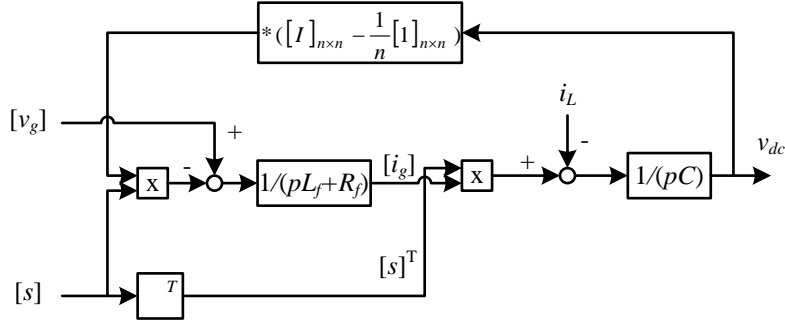


Fig. 4.4: Matrix representation of the model in terms of phase variables.

$$[C] \cdot [v_g] = [C] \cdot L_f \frac{d[i_g]}{dt} + [C] \cdot R_f [i_g] + [C] \cdot v_{dc} \cdot \left( [I]_{n \times n} - \frac{1}{n} [1]_{n \times n} \right) [s] \quad (4.10)$$

For the right-most part of this equation the following identities apply:

$$[C] \frac{1}{n} [1]_{n \times n} [s] = [C] \frac{1}{n} [1]_{n \times n} ([C]^{-1} [C] [s]) = \frac{1}{n} ([C] [1]_{n \times n} [C]^T) ([C] [s]) =$$

$$\frac{1}{n} \begin{bmatrix} \left( \sum_{k=1}^n C_{1k} \sum_{k=1}^n C_{1k} \right) & \left( \sum_{k=1}^n C_{1k} \sum_{k=1}^n C_{2k} \right) & \dots & \left( \sum_{k=1}^n C_{1k} \sum_{k=1}^n C_{nk} \right) \\ \left( \sum_{k=1}^n C_{2k} \sum_{k=1}^n C_{1k} \right) & \left( \sum_{k=1}^n C_{2k} \sum_{k=1}^n C_{2k} \right) & \dots & \left( \sum_{k=1}^n C_{2k} \sum_{k=1}^n C_{nk} \right) \\ \vdots & \vdots & \ddots & \vdots \\ \left( \sum_{k=1}^n C_{nk} \sum_{k=1}^n C_{1k} \right) & \left( \sum_{k=1}^n C_{nk} \sum_{k=1}^n C_{2k} \right) & \dots & \left( \sum_{k=1}^n C_{nk} \sum_{k=1}^n C_{nk} \right) \end{bmatrix} ([C] [s]) =$$

$$\frac{1}{n} \begin{bmatrix} 0 & \dots & 0 & 0 \\ \vdots & \ddots & \vdots & \vdots \\ 0 & \dots & \left( \sum_{k=1}^n C_{(n-1)k} \sum_{k=1}^n C_{(n-1)k} \right) & \left( \sum_{k=1}^n C_{(n-1)k} \sum_{k=1}^n C_{nk} \right) \\ 0 & \dots & \left( \sum_{k=1}^n C_{nk} \sum_{k=1}^n C_{(n-1)k} \right) & \left( \sum_{k=1}^n C_{nk} \sum_{k=1}^n C_{nk} \right) \end{bmatrix} ([C] [s]) = \begin{cases} \begin{bmatrix} 0 & \dots & 0 & 0 \\ \vdots & \ddots & \vdots & \vdots \\ 0 & \dots & 0 & 0 \\ 0 & \dots & 0 & 1 \end{bmatrix} [s_{(\alpha\beta)}], & n - \text{odd} \\ \begin{bmatrix} 0 & \dots & 0 & 0 \\ \vdots & \ddots & \vdots & \vdots \\ 0 & \dots & 1 & 0 \\ 0 & \dots & 0 & 0 \end{bmatrix} [s_{(\alpha\beta)}], & n - \text{even} \end{cases} \quad (4.11)$$

Substituting (4.11) into (4.10) and assuming that the system has an odd number of phases, one can further write that:

$$[v_{g(\alpha\beta)}] = L_f \frac{d[i_{g(\alpha\beta)}]}{dt} + R_f [i_{g(\alpha\beta)}] + v_{dc} \cdot \left( [I]_{n \times n} - \begin{bmatrix} [0]_{(n-1) \times (n-1)} & 0 \\ \vdots & \vdots \\ 0 & \dots & 1 \end{bmatrix}_{n \times n} \right) [s_{(\alpha\beta)}] \quad (4.12)$$

$$\text{where } [0]_{(n-1) \times (n-1)} = \begin{bmatrix} 0 & \dots & 0 \\ \vdots & \ddots & \vdots \\ 0 & \dots & 0 \end{bmatrix}_{(n-1) \times (n-1)}$$

Equation (4.9) can be written, using the decoupling transformation matrix (3.1), as:

$$C \frac{dv_{dc}}{dt} = [s]^T \cdot ([C]^T \cdot [C] \cdot [i_g]) - i_L = ([s]^T \cdot [C]^T) \cdot ([C] \cdot [i_g]) - i_L = ([C] \cdot [s])^T \cdot ([C] \cdot [i_g]) - i_L \quad (4.13)$$

$$C \frac{dv_{dc}}{dt} = [s_{(\alpha\beta)}]^T \cdot [i_{g(\alpha\beta)}] - i_L$$

In the model (4.12)-(4.13) the following transformed matrix vectors are introduced, assuming a system with an odd number of phases:  $[i_{g(\alpha\beta)}] = [i_{\alpha g} \ i_{\beta g} \ i_{x1g} \ \dots \ i_{0g}]^T$ ,  $[s_{(\alpha\beta)}] = [s_{\alpha} \ s_g \ s_{x1} \ \dots \ s_{0g}]^T$ . Equations (4.12) and (4.13) represent the complete model of the system after vector space decomposition is completed by means of the

decoupling transformation matrix. The corresponding block diagram is depicted in Fig. 4.5. This block diagram can be represented in matrix form as in Fig. 4.6. Using (4.12)-(4.13) as the starting point, model in the rotating reference frame is derived next.

**4.3.3 Model in the rotating reference frame**

Equation (4.12) is multiplied from the left with the rotational transformation matrix  $[D]$ , which will transform the model into the grid-oriented reference frame that rotates at the grid angular frequency. This transformation matrix is defined as

$$[D] = \begin{bmatrix} \cos \theta_g & \sin \theta_g & 0 & \dots & 0 \\ -\sin \theta_g & \cos \theta_g & 0 & \dots & 0 \\ 0 & 0 & 1 & \dots & 0 \\ \vdots & \vdots & \vdots & \ddots & \vdots \\ 0 & 0 & 0 & \dots & 1 \end{bmatrix}_{n \times n} \tag{4.14}$$

where  $\theta_g = \int \omega_g dt$ . Using (4.14) in conjunction with (4.12) one gets

$$[D] \cdot [v_g(\alpha\beta)] = [D] \cdot L_f \frac{d[i_g(\alpha\beta)]}{dt} + [D] \cdot R_f [i_g(\alpha\beta)] + [D] \cdot v_{dc} \cdot \left( [I]_{n \times n} - \begin{bmatrix} [0]_{(n-1) \times (n-1)} & 0 \\ \vdots & \vdots \\ 0 & \dots & 1 \end{bmatrix}_{n \times n} \right) [s(\alpha\beta)] \tag{4.15}$$

Matrix  $[D]$  elements are time dependent. Hence:

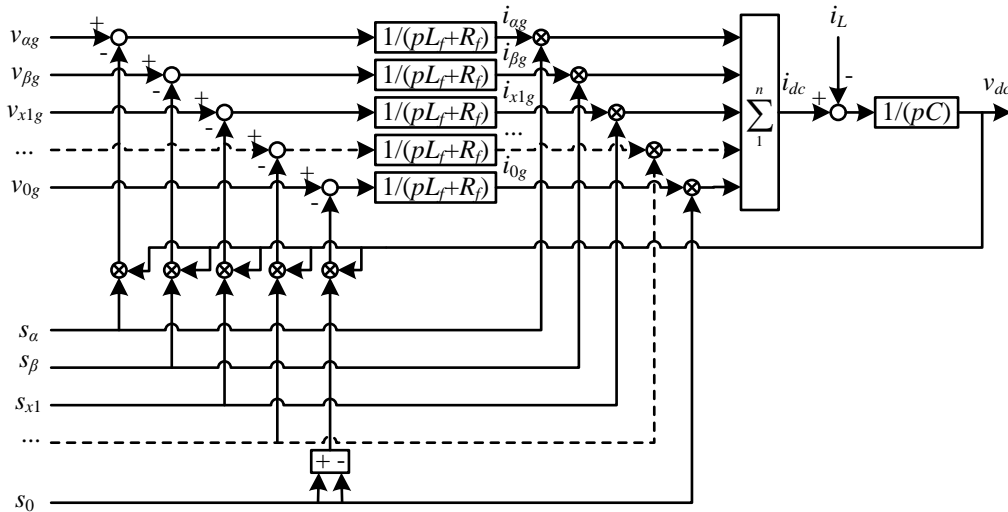


**Fig. 4.5:** Mathematical model of multiphase VSR after vector space decomposition.

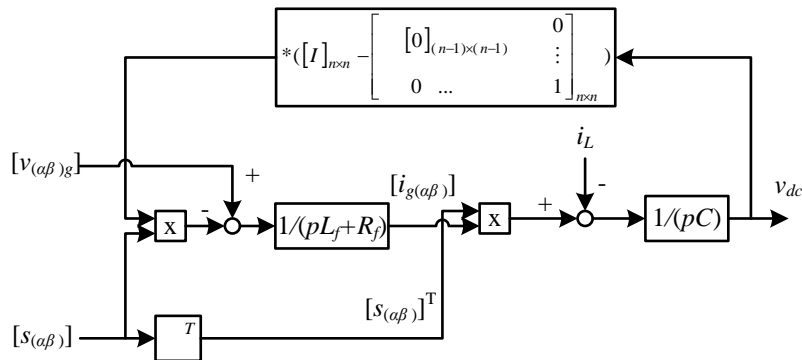


**Fig. 4.6:** Matrix representation of the model in decoupled domain.

$$\begin{aligned}
[D] \cdot L_f \frac{d[i_g(\alpha\beta)]}{dt} &= L_f \frac{d([D] \cdot [i_g(\alpha\beta)])}{dt} - L_f \frac{d[D]}{dt} \cdot [i_g(\alpha\beta)] = \\
&= L_f \frac{d([D] \cdot [i_g(\alpha\beta)])}{dt} - L_f \left( \frac{d[D]}{dt} \cdot [D]^{-1} \right) \cdot ([D] \cdot [i_g(\alpha\beta)]) = \\
&= L_f \frac{d[i_g(dq)]}{dt} - L_f \begin{bmatrix} 0 & \omega_g & 0 & \dots & 0 \\ -\omega_g & 0 & 0 & \dots & 0 \\ 0 & 0 & 0 & \dots & 0 \\ \vdots & \vdots & \vdots & \ddots & \vdots \\ 0 & 0 & 0 & \dots & 0 \end{bmatrix} \cdot [i_g(dq)]
\end{aligned} \tag{4.16}$$

By substituting (4.16) into (4.15) one further has:

$$\begin{aligned}
[v_g(dq)] &= L_f \frac{d[i_g(dq)]}{dt} - L_f \begin{bmatrix} 0 & \omega_g & 0 & \dots & 0 \\ -\omega_g & 0 & 0 & \dots & 0 \\ 0 & 0 & 0 & \dots & 0 \\ \vdots & \vdots & \vdots & \ddots & \vdots \\ 0 & 0 & 0 & \dots & 0 \end{bmatrix} \cdot [i_g(dq)] + R_f [i_g(dq)] + \\
&+ v_{dc} \cdot \left( [I]_{n \times n} - \begin{bmatrix} [0]_{(n-1) \times (n-1)} & 0 \\ 0 & \dots & 1 \end{bmatrix}_{n \times n} \right) [s(dq)]
\end{aligned} \tag{4.17}$$

Equation (4.13) can be written in the rotational reference frame as:

$$\begin{aligned}
C \frac{dv_{dc}}{dt} &= [s(\alpha\beta)]^T \cdot ([D]^T \cdot [D] \cdot [i_g(\alpha\beta)]) - i_L = ([s(\alpha\beta)]^T \cdot [D]^T) \cdot ([D] \cdot [i_g(\alpha\beta)]) - i_L = \\
&= ([D] \cdot [s(\alpha\beta)])^T \cdot ([D] \cdot [i_g(\alpha\beta)]) - i_L = [s(dq)]^T \cdot [i_g(dq)] - i_L
\end{aligned} \tag{4.18}$$

Equations (4.17) and (4.18) represent the complete model in the rotational reference frame. Corresponding block diagram is given in Fig. 4.7.

It can be seen from Fig. 4.7 that there is a coupling between  $d$  and  $q$  axes, described with terms proportional to  $\pm\omega_g L_f$ . This is an important model property that will have to be taken into account when designing current controllers, since a decoupling network will be required for current control (Chapter 5). Block diagram given in Fig. 4.7 can also be represented in matrix form, as shown in Fig. 4.8.

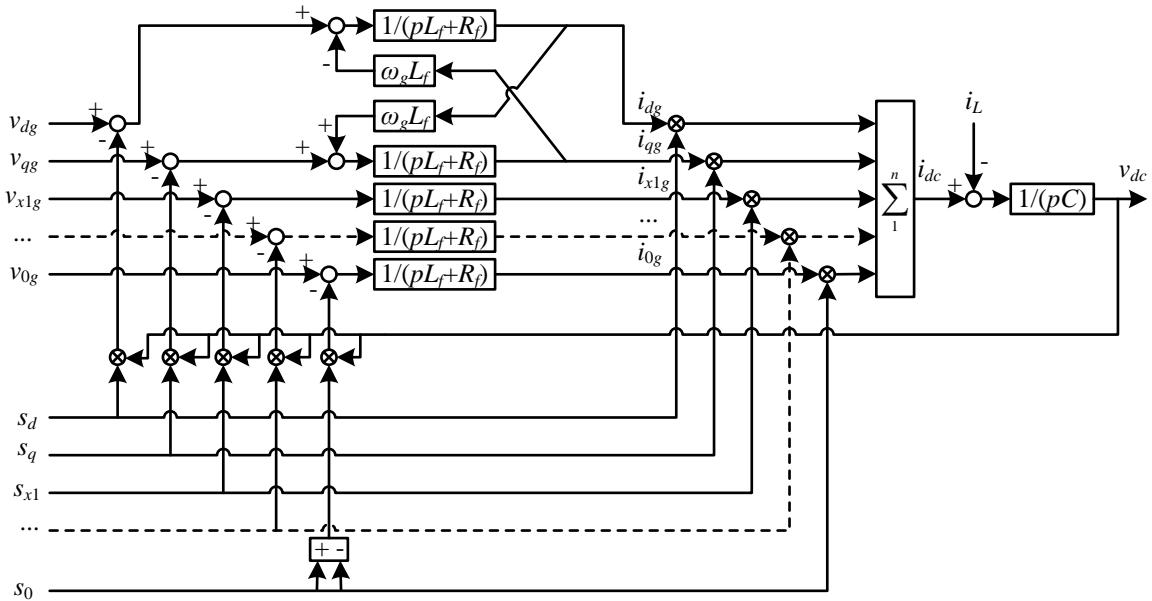


Fig. 4.7: Mathematical model of a multiphase VSR in the rotational reference frame.

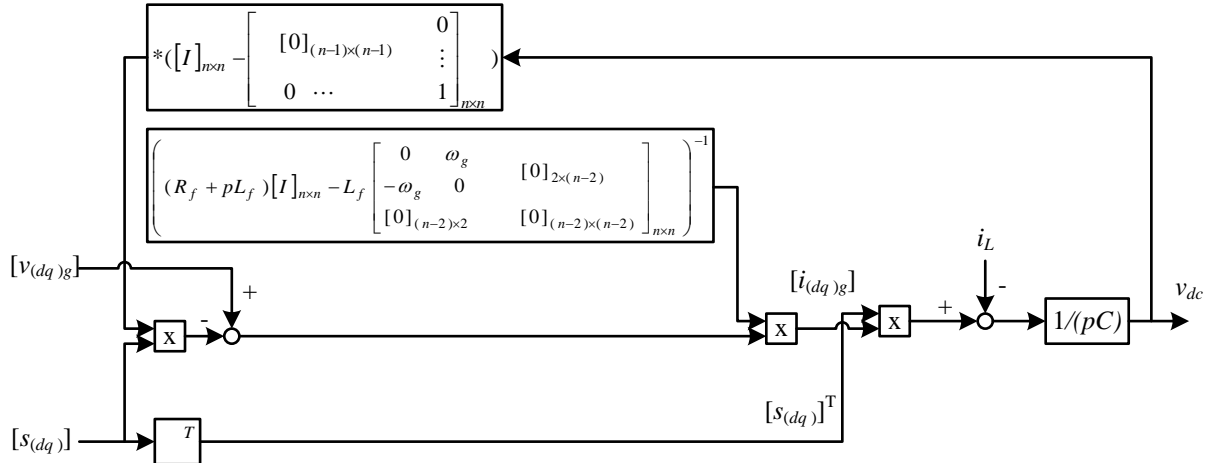


Fig. 4.8: Matrix representation of the model in the rotational reference frame.

### 4.3.5 Closed loop transfer function

The last model type considered here is a closed loop model of the system. It will be used in the next chapter, which discusses the control of the system, in order to set optimum controller parameters. In order to obtain a closed loop model finding an open loop transfer function is a logical first step. The open loop transfer function consists of three blocks: PI controller, PWM block, and an input choke. PWM block can be approximated with a delay of the value between zero and  $2T_s$ , and the disturbance  $V_d$  can be considered as a constant. Block diagram of the current control in the  $d$ - $q$  reference frame is presented in Fig. 4.9. The current control loop open loop transfer function is:

$$W_o(s) = \frac{K_p(1 + pT_i)K_f}{pT_i(pT_{PWM} + 1)(pT_f + 1)} \quad (4.19)$$

where  $K_f = 1/R_f$ . With simplification  $pT_f + 1 \approx pT_f$  the closed loop transfer function can be written as:

$$W_c(s) = \frac{K_p K_f (1 + pT_i)}{K_p K_f \cdot p^0 + K_p K_f T_i \cdot p^1 + T_i T_{PWM} T_f \cdot p^3} \quad (4.20)$$

Two standard ways of choosing a PI controller parameters are the “symmetrical optimum” and “modulus optimum”. According to the symmetrical optimum the parameters should be chosen according to the following rule:

$$a_1^2 = 2a_0 a_2 \quad ; \quad a_2^2 = 2a_1 a_3 \quad (4.21)$$

where  $a_0, a_1, a_2$  and  $a_3$  are coefficients which multiply  $p^0, p^1, p^2$  and  $p^3$  in the denominator. Parameters of the controller can be obtained as:

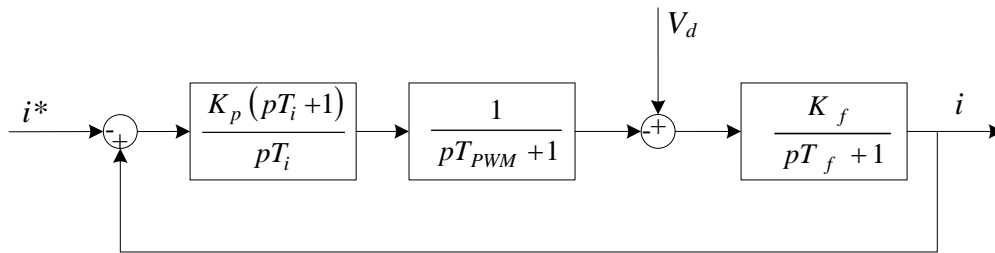


Fig. 4.9: Block diagram of the current control in an axis ( $d$  or  $q$ ).

$$K_p = \frac{T_f}{2T_{PWM} K_f} \quad ; \quad T_i = 4T_{PWM} \quad (4.22)$$

Modulus optimum method is often used when the controlled system has single dominant time constant and other minor time constants, as is the case here. It aims to cancel the most pronounced pole of the system, and parameters obtained using this method are:

$$K_p = \frac{T_f}{2T_{PWM} K_f} \quad ; \quad T_i = T_f \quad (4.23)$$

Although, symmetrical optimum method has a better response to variation of the disturbance signal ( $|v_g| \neq \text{const.}$ ) [Jasinski (2005)], modulus optimum method is chosen here since it is believed to be more appropriate for these applications.

#### 4.4 Conclusion

Multiphase VSCs can be used both as inverters and VSRs with unity power factor. Therefore, VSRs can be used as part of the integrated on-board battery chargers for electric vehicles. In this chapter multiphase VSRs with simple  $R_f-L_f$  filter between the grid and the converter have been investigated.

Basic principles of operation are given at first and operating limits are discussed. Next the mathematical model of a multiphase VSR is derived in terms of phase variables and is then transformed using at first decoupling (vector space decomposition) transformation and then transformation into a rotational reference frame. This is followed by the discussion of the closed loop model for the charging mode of operation.

## CHAPTER 5: CHARGING AND V2G MODES OF OPERATION

### 5.1 Introduction

As already shown in Chapter 3, additional degrees of freedom of multiphase machines make them particularly suitable for integration into the battery charging process. These degrees of freedom can be utilised during the charging/V2G process to transfer the whole or a part of excitation from the torque producing ( $\alpha$ - $\beta$ ) to a non-torque producing plane, in order to avoid torque production. Multiphase configurations that do not produce a torque during the charging process are introduced in Chapter 3, where theoretical analysis of their excitation mapping among the planes is performed. Depending on the voltage supply type at the charging station, configurations are grouped into three major categories: those with multiphase supply, with single-phase supply, and with three-phase supply. This chapter considers control of these configurations in charging and V2G mode, and provides experimental results obtained utilizing the same control algorithms.

The arrangement of configurations is kept as in Chapter 3. However, since control and behaviour of topologies depend on whether a pulsating excitation exists in the first plane of the machine, each group is further divided into two subcategories. The first one is without any excitation in the first plane, and it has the advantage that a torque cannot be produced even if the machine, for non-technical reasons (e.g. charging on a hill slope), starts rotating. It should be noted that this group has a small pulsating field in the rotor which originates from the stator leakage flux. However, this flux exists only in vicinity of stator slots and has very low values. Therefore, in what follows this leakage flux is neglected and the group is referred as without a field in the rotor.

In the second subcategory are topologies in which a pulsating excitation is produced in the first plane during the charging/V2G mode. Now the pulsating flux spreads through the whole rotor and has considerable values, thus this group is referred as with pulsating field in the rotor. In machines with non-laminated rotor losses produced in this way in the rotor iron would be considerable.

### 5.2 Control

The main aim of the control is to realise a charging/V2G process that complies with the grid standards, which set a limit on the total harmonic distortion (THD) of the current and demand unity power factor operation in charging as well as in V2G operation. Although some control similarities are present, the control of topologies that utilise different voltage supply type at the charging station essentially differs. In what follows control is considered separately for the three types of grid voltage supply: multiphase, single-phase and three-phase.

#### 5.2.1 Multiphase supply

In this subsection it is assumed that the charging station is equipped with a multiphase voltage supply. The particular focus is on topologies that may have imminent impact on the charging process of EVs. Therefore, control considerations and experimental verification are omitted for topologies that require multiphase supply that cannot be easily obtained from a three-phase grid, such as for example five-phase and seven-phase supply. On the other hand, this is not a problem with asymmetrical and symmetrical six-phase supply, since they can be obtained from the three-phase grid by means of simple transformers, as will be shown here. Therefore, control algorithm and experimental verification are provided for topologies that require those two supply types.

An important attribute of topologies that have a transformer is that their supply is isolated. A study performed in [Liu et al (2012)] assessed the impact of avoiding isolation for one of currently the most attractive fast charging configurations [De Sousa et al (2010)]. It is shown that, if isolation does not exist, the common mode voltage appears between the battery and the ground. Since typically some small parasitic capacitances exist between the chassis of EV and its battery, this can cause problems in battery management system, as well as high displacement currents that can flow through the protection earth conductor. These currents can significantly exceed the permitted limit that is set due to the safety concerns if a proper mitigating technique is not employed (one of these may be the integration of a filter capacitor between the protection earth conductor and the neutral conductor, [Liu et al (2012)]).

One manner of obtaining asymmetrical and symmetrical six-phase voltage supply is by transformers with two sets of secondary windings that are shown in Fig. 5.1. Asymmetrical supply can be obtained from a transformer that has one set connected in star connection, while the other one is delta-connected – Fig. 5.1a. The number of turns in the delta-connected windings is increased compared to those with star connection by a factor of 1.73 in order to obtain the same voltage levels. By connecting the two secondary windings in star and delta, respectively, required supply phase shift between two three-phase windings of 30 degrees is achieved. Symmetrical six-phase supply can be obtained in a similar manner. Both sets of secondary windings should have a star connection – Fig. 5.1b. However, they should now have the same number of turns in order to obtain equal voltage levels. A phase shift of 180 degrees is achieved by reversing the polarity of the second three-phase winding set with respect to the first one.

An alternative method of obtaining a symmetrical six-phase voltage set is presented in Fig. 5.2. As can be seen, it does not require a special transformer with two sets of secondaries. On the contrary, it utilises the most common type of a transformer, which is a standard three-phase isolating transformer. However, the transformer secondary three-phase winding is utilised in an open-end winding configuration, so that connection of two motor phases is possible to

each of the transformer secondary phases. Regardless of the manner of obtaining a symmetrical six-phase voltage set the operating principle of the topology that utilises it remains the same, and is given by (3.29)-(3.30).

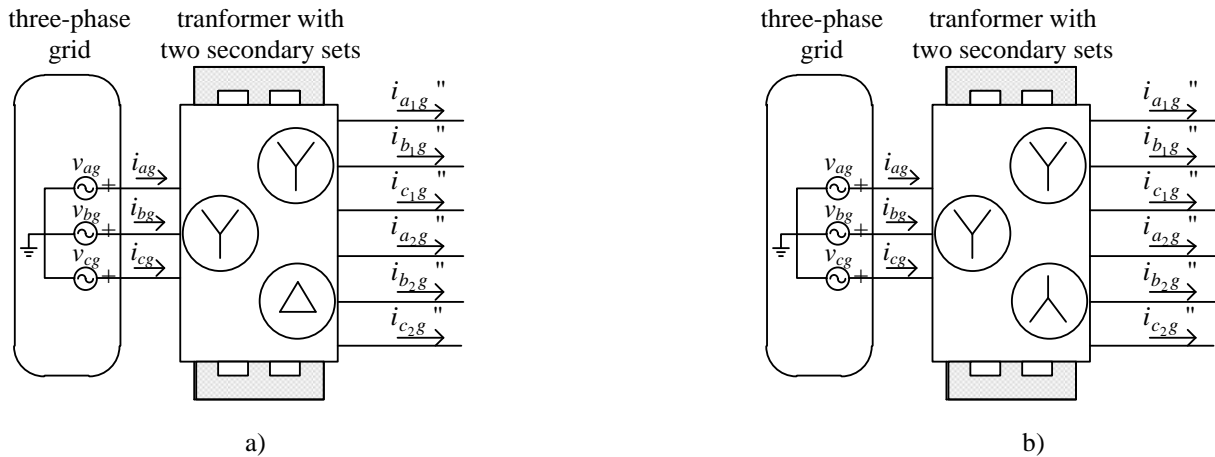


**Fig. 5.1:** Six-phase voltage source obtained by transformer with two secondary sets: a) asymmetrical supply, b) symmetrical supply.

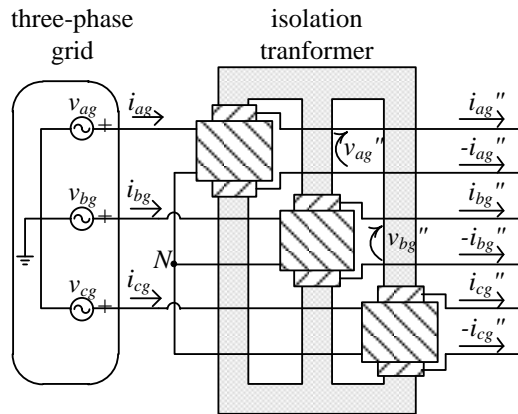


**Fig. 5.2:** An alternative symmetrical six-phase voltage supply (covered in section 5.2.3).

In order to design a control algorithm, it is necessary to consider equivalent schemes of multiphase charging topologies. From Chapter 3 it follows that during the multiphase charging process there is no torque production in the machines, thus they act as simple resistive-inductive components. If there is no field production in the machine, its equivalent scheme has the same parameters for all the phases. If the field in rotor is pulsating, it introduces asymmetry in the equivalent scheme parameters. Transformer also influences equivalent scheme by its resistance and leakage inductance. Depending on whether a transformer with two (Fig. 5.1) or a single (Fig. 5.2) secondary set is used, the equivalent scheme takes the form presented in Fig. 5.3 and Fig. 5.4, respectively.

It can be seen that Fig. 5.3 represents a six-phase VSC. However, the equivalent scheme for the case when a transformer from Fig. 5.2 is utilised differs significantly. This is regardless of the fact that the principle of operation of the rest of the system remains unaltered from the one described by (3.29)-(3.30). Since the equivalent scheme in case of the supply type from Fig. 5.2 is in essence three-phase, its control is considered in section 5.2.3 together with other topologies that use the three-phase supply. Thus, the remainder of this subsection focuses on control of the scheme from Fig. 5.3.

The principle of operation of a multiphase VSC has been discussed in Chapter 4. A complete mathematical model of a general case of multiphase VSC, derived in a reference system in which control is performed, has also been presented in Chapter 4. Starting from the mathematical model a control algorithm can be developed, so that it takes into consideration relevant electrical aspects of the converter. In order to achieve unity power factor operation grid voltage oriented control is chosen for controlling the multiphase converter. The control algorithm of the system from Fig. 5.3 is depicted in Fig. 5.5. In what follows its functional blocks are explained in the order in which real signals are processed in the controller.

The control commences by gathering feedback signals obtained from measurements. Those are required for grid currents, grid voltages and dc-bus voltage. In order to obtain unity power factor, the knowledge of the grid voltage position is mandatory. In Fig. 5.5 it is obtained from the grid voltage measurements by means of phase locked loop (PLL), shown in Fig. 5.6. The resonant filter filters the grid voltage without causing a phase delay. As shown in

[Limongi et al (2007)], PLL of Fig. 5.6 has a superior performance for a distorted grid voltage, compared to a standard PLL. It is capable of obtaining the position of a single-phase grid as well, which is discussed in section 5.2.2. The part on the right-hand side of the resonant filter represents a standard PLL in the synchronous reference frame. It should be noted that PLL algorithm gets executed at the initialisation of the charging process. However, the charging process itself starts only after the PLL gets stabilised, i.e. the grid position is accurately obtained.

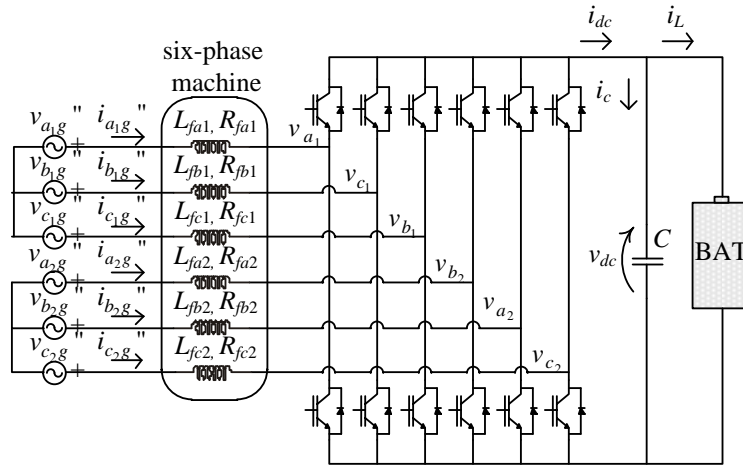


**Fig. 5.3:** Equivalent scheme of the six-phase topologies with supply as in Fig. 5.1.

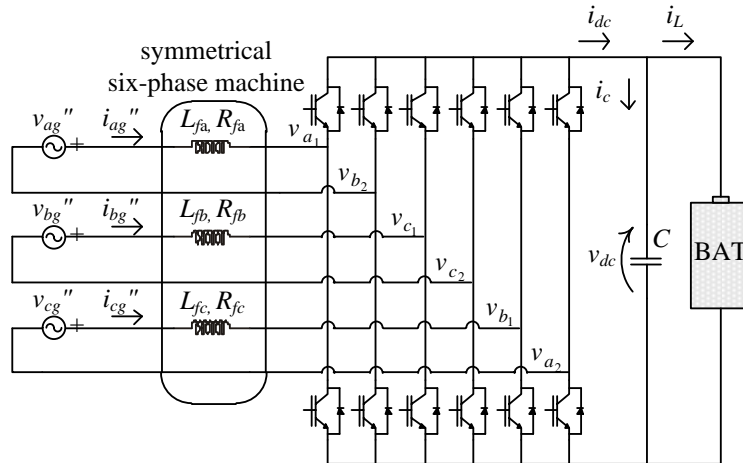


**Fig. 5.4:** Equivalent scheme of the symmetrical six-phase topology with supply as in Fig. 5.2 (covered in section 5.2.3).

The aim of the control is to place the six grid currents in phase with the six grid phase voltages (to obtain unity power factor). This is accomplished by controlling the transformer secondary variables. In order to observe phase deviation of the grid currents from the grid phase voltages, the currents are transformed into the grid voltage oriented reference frame. This is done by applying appropriate decoupling transformation for the six-phase systems, and then the rotational transformation (in Fig. 5.5 these two are lumped together in one block called “coordinate transformation”). For asymmetrical six-phase system the decoupling matrix is given with (3.20), while for the symmetrical system its form is determined by (3.26) and (3.31). The rotational transformation is performed by utilising the information on the grid position from the PLL. What is achieved in this way is that the grid current component, which is in phase with the grid voltage, is separated and appears as a dc quantity. If the charging process utilises only this component ( $i_{dg}$ ), the unity power factor operation during charging results. The current component that is out of phase with the grid voltage ( $i_{qg}$ ), and current components from the  $x$ - $y$  plane should be controlled to zero.

The most conventional way of battery charging is CC-CV (constant current – constant voltage) method [Dusmez et al (2011)]. It charges the battery with a constant (maximum allowed) current until the battery voltage reaches certain cut-off level. The charging then continues at a constant voltage until the current drops below 10% of its maximum. For the CC mode the reference for the component  $i_{dg}$  is the desired value of the grid current  $d$ -axis component. For the CV mode the dc-bus voltage is the input reference to the system. As the  $i_{dg}$  component is directly proportional to the voltage drop on the battery’s internal resistance, its reference can be obtained by a PI voltage controller, which is shown as the outer control loop in Fig. 5.5.

When the current reference is obtained (in CC or CV mode),  $d$ -component of the grid current is controlled to follow it in the block “current controllers” in Fig. 5.5. In the same block the other three current components are

controlled to their references, which are zero. After the controller action, the output of “current controllers” block is the voltage reference, in the rotating reference frame, for the VSC. However, it can be seen that the  $d$ -component of the grid voltage is summed with the  $d$ -component of the output of the “current controllers” block. This is done in order to prevent high currents at the beginning of the charging process. This requires that the decoupling transformation matrix utilised in the PLL block (Fig. 5.6) and the one that is used for the transformation of the currents (Fig. 5.5) use the same scaling factor that governs power properties of the transformation.

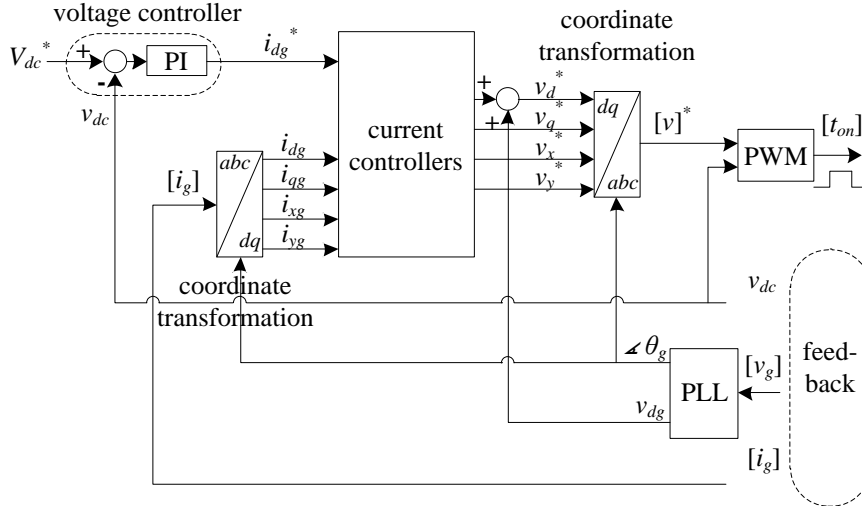


Fig. 5.5: VOC control algorithm for multiphase VSC.

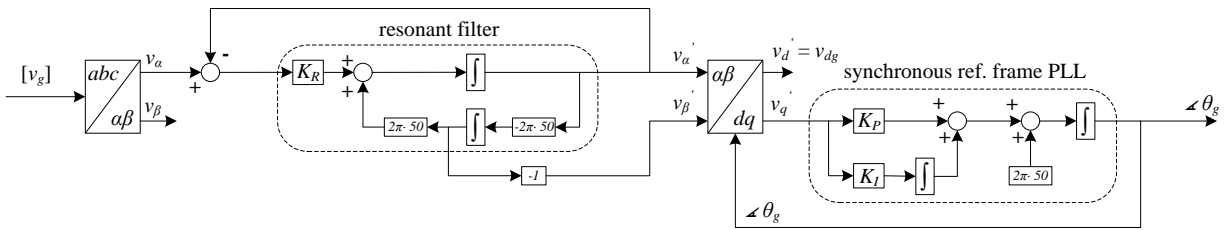


Fig. 5.6: PLL algorithm (the input is in principle any  $n$ -phase set of voltages, although it is labelled as  $abc$ )

When inverse rotational and inverse decoupling transformations are applied to the reference voltage signals in the rotating reference frame, references for inverter phase voltages are obtained. These enter PWM block which uses carrier based modulation strategy with zero-sequence injection. However, since the system has two, by transformer, isolated neutral points, zero-sequence injection can be applied to each set separately. This improves the dc-bus utilization which is in essence equal to the one of three-phase systems.

It should be noted that this control algorithm can be used for V2G operation without any changes. The only requirement is that a minus sign should be placed in front of the reference for the grid current component  $i_{dg}^*$ .

The “current controllers” block depends on whether a field in the machine’s rotor is present or not. Thus, in the next two subsections this block is considered separately for the asymmetrical system (that does not have any field production in the rotor) and the symmetrical system (in which the rotor field pulsates).

**5.2.1.1 Topologies without field production in the rotor**

According to (3.24)-(3.25) there is no excitation in the first plane and subsequently no field production in the rotor in the case of the charging process with the asymmetrical six-phase supply. The direct consequence is that the machine contributes to the equivalent scheme only with its stator resistance and stator leakage inductance. Since these parameters are the same for all the phases, and the transformer is assumed to be without asymmetries, the equivalent scheme of Fig. 5.3 has the same filter parameters in all phases. Thus,  $L_{fa1}=L_{fb1}=...=L_{fc2}$ ,  $R_{fa1}=L_{fb1}=...=L_{fc2}$  and the converter is balanced. This fact facilitates converter’s current control.

The “current controllers” block from Fig. 5.5 is given in more detail in Fig. 5.7. When the current reference is obtained (in CC or CV mode),  $d$ -component of the grid current is controlled to follow it. Since the  $d$ -current component reference is a dc quantity, the  $d$ -current component can be controlled with a simple PI controller shown at the top of Fig. 5.7. It can be seen that reference current is subtracted from measured current, which is opposite compared to the standard variable-speed drive current controllers. The reason for this is that when amplitude of the inverter voltage increases, voltage across the filter (i.e. charging current) decreases, and vice versa. Similarly to the  $d$ -component, the  $q$ -component is controlled to zero with a PI controller. However, from Fig. 4.7 it is obvious that the mathematical model

of a multiphase VSR contains certain cross-coupling between  $d$ - $q$  components. Therefore, the decoupling network included in Fig. 5.7 is necessary to eliminate the coupling effect. The block “PI controllers” shown in Fig. 5.7 suffices for the control of grid current fundamental in symmetrical (balanced) systems, such as the one considered here.

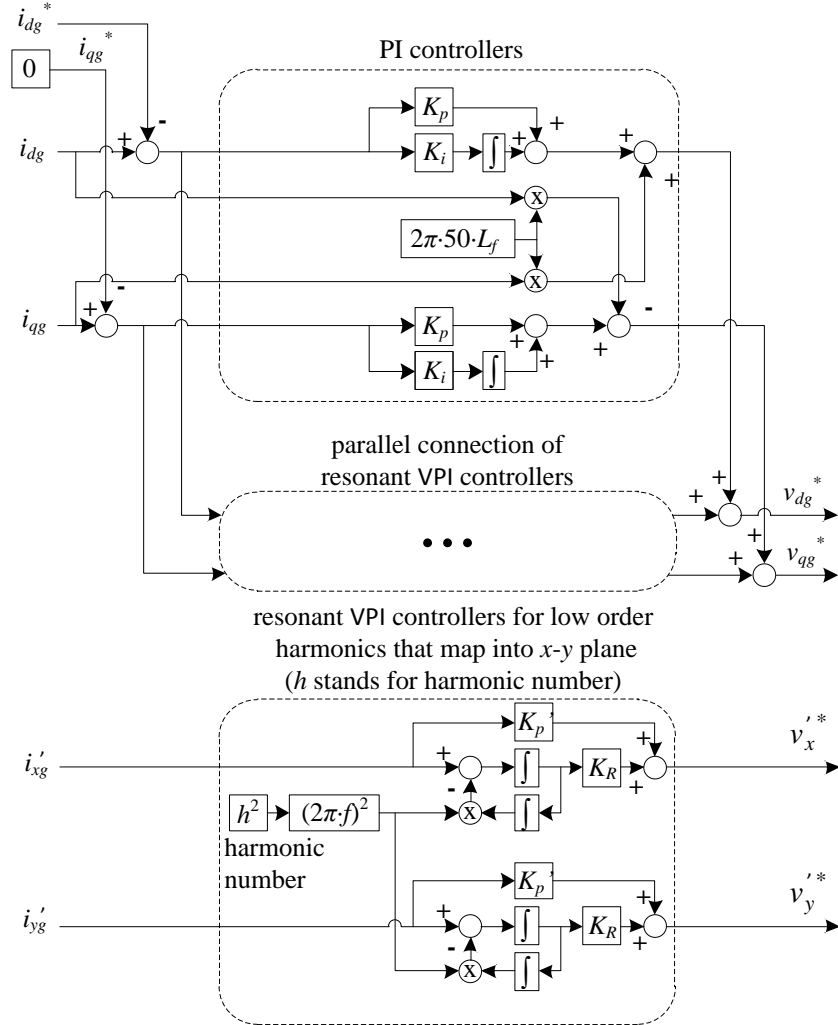


**Fig. 5.7:** Current control algorithm of six-phase charging configurations.

On the other hand, grid current does not contain only fundamental. Low-order odd harmonics are inevitably produced due to the inverter dead time and the potential grid voltage distortion, and they require control as well. Since they are ac quantities in this reference frame, the PI controller of Fig. 5.7 cannot suppress them; additional controllers are thus necessary. It is shown in [Che et al (2014)] that the dominant harmonics in asymmetrical six-phase systems are 5<sup>th</sup>, -7<sup>th</sup>, -11<sup>th</sup> and 13<sup>th</sup> (as seen from the stationary reference frame). The minus sign refers to the anti-synchronous direction of rotation. The -11<sup>th</sup> and 13<sup>th</sup> map into the first ( $\alpha$ - $\beta$ ) plane, while the 5<sup>th</sup> and -7<sup>th</sup> map into the second ( $x$ - $y$ ) plane. The first plane rotates in the synchronous direction, and -11<sup>th</sup> and 13<sup>th</sup> harmonics are seen in this reference frame as the -12<sup>th</sup> and 12<sup>th</sup>. Since resonant controllers are capable of controlling the harmonics in both directions at the same time, single resonant controller tuned at the 12<sup>th</sup> harmonic in one axis can control both the -12<sup>th</sup> and 12<sup>th</sup> harmonic (seen from the synchronous reference frame). In order to control harmonics from the second plane in a similar manner, the coordinate system of the second plane has to rotate in anti-synchronous direction (this is ensured in the rotational transformation matrix). It should be noted that the  $x$ - $y$  current and voltage axis components in Fig. 5.7 are those obtained after application of decoupling and subsequent rotational transformation into anti-synchronous reference frame (hence the superscript  $'$ ). In the  $x'$ - $y'$  plane the 5<sup>th</sup> and the -7<sup>th</sup> harmonic are seen as the 6<sup>th</sup> and -6<sup>th</sup>, respectively, and they can be conveniently controlled with a single resonant controller placed in both axes, which is shown at the bottom of Fig. 5.7. Vector proportional-integral (VPI) type of resonant controllers [Lascu et al (2007)] is chosen since they are shown to be superior to standard proportional-resonant (PR) controllers, which are not capable of achieving proper decoupling for both positive and negative sequence simultaneously [Yepes (2011)]. VPI controllers in the  $x'$ - $y'$  plane are tuned to the 6<sup>th</sup> harmonic by the block “harmonic number”. Similarly, those from the first ( $\alpha$ - $\beta$ ) plane are set to the 12<sup>th</sup> harmonic. Although they are identified in Fig. 5.7 purely with “parallel connection of resonant VPI controllers”,

they have the same form as those in the  $x'$ - $y'$  plane. The wording used to describe the block only signifies that multiple VPI controller pairs can be paralleled together in order to suppress a wide range of harmonics, as is shown in the next subsection that considers control of the symmetrical six-phase configuration.

### 5.2.1.2 Topologies with pulsating field in the rotor

If the symmetrical six-phase system is considered, the current control diagram of Fig. 5.7 continues to be valid. Grid current components  $i_{dg}$  and  $i_{qg}$  are again dc quantities and are controlled to their references with standard PI controllers. However, low order harmonics and their mapping are different. Now the dominant harmonics are the  $-5^{\text{th}}$ ,  $7^{\text{th}}$ ,  $-11^{\text{th}}$  and  $13^{\text{th}}$  (as seen from the stationary reference frame). It can be noticed that the  $-5^{\text{th}}$  and  $7^{\text{th}}$  harmonic have the opposite direction of rotation compared to the asymmetrical six-phase system. The harmonic mapping is also different since all four dominant harmonics map into the first plane. Therefore, there is no need for any current controller in the  $x'$ - $y'$  plane, which was necessary with the asymmetrical six-phase system. Since the first plane rotates at the synchronous speed, the  $-5^{\text{th}}$ ,  $7^{\text{th}}$ ,  $-11^{\text{th}}$  and  $13^{\text{th}}$  harmonic are seen in it as the  $-6^{\text{th}}$ ,  $6^{\text{th}}$ ,  $-12^{\text{th}}$  and  $12^{\text{th}}$  harmonic, respectively. Similarly to the asymmetrical six-phase case, the  $-6^{\text{th}}$  and  $6^{\text{th}}$  harmonic can be controlled by a single VPI resonant controller, tuned for the  $6^{\text{th}}$  harmonic, in both  $d$  and  $q$  axis. In the same manner the  $-12^{\text{th}}$  and  $12^{\text{th}}$  harmonic are controlled by the VPI controller tuned for the  $12^{\text{th}}$  harmonic. All four dominant harmonics are thus suppressed by two pairs of resonant VPI controllers. These appear in Fig. 5.7 within the block “parallel connection of VPI resonant controllers”.

Unlike in the previous case, it is clear from (3.29) that there is excitation in the first plane in case of the symmetrical six-phase charging system. The type of the field produced is pulsating, which is not capable of producing a starting torque. However, it has impact on the parameters of the equivalent scheme (Fig. 5.3). When a field pulsates it induces some currents in the rotor; thus rotor resistance and leakage inductance start to influence the system. However, the rotor has the highest impact on phases that produce the most of the pulsating flux. This flux is in the direction of the  $\alpha$ -axis (3.29); thus phases that influence it the most are  $a_1$  and  $b_2$ , since they lay on the  $\alpha$ -axis. Therefore, the parameters  $L_{a1f}$ ,  $R_{a1f}$  and  $L_{b2f}$ ,  $R_{b2f}$  are the highest since they are influenced by the leakage inductance and resistance of phases  $a_1$  and  $b_2$ , respectively, in addition to the highest part of rotor resistance and leakage inductance. Clearly, the equivalent scheme does not have equal parameters anymore, so the system is unbalanced.

The parameter asymmetry primarily gets manifested through a fundamental component that rotates in anti-synchronous direction. From the  $d$ - $q$  reference frame it is seen as the  $-2^{\text{nd}}$  harmonic (harmonic that has the frequency two times higher than the synchronous and that rotates in the opposite direction). In order to have the same grid current amplitudes in all phases this component has to be controlled to zero. This is achieved by placing another VPI resonant controller that is tuned to the second harmonic in parallel to the existing ones, within the block “parallel connection of VPI resonant controllers”. This concludes the current control of the system.

For easier understanding, and clearer view, the current control techniques discussed in this and the previous subsections are summarised in Table 5.1.

**Table 5.1:** Summary of the current control in the case of charging with multiphase supply.

	<b>Without field in the rotor (asymmetrical six-phase system)</b>	<b>With pulsating field in the rotor (symmetrical six-phase system)</b>
balanced system (equal per-phase filter parameters)	yes	no
dominant (dead-time induced) harmonics	$5^{\text{th}}$ , $-7^{\text{th}}$ , $-11^{\text{th}}$ and $13^{\text{th}}$	$-5^{\text{th}}$ , $7^{\text{th}}$ , $-11^{\text{th}}$ and $13^{\text{th}}$
dominant harmonics that map into the first ( $\alpha$ - $\beta$ ) plane	$-11^{\text{th}}$ and $13^{\text{th}}$	$-5^{\text{th}}$ , $7^{\text{th}}$ , $-11^{\text{th}}$ and $13^{\text{th}}$
dominant harmonics that map into the second ( $x$ - $y$ ) plane	$5^{\text{th}}$ and $-7^{\text{th}}$	none
number of PI controller pairs	single controller pair	single controller pair
number of resonant VPI controller pairs in the $\alpha$ - $\beta$ plane and their tuning ( $h$ )	single controller pair $h = 12$	three controller pairs $h = 2, 6$ and $12$
number of resonant VPI controller pairs in the $x'$ - $y'$ plane and their tuning ( $h$ )	single controller pair $h = 6$	no controllers

### 5.2.2 Single-phase supply

Single-phase chargers, although slower than the three-phase counterparts, are a potentially great asset and addition to the three-phase chargers due to the wide-spread existence of single-phase mains. In Chapter 3 multiphase

charger topologies that can be incorporated into single-phase charging process have been introduced at the theoretical level, and their principle of operation elaborated. This subsection discusses their control.

The equivalent scheme of single-phase chargers utilising multiphase machines is relatively straightforward to arrive at. Section 3.3 proves that machines in this process act as pure resistive-inductive elements. The chargers' equivalent scheme is then as given in Fig. 5.8. While in the physical system both terminals of a single-phase grid are attached to the machine phases, in Fig. 5.8 machine parameters from both grid branches are merged together. Thus, the filter  $L_f, R_f$  in Fig. 5.8 consists of a series connection of two  $RL$  elements and has the value of their sum. The resulting scheme is a well-known single-phase full-bridge converter.

The control algorithm for the single-phase full bridge converter of Fig. 5.8 is given in Fig. 5.9. The measurements of grid voltage and current, and dc-bus voltage are required again. The grid voltage position is found by a single-phase PLL. As already pointed out, the PLL shown in Fig. 5.6 is capable of tracking single-phase voltage as well. The only difference from multiphase and three-phase operation is that the input of the resonant filter in Fig. 5.6 is a single-phase grid voltage rather than the grid voltage  $\alpha$  component. The operating principle remains the same. The output of the PLL is again the grid voltage position, and, this time, the amplitude of the grid voltage rather than its  $d$  component.

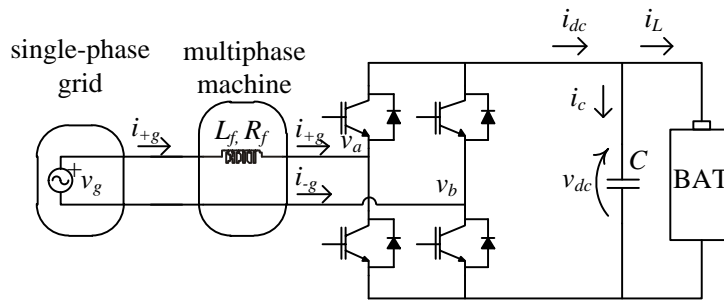


Fig. 5.8: Equivalent scheme of the charger supplied from single-phase mains.

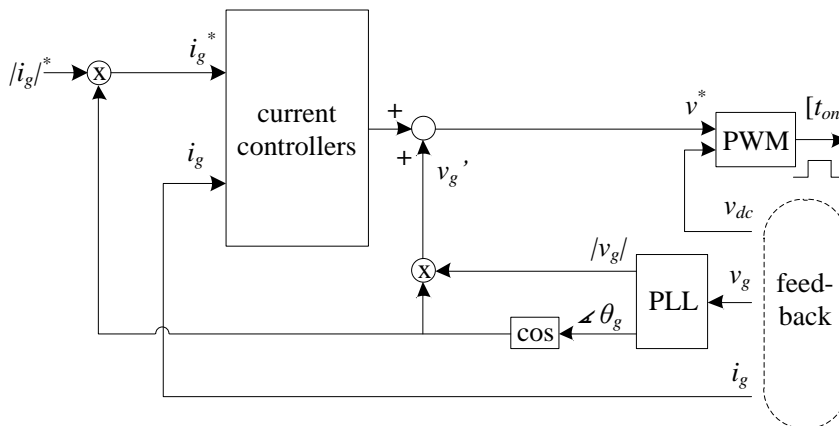


Fig. 5.9: Control algorithm for the single-phase charging/V2G process.

The input of the system is a reference for the current amplitude. It should be multiplied by a sine function in order to create the phase current reference. In order to achieve unity power factor that sine wave should follow the phase of the grid current. In Fig. 5.9 this is obtained from grid voltage position  $\theta_g$  by finding its cosine. The resulting sinusoid has two functions. When multiplied with the grid current amplitude reference  $|i_g|^*$  the reference  $i_g^*$  for the grid phase current is obtained. This reference is then used in the “current controllers” block to control the grid current. This block is elaborated in more detail in the next two subsections. The other function of the resulting sinusoid is that, when multiplied with the grid voltage amplitude  $|v_g|$ , from PLL, it produces filtered grid voltage signal  $v_g'$ . It then sums with the output of the current control in order to prevent high current at the start of the charging process. This sum represents phase voltage reference. It should be noted that, instead of the signal  $v_g'$ , it is possible to use the measured grid voltage signal  $v_g$ . However, the signal  $v_g'$  is a better option since it filters the unwanted noise from the grid voltage, without causing a phase deviation from it. The phase voltage reference then enters the final block, which is a PWM unit. The modulation strategy is the application of modulation signals in phase opposition to the two inverter legs.

The same control algorithm of Fig. 5.9 can be used for the V2G operation. The only difference is that a minus sign should be placed in front of the reference for the grid current amplitude.

### 5.2.2.1 Topologies without field production in the rotor

From the theoretical analysis performed in section 3.3 it follows that six-, nine- and ten-phase machines, in both asymmetrical and symmetrical configuration, with the connection diagrams given in section 3.3, do not get excitation in the first plane during the charging process. Since there is no field production in their rotors, their stator winding's resistance and leakage inductance play a role of current filter. It can be shown that for the six-phase and nine-phase machine the equivalent filter resistance and inductance are  $2/3$  of the per-phase stator resistance and leakage inductance values. In the case of the ten-phase machine the scaling factor is  $2/5$ . In either case, it is a single impedance represented schematically in Fig. 5.8.

A detailed representation of the block “current controllers” of Fig. 5.9 is given in Fig. 5.10. A good feature of the resonant controllers is that they are particularly suited for applications in single-phase systems. The current is controlled to its reference by a resonant VPI controller, shown at the top of Fig. 5.10. The controller is tuned to the first harmonic. Just like in the case of a multiphase supply, the reference current is subtracted from the real one. The reason is again the same: for higher output values of the current controller the charging power is lower, and vice versa.

Unlike in the six-phase systems with two isolated neutral points, in single-phase systems triplen harmonics (that are multiples of three) can flow. Thus, the control should compensate all odd low-order harmonics produced by the converter dead time. These are predominantly the 3<sup>rd</sup>, 5<sup>th</sup>, 7<sup>th</sup>, 9<sup>th</sup>, 11<sup>th</sup>, 13<sup>th</sup> and 15<sup>th</sup> harmonic. Each of these harmonics can be controlled by a resonant VPI controller that is tuned to the specific harmonic that it attempts to zero. These controllers can be placed in parallel in order to suppress a wide range of harmonics. In Fig. 5.10 it is shown how the parallel connection of resonant VPI controllers zeroes all harmonics up to the 15<sup>th</sup>. It should be noted that harmonics higher than 15<sup>th</sup> can be controlled in the same manner. The cut-off point selection is somewhat arbitrary and the control up to the 15<sup>th</sup> harmonic is chosen here since it provided satisfactory results.

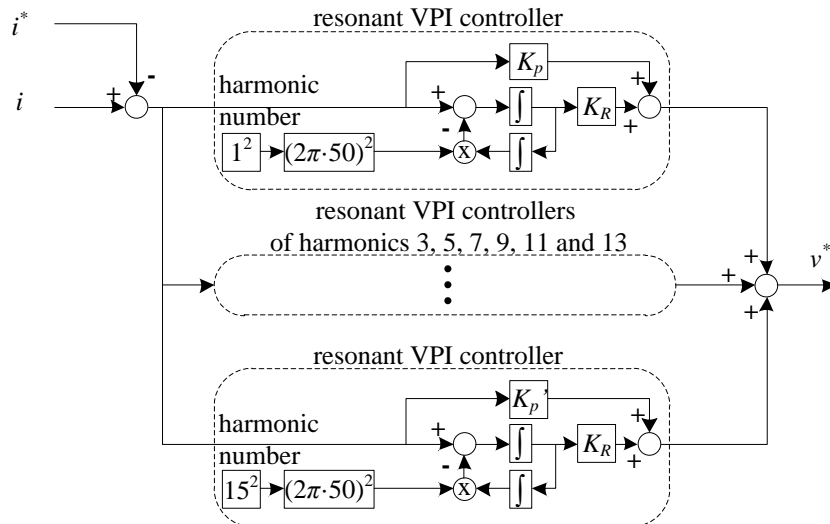


Fig. 5.10: Current control algorithm for the single-phase charging process.

### 5.2.2.2 Topologies with the pulsating field in the rotor

In the case of a single-phase charging using a five-phase machine a production of the pulsating field in the rotor takes place according to (3.68). Exactly the same situation would result with single-phase charging accomplished using a machine with any other (higher) prime phase number. The discussion is here however restricted to the five-phase machine.

The pulsating field introduces asymmetry in the equivalent per-phase parameters of the machine. Similarly as for the case of a multiphase supply, the phases that are the closest to the direction of the pulsation have the highest equivalent resistance and inductance. Moreover, different numbers of machine phases are placed in parallel before the connection to the single-phase grid terminals. On one side three phases are paralleled, while on the other side only two phases are in parallel connection. However, all this asymmetry is not seen from the outer charging/V2G system. In simple terms, all that the outer system sees is two sets of parallel connections of impedances which are then connected in series. As a result single impedance is obtained, which can be again represented as in Fig. 5.8. Compared to the systems without field production in the rotor, the situation here, observed from outside the machine, differs only by the value of this impedance. Therefore, equivalent scheme remains unaltered. As a consequence, the current control algorithm shown in Fig. 5.10 can be used again without any modifications.

Although somewhat trivial, the current control of single-phase chargers is summarised in Table 5.2 for the sake of completeness.

**Table 5.2:** Summary of current control in the case of charging using single-phase supply.

	<b>Without field in the rotor (6, 9 and 10-phase system)</b>	<b>With pulsating field in the rotor (5-phase system)</b>
balanced system (equal filter parameters)	n/a (system has single impedance)	n/a (system has single impedance)
dominant (dead-time induced) harmonics	3 <sup>rd</sup> , 5 <sup>th</sup> , 7 <sup>th</sup> , 9 <sup>th</sup> , 11 <sup>th</sup> , 13 <sup>th</sup> and 15 <sup>th</sup>	3 <sup>rd</sup> , 5 <sup>th</sup> , 7 <sup>th</sup> , 9 <sup>th</sup> , 11 <sup>th</sup> , 13 <sup>th</sup> and 15 <sup>th</sup>
number of resonant VPI controllers and their tuning ( $h$ )	eight controllers $h = 1, 3, 5, 7, 9, 11, 13$ and 15	eight controllers $h = 1, 3, 5, 7, 9, 11, 13$ and 15

### 5.2.3 Three-phase supply

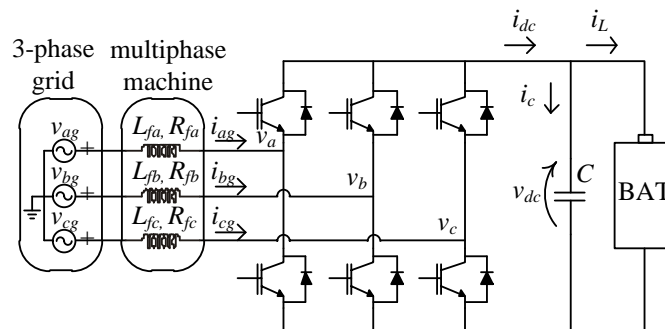
Topology and principle of operation of multiphase chargers featuring direct connection to three-phase mains are covered in section 3.4. This subsection considers their control. What all topologies have in common is the equivalent charging/V2G scheme, presented in Fig. 5.11. It can be seen that it is a standard three-phase boost PFC converter. A standard manner of its control, when unity power factor operation is mandatory, is by voltage oriented control (VOC) algorithm presented in Fig. 5.12. It can be seen that it has great similarity with the one shown in Fig. 5.5, that is used for multiphase VSCs. The only difference is that now there are no  $x$ - $y$  components, so that their control is no longer required. Therefore, the decoupling and rotational matrix (in Fig. 5.12 lumped together in the single block labelled “coordinate transformation”) are now for three-phase systems, and have their well-known form. The rest of the system, as well as the principle of operation, remain the same as those for multiphase VSC.

Measurements of grid currents, grid voltages and dc-bus voltage are required once more. PLL, shown in Fig. 5.6, obtains information on grid position and its voltage  $d$ -component from three grid voltages. The information is used for rotational transformation in order to transform grid currents into the coordinate frame that is oriented according to the grid voltage. The result is that the grid current component, which is in phase with the grid voltage, is separated and appears as a dc quantity. If the charging process utilises only this component ( $i_{dg}$ ), the unity power factor operation during charging results. Thus, the current component that is out of phase with the grid voltage ( $i_{qg}$ ) has zero reference, while the reference for the  $d$ -component is obtained by CC or CV mode. These two current components are controlled to their references in the block “current controllers”. This block differs significantly from the one for multiphase VSCs, and is considered separately in the following two subsections. Grid voltage  $d$ -component, from PLL, is added to the  $d$ -component of the current controller output. This is done again for the same reason as in chargers utilising multiphase and single-phase supply, i.e. in order to prevent high currents at the beginning of the charging process. The resulting signals are references for the converter voltage in the  $d$ - $q$  reference frame. After inverse rotational and inverse decoupling transformation phase voltage references are obtained, which then enter PWM unit. This concludes the control subsystem. A simple carrier-based PWM with the standard type of zero-sequence injection is used as the modulation strategy.

V2G operation is obtained by placing the minus sign in front of the reference for the  $d$ -component of grid current, this being just the same as for the charging from a multiphase voltage source.

#### 5.2.3.1 Topologies without the field in the rotor

From section 3.4 it follows that there are two types of charger topologies employing multiphase machines that do not have field production in the rotor during the charging process. One employs asymmetrical or symmetrical nine-phase machine (Fig. 3.8), while the other (Fig. 3.9) utilises a symmetrical six-phase machine. The one with symmetrical six-phase machine utilises the principle of field cancellation between windings in phase opposition (3.82)-(3.83) when the same currents flow through them. Both types have very similar control. However, the control (and experimental verification) for the latter one is not considered here since it is presented in [De Sousa et al (2010)].

**Fig. 5.11:** Equivalent scheme of chargers supplied from three-phase mains.

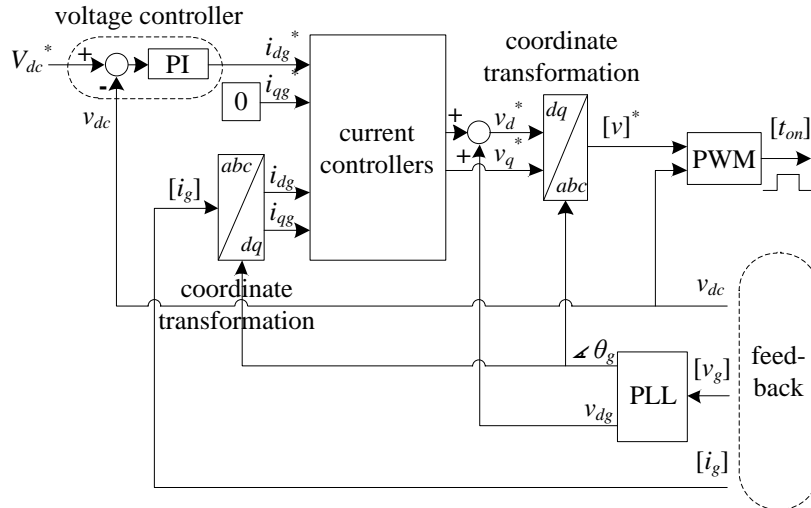


Fig. 5.12: VOC algorithm for the configuration from Fig. 5.11.

In the case of a nine-phase topology absence of the field in the rotor during the charging process follows from (3.72) and (3.76). As a consequence filter impedances in Fig. 5.11 are the same and equal to the parallel connection of three impedances composed of the stator resistance and stator leakage inductance. Thus, the system is balanced.

The “current controllers” block of Fig. 5.12 is shown in detail in Fig. 5.13. It can be seen that it is similar to the one in Fig. 5.7, except that it now does not include controllers for  $x$ - $y$  components. PI controllers with decoupling network are used once more for the control of the current fundamental. They are sufficient for its control since the system is balanced.

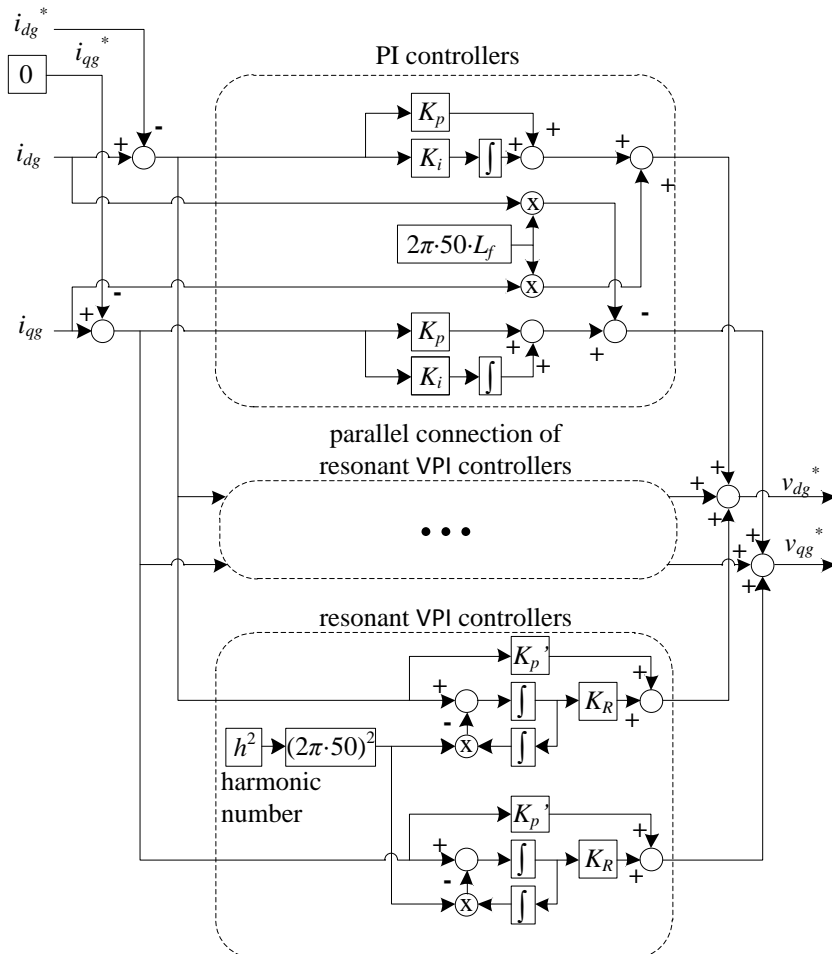


Fig. 5.13: Current control algorithm for the three-phase charging process.

All the dominant dead-time harmonics map now into the  $\alpha\text{-}\beta$  plane, since only a single plane exists. These are the  $-5^{\text{th}}$ ,  $7^{\text{th}}$ ,  $-11^{\text{th}}$  and  $13^{\text{th}}$  (as seen from the stationary reference frame). Since the  $d\text{-}q$  plane rotates at the synchronous speed, these harmonics appear in it as the  $-6^{\text{th}}$ ,  $6^{\text{th}}$ ,  $-12^{\text{th}}$  and  $12^{\text{th}}$ , respectively. Similarly as in the case of a multiphase supply, resonant VPI controllers can be used to control both positive and negative sequences of harmonics at the same time. Thus a single resonant VPI controller in both  $d$  and  $q$  axis is used to control both the  $-6^{\text{th}}$  and the  $6^{\text{th}}$  harmonic. In order to do so the VPI controller is tuned for the  $6^{\text{th}}$  harmonic by setting  $h = 6$  (Fig. 5.13). A resonant VPI controller tuned for the  $12^{\text{th}}$  harmonic zeroes both the  $-12^{\text{th}}$  and  $12^{\text{th}}$  harmonics in the same manner. Thus with two resonant VPI controllers, placed in both axes, the control of all four dominant harmonics is achieved. The presented control is sufficient to keep the grid current without low order harmonics up to the  $15^{\text{th}}$ , since harmonics that are multiples of three cannot flow in the system. This is unlike one of the cases that are considered in the next subsection.

### 5.2.3.2 Topologies with the pulsating field in the rotor

Current control methods for topologies that develop pulsating field in the rotor during the charging process, obtained from the three-phase supply, are considered here. These include two types. The first one is represented by topologies employing five-phase and asymmetrical and symmetrical six-phase machines in conjunction with direct grid connection (Fig. 3.11, Fig. 3.10). The second type is represented by a topology employing symmetrical six-phase machine with isolated six-phase supply obtained from a transformer with secondary windings in open-end configuration (Fig. 5.2). It is considered here regardless of the fact that its supply is six-phase, and therefore more appropriate to be placed in section 5.2.1. However, although the topology operates as a six-phase charger, it is obvious that its equivalent scheme (Fig. 5.4) is a three-phase system. Thus, it should be controlled as a three-phase, rather than a multiphase system (section 5.2.1). It should be noted that only its control is considered here in conjunction with three-phase systems, while experimental results for the topology are given together with other multiphase charging systems (section 5.3.1). The justification for this is that its principle of operation (3.29)-(3.30) is the same as for the supply obtained from a symmetrical six-phase voltage source, like the one presented in Fig. 5.1b.

In both charging types the effect of the pulsating field is the same as in the topologies considered in section 5.2.1.2. This means that it has an impact on parameters of the equivalent scheme (Fig. 5.11). The influence is yet again the highest on phases that produce the most of the pulsating flux, which introduces inequality between filter parameters. Therefore, the system is unbalanced.

The controllers for the fundamental and dead-time harmonics that are discussed in the previous subsection ( $-5^{\text{th}}$ ,  $7^{\text{th}}$ ,  $-11^{\text{th}}$  and  $13^{\text{th}}$ ) remain the same (Fig. 5.13). However, the system unbalance, primarily reflected through a fundamental component that rotates in the anti-synchronous direction, requires additional controllers. Thus an additional pair of resonant VPI controllers is placed in parallel to those controllers discussed in the previous subsection. The controller pair is tuned to the  $2^{\text{nd}}$  harmonic, since the fundamental component that rotates in the anti-synchronous direction is seen from the synchronous reference frame as the  $2^{\text{nd}}$  harmonic.

It should be noted that, although the system unbalance has the most noticeable effect on fundamental component, it also affects low-order harmonics. That is, the unbalance introduces low-order harmonics that rotate in the opposite direction compared to those from a balanced system. Therefore, in addition to the standard harmonics which appear in three-phase systems ( $-5^{\text{th}}$ ,  $7^{\text{th}}$ ,  $-11^{\text{th}}$  and  $13^{\text{th}}$ ) their counter-parts ( $5^{\text{th}}$ ,  $-7^{\text{th}}$ ,  $11^{\text{th}}$  and  $-13^{\text{th}}$ ) are also introduced. From the synchronous reference frame these additional harmonics are seen as the  $4^{\text{th}}$ ,  $-8^{\text{th}}$ ,  $10^{\text{th}}$  and  $-14^{\text{th}}$ . They can be controlled by four resonant VPI controller pairs tuned at  $4^{\text{th}}$ ,  $8^{\text{th}}$ ,  $10^{\text{th}}$  and  $14^{\text{th}}$  harmonic placed in parallel to the already existing ones in Fig. 5.13. It should be noted that not all unbalanced systems require this additional control. In fact, the effect of unbalance on low-order harmonics is minor in systems that have reasonably high equivalent scheme impedances. Here the additional control is only included in topologies that employ six-phase machines with direct connection to the three-phase grid. They are chosen since six-phase machines that are used for experimental verification have rather small inductances in the second plane. At the same time, additional control is not included for the six-phase topology with transformer supply since the parameters of the equivalent scheme are supported and increased by transformer parameters.

Finally, in the case of six-phase topology with transformer supply according to Fig. 5.2, the control has an additional aspect that has not been addressed until now. As can be seen from Fig. 5.2, the secondary side of the transformer does not have a neutral point. This means that zero-sequence current can flow on this side of the transformer, provided that the conditions that govern simultaneous zero-sequence current flow at both sides of the transformer are met. Thus, unlike in standard three-phase systems, the harmonics that map into zero-sequence can flow for certain primary winding connections. These are the harmonics whose order is a multiple of three, with the dominant being the  $3^{\text{rd}}$  harmonic. This harmonic can be controlled using the zero-sequence current, with the VPI resonant controller tuned at the  $3^{\text{rd}}$  harmonic frequency, as shown in Fig. 5.14. Needless to say, in this case the zero-sequence current component also has to be fed into the "current controllers" block in Fig. 5.12. The same controllers, tuned at the  $9^{\text{th}}$  and  $15^{\text{th}}$  harmonic, may be added in order to zero the  $9^{\text{th}}$  and  $15^{\text{th}}$  harmonic in parallel to the controller shown in Fig. 5.14. The PWM algorithm cannot utilise zero-sequence injection any more, since zero-sequence currents can flow.

It should be noted that, if the transformer primary is grounded (as the case is in the performed experiments), zero-sequence harmonics can penetrate into the grid. It is also important to emphasise that the need for the zero-sequence current controller arises here due to the specific open-end secondary winding arrangement of Fig. 5.2. If a transformer with two three-phase secondaries, connected in star with isolated neutral points and with phase shifted outputs by  $180^\circ$ , is used instead (Fig. 5.1b) there is no need for the zero-sequence current control.

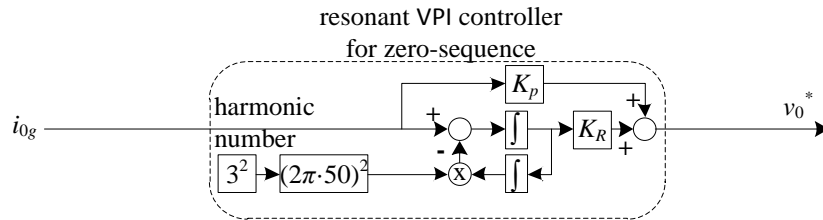


Fig. 5.14: Additional current controller required for the zero-sequence current control.

Rather complex current control schemes, discussed in the last two subsections, are summarised in Table 5.3.

Table 5.3: Summary of current control techniques in the case of three-phase charging supply

	Without rotor field	With pulsating field in the rotor		
	9-phase (Fig. 3.8)	6-phase (Figs. 3.4b and 5.2)	6-phase (Fig. 3.10)	5-phase (Fig. 3.11)
balanced system (equal per-phase filter parameters)	yes	no	no	no
dead-time harmonics that map into the ( $\alpha$ - $\beta$ ) plane	$-5^{\text{th}}, 7^{\text{th}}, -11^{\text{th}}, 13^{\text{th}}$	$-5^{\text{th}}, 7^{\text{th}}, -11^{\text{th}}, 13^{\text{th}}$	$-5^{\text{th}}, 7^{\text{th}}, -11^{\text{th}}, 13^{\text{th}}$ and $5^{\text{th}}, -7^{\text{th}}, 11^{\text{th}}, -13^{\text{th}}$	$-5^{\text{th}}, 7^{\text{th}}, -11^{\text{th}}, 13^{\text{th}}$
dead-time harmonics that map into zero- sequence	they cannot flow	$3^{\text{rd}}$ (dominant) and $9^{\text{th}}, 15^{\text{th}}$ (minor)	they cannot flow	they cannot flow
number of PI controller pairs	single controller pair	single controller pair	single controller pair	single controller pair
number of resonant VPI controller pairs in the $\alpha$ - $\beta$ plane and their tuning ( $h$ )	two controller pairs $h = 6, 12$	three controller pairs $h = 2, 6$ and $12$	seven controller pairs $h = 2, 4, 6, 8, 10, 12,$ and $14$	three controller pairs $h = 2, 6$ and $12$
number of resonant VPI controllers for the zero-sequence and their tuning ( $h$ )	no controllers	single controller $h = 3$ (optionally $h = 9, 15$ )	no controllers	no controllers

### 5.3 Experimental results

A detailed control analysis of the charging topologies, introduced in Chapter 3, was performed in section 5.2. The analysis began from equivalent schemes that are valid for the charging/V2G process, and that take into consideration all electrical aspects of machines during this process. Control algorithms were developed for three different types of voltage supply: multiphase, single-phase and three-phase. The effect of the occurrence of a pulsating field in rotors of some machines (assuming that the utilised machine is of induction type) during the charging/V2G process was identified, and additional control for parameter unbalance, introduced in the equivalent schemes, was proposed. In this section these control algorithms, detailed in 5.2, as well as the operating principles developed in Chapter 3, are validated by means of experiments.

During the charging/V2G process the particular focus is on meeting grid standards and regulations. They are reflected in the limit for the allowed current THD, and the requirement for the unity power factor operation. Therefore, a special attention is paid here to the grid current and grid current spectrum is included for all the considered topologies. This is at the same time used to validate current control algorithms, and harmonic elimination strategies that are, for the three types of voltage supply, summarised in Tables 5.1 - 5.3. Moreover, the grid current is always presented on the same graph with grid voltage, in order to confirm unity power factor operation that meets the grid requirement. This is

at the same time used in order to validate basic control algorithms, which are, for the three types of voltage supply, presented in Figs. 5.5, 5.9 and 5.12.

One very important aspect of integrated chargers is whether a torque is produced during the charging/V2G process. Although the torque production can be monitored through its impact on the machine speed, so that if machine's rotor does not move the torque is not produced, this method is not entirely accurate. That is, although the rotor may stay at standstill, the torque incapable of surpassing friction can still be generated. On the other hand, this torque is almost impossible to measure. However, the torque existence or otherwise can be monitored indirectly by detecting the existence (or non-existence) of the rotating field in the machine, which cannot be produced if there is pulsating excitation or no excitation in the first plane. Thus, the excitation mapping into machine's planes becomes very significant. For each charging topology the mapping has been predicted by theoretical analysis reported in Chapter 3. Here the theory is verified by presenting experimental results of excitation mapping for all the considered topologies. An exception is the single-phase charging/V2G process, which by default cannot produce a rotating field, so that the information on excitation mapping into different planes is omitted.

Finally, for each topology and in each operating mode battery charging current is presented. This is done since, considering fixed battery voltage, from this current battery charging/discharging power can be easily obtained. On the other hand, grid-side power is also determined by grid currents, as grid voltage levels are fixed. Therefore, efficiency of each topology can be easily obtained by division of these two (output and input) powers. However, explicit data on efficiency are not provided here since neither machines nor converters are optimised for vehicular applications.

Experimental rig data are given in the Appendix A. Instead of a battery (and a dc-dc converter, if needed), an amplifier "Spitzenberger & Spies" is utilised to provide the constant dc voltage. In order to provide isolated voltage supply, as the real battery would provide, the four-quadrant amplifier is supplied by an isolation transformer. It is also equipped with a resistor bank (RL 4000) to be able to sink the power during charging mode. A resistor of 0.5Ω is placed between the amplifier and the voltage source converter in order to emulate battery's internal resistance. Grid phase voltages are 240V rms, 50Hz. The switching frequency of the converter is 10kHz, and asymmetrical PWM [Holmes and Lipo (2003)] is used; thus the sampling frequency is 20kHz. The dead time is 6μs. Control is performed in CC mode and the algorithms are implemented using dSPACE ds1006 processor board.

The presentation of experimental results follows the order of appearance of topologies in Chapter 3 and their control algorithms in section 5.2. Therefore, the starting point are the charging schemes which employ multiphase voltage source. Charging from the single-phase mains is covered next and, finally, the results are reported for the configurations that utilise three-phase mains. Similarly as in section 5.2, types in which a pulsating field is produced in machine's rotor and those in which there is no field production in rotor are considered separately. Experimental results are given for both charging and V2G process.

### 5.3.1 Multiphase supply

Chargers employing multiphase supply are capable of achieving high charging powers. However, as already noted in section 5.2.1, only those supply types that can be easily obtained from three-phase voltage sources are considered here. This comes down to asymmetrical (Fig. 5.1a) and symmetrical six-phase supply (Fig. 5.1b and Fig. 5.2). Symmetrical six-phase voltage supply, depicted in Fig. 5.2, is used, rather than the one of Fig. 5.1b, since it is believed that it is more suitable for real-world applications. Therefore, in the following two subsections experimental results in charging and V2G mode are given for the configurations of Fig. 5.1a and Fig. 5.2. The analysis starts with the asymmetrical topology.

#### 5.3.1.1 Topologies without the field in the rotor

The charging topology employing an asymmetrical six-phase machine is considered first, since a field is not produced in the machine rotor during the charging process (3.24). The consequence is that parameters of its equivalent scheme (Fig. 5.3) are equal to each other, and the system is balanced. Therefore, the topology is operated using the control algorithm detailed in section 5.2.1.1 – Figs. 5.5 and 5.7. In order to produce an asymmetrical six-phase voltage supply two transformers with connections Yy0 and Yd5 are employed in the laboratory. The transformers have their primary sides connected to the same three-phase grid and have such transformation ratios that on the output they give asymmetrical six-phase voltage supply of the same phase voltage value. Transformer neutral points are not grounded.

The dc-bus voltage is set to 720V, and the configuration is controlled in the CC mode. The grid current reference  $i_{dg}^*$  is set to 4A. In Fig. 5.15a grid phase voltages  $v_{ag}$ ,  $v_{bg}$  and machine currents  $i_{a1}$ ,  $i_{c1}$  are presented. The balanced operation with unity power factor is evident. Both phase currents have the same ripple since there is no field in the machine to introduce asymmetry in the equivalent charging/V2G scheme. The relatively high current ripple is due to the small machine leakage inductance in the  $x$ - $y$  plane (which is, according to (3.25), the plane through which the power is transferred) which is, due to the stator winding design of the used machine, more than ten times lower than in the first plane (see machine data in Appendix A). Machine current  $i_{a1}$  spectrum is given in Fig. 5.15b, and it contains only small low order harmonics. The grid current  $i_{ag}$  is of almost identical shape, as is evidenced with the spectrum in Fig. 5.15c, although its amplitude is two times higher (since three grid currents are transformed into six currents at the output of the transformer).

Grid current components, on the transformer secondary side, are given in Fig. 5.16. While  $q$ -,  $x$ - and  $y$ -component are kept at zero, the  $d$ -component has a non-zero value and it follows the reference well. On the other hand, if machine current components are observed (Fig. 5.17), it can be seen that the charging process utilises only the second plane, leaving the field/torque-producing plane without excitation. This is in accordance with (3.24)-(3.25). Since the field is not produced in the machine, there is no torque production and, consequently, no rotor movement, as is evident from Fig. 5.18. The same figure shows battery charging current  $i_L$ , which has a positive dc value.

V2G mode is realised with the reference  $i_d^* = -2A$ . Fig. 5.19a shows that the currents  $i_{a1}$ ,  $i_{c1}$  are shifted by  $180^\circ$  with respect to the voltages, proving the unity power factor operation. It can be seen that the currents are balanced. Machine current  $i_{a1}$  spectrum (Fig. 5.19b) again contains only small low order harmonics. Grid current components are shown in Fig. 5.20. The  $d$ -component of the current now has a negative value. The  $q$ -component is kept at zero, which indicates that this mode of operation is performed also at unity power factor. Machine current components are given in Fig. 5.21. If compared to Fig. 5.17 it can be seen that they have opposite signs. However, the first plane remained without excitation. Machine speed and battery charging current  $i_L$  are shown in Fig. 5.22. Again, the speed is zero, while the battery charging current  $i_L$  changed direction when compared to Fig. 5.18. The change in direction demonstrates that the power is transferred from the battery into the grid.

Finally, a transient from V2G into the charging mode is initiated by changing the reference in a step-wise manner to  $i_{dg}^* = 4A$ . Grid phase voltage  $v_{ag}$ , machine current  $i_{a1}$ , and battery charging current are depicted in Fig. 5.23a, which clearly shows rather fast transient response. Battery charging current  $i_L$  is negative in V2G mode and has a value of  $-1.9A$ . During the transient it gradually increases to reach the final value of  $i_L = 2.9A$  in the charging mode. Grid current components during the transient are shown in Fig. 5.23b. The  $q$ -component does not deviate from zero during the transient, while the  $d$ -component quickly reaches its new reference.

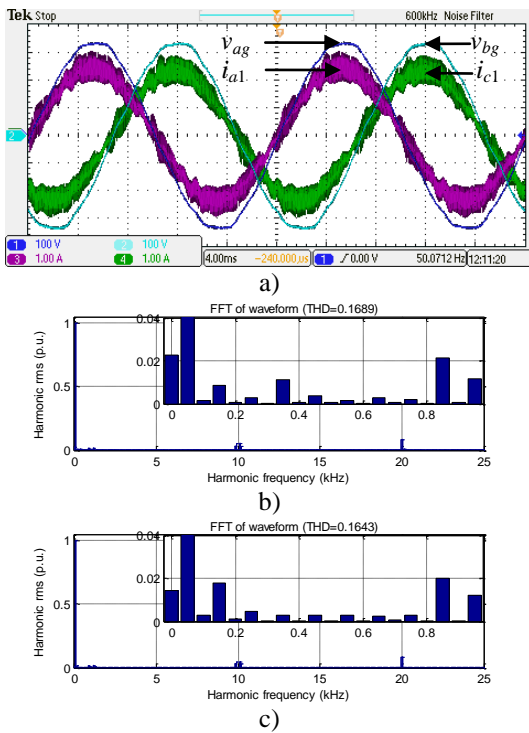


Fig. 5.15: a) Grid phase voltages  $v_{ag}$ ,  $v_{bg}$  and machine currents  $i_{a1}$ ,  $i_{c1}$ , b) spectrum of machine current  $i_{a1}$  c) grid current  $i_{ag}$  spectrum.

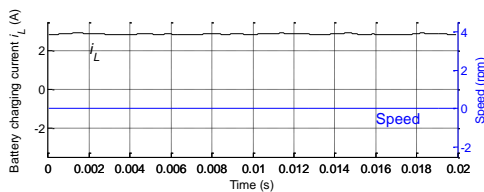


Fig. 5.18: Battery charging current  $i_L$  and machine speed.

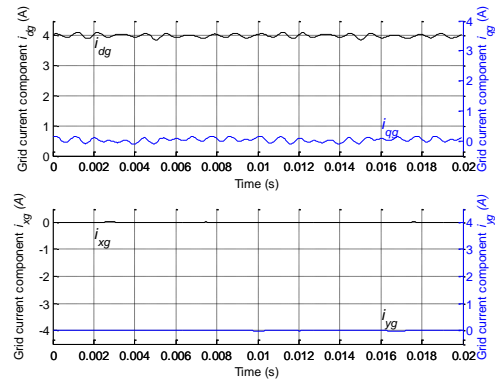


Fig. 5.16: Grid current components (on the transformer secondary side).

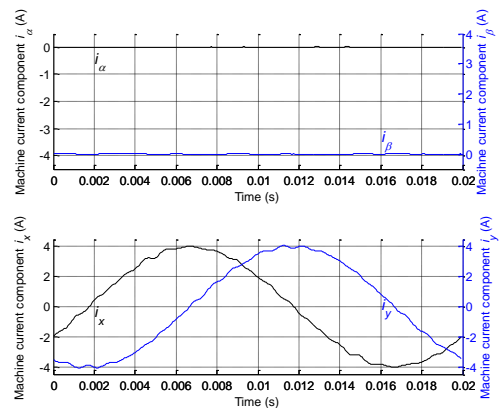
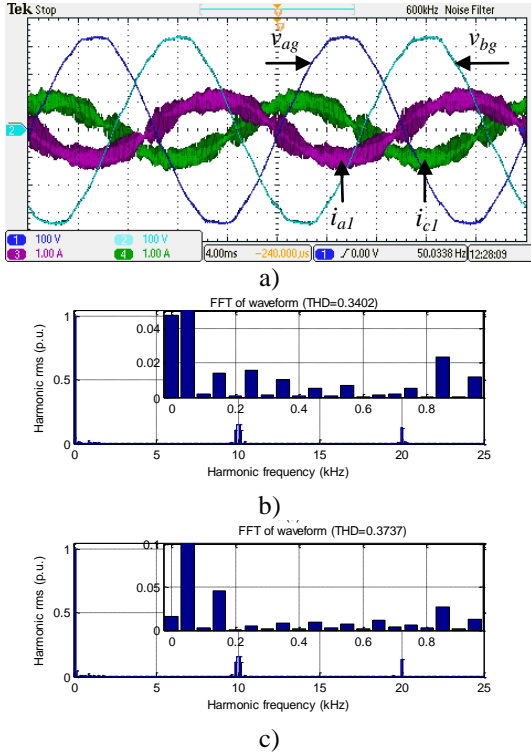
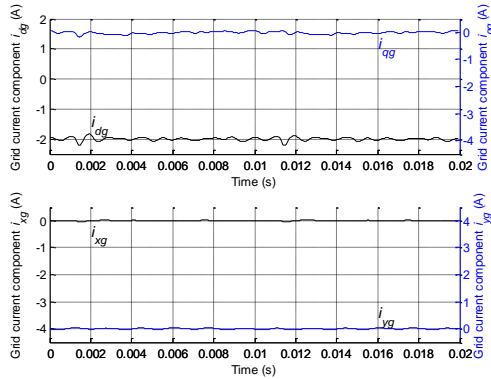


Fig. 5.17: Machine current components.



**Fig. 5.19:** a) Grid phase voltages  $v_{ag}$ ,  $v_{bg}$  and machine currents  $i_{a1}$ ,  $i_{c1}$ , b) spectrum of machine current  $i_{a1}$  c) grid current  $i_{ag}$  spectrum.



**Fig. 5.20:** Grid current components (on the transformer secondary side).

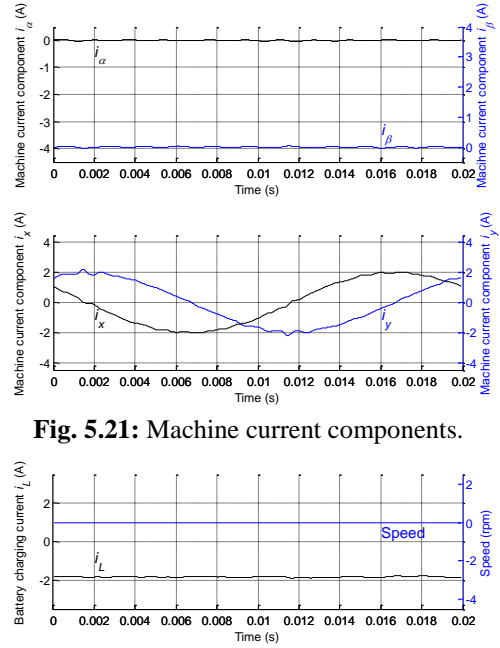


**Fig. 5.21:** Machine current components.

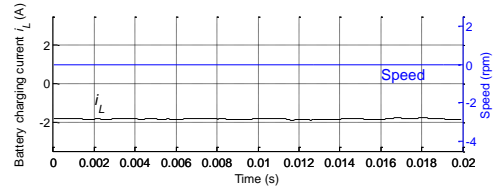


**Fig. 5.22:** Battery charging current  $i_L$  and machine speed.

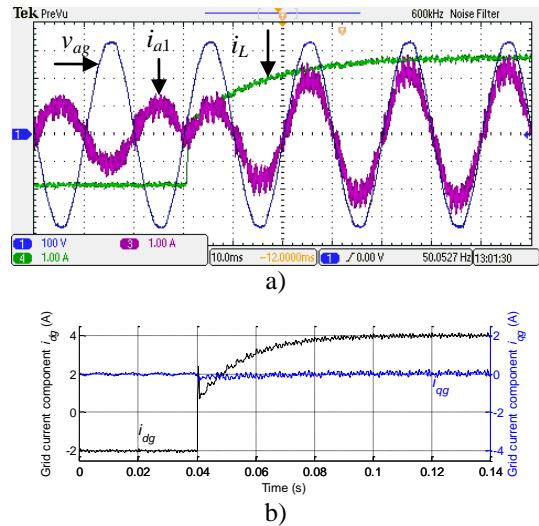


**Fig. 5.23:** Transient from V2G ( $i_d^* = -2A$ ) into the charging mode ( $i_d^* = 4A$ ): a) grid voltage  $v_{ag}$ , machine phase current  $i_{a1}$  and battery charging current  $i_L$ , b) grid current components  $i_{dg}$  and  $i_{qg}$ .

### 5.3.1.2 Topologies with the pulsating field in the rotor

In this subsection influence of the pulsating field generation in the machine's rotor on charging/V2G process is addressed. The symmetrical six-phase charging/V2G topology is supplied using the voltage source shown in Fig. 5.2. As noted previously, while the charging/V2G scheme of Fig. 5.2 is in principle the same as in Fig. 5.1b (Fig. 3.4b), the source of the two three-phase voltage systems with 180° phase shift is here a transformer with a single secondary that is kept in the open-end winding configuration (instead of a transformer with two secondaries, as in Fig. 5.1b).

An advantage of this topology is that the dc-bus voltage does not have to be higher than the peak of the grid line-to-line voltage (assuming a transformer with 1:1 transformation ratio). Thus, the topology may use semiconductors of lower voltage rating. The experiment is performed here with the dc-bus voltage of 450V.

The topology is controlled by the control algorithms given in section 5.2.3 (Figs. 5.12 - 5.14), which are valid for three-phase systems. Nonetheless, experimental results of this topology are given here, rather than in the section with other three-phase system based solutions, since the principle of operation remains the same regardless of whether voltage supply from Fig. 5.2 or Fig. 5.1b is utilised. It is still governed by (3.29)-(3.30), which describe six-phase systems.

The reference value for the  $d$ -component of the transformer secondary current is set to  $i_{dg}^* = 2A$  for the charging process (since power invariant three-phase decoupling transformation is utilised, corresponding machine's phase current rms is 1.15A). In Fig. 5.24a grid voltage  $v_{ag}$ , grid current  $i_{ag}$ , and the battery charging current  $i_L$  are presented. It can be seen that the grid current is sinusoidal and in phase with the voltage, demonstrating unity power factor operation. The battery charging current is a dc current and it has a value of  $i_L = 1.65A$ . Fig. 5.24b shows the spectrum of the grid current  $i_{ag}$ . It can be seen that it contains zero-sequence harmonics (primarily the 3<sup>rd</sup>, 9<sup>th</sup>, and 15<sup>th</sup>) since the experiment is performed with grounded neutral point of the transformer's primary. These harmonics exist purely due to the non-ideal nature of the transformer. Additional measurements (not included here) show that they have the same absolute value in the transformer no-load test, when transformer secondary terminals are left open, as they have during charging or V2G operation with any reference. Thus, these harmonics are not a consequence of the dead time of the inverter (flux saturation is a typical source of harmonics observed here). From Fig. 5.24b it can be seen that harmonics other than the zero-sequence ones are negligible (below 1% of the fundamental).

Fig. 5.25a shows machine currents  $i_{a1}$ ,  $i_{c1}$  and  $i_{b1}$  (which correspond to the secondary currents  $i_{ag}''$ ,  $i_{bg}''$  and  $i_{cg}''$ , respectively) in addition to the transformer voltage between two terminals of the phase  $a$  secondary winding  $v_{ag}$  (as noted, each of the three secondary phase windings has two accessible terminals, giving the total number of independent terminals as equal to six, Fig. 5.2). The unity power factor operation is obvious. By comparing the currents  $i_{a1}$ ,  $i_{c1}$  and  $i_{b1}$ , it can be seen that  $i_{c1}$  and  $i_{b1}$  have higher ripple. This is due to the unequal equivalent per-phase parameters of the machine during the charging/V2G mode, as explained in sections 5.2.1.2 and 5.2.3.2 (this should not be confused with the machine's phase parameters in propulsion mode of operation, since the machine itself has identical phase parameters). Nonetheless, the fundamental rms of these three currents is the same and this validates the control part of Fig. 5.13 that deals with the asymmetry control. Machine current  $i_{a1}$  spectrum is given in Fig. 5.25b and it indicates excellent current quality with negligible low order harmonics (below 1% of the fundamental). Since the transformer secondary does not contain a neutral point, harmonics that are multiples of three can flow. Indeed, machine  $i_{a1}$  current spectrum in Fig. 5.25b shows that it does contain the 3<sup>rd</sup> and 9<sup>th</sup> harmonics. However, the triplen harmonics are controlled well by zero-sequence current control of Fig. 5.14 and are of acceptably low values. It should be noted that, with respect to Fig. 5.14, the zero-sequence current control in the experiment, in addition to the control of the 3<sup>rd</sup> harmonic, controls also the 9<sup>th</sup> harmonic, in the similar manner as shown in Fig. 5.14 for the 3<sup>rd</sup> harmonic.

Transformer secondary side current components after rotational transformation are shown in Fig. 5.26. The  $q$ -component is controlled at zero, and  $d$ -current component follows its reference without a steady-state error. Fig. 5.26 also confirms unity power factor operation as well as balanced operation, since traces do not contain the second harmonic.

Machine current components are depicted in Fig. 5.27. As predicted by (3.29)-(3.30) the charging process utilises only  $\alpha$ - and  $y$ -component. Since the  $\beta$ -component is controlled at zero, only a pulsating field exists in the machine, which is, however, not capable of producing a starting torque. Thus the machine stays at standstill.

By changing the reference current from  $i_{dg}^* = 2A$  to  $-2A$  the configuration automatically enters V2G mode (the control is unaltered and is in the CC mode). From Fig. 5.28a it can be seen that the grid current  $i_{ag}$  is in phase opposition with the grid phase voltage  $v_{ag}$ , which yields a unity power factor in V2G mode. Battery charging current is again a dc component with a value of  $i_L = -2.05A$ , and it contains very little ripple.

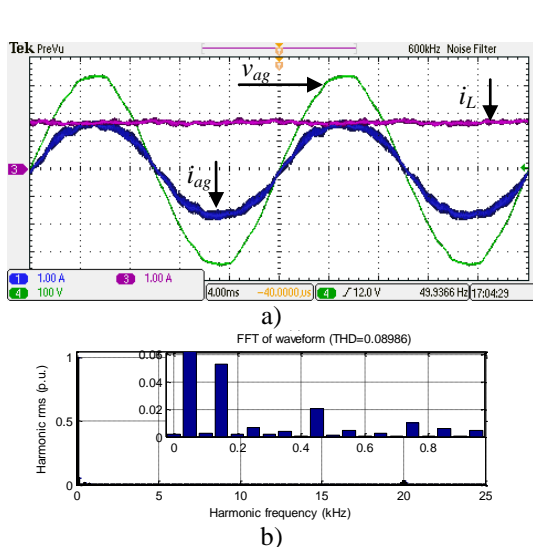


Fig. 5.24: a) Grid voltage  $v_{ag}$ , grid current  $i_{ag}$ , and battery charging current  $i_L$ , b) grid current spectrum.

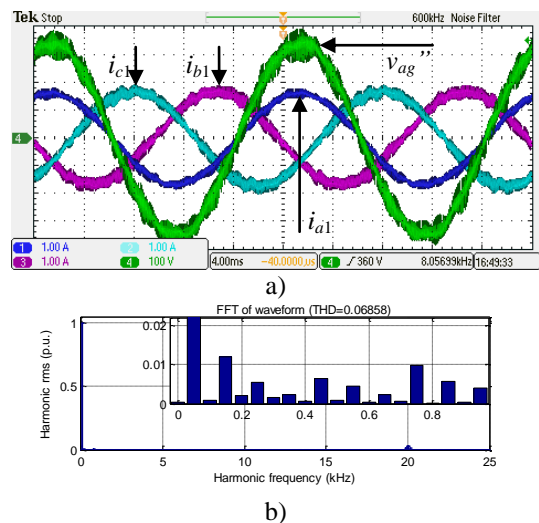
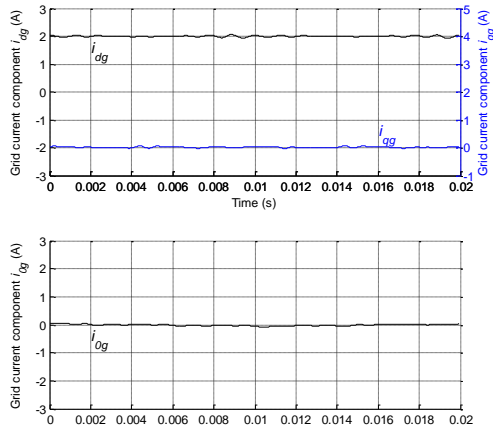
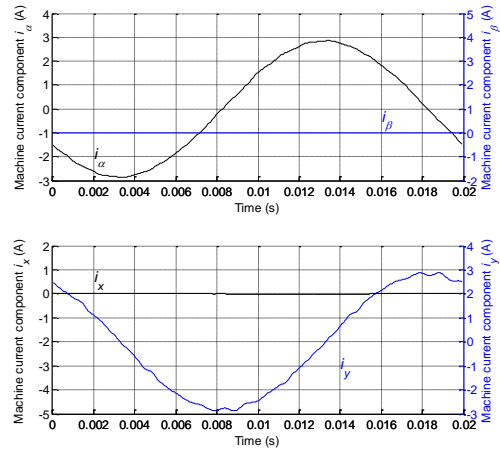


Fig. 5.25: a) Transformer secondary phase voltage  $v_{ag}''$  and machine currents  $i_{a1}$ ,  $i_{c1}$  and  $i_{b1}$ , b) machine current  $i_{a1}$  spectrum.



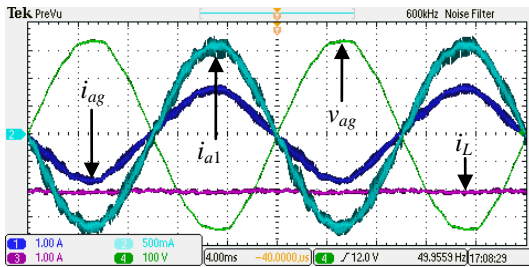
**Fig. 5.26:** Grid current components (on the transformer secondary side).



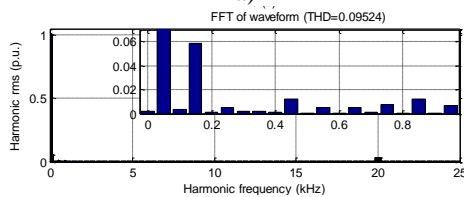
**Fig. 5.27:** Machine current components.

Compared to Fig. 5.24a this current is higher by absolute value since in V2G mode battery power has to be higher than the grid-side power to cover the losses, while in the charging mode the battery charging power is lower than the grid-side power due to the losses being covered from the grid. Fig. 5.28b and Fig. 5.28c demonstrate very good current quality in this mode as well (low order harmonics of the machine current  $i_{a1}$  are again below 1% of the fundamental, and the same considerations as in the charging mode apply to the 3<sup>rd</sup> harmonic of the grid current, which is not introduced by the inverter).

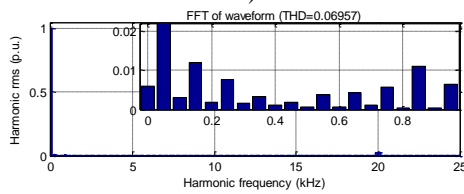
Grid current components are presented in Fig. 5.29. While the  $q$ -component is again kept at zero, the  $d$ -component follows its reference without a steady-state error. Fig. 5.29 confirms unity power factor operation and balanced control in the V2G mode of operation. Machine current components are depicted in Fig. 5.30. It is obvious that only a single current component ( $\alpha$ -component) is utilised in the first plane, so that the field is pulsating. If compared to Fig. 5.27, current components have the opposite sign.



a)



b)



c)

**Fig. 5.28:** a) Grid phase voltage  $v_{ag}$ , grid current  $i_{ag}$ , machine current  $i_{a1}$  and battery charging current  $i_L$ , b) grid current spectrum, c) machine current spectrum.

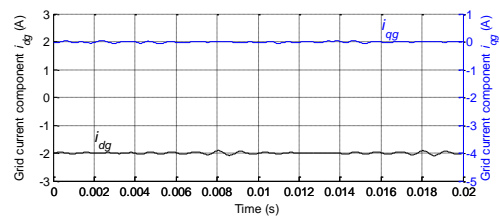


**Fig. 5.29:** Grid current components (on the transformer secondary side).

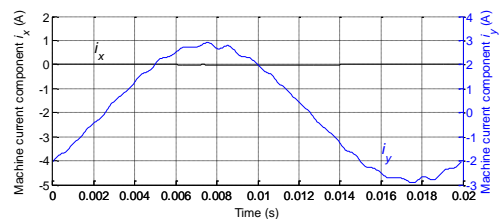
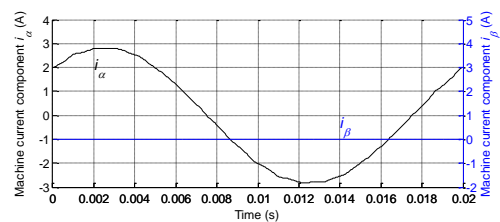


**Fig. 5.30:** Machine current components.

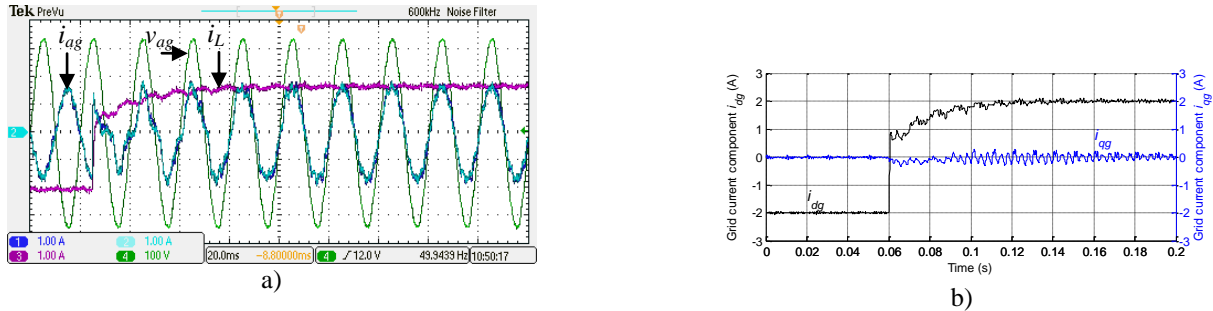


**Fig. 5.31:** Transient from V2G ( $i_d^* = -2\text{A}$ ) into the charging mode ( $i_d^* = 2\text{A}$ ): a) grid phase voltage  $v_{ag}$ , grid current  $i_{ag}$  (dark blue trace), machine current  $i_{a1}$  (light blue trace) and battery charging current  $i_L$ , b) grid current components  $i_{dg}$  and  $i_{qg}$ .

Finally, a transient from V2G into the charging mode is shown in Fig. 5.31. From Fig. 5.31a it can be seen that grid current  $i_{ag}$  quickly reaches its reference, while Fig. 5.31b demonstrates that the grid current component  $i_{qg}$  is kept at zero during the whole process, so that the unity power factor is achieved even in transient.

It should be noted here that resolver readings were continuously monitored in these experiments, as well as in all the subsequent experimentation related to other topologies and other operating modes, and that they proved that the rotor does not move (even in transients). Since each time the traces were completely uniform (and of zero value, similar to Fig. 5.18 and Fig. 5.22), speed traces are omitted from the results for the majority of configurations further on. For example, in charging/V2G topologies that employ single-phase grid, which are covered next, these traces are completely removed.

### 5.3.2 Single-phase supply

Charging/V2G operation from a single-phase voltage supply is considered next. Experimental results are given for four topologies, which employ: i) asymmetrical nine-phase, ii) asymmetrical and iii) symmetrical six-phase, and iv) five-phase machine. As already discussed in section 5.2.2 the control is the same for all four topologies, and governed by Figs. 5.9 and 5.10. Again, as in two previous subsections, harmonics up to the 15<sup>th</sup> are controlled. However, in single-phase charging process the excitation mapping into machine planes becomes meaningless and is therefore omitted. On the other hand, in the previous two subsections it was very important to show excitation mapping into different planes in order to prove that there was no excitation in the first (torque-producing) plane that could establish a rotating field; thus the rotor does not have to be mechanically locked during charging. Moreover, the information on whether a pulsating excitation is produced in the first plane was used to identify the most appropriate control method for the configuration. Unlike this, in single-phase charging process it is already known that the torque cannot be produced. Furthermore, in section 5.2.2.2 it was concluded that whether or not a pulsating field is produced is not important from the control point of view. For the reasons stated above and in order to put focus on viable information only, the decision to omit the excitation mapping into the planes was made. It suffices to say here that the mapping matches the theoretical results given in Chapter 3, section 3.3.

Since the equivalent scheme and control of all four configurations are the same, the corresponding experimental results are presented in parallel. This is particularly useful in order to observe influence of the filter (i.e. machine phases) impedance on the charging/V2G process. The task is facilitated by the fact that presenting experimental results of single-phase charging process is particularly simple, since all the required information can be shown using a single (four-channel) oscilloscope recording. It contains grid voltage  $v_g$ , grid current  $i_g$ , machine phase  $a$  current  $i_a$ , and battery charging current  $i_L$ . These data are given for all operating modes which include: charging process, charging process with interleaving, V2G process and transient between V2G and charging process.

For all topologies and in all operating modes, battery dc-bus voltage is set to 600V. Experimental results for the charging process are given in Fig. 5.32a - Fig. 5.32d, for the asymmetrical nine-phase, asymmetrical and symmetrical six-phase, and five-phase machine, respectively. The grid current reference is set to 3A. At first, it is obvious that all topologies perform charging at unity power factor, since grid currents are in phase with grid voltages. If grid currents are compared, it can be seen that although their amplitudes are the same, the current ripple varies significantly. The ripple is the highest in Fig. 5.32c, which employs symmetrical six-phase machine, since its stator leakage inductance is three to five times smaller than in any other machine (see machine data in Appendix A). The other three machines have comparable stator leakage inductances, among which the five-phase one is the highest; thus its grid current ripple is the lowest (Fig. 5.32d). However, from grid current spectra of all machines, shown just below the oscilloscope recordings, it can be seen that the difference is just in the switching ripple. The spectra show that there are not any low-order harmonics higher than 0.5% of the fundamental. This is a result of proper operation of the current control algorithm of Fig. 5.10, which manages control of the first 15 harmonics.

Using the same oscilloscope recordings, machine phase  $a$  current  $i_a$  is also shown for all four topologies. It can be seen that it is identical in terms of appearance with the corresponding grid current. Moreover, their spectra,

shown below the grid current spectra, show great similarity with the grid current spectra. This is an obvious consequence of the fact that the phase current is just the scaled grid current. In the case of an asymmetrical nine-phase and asymmetrical and symmetrical six-phase machine, sets of three machine phases are paralleled together, so that the machines' phase  $a$  currents  $i_a$  are three times lower than the grid current  $i_g$ , as is evident from the oscilloscope recordings. On the other hand, in the case of a five-phase machine, three machine phases are paralleled on one side, while only two phases are in parallel on the other side. This is why machine's phase  $a$  current is only two times lower than the grid current  $i_g$ . If the machine current ripples are observed, it can be seen that they are proportionally the same as in the grid current. Once more, the ripple related to the symmetrical six-phase machine is the highest.

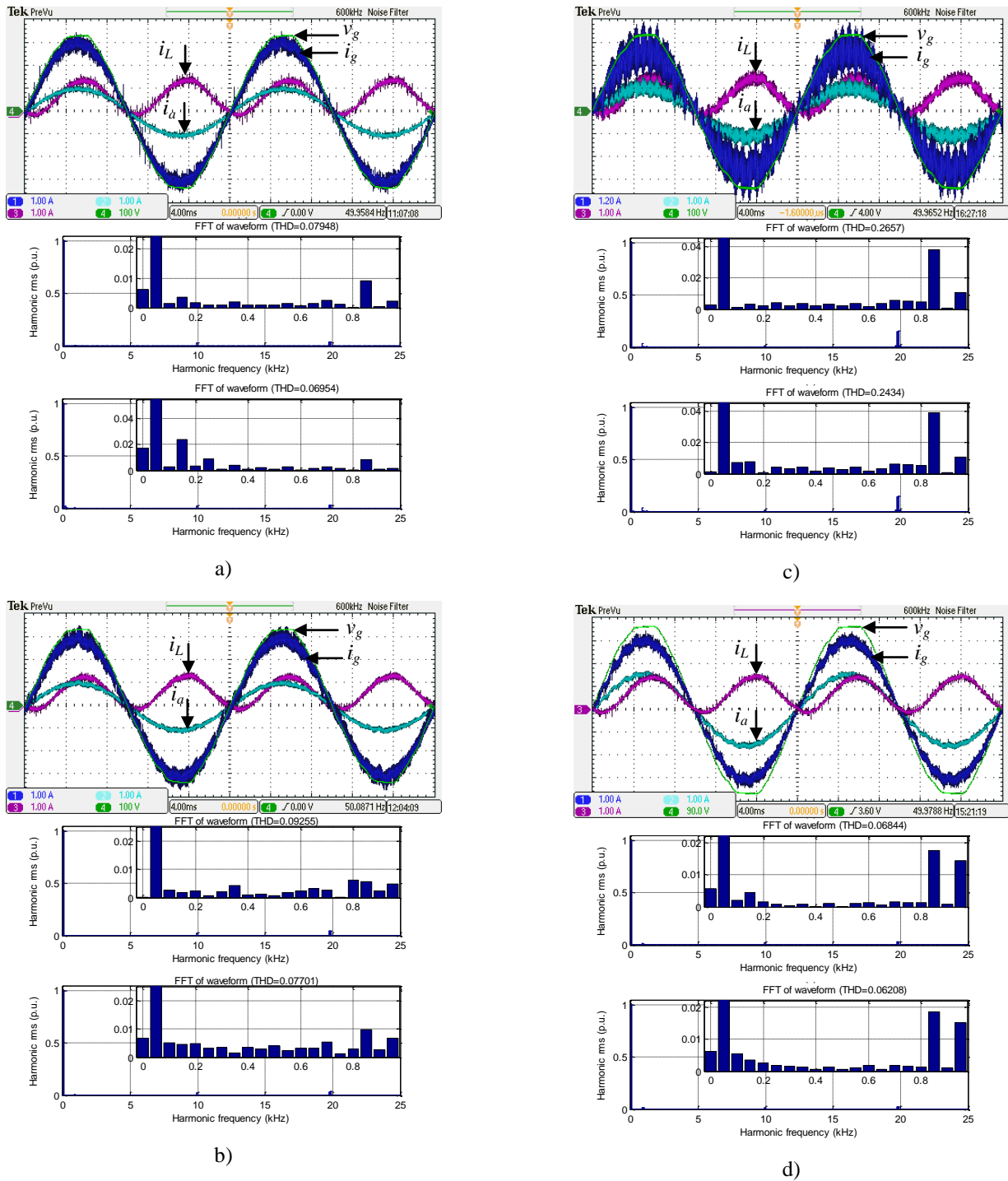


**Fig. 5.32:** Single-phase charging with: a) asymmetrical nine-phase, b) asymmetrical six-phase, c) symmetrical six-phase and d) five-phase machine. The oscilloscope traces show grid voltage  $v_g$ , grid current  $i_g$ , machine phase  $a$  current  $i_a$  and battery charging current  $i_L$ . Current spectra are given for the grid current  $i_g$  (upper graphs) and machine phase  $a$  current  $i_a$  (lower graphs).

The final trace that oscilloscope recordings show is the battery charging current. As the input power is a product of grid voltage and grid current, it is of sinusoidal waveform. Therefore, the power that enters the battery is also sinusoidal. Considering the fixed value of the battery voltage, the battery charging current has to be sinusoidal. That this is indeed the case can be seen from the oscilloscope traces. It is interesting to notice that this current has the highest ripple in the case of a symmetrical six-phase machine. This is a direct consequence of the fact that input power ripple is the highest for this machine, which then reflects on output power ripple, which is determined only by the battery charging current ripple. The presented data regarding battery charging current  $i_L$  are very important since they contain information on energy losses. The magnitude of the losses can be determined at instants when the input power is zero. In those instants the battery is charged by the energy accumulated in machine windings. When that energy is utilised the battery has to produce some power that covers the losses, so that the charging current changes sign. This phenomenon is evident from the oscilloscope recordings. However, the dc component of this current determines how long the charging will last, and it can be seen that it has a significant value for all topologies. It should be noted here that, in order to prolong the battery life, it is beneficial to put a filter at the dc-side of the topologies, so that only the dc current component penetrates the battery.

The single-phase charging topologies employing multiphase machines have an additional advantage that can facilitate meeting of grid standards and regulations, namely they enable use of interleaving strategy. Interleaving is a modulation strategy according to which converter legs, connected to the same grid terminal and which have the same reference, are not switched simultaneously. Instead, carriers are shifted by 360 degrees divided by the number of inverter legs sharing the same grid terminal. In the case of asymmetrical nine-phase, and asymmetrical and symmetrical six-phase machine there are three inverter legs sharing a common grid terminal at each side. Thus, the phase shift between carriers is 120 degrees. In the case of a five-phase machine, positive grid terminal has two machine phases attached (Fig. 3.7), while the negative has three. Therefore, carriers of the first two phases are mutually shifted by 180 degrees, while the mutual shift of carriers of the remaining three phases is 120 degrees. The effect of applying interleaved modulation strategy on the four studied topologies during the battery charging process is shown in Fig. 5.33. Since the operating conditions remained the same as for the process without interleaving, a comparison can be made. At first it is clear that the grid current ripple has been reduced significantly in all topologies. Once more, symmetrical six-phase machine has the highest and the five-phase machine the lowest grid current ripple. The reduction is a consequence of the fact that the major part of the machine's phase current ripple gets closed through other machine phases and does not enter the grid.

On the other hand, if machine currents are observed, it can be seen that the ripples have increased significantly. Switching harmonics can now circulate and flow through a closed path formed by three paralleled phases (or two and three in the case of a five-phase machine), which was not the case when they had simultaneous carriers. It is important to note that a conclusion cannot be made about the grid current ripple on the basis of the machine current ripples (as was the case when interleaving was not employed), since the major part of the ripple does not enter the grid. The increase of the current ripple in all machines (except the asymmetrical six-phase one) is around three times. However, in the asymmetrical six-phase machine the increase in the current ripple is substantially more than that. The reason is briefly addressed in what follows.

Multiphase machines may have different parameters in different planes. The effect is especially pronounced if multiple phases share the same stator slot, in which case the inductance in the second plane can be a few times lower than stator leakage inductance of the first plane. This is exactly the case with the particular asymmetrical six-phase machine that is used in the experiments, in which second plane inductance is around twelve times lower than the stator leakage inductance of the first plane (see machine data in Appendix A). However, there is also the third parameter which is the zero-sequence inductance. This parameter has not received much attention in the past since it does not have any effect on the propulsion mode (and, in general, on the operation of the machine as a variable-speed electric drive, since this is done using two isolated neutral points). However, here a totally different application of multiphase machines is considered, which utilises zero-sequence axes, thus this parameter affects the system. When interleaving process is not utilised all current components due to the switching harmonics are damped by this zero-sequence inductance. However, if interleaving process is used the majority of switching harmonics drift into the second plane. Thus, they are now damped by the lower inductance instead of the higher one. As a consequence, the switching ripple increases enormously, as is obvious from Fig. 5.33b.

Finally, conclusions regarding the effect of interleaving process on charging efficiency can be drawn based on the battery charging current  $i_L$ . It can be seen that it has a lower ripple in all topologies. However, this current's dc value determines the charging power, and therefore the efficiency. From oscilloscope traces it can be seen that in the case of asymmetrical nine-phase and five-phase machine the dc value remains similar as before interleaving strategy was applied. Since in this case the interleaving strategy does not significantly influence the efficiency of the charging process, its utilization is recommended in order to comply with grid standards and regulations. However, in the case of asymmetrical and symmetrical six-phase machine the dc value of the battery charging current is now close to zero. Thus the major part of energy that is taken from the grid gets used to cover the losses in the machine windings. Therefore, the interleaving strategy in these two cases should be avoided.

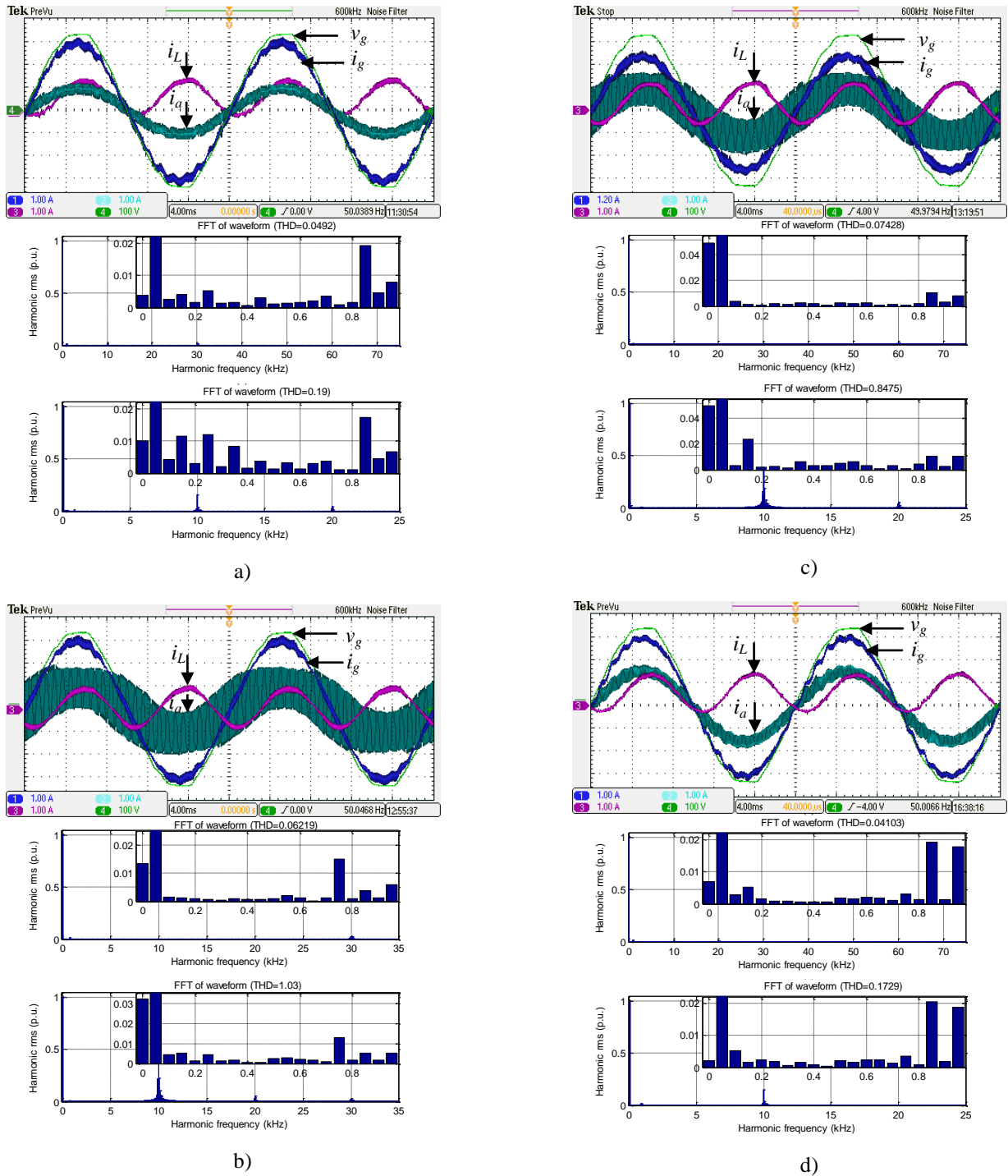


**Fig. 5.33:** Interleaved single-phase charging with: a) asymmetrical nine-phase, b) asymmetrical six-phase, c) symmetrical six-phase and d) five-phase machine. The oscilloscope traces show grid voltage  $v_g$ , grid current  $i_g$ , machine phase  $a$  current  $i_a$  and battery charging current  $i_L$ . Current spectra are given for the grid current  $i_g$  (upper graphs) and machine phase  $a$  current  $i_a$  (lower graphs).

The interleaving strategy has the same effect on V2G process as on the charging process. Therefore in Fig. 5.34 experimental results of V2G operation are given only for the case when interleaving strategy is not employed. The current reference is set to  $-3A$ , and the same four topologies are studied. Unity power factor operation is again obvious. If compared with the charging mode (Fig. 5.32), it can be seen that grid currents have almost the same ripples and spectra, however now they have opposite signs. The same is valid for the machine currents. The only difference can be seen in the battery charging currents, since they do not change the sign during the operation. They are always negative. This is a consequence of a fact that even when the output power, which gets injected into the grid, crosses

zero, still some energy has to be provided from the battery to cover the losses, mostly on the filter. Therefore, the battery charging current never reaches zero value.

Finally, transient from the charging into the V2G mode of operation is shown in Fig. 5.35. In all four topologies grid currents reach their references quickly, although some low-order harmonics appear during the transient. However, the energy almost instantly changes its direction as can be seen from battery charging currents.

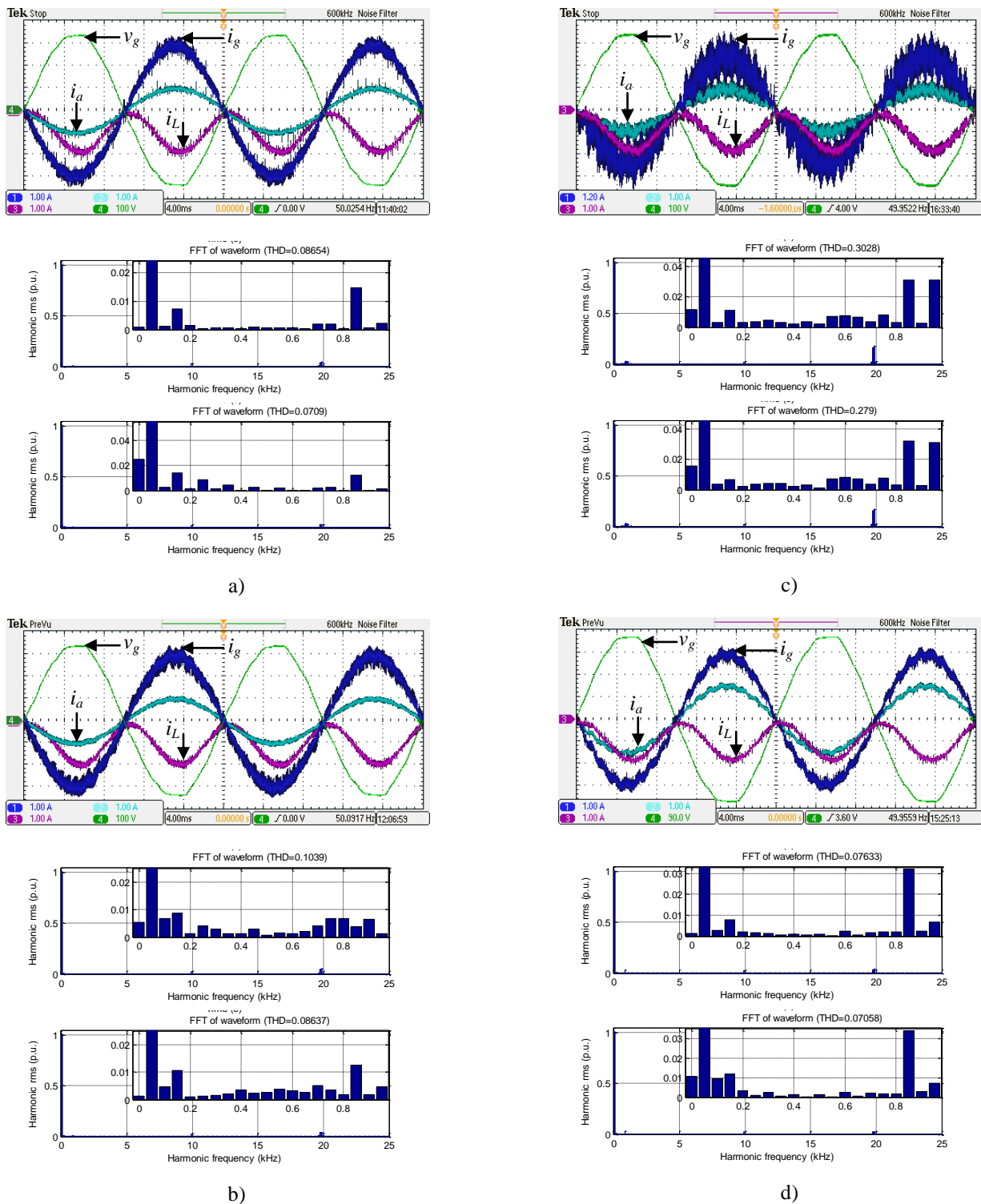


**Fig. 5.34:** Single-phase V2G with: a) asymmetrical nine-phase, b) asymmetrical six-phase, c) symmetrical six-phase and d) five-phase machine. The oscilloscope traces show grid voltage  $v_g$ , grid current  $i_g$ , machine phase  $a$  current  $i_a$  and battery charging current  $i_L$ . Current spectra are given for grid current  $i_g$  (upper graphs) and machine phase  $a$  current  $i_a$  (lower graphs).

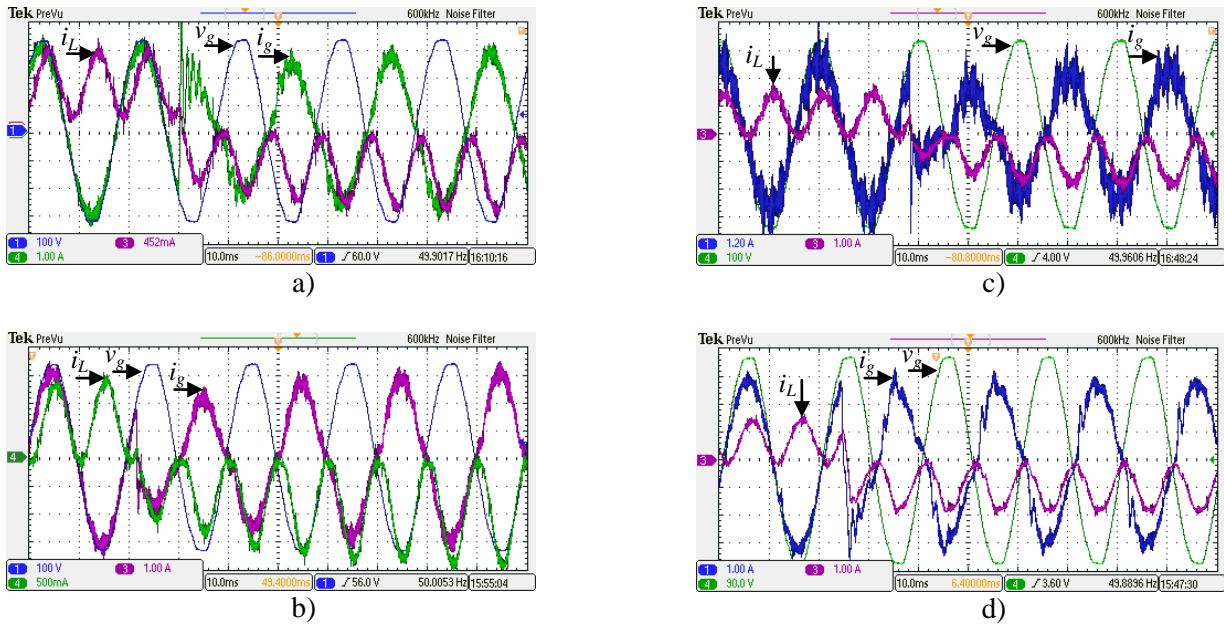


**Fig. 5.35:** Transient from charging into V2G mode of operation with: a) asymmetrical nine-phase, b) asymmetrical six-phase, c) symmetrical six-phase and d) five-phase machine. The oscilloscope traces show grid voltage  $v_g$ , grid current  $i_g$ , and battery charging current  $i_L$ .

This concludes the analysis of the single-phase charging/V2G topologies. In what follows fast charging from three-phase mains is investigated.

### 5.3.3 Three-phase supply

Charging from three-phase mains is the main type of fast integrated battery charging, thanks to the wide-spread existence of three-phase mains. In the following two subsections four topologies that take advantage of this type of charging are considered. The first subsection considers topology employing an asymmetrical nine-phase machine, while the subsequent one analyses operation of topologies utilizing an asymmetrical and a symmetrical six-phase machine and a five-phase machine. Topologies are operated according to the control algorithms given in Figs. 5.12 and 5.13, and employ current control techniques that are summarised in Table 5.3.

#### 5.3.3.1 Topologies without the field in the rotor

Nine-phase configuration (Fig. 3.8) is the only charging topology that is considered here, which does not produce a field in the rotor during the three-phase charging process, as follows from (3.76). The topology does not require any hardware reconfiguration between the propulsion and the charging mode. For the charging mode the three-phase grid is simply attached to the three nine-phase machine's neutral points. In the experiments, instead of a nine-phase inverter, the machine is connected to two eight-phase inverters, one of which provides voltages to six machine phases and the other to the three remaining phases. The dc-buses of the two inverters are connected.

The charging and V2G modes of operation are executed in the constant current (CC) regime, in which the grid current magnitude is regulated to a constant value. The reference current is  $i_{dg}^* = 4\text{A}$ , which corresponds to 1.73 smaller rms value of the phase currents, due to the power invariant three-phase decoupling transformation on the grid side. The dc-bus voltage is set to 720V for charging and V2G operation.

Fig. 5.36a shows grid phase voltage, grid phase current and machine's phase current. As can be seen, the fundamental of the grid current and phase voltage are in phase, so that the operation is with unity power factor at the grid side. The FFTs of the grid and machine phase currents are shown in Fig. 5.36b and 5.36c, respectively.

The amplitude of the current ripple is dependent on the machine's stator leakage inductance (25mH per phase here – see Appendix A), since it performs the function of the current filter (due to the three phases being effectively paralleled, the equivalent filter inductance in the sense of Fig. 5.11 is  $25/3=8.33\text{mH}$ ). The grid current is the sum of the three phase currents in the machine, which are practically the same. Therefore the grid current is three times higher than the machine's phase current (rms values of 2.3A and 0.73A, respectively) and the grid current and machine current have very similar spectra. The low order harmonics are small; the highest ones reach around 1% of the fundamental. This is considered to be a good result, taking into account the high switching period/dead time ratio. It should be noted that harmonics above the 15<sup>th</sup> are not controlled. This is an arbitrary choice here and the order of the harmonics that are

controlled can be easily increased by adding further resonant VPI current controllers in parallel to those used here, in Fig. 5.13.

The grid current components  $i_{dg}$  and  $i_{qg}$  in the grid voltage oriented reference frame are depicted in Fig. 5.37. The  $q$ -axis component reference is fixed to zero, and the battery is charged with the  $d$ -axis component. Both components follow their references very well. Since the control operates in the grid oriented reference frame and the average value of the  $q$ -axis current component is zero, Fig. 5.37 also confirms that the charging takes place at unity power factor.

Mapping of the machine phase currents into inactive planes is illustrated in Fig. 5.38, where  $i_{\alpha}$ ,  $i_{\beta}$ ,  $i_{x2}$  and  $i_{x3}$  are shown. There is a negligible excitation in any of these three planes. According to (3.76)-(3.80), the non-zero current components are in the first  $x$ - $y$  plane and along the zero-sequence axis. This is indeed the case, as is obvious from Fig. 5.39, where  $i_{x1}$ ,  $i_{y1}$  and  $i_0$  are presented. There is also an asymmetrical distribution of the components in the  $x_1$ - $y_1$  plane (see (3.77)), as is evident in Fig. 5.39.

The battery charging current  $i_L$  is shown in Fig. 5.40. It can be seen that it is practically constant, about 2.13A, with hardly any ripple. The speed trace is also included in Fig. 5.40 – as can be seen, the speed is kept at zero naturally, meaning that there is no torque developed; this is also evident from Fig. 5.38 where  $\alpha$ - $\beta$  current components have zero value throughout.

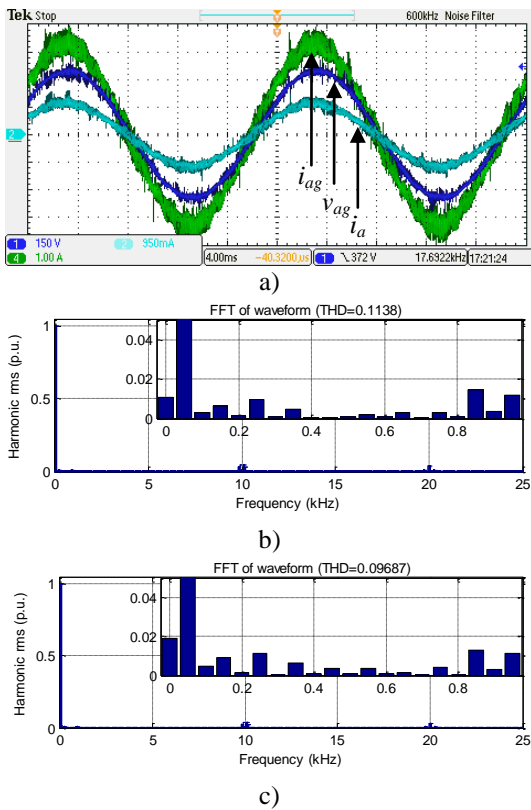


**Fig. 5.36:** Charging mode: (a) CH1 - grid phase voltage  $v_{ag}$  (150V/div), CH4 - grid phase current  $i_{ag}$  (1A/div) and CH2 - machine phase current  $i_a$  (1A/div) waveforms, (b) grid phase current and (c) machine phase current spectra – oscilloscope recordings and FFTs of measured variables.

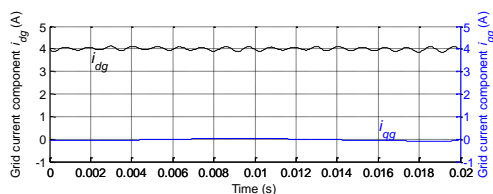


**Fig. 5.37:** Grid current components  $i_{dg}$  and  $i_{qg}$ , in charging mode, obtained within the controller after grid current transformation into voltage oriented reference frame.

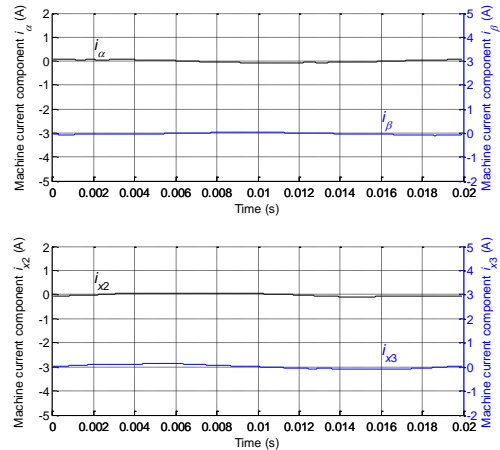


**Fig. 5.38:** Machine current components in inactive planes ( $i_{\alpha}$ ,  $i_{\beta}$ ,  $i_{x2}$ , and  $i_{x3}$ ), obtained within the controller after machine’s measured phase currents are transformed using (3.47).

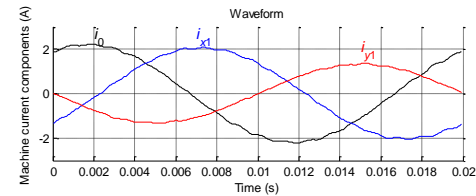


**Fig. 5.39:** Charging mode: waveforms of the machine current components  $i_{x1}$ ,  $i_{y1}$  and  $i_0$ , obtained within the controller after machine’s measured phase currents are transformed using (3.47).

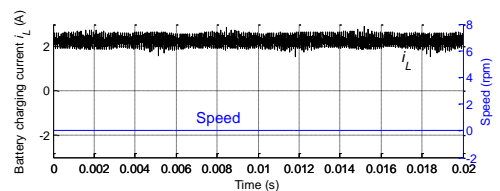


**Fig. 5.40:** Battery current  $i_L$  and machine’s speed during charging.

Similarly as in the case of single-phase voltage source, interleaving process can be employed in order to facilitate compliance with the grid standards. Since three inverter legs are connected to the each grid phase, phase shift between their carriers should be 120 degrees. Figs. 5.41-5.44 depict experimental results obtained by the same charging process, with the employment of the interleaving modulation strategy.

By comparing Figs. 5.41 and 5.36 it can be seen that the grid current  $i_{ag}$  has smaller ripple in the process with interleaved modulation strategy. On the other hand, similarly as in the case of single-phase voltage source, it increases the ripple of machine current  $i_a$ . In both cases low-order harmonics are similar, which is due to the proper operation of the current controllers in the control scheme of Fig. 5.13. Therefore, the difference is only in the switching ripple.

Grid current components are shown in Fig. 5.42 and the similarity with Fig. 5.37 is obvious. The same similarity can be noticed between Figs. 5.43 and 5.39, which show machine current components with and without the employment of interleaving modulation strategy.

Finally, dc-bus current is shown in Fig. 5.44. It has a dc value that is almost the same as in Fig. 5.40. Therefore, a conclusion can be made that interleaving modulation strategy does not degrade the efficiency of the charging process in this topology. Since it significantly reduces the grid current ripple, the employment of interleaving modulation strategy is highly recommended. It should be noted that it has the same effect on V2G process, thus experimental results are shown only for the standard modulation strategy for this mode of operation.

By setting the reference grid  $d$ -axis current to a negative value, the power flow direction reverses and V2G mode is entered. Fig. 5.45 shows the grid phase voltage, grid phase current and machine phase current waveforms (with FFTs of the grid and machine phase currents) for this mode of operation. Results apply to the reference current  $i_{dg}^* = -3A$ .

The grid and machine current rms values are 1.75A and 0.57A, respectively. The grid currents are in phase opposition with the grid voltage, which confirms the opposite power flow direction, compared to the charging mode, as well as the unity power factor operation. The amplitudes of the two currents are again in the ratio of 3 and the FFTs are similar. The low order harmonics have slightly larger magnitudes in V2G than in charging mode.

Comparison of the oscilloscope recordings of the grid currents in the charging and V2G modes, given in Figs. 5.45 and 5.36, respectively, shows similar grid current ripple. Harmonic per-unit values are however different, primarily because the fundamental grid current differs in the two modes.

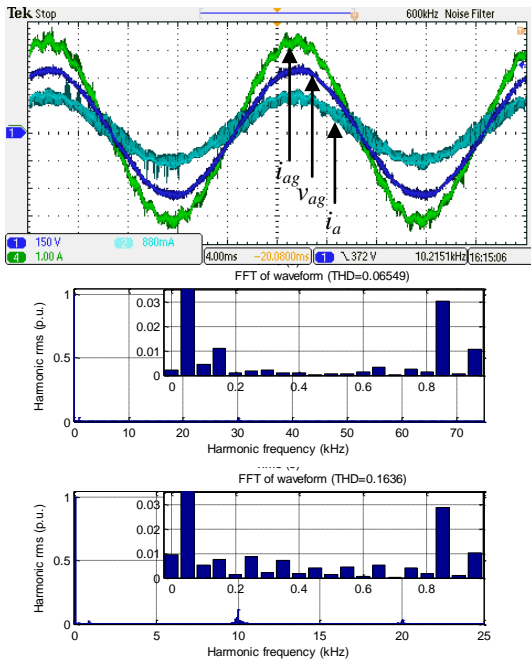


**Fig. 5.41:** Charging mode with interleaving: (a) CH1 - grid phase voltage  $v_{ag}$  (150V/div), CH4 - grid phase current  $i_{ag}$  (1A/div) and CH2 - machine phase current  $i_a$  (1A/div) waveforms, (b) grid phase current and (c) machine phase current spectra – oscilloscope recordings and FFTs of measured variables.

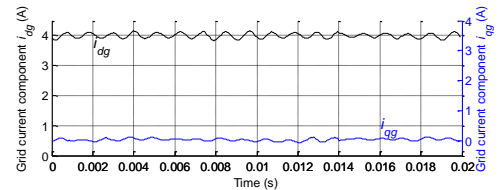


**Fig. 5.42:** Grid current components  $i_{dg}$  and  $i_{qg}$ , in charging mode, obtained within the controller after grid current transformation into voltage oriented reference frame.

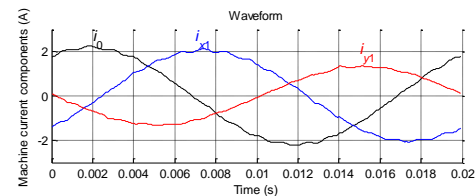


**Fig. 5.43:** Charging mode: waveforms of the machine current components  $i_{x1}$ ,  $i_{y1}$  and  $i_0$ , obtained within the controller after machine's measured phase currents are transformed using (3.47).

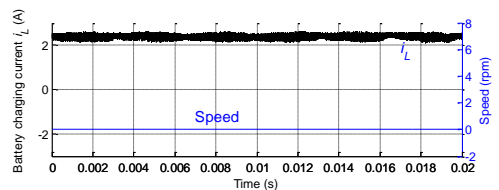


**Fig. 5.44:** Battery current  $i_L$  and machine's speed during charging.

The grid current components  $i_{dg}$  and  $i_{qg}$  for V2G mode are presented in Fig. 5.46. Once again, the reference currents are realised and the unity power factor operation reconfirmed.

The mapping of the machine currents into the planes is the same as in the charging mode. Currents  $i_{\alpha}$ ,  $i_{\beta}$ ,  $i_{x2}$  and  $i_{x3}$  are in essence zero, since the grid currents map in the machine into  $i_0$ ,  $i_{x1}$  and  $i_{y1}$  currents (Fig. 5.47). If compared with Fig. 5.39, it can be seen that they have the opposite sign. The results are in accordance with (3.76)-(3.80).

The battery charging current  $i_L$  is given in Fig. 5.48. It again has a constant value, around  $-1.95A$ . Although the grid current amplitude is reduced by approximately 25% (compared to the charging mode), the battery current  $i_L$  changes much less. The reason is the same as in the case of multiphase voltage supply. It is explained by the fact that in the V2G mode the battery has to produce the power for  $RI^2$  losses in the filter (i.e. the machine) in addition to the power that is injected into the grid. On the other hand, in the charging mode the battery charging power is what is left from the grid power after the filter losses are covered. In V2G mode speed of the machine is again kept at zero, as can be seen in Fig. 5.48.

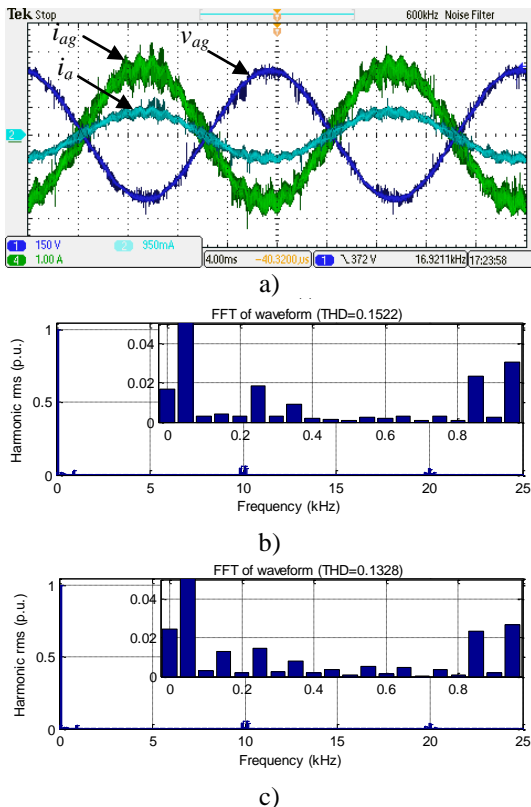


**Fig. 5.45:** V2G mode: (a) CH1 - grid phase voltage  $v_{ag}$  (150V/div), CH4 - grid phase current  $i_{ag}$  (1A/div) and CH2 - machine phase current  $i_a$  (1A/div) waveforms, (b) grid phase current and (c) machine phase current spectra - oscilloscope recordings and FFTs of measured variables.

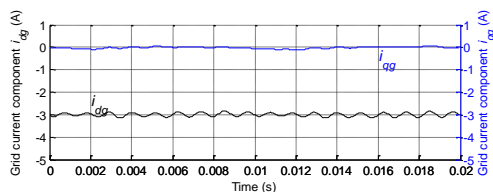


**Fig. 5.46:** Grid current components  $i_{dg}$  and  $i_{qg}$ , in V2G mode, obtained within the controller after grid current transformation into voltage oriented reference frame.

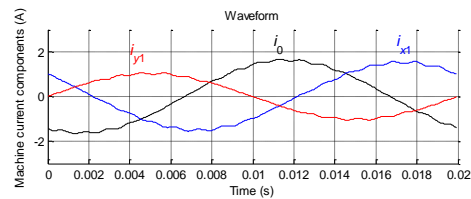


**Fig. 5.47:** V2G mode: waveforms of the machine current components  $i_{x1}$ ,  $i_{y1}$  and  $i_0$ , obtained within the controller after machine's measured phase currents are transformed using (3.47).

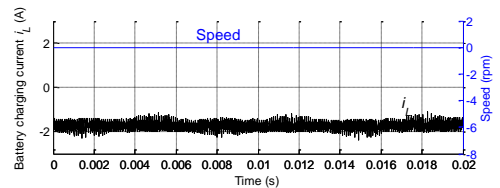


**Fig. 5.48:** Battery current  $i_L$  and machine's speed during V2G operation.

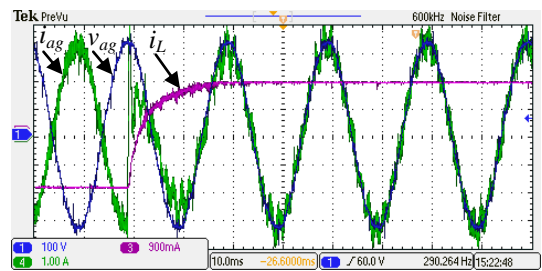


**Fig. 5.49:** Transient operation: CH1 - grid phase voltage  $v_{ag}$  (100V/div, blue trace), CH3 - dc-bus current  $i_{dc}$  (1A/div, purple trace), and CH4 - grid phase current  $i_{ag}$  (1A/div, green trace) waveforms for transition from V2G to charging mode (oscilloscope recordings).

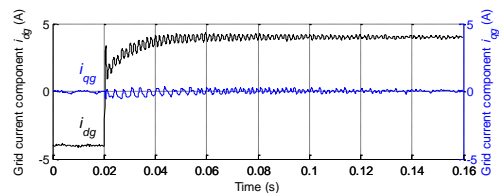


**Fig. 5.50:** Grid current components  $i_{dg}$  and  $i_{qg}$ , during transition from V2G into charging mode, obtained within the controller after grid current transformation into voltage oriented reference frame.

The transition from V2G to charging mode is illustrated next. The waveforms of the grid voltage, grid phase current and battery current are shown in Fig. 5.49, while Fig. 5.50 shows the grid current components  $i_{dg}$  and  $i_{qg}$ . The transition is from  $i_{dg}^* = -4\text{A}$  to  $i_{dg}^* = 4\text{A}$ . Both figures indicate a fast transition between these two reference values. However, the VPI controllers need more time to eliminate the harmonics from the current waveform. From Fig. 5.49 it can be seen that although grid currents have the same amplitudes for the two modes of operation, the battery charging current  $i_L$  is higher by absolute value for the V2G mode than for the charging mode, for the reason already discussed in the previous paragraph.

### 5.3.3.2 Topologies with the pulsating field in the rotor

In this subsection topologies in which a pulsating field appears in the rotor during charging/V2G process are experimentally analysed. For the three-phase charging/V2G process these are the topologies that utilise an asymmetrical six-phase, a symmetrical six-phase machine, and a five-phase machine. Since the first two topologies have exactly the same control algorithm (see Table 5.3) the applicable experimental results are shown in parallel to allow direct comparison. In what follows experimental results for the topology utilising an asymmetrical six-phase machine are shown on the left, while those with the symmetrical six-phase machine are depicted on the right.

The field production in an asymmetrical and a symmetrical six-phase machine is predicted by (3.88) and (3.86), respectively. Experiments are performed with the voltage of the amplifier set to 740V. The control is in CC mode and governed by the control algorithms given in Fig. 5.12 and Fig. 5.13. In the charging mode the reference for the  $d$ -current component of the asymmetrical and symmetrical six-phase machines is set to  $i_d^* = 1.8\text{A}$  and  $2\text{A}$ , respectively (this leads to 1.73 times lower rms values of phase currents due to the use power-invariant decoupling transformation).

Grid phase voltage  $v_{ag}$  and grid current  $i_{ag}$  are shown for the two topologies in Fig. 5.51a and Fig. 5.52a, respectively. It can be seen that grid current follows the shape of the voltage, and that unity power factor is achieved. Grid current  $i_{ag}$  has good current quality in both topologies, as is obvious from Figs. 5.51b and 5.52b that show its spectrum. Low-order harmonics that are controlled have values less than 1% of the fundamental. Spectrum of Fig. 5.52b shows significant 17<sup>th</sup> harmonic; this is a consequence of the fact that only the first 15 harmonics are controlled. Finally, grid components that are controlled are shown in Figs. 5.51c and 5.52c. The fact that the  $q$ -component is kept at zero reconfirms unity power factor operation. The  $d$ -component follows its reference without a steady-state error. This component does not contain second harmonic which means that the three grid currents have the same rms values; this validates the control part that deals with asymmetry (Fig. 5.13).

All three grid currents are shown in Figs. 5.53a and 5.54a, for the two topologies. A difference between switching ripples of the three phases is obvious. This originates from the difference in equivalent scheme parameters for these phases, as can be seen from Fig. 5.11, and is explained in section 5.2.3.2. Clearly, the asymmetry is more pronounced in Fig. 5.53a for the case of the asymmetrical six-phase machine, with the reason explained in the next two paragraphs. On the other hand, although the asymmetry of the equivalent parameters exists, it is obvious from Figs. 5.53a and 5.54a that these three currents have the same fundamental rms values, which again verifies asymmetry control part of the algorithm. Spectra of grid currents  $i_{bg}$  and  $i_{cg}$  are shown in Figs. 5.53b, 5.53c and 5.54b, 5.54c, and they show that low-order harmonics have again very low values. Phases  $b$  and  $c$  in the case of the symmetrical six-phase machine have once more a high 17<sup>th</sup> harmonic. Thus the difference for both configurations exists only in the switching ripple, whose detailed analysis is provided below.

In the case of asymmetrical six-phase topology, the high switching ripple occurs due to the low machine inductance in the second ( $x$ - $y$ ) plane, and, as shown in (3.89), a part of currents flows through this plane. Specifics of the machine design indicate that this inductance is more than ten times lower than the corresponding inductance in the first ( $\alpha$ - $\beta$ ) plane. This is particularly useful to demonstrate the rotor effect on the equivalent scheme parameters. As explained in section 5.2.3.2 the pulsating field has the lowest effect on phase  $b$  since the machine phases that are connected to this grid phase are shifted from the field by the highest angle (75 degrees). Thus this phase almost completely relies on stator parameters, which are very low in the  $x$ - $y$  plane and lead to very high current ripple as a consequence. The rotor effect on grid phase  $c$  is greater than on the phase  $b$  since the spatial shift from the direction of the field pulsation is lower (45 degrees), and this is why it has a lower ripple. Finally, grid phase  $a$  is influenced the most by the rotor since the machine phases that are connected to it lie almost on the direction of the pulsating field (they are shifted from it by 15 degrees). Since the rotor leakage inductance is much higher than the stator leakage inductance in the  $x$ - $y$  plane, this current has by far the smallest ripple among the phases.

In the case of the symmetrical six-phase machine the reason for the high switching ripple is the low machine stator leakage inductance (see Appendix). The spatial shift of phases  $a$  and  $c$  from the direction of the pulsating field is now the same and equal to 30 degrees. Therefore, the pulsating field equally affects phases  $a$  and  $c$ , and they have switching ripples similar to each other. Only the ripple of phase  $b$  differs since it is spatially shifted from the direction of the field by 90 degrees. Therefore, it is not affected by the pulsating field.

It can be concluded that the usage of the asymmetrical six-phase machine with very low inductance in  $x$ - $y$  plane is very useful in order to demonstrate the rotor effect on the switching ripple. Although this phenomenon would also appear in a hypothetical asymmetrical six-phase machine, which were to have the same inductance in the two

planes, its effect would be much lower and hard to notice. It would be similar to the one of the symmetrical six-phase machine. That would typically mean that this interesting phenomenon would be negligible. It is very important to emphasize here that in six-phase machines with standard values of stator leakage inductance, and in which stator windings of different phases do not share the same stator slot, current switching ripple would be much lower, and similar to those of all the other charging topologies considered so far. Therefore, the high ripple is not a consequence of the charger topology, but of specifics of the design of the two six-phase machines.

Figs. 5.55a and 5.56a show grid phase voltage  $v_{ag}$ , machine currents  $i_{a1}$ ,  $i_{a2}$  (placed on top of each other), and battery charging current  $i_L$ . It can be seen that the two machine currents are identical. Spectrum of one of these two currents is given in Figs. 5.55b and 5.56b, and, if compared to spectrum of grid current  $i_{ag}$  (Figs. 5.51a and 5.52a), a great similarity can be noticed. Naturally, the grid current amplitude is two times greater than the phase current of the machine, as it represents their sum. For the asymmetrical and symmetrical topology, the battery charging current  $i_L$  has a dc value of 0.9A and 1.1A, respectively. However, from Figs. 5.55 and 5.56 it can be seen that it contains a small second (Fig. 5.55) and fourth harmonic (Fig. 5.56). This was also noticed and explained in simulations performed in [Subotic et al (2014a)]. The reason of the existence of this is that power that is lost on the filter (i.e. machine) is time dependant due to asymmetry of equivalent machine parameters. Thus, it is the highest when absolute value of the current that flows in the phase with the greatest impedance (phase  $a$ ) is highest. Since the power that is taken from the grid is constant, the battery charging current  $i_L$  has the minimum when absolute value of the grid current  $i_{ag}$  has the maximum – as is evident from Figs. 5.55a and 5.56a.

Machine current components are shown in Figs. 5.57 and 5.58. It can be seen that there is excitation in the torque producing ( $\alpha$ - $\beta$ ) plane. However, for both topologies both components in this plane vary at the same rate (i.e. they are proportional to each other), meaning that the excitation is in only one direction. This leads to a pulsating field production which is not capable of making a starting torque. The excitation in  $x$ - $y$  plane is also in one direction only and is in accordance with (3.89) and (3.87).

In order to achieve V2G operation, the control in CC mode does not have to be altered. Only the reference for the  $d$ -current component has to have negative sign. For the asymmetrical and symmetrical six-phase topology it is set to  $i_d^* = -1A$  and  $-2A$ , respectively.

In Figs. 5.59a and 5.60a grid phase voltage  $v_{ag}$  and grid current  $i_{ag}$  are given. It can be seen that the current is in phase opposition with the voltage. Thus the unity power factor is achieved in this mode as well. From the spectrum of the grid current  $i_{ag}$  presented in Figs. 5.59b and 5.60b it can be seen that controlled low-order harmonics (up to the fifteenth) have small values. If compared with Figs. 5.51b and 5.52b it can be seen that these are very similar. They slightly differ in the case of the asymmetrical six-phase machine but only in terms of relative values with respect to the fundamental – their absolute values are approximately the same. Grid current components are shown in Figs. 5.59c and 5.60c. The  $q$ -component is again kept at zero in order to obtain unity power factor operation. The  $d$ -component follows the reference in this mode as well, and again it does not contain the second harmonic, which is an indication of the balance between grid currents.

Figs. 5.61a and 5.62a show grid phase voltage  $v_{ag}$ , two machine currents  $i_{a1}$  and  $i_{a2}$  that constitute grid phase  $a$  current, and battery charging current  $i_L$ . It can be seen that these currents are in phase with the voltage, and equally share the grid current. Spectrum of one of these two currents is given in Fig. 5.61b, from which a great similarity with spectrum of grid current  $i_{ag}$  in Figs. 5.59b and 5.60b is obvious. Battery charging current now has the negative sign. Still, it contains the second (Fig. 5.61a) and the fourth harmonic (Fig. 5.62a), with the reason being explained in the previous subsection. However, the battery charging current  $i_L$  has a greatest absolute value in instants when grid current that goes through a phase with the highest impedance (phase  $a$ ) is at its positive or negative peak. In these instants losses are the greatest, thus the battery has to provide a higher power in order to inject the same energy into the grid.

For this mode of operation machine current components are shown in Figs. 5.63 and 5.64. Again, there is only unidirectional excitation, which is valid for both planes. If compared to excitation in the charging mode it can be seen that the components are in phase opposition with those from Figs. 5.57 and 5.58.

Finally, for the asymmetrical and symmetrical six-phase topology a transient from V2G into the charging mode is performed by setting the reference to  $i_d^* = 1A$  and  $2A$ , respectively. Waveforms of the grid phase voltage  $v_{ag}$ , grid current  $i_{ag}$  and battery charging current  $i_L$  during the transient are shown in Figs. 5.65a and 5.66a. Good transient response is obvious. After receiving a new reference value, grid current  $i_{ag}$  quickly changes the phase in order to maintain unity power factor in the charging mode. It can be seen that the battery charging current again contains the second (Fig. 5.65a) and the fourth harmonic (Fig. 5.66a) in both modes, which is in Fig. 5.65a more pronounced due to a changed oscilloscope scale. Although the power that is taken from or injected into the grid is the same for both modes, it can be seen that the battery charging current  $i_L$  is by absolute value lower in the charging mode. The reason for this has already been explained in conjunction with the discussion of the previous topologies. Grid current components during the transient are given in Figs. 5.65b and 5.66b, and it can be seen that the  $d$ -component follows the reference well. The  $q$ -component does not deviate from zero during the whole transient in order to keep unity power operation.

The final three-phase charging/V2G topology considered here is the one utilising a five-phase machine (Fig. 3.11). Unlike the other considered topologies it has an advantage that EMI (electro-magnetic interference) filter, which

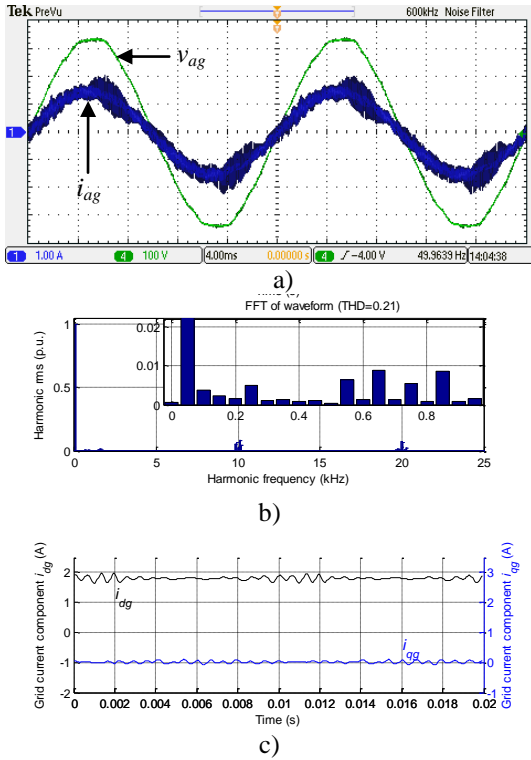


**Fig. 5.51:** a) Grid phase voltage  $v_{ag}$ , grid current  $i_{ag}$ , b) spectrum of grid current  $i_{ag}$ , c) grid current components  $i_{dg}$  and  $i_{qg}$ .

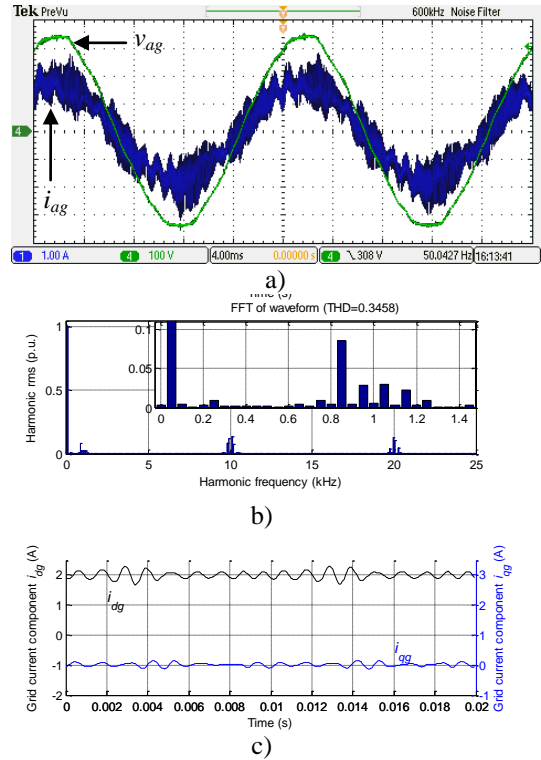


**Fig. 5.52:** a) Grid phase voltage  $v_{ag}$ , grid current  $i_{ag}$ , b) spectrum of grid current  $i_{ag}$ , c) grid current components  $i_{dg}$  and  $i_{qg}$ .

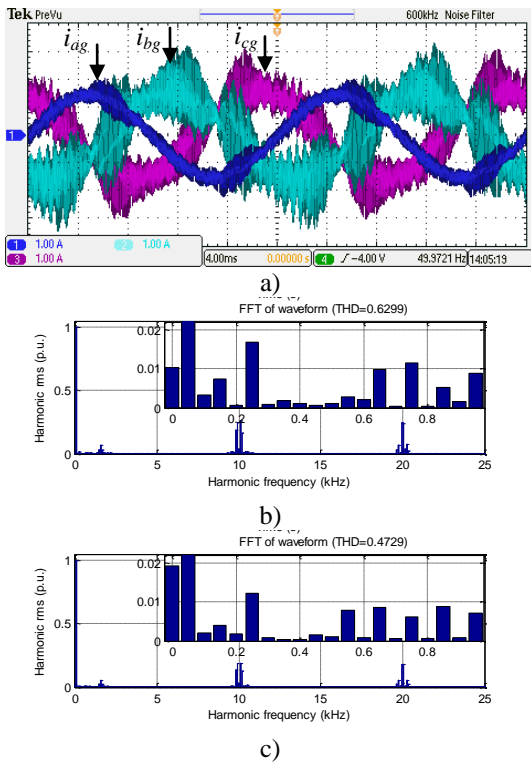


**Fig. 5.53:** a) Grid currents  $i_{ag}$ ,  $i_{bg}$  and  $i_{cg}$ , b) spectrum of grid current  $i_{bg}$ , c) spectrum of grid current  $i_{cg}$ .

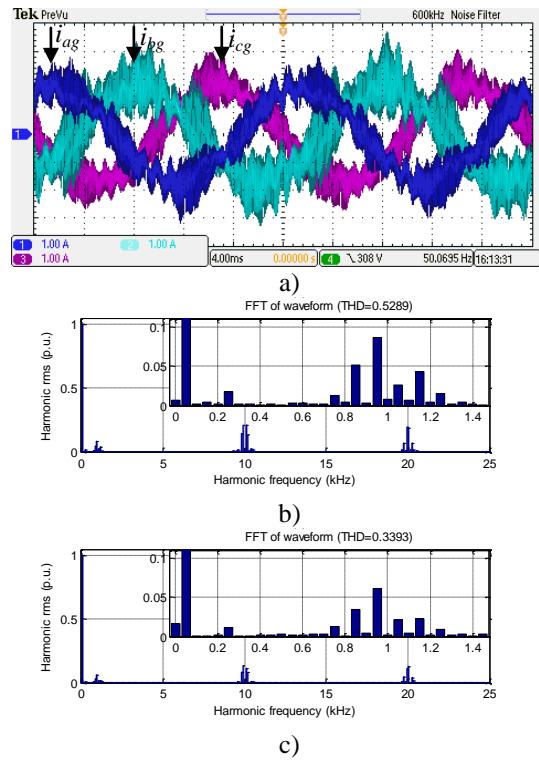


**Fig. 5.54:** a) Grid currents  $i_{ag}$ ,  $i_{bg}$  and  $i_{cg}$ , b) spectrum of grid current  $i_{bg}$ , c) spectrum of grid current  $i_{cg}$ .

can exist between the grid and the machine, does not influence the propulsion mode of operation, since in this mode it is short-circuited by two switches, used for hardware reconfiguration. In the experiment the EMI filter is not used, thus all the filtering is performed by the machine windings. Reference for the  $d$  current component is set to 2A, which

corresponds, due to the power invariant three-phase decoupling matrix, to the grid current rms value of 1.15A. The dc-bus voltage is 720V.

Grid phase voltage  $v_{ag}$  and three grid currents are shown in Fig. 5.67a. Unity power factor operation is obvious. Similarly as for the last two considered topologies, it can be noticed that grid current ripple is not the same among the phases, and it is the highest in grid phase  $b$ . The reason is again the same. However, although parameter asymmetry exists it can be seen that grid currents have once more the same fundamental amplitudes, which verifies the “asymmetry control” block in Fig. 5.13. Spectra of the grid currents  $i_{ag}$ ,  $i_{bg}$  and  $i_{cg}$  are shown in Fig. 5.67b, Fig. 5.67c and Fig. 5.67d, and they show good current quality. However, it can be seen that THD is the highest in phase  $b$ , as it has the lowest equivalent impedance.

Grid current components are shown in Fig. 5.68. The  $q$ -component is kept at zero, while the  $d$ -component follows the reference without a steady state error. It can be seen that it does not contain the second harmonic, which again validates the asymmetry control part of Fig. 5.13.

Machine currents  $i_b$  and  $i_e$  are separately shown in Fig. 5.69a, together with the grid phase voltage  $v_{ag}$  and battery charging current  $i_L$ . These two currents are close to being completely identical, and, since they appear on top of each other, they look like a single trace. Spectrum of one of these two currents is shown in Fig. 5.69b. If compared to Fig. 5.67c the similarity is obvious, which is to be expected, since these two machine currents constitute the grid current  $i_{bg}$ .

Machine current components are shown in Fig. 5.70. In the torque producing ( $\alpha$ - $\beta$ ) plane only  $\alpha$  component is excited, thus the field is pulsating and the starting torque cannot be produced. The  $x$ - $y$  plane also has only one direction of excitation and it is in the direction of the  $x$ -component, which is in accordance with (3.92). V2G mode is obtained by setting the reference to  $i_d^* = -2A$ . Grid phase voltage  $v_{ag}$ , and three grid currents are for this mode of operation shown in Fig. 5.71a. Grid current  $i_{ag}$  is in phase opposition with the voltage, thus unity power factor is again achieved. The currents again have the same amplitudes. The spectrum of the current  $i_{cg}$  is shown in Fig. 5.71b.

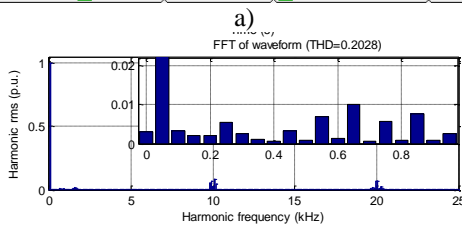
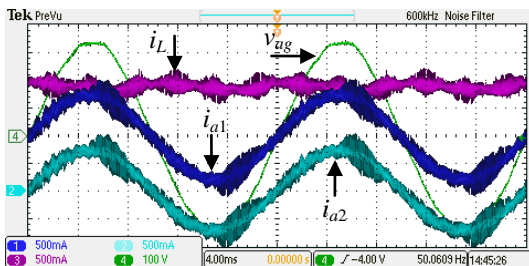


**Fig. 5.55:** a) Grid phase voltage  $v_{ag}$ , machine currents  $i_{a1}$ ,  $i_{a2}$  and battery charging current  $i_L$ , b) spectrum of grid current  $i_{a1}$ .

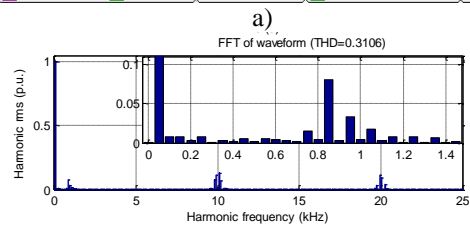
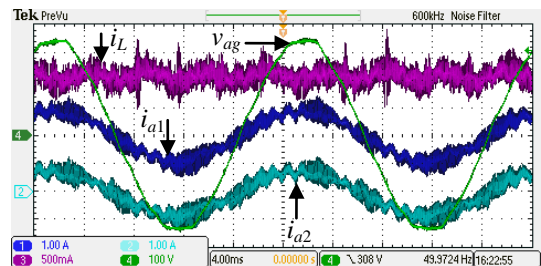


**Fig. 5.56:** a) Grid phase voltage  $v_{ag}$ , machine currents  $i_{a1}$ ,  $i_{a2}$  and battery charging current  $i_L$ , b) spectrum of grid current  $i_{a1}$ .

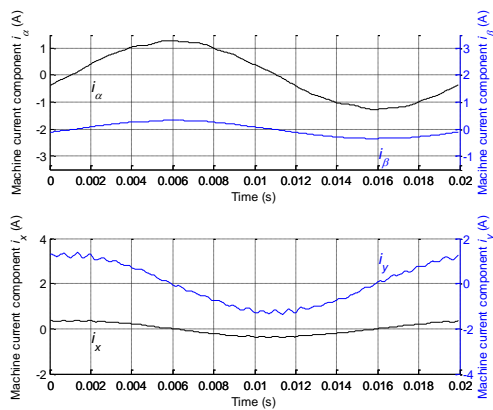


**Fig. 5.57:** Machine current components in the first ( $\alpha$ - $\beta$ ) and the second ( $x$ - $y$ ) plane.

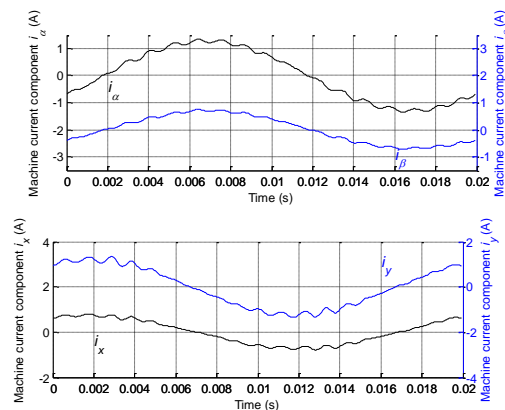


**Fig. 5.58:** Machine current components in the first ( $\alpha$ - $\beta$ ) and the second ( $x$ - $y$ ) plane.

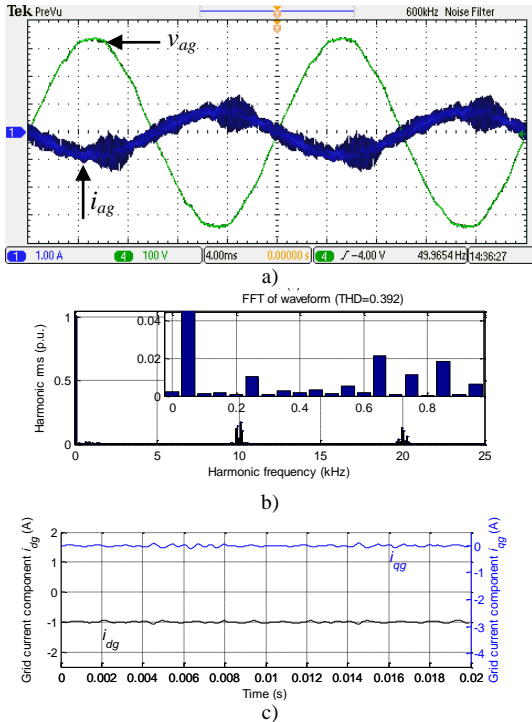


**Fig. 5.59:** a) Grid phase voltage  $v_{ag}$ , grid current  $i_{ag}$ , b) spectrum of grid current  $i_{ag}$ , c) grid current components  $i_{dg}$  and  $i_{qg}$ .

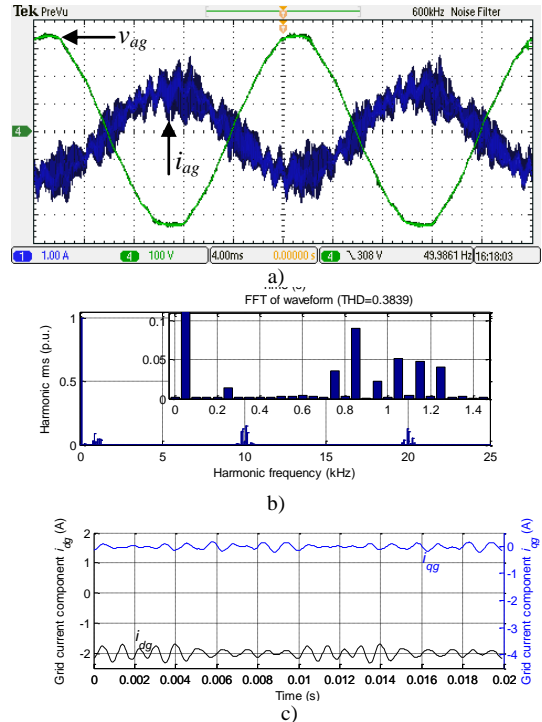


**Fig. 5.60:** a) Grid phase voltage  $v_{ag}$ , grid current  $i_{ag}$ , b) spectrum of grid current  $i_{ag}$ , c) grid current components  $i_{dg}$  and  $i_{qg}$ .

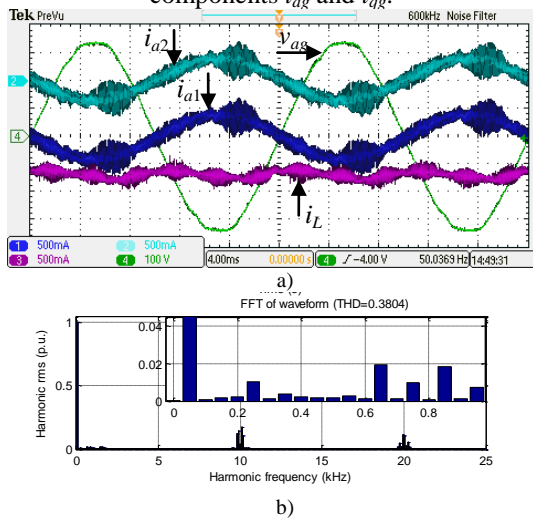


**Fig. 5.61:** a) Grid phase voltage  $v_{ag}$ , machine currents  $i_{a1}$ ,  $i_{a2}$  and battery charging current  $i_L$ , b) spectrum of grid current  $i_{a1}$ .

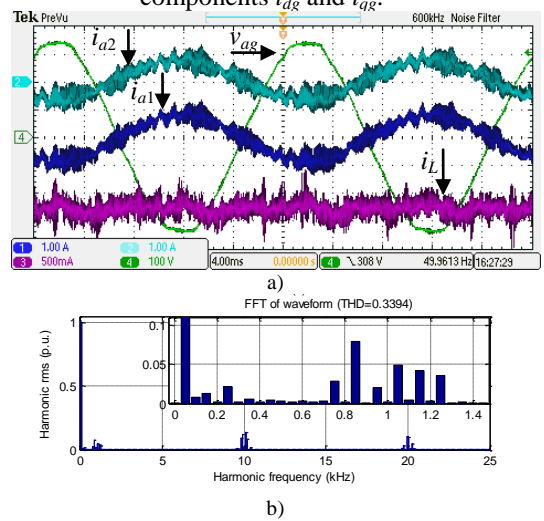


**Fig. 5.62:** a) Grid phase voltage  $v_{ag}$ , machine currents  $i_{a1}$ ,  $i_{a2}$  and battery charging current  $i_L$ , b) spectrum of grid current  $i_{a1}$ .

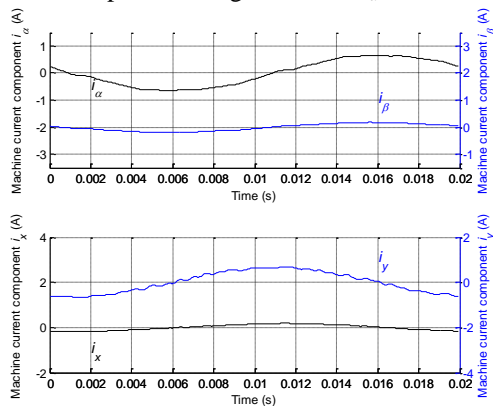


**Fig. 5.63:** Machine current components.

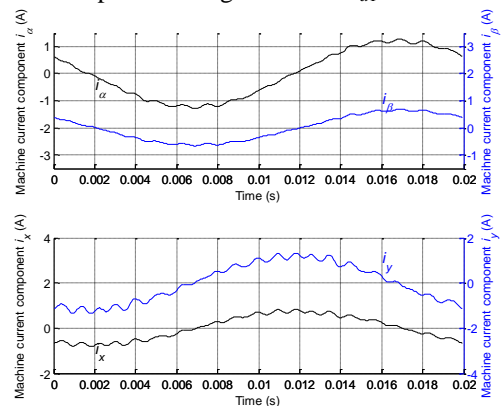


**Fig. 5.64:** Machine current components.

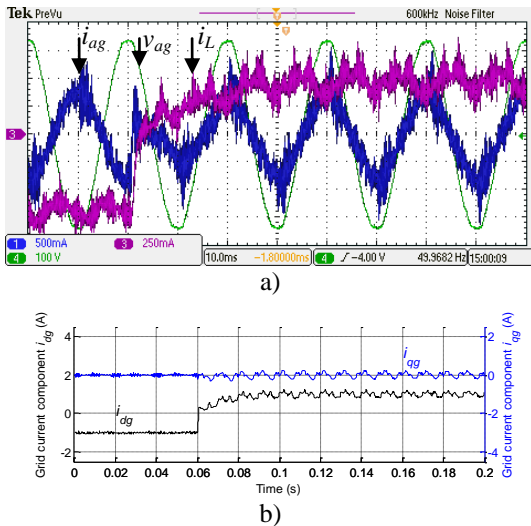


Fig. 5.65: a) Grid phase voltage  $v_{ag}$ , grid currents  $i_{ag}$ , and battery charging current  $i_L$ , b) grid current components  $i_{dg}$ , and  $i_{qg}$ .

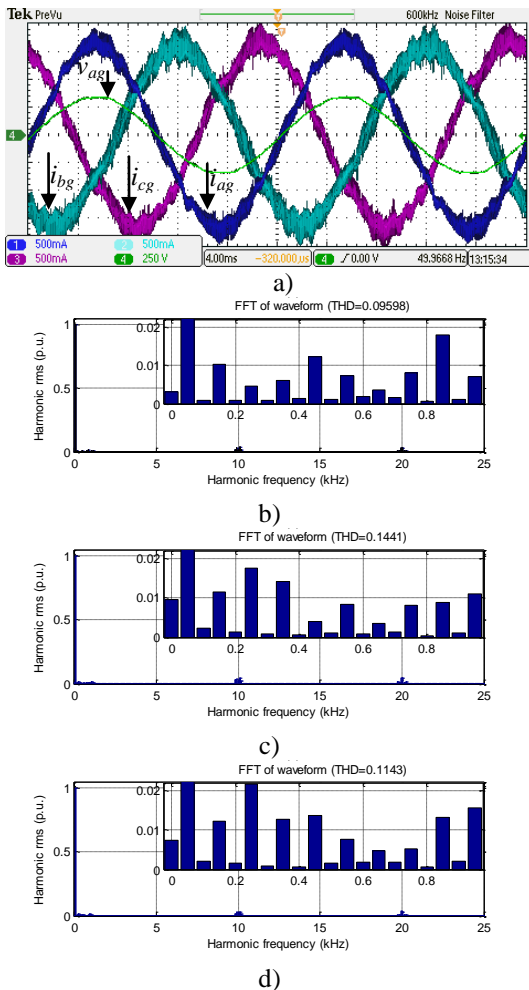


Fig. 5.67: a) Grid phase voltage  $v_{ag}$ , grid currents  $i_{ag}$ ,  $i_{bg}$ ,  $i_{cg}$ , b) spectrum of grid current  $i_{ag}$ , c) spectrum of grid current  $i_{bg}$ , d) spectrum of grid current  $i_{cg}$ .

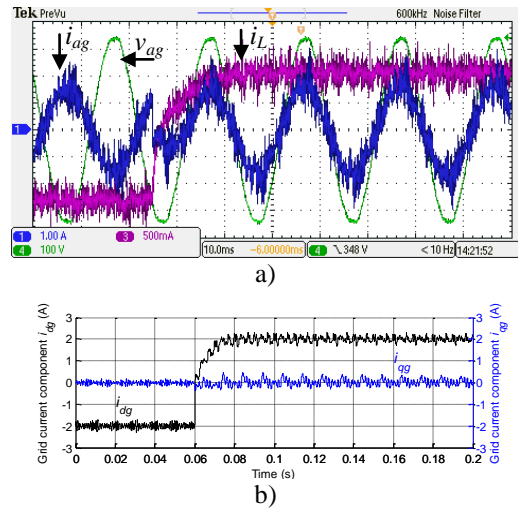


Fig. 5.66: a) Grid phase voltage  $v_{ag}$ , grid currents  $i_{ag}$ , and battery charging current  $i_L$ , b) grid current components  $i_{dg}$ , and  $i_{qg}$ .

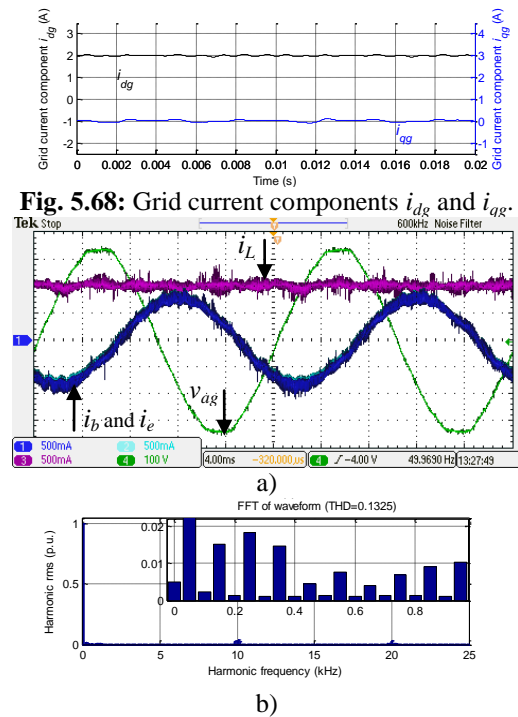


Fig. 5.69: a) Grid voltage  $v_{ag}$ , machine currents  $i_b$  and  $i_e$ , battery charging current  $i_L$ , b) spectrum of machine current  $i_b$ .

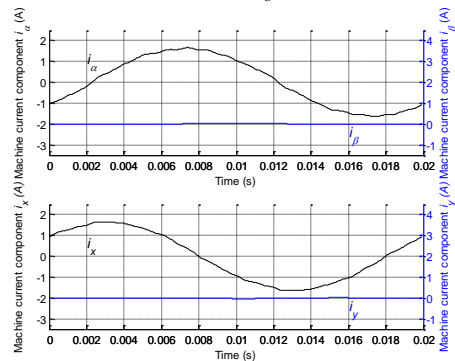


Fig. 5.70: Machine current components in the first ( $\alpha$ - $\beta$ ) and the second plane ( $x$ - $y$ ).

Machine currents  $i_c$  and  $i_d$  that constitute the grid current  $i_{cg}$  are shown in Fig. 5.72, together with the grid phase voltage  $v_{ag}$  and battery charging current  $i_L$ . Similar to the machine currents  $i_b$  and  $i_e$ , these two currents are mutually indistinguishable and appear as a single trace. Spectrum of one of these two currents is shown in Fig. 5.73 and it shows great similarity with Fig. 5.71b. Battery charging current is, like in the charging mode, a dc quantity. However, if compared to Fig. 5.69a it can be seen that it has a higher absolute value, the reason being once more the same as for the previous topologies.

By stepping the  $d$  current component reference to 2A the transient from V2G into the charging mode is achieved. Fig. 5.74a shows grid phase voltage  $v_{ag}$ , grid current  $i_{ag}$  and battery charging current  $i_L$  during this transient. Fast transient response is obvious. From Fig. 5.74b it can be seen that while the  $d$  current component follows the reference well, the  $q$ -component is kept at zero during the whole transient. As a consequence the field in the machine pulsates in the same direction, so that the machine does not have to be mechanically locked even in transient.

It should be again noted that in all experiments resolver readings proved that the rotor does not move in either mode (multiphase, single-phase or three-phase; charging, V2G or transient). These traces are omitted since the readings were very uniform and did not deviate from zero.

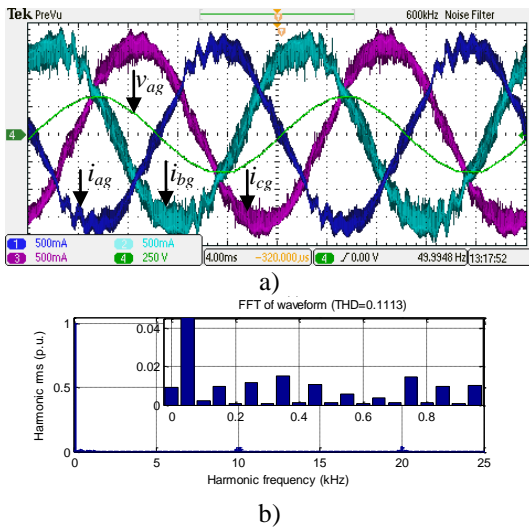


Fig. 5.71: a) Grid phase voltage  $v_{ag}$ , grid currents  $i_{ag}$ ,  $i_{bg}$ ,  $i_{cg}$ , b) spectrum of grid current  $i_{cg}$ .

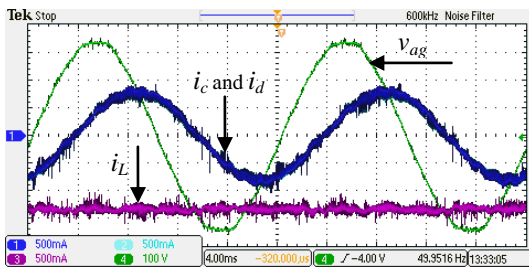


Fig. 5.72: Grid voltage  $v_{ag}$ , machine currents  $i_c$  and  $i_d$ , battery charging current  $i_L$ .

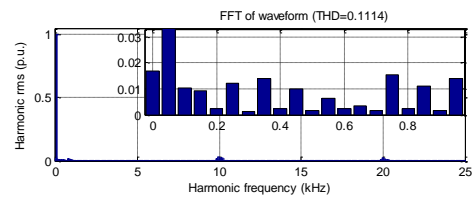


Fig. 5.73: Spectrum of the machine current  $i_c$ .

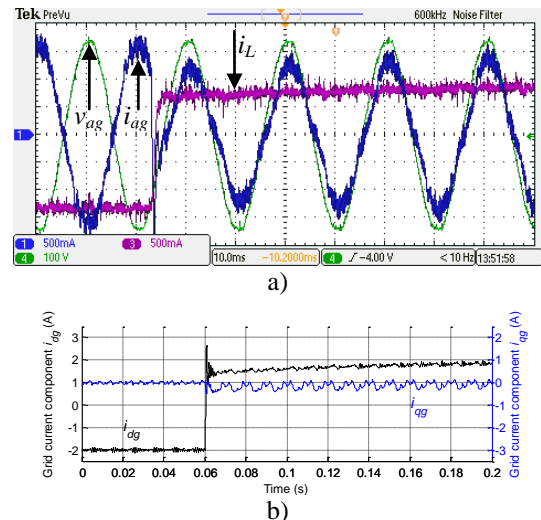


Fig. 5.74: a) Grid voltage  $v_{ag}$ , grid current  $i_{ag}$  and battery charging current  $i_L$ , b) grid current components  $i_{dg}$  and  $i_{qg}$ .

### 5.4 Conclusion

Control and performance analysis of charging/V2G topologies introduced in Chapter 3 is elaborated in this chapter. Control algorithms leading to the unity power factor operation are developed for the three types of voltage supply. For each supply type current control is considered separately for topologies in which there is no field production in the machine rotor and in which the field appears. For all topologies conducted experiments show good performance in both charging and V2G mode. They also represent good verification of operating principles that were introduced in Chapter 3, on a theoretical level. Moreover, in the experiments, common features of all topologies are that they operate with unity power factor, and that the first fifteen harmonics are controlled. Continuous speed measurement readings proved that machines' rotors do not move in any of the topologies and in any of the operating modes. Therefore, mechanical locking is not required, as predicted in Chapter 3.

## CHAPTER 6: PROPULSION MODE OF OPERATION

### 6.1 Introduction

In the previous chapter control and experimental results were presented for a multitude of charging configurations employing multiphase machines. The charging experiments are preformed incorporating the following four machine types: asymmetrical nine-phase, asymmetrical and symmetrical six-phase, and five-phase machine. All the utilised machines are induction motors. This chapter deals with the propulsion mode of operation for the same four machine types. In the next section control for each machine is developed, while the subsequent one offers experimental results obtained using these control algorithms.

### 6.2 Control

Control of multiphase machines in propulsion mode of operation has reached a mature stage. Field oriented control (FOC) algorithm for multiphase machines is detailed in [Levi et al (2007)], where a detailed analysis of the operating principles is provided. It is illustrated schematically in Fig. 6.1 and a great similarity with the standard three-phase FOC algorithm is obvious. However, there are three important differences. To start with, in the case of a machine with more than one isolated neutral point, zero-sequence injection used in the PWM unit has to be applied to each subset of phases separately. A subset of phases is determined by all machine phases connected to the same isolated neutral point. The second difference is that block “coordinate transformation” has multiphase rather than three-phase form. This includes decoupling and rotational transformation. The multiphase form of the decoupling transformation varies depending on the type of the machine’s stator winding. In the case of an asymmetrical nine-phase machine with three-isolated neutral points it is given with

$$[C] = \sqrt{\frac{2}{9}} \begin{bmatrix} a_1 & a_2 & a_3 & b_1 & b_2 & b_3 & c_1 & c_2 & c_3 \\ \alpha & 1 & \cos(\alpha) & \cos(2\alpha) & \cos(6\alpha) & \cos(7\alpha) & \cos(8\alpha) & \cos(12\alpha) & \cos(13\alpha) & \cos(14\alpha) \\ \beta & 0 & \sin(\alpha) & \sin(2\alpha) & \sin(6\alpha) & \sin(7\alpha) & \sin(8\alpha) & \sin(12\alpha) & \sin(13\alpha) & \sin(14\alpha) \\ x_1 & 1 & \cos(5\alpha) & \cos(10\alpha) & \cos(12\alpha) & \cos(17\alpha) & \cos(4\alpha) & \cos(6\alpha) & \cos(11\alpha) & \cos(16\alpha) \\ y_1 & 0 & \sin(5\alpha) & \sin(10\alpha) & \sin(12\alpha) & \sin(17\alpha) & \sin(4\alpha) & \sin(6\alpha) & \sin(11\alpha) & \sin(16\alpha) \\ x_2 & 1 & \cos(7\alpha) & \cos(14\alpha) & \cos(6\alpha) & \cos(13\alpha) & \cos(2\alpha) & \cos(12\alpha) & \cos(\alpha) & \cos(8\alpha) \\ y_2 & 0 & \sin(7\alpha) & \sin(14\alpha) & \sin(6\alpha) & \sin(13\alpha) & \sin(2\alpha) & \sin(12\alpha) & \sin(\alpha) & \sin(8\alpha) \\ 0_1 & \sqrt{3/2} & 0 & 0 & \sqrt{3/2} & 0 & 0 & \sqrt{3/2} & 0 & 0 \\ 0_2 & 0 & \sqrt{3/2} & 0 & 0 & \sqrt{3/2} & 0 & 0 & \sqrt{3/2} & 0 \\ 0_3 & 0 & 0 & \sqrt{3/2} & 0 & 0 & \sqrt{3/2} & 0 & 0 & \sqrt{3/2} \end{bmatrix} \quad (6.1)$$

where  $\alpha = \pi/9$ . For asymmetrical and symmetrical six-phase machines it is determined by (3.20) and

$$[C] = \sqrt{\frac{2}{6}} \begin{bmatrix} a_1 & b_1 & c_1 & a_2 & b_2 & c_2 \\ \alpha & 1 & \cos(2\pi/3) & \cos(4\pi/3) & \cos(\pi/3) & \cos(3\pi/3) & \cos(5\pi/3) \\ \beta & 0 & \sin(2\pi/3) & \sin(4\pi/3) & \sin(\pi/3) & \sin(3\pi/3) & \sin(5\pi/3) \\ x & 1 & \cos(4\pi/3) & \cos(8\pi/3) & \cos(2\pi/3) & \cos(6\pi/3) & \cos(10\pi/3) \\ y & 0 & \sin(4\pi/3) & \sin(8\pi/3) & \sin(2\pi/3) & \sin(6\pi/3) & \sin(10\pi/3) \\ 0_+ & 1 & 1 & 1 & 0 & 0 & 0 \\ 0_- & 0 & 0 & 0 & 1 & 1 & 1 \end{bmatrix} \quad (6.2)$$

respectively, while in the case of a five-phase machine it is governed by (3.2). The rotational transformation also differs. Although it can be used to transform only variables of the first ( $\alpha$ - $\beta$ ) plane into the rotating field oriented reference frame, multiphase machines, in general, require rotating transformation of variables of other planes as well, for the purposes of the current control. Their forms are discussed for each machine individually in what follows. Finally, the third difference is in the block “current controllers”, where one now has to control more than two variables. This block is also considered separately for each stator winding type in what follows.

Schematic representation of a general “current controllers” block, which can be used for control of all four stator winding types considered here, is presented in Fig. 6.2. Similarly as for the charging process, fundamental is controlled by PI controllers with a decoupling network, and this is the same feature for all multiphase machines. It can be seen that the fundamental control is the same as for a three-phase machine, and that the current components obtained from measurements are subtracted from their references (in contrast to the situation in the charging mode). Although control of the current fundamental is the same for three-phase and all multiphase machines, the control of low-order harmonics, caused here by the inverter dead-time effect, differs from three-phase systems, and significantly varies

between multiphase machines with different number of phases. Thus in what follows the focus is on the control of low-order (dead-time) harmonics that will appear in planes other than the first.

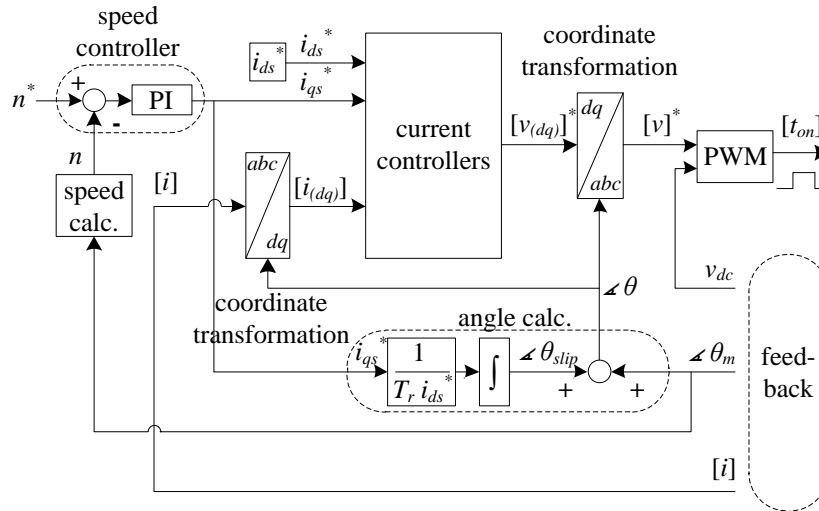


Fig. 6.1: RFOC control algorithm for multiphase machines

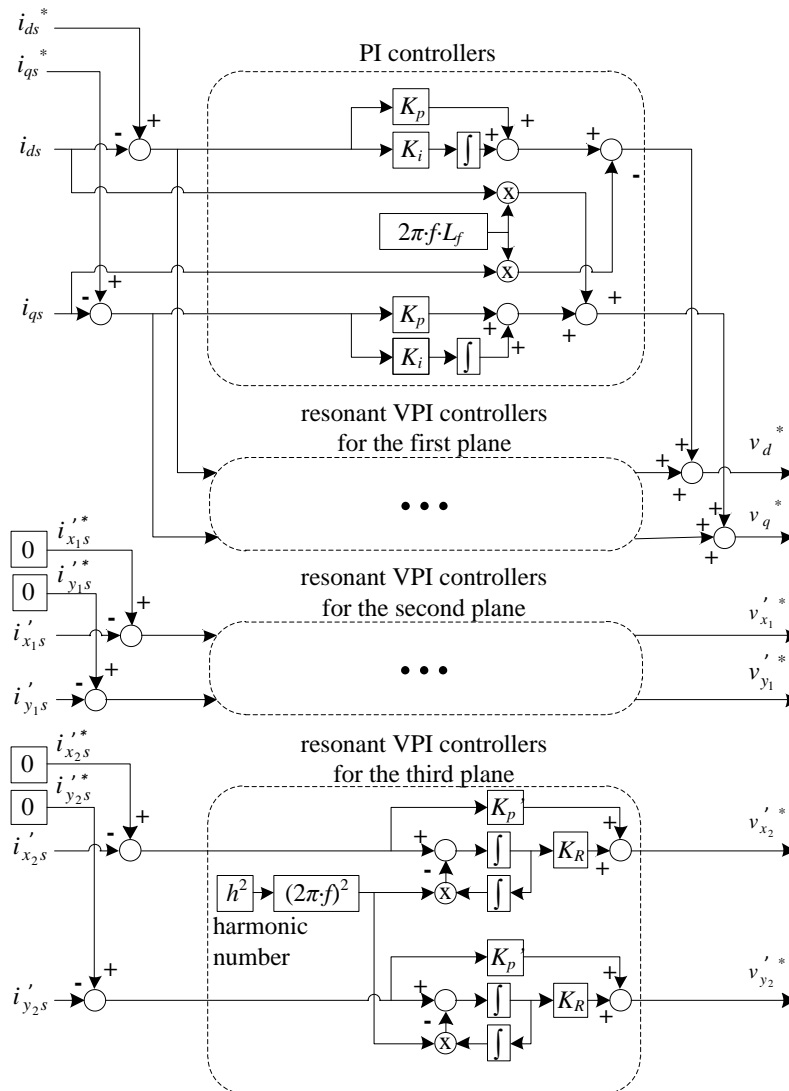


Fig. 6.2: Current controllers for propulsion mode of operation. Index  $s$  in stator current component symbols is omitted further on, for simplicity.

The discussion of the current control of low-order harmonics commences here with an asymmetrical nine-phase machine with three isolated neutral points. The dead-time harmonics are spread across three planes ( $\alpha\text{-}\beta$ ,  $x_1\text{-}y_1$  and  $x_2\text{-}y_2$ ) and three zero-sequence axes. However, zero-sequence harmonics cannot flow due to the isolated neutral points, thus only the control of dead-time harmonics of the three planes is required. The dominant dead-time harmonics are the 5<sup>th</sup>, 7<sup>th</sup>, -11<sup>th</sup> and -13<sup>th</sup>. The minus sign signifies anti-synchronous direction of rotation. Note the important difference regarding the direction of rotation of the harmonics in the asymmetrical nine-phase system and the three-phase system. These harmonics map into machine planes according to the following rules: the 5<sup>th</sup> and -13<sup>th</sup> map into the second ( $x_1\text{-}y_1$ ) plane, and the 7<sup>th</sup> and -11<sup>th</sup> map into the third ( $x_2\text{-}y_2$ ) plane. It was shown in Chapter 5 how a single pair of resonant controllers can control two harmonics in two axes. In order to achieve the same in the propulsion mode, performing a rotational transformation for the variables of the  $x\text{-}y$  planes has to be considered. It should be noted that this was already done in the charging mode in case of a supply from a multiphase voltage source (section 5.2.1.1), where the rotation of the  $x'\text{-}y'$  plane at the synchronous speed and anti-synchronous direction was performed. In propulsion mode, in this particular case, the  $x_1'\text{-}y_1'$  plane has to rotate in the anti-synchronous direction, but now at the speed four times greater than synchronous. From the reference frame that rotates at this speed and direction the 5<sup>th</sup> and the -13<sup>th</sup> harmonic are seen as the 9<sup>th</sup> and -9<sup>th</sup>, respectively. Hence both can be controlled with a single VPI controller in the same manner in which it was done for the charging/V2G mode. The resonant VPI controller is tuned for the 9<sup>th</sup> harmonic. Similarly, the harmonics of the third plane can be controlled in the reference frame that rotates at twice the synchronous speed in the opposite direction. Then the 7<sup>th</sup> and -11<sup>th</sup> harmonics (in the stationary reference frame) are seen as 9<sup>th</sup> and -9<sup>th</sup>, and again they can be controlled with VPI controller with the resonant frequency nine times the synchronous. Thus, only two pairs of resonant VPI controllers are necessary, both tuned for the 9<sup>th</sup> harmonics, and the one in the first plane in Fig. 6.2 is not required.

If an asymmetrical six-phase machine with two isolated neutral points is considered, there are only two planes. Dominant dead-time harmonics are the 5<sup>th</sup>, -7<sup>th</sup>, -11<sup>th</sup> and 13<sup>th</sup> (as seen from the stationary reference frame). The -11<sup>th</sup> and 13<sup>th</sup> map into the first plane. Since it rotates at synchronous speed they are seen from this reference frame as -12<sup>th</sup> and 12<sup>th</sup>, respectively. Thus both can be controlled with a resonant VPI controller tuned at 12<sup>th</sup> harmonic, placed in the first plane (Fig. 6.2). It is very important to note that the input of this controller is not the difference between the reference for the 12<sup>th</sup> current harmonic (which is zero) and the measured  $d$  current component; instead it is the difference between the same zero reference and the difference between the real  $d$ -component and the reference for the fundamental (Fig. 6.2). Unlike the -11<sup>th</sup> and 13<sup>th</sup> harmonic, the 5<sup>th</sup> and -7<sup>th</sup> harmonic (seen from the stationary reference frame) map into the second plane. The second plane needs to rotate at synchronous speed in anti-synchronous direction in order for them to be seen as the 6<sup>th</sup> and -6<sup>th</sup> harmonic. Both can now be controlled with a resonant VPI controller tuned at the 6<sup>th</sup> harmonic. In this case, and in both cases that follow, the controller in the third plane in Fig. 6.2 is not required, since there are only two planes.

Unlike in the asymmetrical six-phase machine, in symmetrical six-phase machine all dominant dead-time harmonics map into the first plane. These are the -5<sup>th</sup>, 7<sup>th</sup>, -11<sup>th</sup> and 13<sup>th</sup>. From the first plane they are seen as -6<sup>th</sup>, 6<sup>th</sup>, -12<sup>th</sup> and 12<sup>th</sup>. Thus all four harmonics can be controlled with two pairs of resonant VPI current controllers tuned at the 6<sup>th</sup> and 12<sup>th</sup> harmonic. The controllers in the second and third plane in Fig. 6.2 are not required.

In the case of a five-phase machine the -9<sup>th</sup> and 11<sup>th</sup> dead-time harmonics map into the first plane, while the -3<sup>rd</sup>, 7<sup>th</sup>, -13<sup>th</sup> and 17<sup>th</sup> map into the second. From the first plane the -9<sup>th</sup> and 11<sup>th</sup> harmonic are seen as the -10<sup>th</sup> and 10<sup>th</sup>, so that they can be controlled by a pair of resonant VPI controllers tuned at the 10<sup>th</sup> harmonic. The speed of rotation of the second plane is chosen as twice the synchronous in order for the -3<sup>rd</sup>, 7<sup>th</sup>, -13<sup>th</sup> and 17<sup>th</sup> harmonics (as seen from the stationary reference frame) to be seen as the -5<sup>th</sup>, 5<sup>th</sup>, -15<sup>th</sup> and 15<sup>th</sup>. Now, these harmonics can be zeroed by two pairs of resonant VPI controllers tuned at the 5<sup>th</sup> and the 15<sup>th</sup> harmonic. If the control of higher order harmonics is not of particular interest, the one tuned at the 15<sup>th</sup> harmonic can be omitted.

In order to provide clarity as well as a quick reference the current control techniques for the four considered stator winding types are summarised in the Table 6.1.

### 6.3 Experimental results

Experiments in propulsion mode of operation are conducted for all four considered machines and the results are reported in this section. In the case of the asymmetrical nine-phase machine simple removal of grid connections is sufficient for the drive to be ready for the propulsion mode of operation. The other three machines require hardware reconfiguration. When it is performed, the drives operate according to the control algorithms given in Figs. 6.1 and 6.2. Rotor position is in the case of the nine-phase machine obtained by an encoder, while in the others a resolver is utilised.

Since a dc-dc converter typically exists between the battery and the inverter but is not used in the laboratory set-up, different values of the dc-bus voltage are considered for the propulsion mode of operation. In the case of the symmetrical six-phase machine dc-bus voltage is set to 400V while it is 600V in the other three cases. The control algorithms are implemented in the dSPACE in order to verify that the machine works well in the propulsion regime. Since the control of all four machines is similar, the corresponding experimental results are shown together.

**Table 6.1:** Summary of the current control schemes for the four considered machines with different stator winding types (speed of rotation of a plane is indicated with the corresponding synchronous speed multiplier).

	<b>Asymmetrical 9-phase machine</b>	<b>Asymmetrical 6-phase</b>	<b>Symmetrical 6-phase</b>	<b>5-phase</b>
dominant dead-time harmonics	5 <sup>th</sup> , 7 <sup>th</sup> , -11 <sup>th</sup> and -13 <sup>th</sup>	5 <sup>th</sup> , -7 <sup>th</sup> , -11 <sup>th</sup> and 13 <sup>th</sup>	-5 <sup>th</sup> , 7 <sup>th</sup> , -11 <sup>th</sup> and 13 <sup>th</sup>	-3 <sup>rd</sup> , 7 <sup>th</sup> , -9 <sup>th</sup> , 11 <sup>th</sup> and -13 <sup>th</sup> (and 17 <sup>th</sup> )
harmonics that map into the 1 <sup>st</sup> plane	none	-11 <sup>th</sup> and 13 <sup>th</sup>	-5 <sup>th</sup> , 7 <sup>th</sup> , -11 <sup>th</sup> and 13 <sup>th</sup>	-9 <sup>th</sup> and 11 <sup>th</sup>
harmonics that map into the 2 <sup>nd</sup> plane	5 <sup>th</sup> and -13 <sup>th</sup>	5 <sup>th</sup> and -7 <sup>th</sup>	none	-3 <sup>rd</sup> , 7 <sup>th</sup> and -13 <sup>th</sup> (and 17 <sup>th</sup> )
harmonics that map into the 3 <sup>rd</sup> plane	7 <sup>th</sup> and -11 <sup>th</sup>	n/a	n/a	n/a
speed of rotation of the 1 <sup>st</sup> plane	1	1	1	1
speed of rotation of the 2 <sup>nd</sup> plane	-4	-1	0	2
speed of rotation of the 3 <sup>rd</sup> plane	-2	n/a (does not exist)	n/a (does not exist)	n/a (does not exist)
number of controller pairs in the 1 <sup>st</sup> plane and their tuning ( <i>h</i> )	none	single <i>h</i> = 12	two <i>h</i> = 6 and 12	single <i>h</i> = 10
number of controller pairs in the 2 <sup>nd</sup> plane and their tuning ( <i>h</i> )	single <i>h</i> = 9	single <i>h</i> = 6	none	two <i>h</i> = 5 and 15
number of controller pairs in the 3 <sup>rd</sup> plane and their tuning ( <i>h</i> )	single <i>h</i> = 9	n/a	n/a	n/a

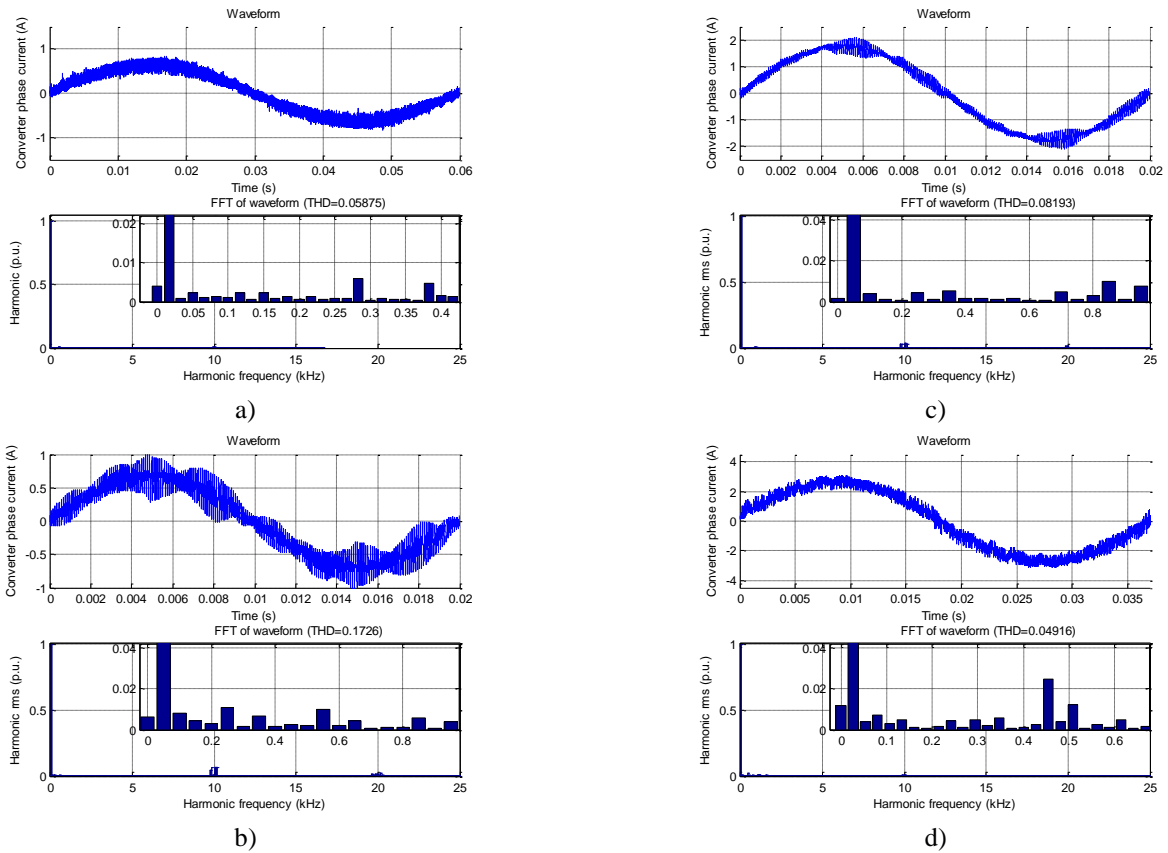


**Fig. 6.3:** Steady state operation of: a) nine-phase machine at 1000 rpm,  $i_d^* = 1.5A$ , b) asymmetrical six-phase machine at 1000 rpm,  $i_d^* = 1.2A$ , c) symmetrical six-phase machine at 1000 rpm,  $i_d^* = 3A$ , d) five-phase machine at 800 rpm,  $i_d^* = 4.5A$ . Index *s* in stator current component symbols is omitted.

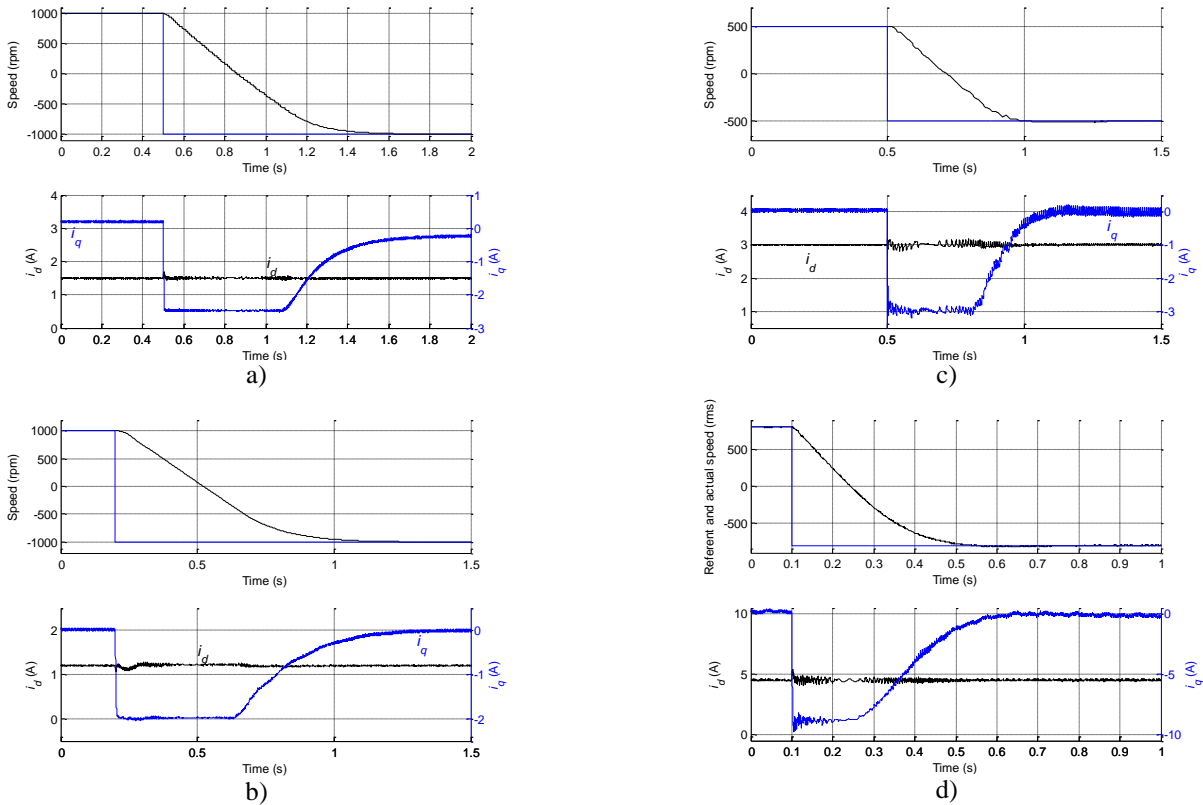


**Fig. 6.4:** Speed reference, real speed and machines' stator current  $d$ - $q$  components during reversal transient for: a) nine-phase machine (-1000 to 1000 rpm), b) asymmetrical six-phase machine (-1000 to 1000 rpm), c) symmetrical six-phase machine (-1000 to 1000 rpm), d) five-phase machine (-800 to 800 rpm).

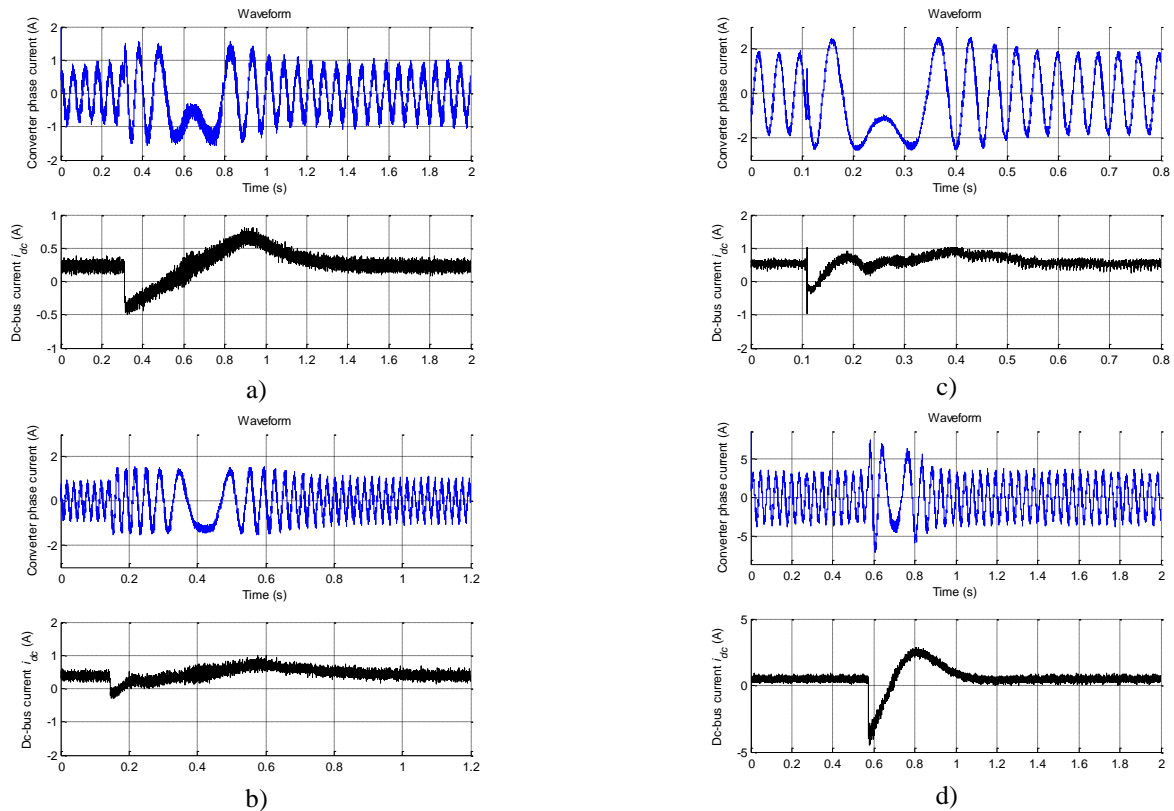


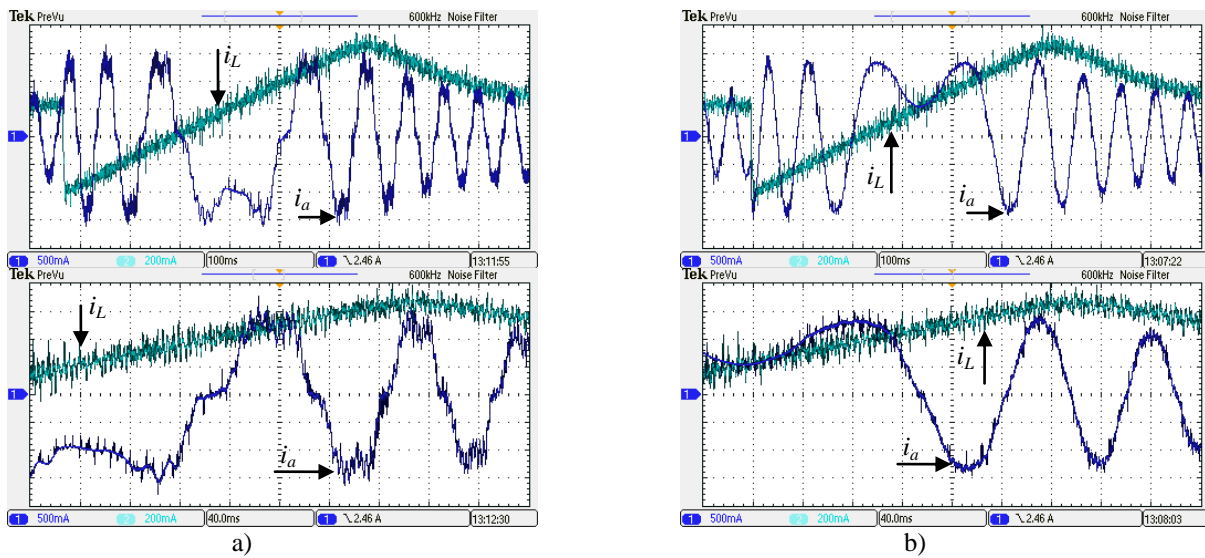
**Fig. 6.5:** Machine phase  $a$  current and battery discharging current during the reversal transient: a) nine-phase machine with  $i_{q\max}^* = 2.5A$  (-1000 to 1000 rpm), b) asymmetrical six-phase machine with  $i_{q\max}^* = 2.5A$  (-1000 to 1000 rpm), c) symmetrical six-phase machine with  $i_{q\max}^* = 3A$  (500 to -500 rpm), d) five-phase machine with  $i_{q\max}^* = 9A$  (800 to -800 rpm).

At first, in order to demonstrate proper operation of the current control algorithms, summarised in Table 6.1, oscilloscope recordings of machines' phase  $a$  current and spectra are given in Figs. 6.3a – 6.3d for steady state operation of the asymmetrical nine-phase, asymmetrical and symmetrical six-phase, and the five-phase machine, respectively. Current spectra show satisfactory performance with values of controlled low-order harmonics below 1% of the fundamental. It should be noted that in the case of the nine-phase machine 29<sup>th</sup> harmonic is controlled as well. This harmonic is significant only due to the specific design of the nine-phase machine that is used in experiments.

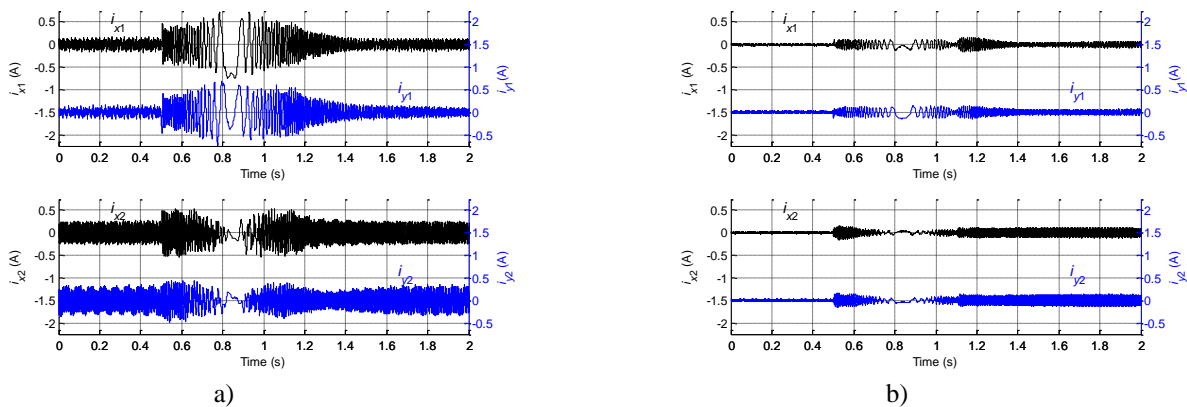
A reversal transient under no-load conditions is considered next. Figs. 6.4 and 6.5 show obtained experimental results. At first, from Fig. 6.4 it can be seen that speed tracks its reference fast without an overshoot. The current  $d$ -component is maintained at a desired value, while the  $q$ -component governs the torque production. It can be seen that the  $q$ -component is slightly positive at the beginning of the transient and at this point it is used only to cover mechanical and iron losses in the machine. It has the same absolute value, but the opposite sign, close to the end of the transient, since again it has to cater for the same losses. During the transient current  $q$ -component is in the limit and this governs the maximum torque developed by the motor during the transient. It is obvious that the change of one current component does not cause a change in the other, which is a consequence of the decoupled control and correct field orientation.

Fig. 6.5 shows machines' phase current and battery discharging current. At the beginning and at the end of the transient the dc-bus current has the same value, since the battery has to provide power in order to cover the no-load losses in the motor. One interesting feature of the system is that the energy released during electric braking is automatically used to recharge the battery. This is evident in the trace of the dc-bus current in the beginning of the transient, when the current is negative.

The final aspect of the operation during the reversal transient, addressed here, is harmonic suppression. Since it is the same for all four machines, in order to avoid repetition, the analysis is here presented only for the case of the asymmetrical nine-phase machine. In order to demonstrate valid harmonic suppression even during transient operation, zoomed-in graphs are shown in Fig. 6.6 for two cases. The first one, to the left, is when the harmonic suppression is



**Fig. 6.6:** Zoomed-in representation of the nine-phase machine's phase  $a$  current during the transient: a) harmonic elimination is disabled, b) harmonic elimination is enabled. Graphs also contain battery discharging current.



**Fig. 6.7:** Nine-phase machine current components in parasitic planes: a) harmonic elimination is disabled, b) harmonic elimination is enabled.

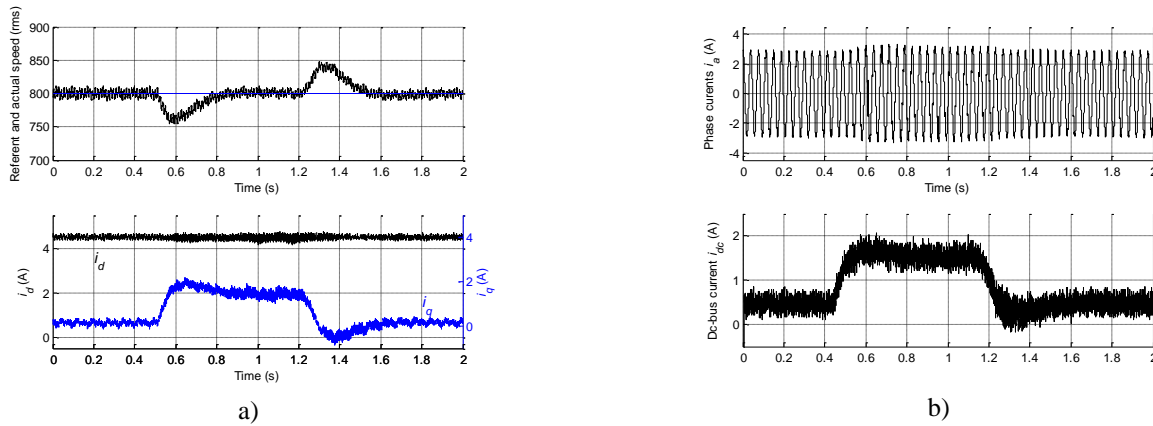


**Fig. 6.8:** Five-phase machine's load rejection transient: a) reference and measured speed, and stator current components in the first plane, b) machine phase  $a$  current and battery charging current.

disabled; on the right-hand side is the corresponding graph with the harmonic suppression enabled. From Fig. 6.6a it can be seen that if harmonics are not controlled they can be significant. The one that is the most pronounced is the 29<sup>th</sup>, while the existence of lower-order harmonics is obvious as well. On the other hand, when harmonic control is enabled all these harmonics are controlled to zero. From Fig. 6.6b it is clear that they do not exist even during the reversal transient. In order to support this statement, machine current component in parasitic ( $x$ - $y$ ) planes are shown in Fig. 6.7 for the same two cases. It is obvious that when harmonic control is disabled these components contain significant low-order harmonics, while when the harmonic control is enabled they are zeroed in both steady state and transient operation.

The final performed test is the load rejection transient. Again, in order to avoid repetition, it is reported for one machine only. The five-phase machine is chosen this time for illustration. A load torque is applied to the machine and removed after 0.7 seconds in a step-wise manner. The results are shown in Fig. 6.8. As can be seen from Fig. 6.8a, after the load torque application the speed control quickly restores the required drive speed. The same is valid when the load is removed. Current components show that load disturbance does not affect the  $d$ -component of the current. On the other hand,  $q$ -component changes in order to provide counterbalancing of the load torque and restoration of the reference speed. From Fig. 6.8b it can be seen that the machine phase  $a$  current only slightly increases during the test, indicating that the applied load torque is relatively small. The change is however obvious in the battery discharging current, since more energy is required to maintain the speed when the load is increased.

The presented results demonstrate excellent performance of all four drives in propulsion mode of operation, as is to be expected from RFOC.

#### 6.4 Conclusion

In this chapter propulsion mode of operation of integrated multiphase charging/V2G topologies is investigated. Four machines with different stator winding types are considered: asymmetrical nine-phase, asymmetrical and symmetrical six-phase, and a five-phase machine. For all machines control algorithm is developed first. Similarly as for the charging mode, the first fifteen current harmonics are controlled. Experimental results are reported for the steady state operation, reversal transient, and load rejection. Experimental results demonstrate excellent performance of drives in propulsion mode of operation.

## CHAPTER 7: CONCLUSIONS AND FUTURE WORK

### 7.1 Conclusions

The Thesis focuses on various integrated methods for charging the batteries of EVs. It employs integration of an inverter and a machine of induction or synchronous type, as those are the two machine types that are most commonly used in EVs. Charging from a single-phase, three-phase and multiphase source is analysed. A special attention is placed on preventing the rotor from moving during the charging process by not generating a rotating field during this mode of operation. Possibilities of multiphase machine integration into the charging process are investigated and it is shown in the Thesis how additional degrees of freedom of these machines can be employed for charging the batteries of EVs without a torque production. Voltage oriented control (VOC) is utilised as a control algorithm during charging. It is extended to cover the control of multiphase systems.

The Thesis commences with a literature survey of existing charging solutions, starting from off-board, through non-integrated on-board, and finishing with integrated on-board chargers. For each type and each configuration the advantages and drawbacks are examined. Further, a comprehensive quantitative comparison in the tabular format is provided for all on-board charging solutions. This is done to identify the best configurations which are then used as benchmarks for the research on new charging solutions.

Next, in Chapter 3, a supply from a multiphase source is considered, and new charging configurations are proposed. Assuming supply from a five and seven-phase source, detailed analysis is performed, and a generalisation is made for all odd numbers of phases. Regarding the even phase numbers, only the asymmetrical and symmetrical six-phase systems are assessed because their voltage sources can be easily obtained from a three-phase source and a three-phase transformer with dual secondary winding or single secondary winding in open-end configuration. In all the configurations theoretical analysis is used to show how the excitation is transferred from the flux/torque producing  $\alpha$ - $\beta$  plane to the non-flux/torque producing planes, so that the machine naturally stays at standstill and its stator winding leakage inductances are utilised for filtering during the charging process.

Charging from a single-phase source is considered next, since it is currently used in the EV industry and is a desirable additional asset to a three-phase charger. Theoretical analysis is performed for systems with integration of asymmetrical and symmetrical six-phase, nine-phase, and ten-phase machines with multiple isolated neutral points. It is shown how the isolated neutral points can be conveniently used to attach a single-phase supply to a machine, and avoid torque production by performing field cancelation within each set of windings. Obvious advantage of these charging systems is that there is no need for hardware reconfiguration between the propulsion and charging mode of operation. A solution employing a five-phase machine, which however requires hardware reconfiguration, is also considered. Some research has already been done in the past for integration of an equivalent of a six-phase machine; all the other configurations, introduced in Chapter 3, are novel and have been developed in this project for the first time.

Finally, integration of multiphase machines into three-phase battery charging systems for EVs is considered. A set of entirely new topologies is developed. At present there is only a single solution that allows integration of induction or synchronous machines into three-phase charging process without an average torque production. Thus in this report other charging configurations with the same advantage are presented. Asymmetrical and symmetrical nine-phase machines with three isolated neutral points are here the starting point. For these machine types it is analytically shown how the excitation can be transferred from the flux/torque producing to the non-flux/torque producing planes. These two configurations do not require any hardware reconfiguration for the changeover from the propulsion to the charging mode of operation. The one existing solution, mentioned before, is analysed from the perspective of multiphase machines, so that the three-phase machine with access to the phase mid-points is approached from the point of view of a symmetrical six-phase machine. A slight modification to the existing scheme is also presented and it is shown that it provides better voltage filtering at the cost of introducing new elements for hardware reconfiguration between the two modes of operation. This is followed by a solution for integrating a symmetrical and an asymmetrical six-phase machine. Theoretical analysis shows that a pulsating field exists in a machine in this case, but an average torque is still not produced during the charging mode. The pulsating field is also present in a topology employing a five-phase machine, which is the last considered configuration.

All of the configurations encompassed by this report require a multiphase VSR. As opposed to three-phase VSRs, which can nowadays be regarded as well-known, multiphase VSRs have not been covered in the literature. Still, the principles of operation and the most parts of the control algorithm are the same as for a three-phase VSR. Principles of operation of multiphase VSRs are discussed in Chapter 4, and their mathematical model is derived. It is shown that the main difference is the existence of multiple planes in certain cases in the decoupled model, in contrast to a single  $\alpha$ - $\beta$  plane that exists in the three-phase VSR.

Comprehensive development of control algorithms for charging mode of operation for all considered topologies is provided in Chapter 5. They all aim at unity power factor operation and suppression of low order harmonics up to the 15<sup>th</sup>. Experimental results, presented in the same chapter, validate the proposed algorithms. They demonstrate that in each topology either the whole or a part of the excitation is indeed transferred from the flux/torque producing plane into a passive plane, which validates theoretical considerations elaborated in Chapter 3. Continuous speed measurements demonstrated that all machines stayed at standstill during the charging operation. As machines

were not mechanically locked during the process, this validates torque-free operation. It should be noted that it is possible that some very small torque incapable of surpassing the friction torque gets produced in practice. However, this torque cannot be measured or identified by other means on a physical system since the machine is at standstill. A possible cause of torque production could be unbalance between per-phase parameters of hard-paralleled machine phases. On the other hand, the absence of even the residual torque can be ascertained from excitation mappings of machine currents. Results show that the excitation in the torque producing plane is either pulsating or non-existent, which clearly validates torque-free operation. They also validate the proposed control as unity power factor operation, and excellent grid current quality is achieved in all topologies. Low-order harmonics of currents are reduced to typically below 1% of the fundamental.

Propulsion mode of operation is considered as well. However, since it is well-known for three-phase as well as for multiphase machines, the discussion is kept brief. Experiments are performed with a five-phase, asymmetrical and symmetrical six-phase, and an asymmetrical nine-phase machine and the results are given in Chapter 6. Excellent performance is achieved in both steady state and transient operation.

## 7.2 Future work

The Thesis developed a multitude of novel integrated charging solutions for battery charging of EVs. However, novel solutions lead to certain aspects of integrated chargers that were not considered before. Until now a comprehensive study on impact of the charging process on a multiphase machine, that is being integrated, has not been performed. A specific type of integrated chargers that have a pulsating field in the rotor during a fast charging process is introduced in the Thesis. Therefore, a study on impact of the charging process on machines in these topologies has obviously never been performed. Moreover, the exact equivalent scheme of topologies having a pulsating field in the rotor during the charging process has not been considered either at this point in time.

Although the topologies covered in the Thesis are capable of achieving excellent performance in both charging and propulsion modes, their industrial application suitability would require further analysis. An aspect that would require a particular attention is optimisation of a multiphase machine design for operation in both propulsion and the charging modes. This is however not an easy task since fast transient in propulsion mode requires minimization of leakage inductances, while the charging process demands exactly the opposite. The analysis is hindered by the fact that even for the propulsion mode the available knowledge regarding multiphase machine design is far from the level of the three-phase counterparts. All of this demands further investigation and desirable future work can be briefly summarised as follows:

- Development of dynamic and steady state induction machine models for the configurations with the pulsating field in the rotor. Ideally, the models should be analytically derived and then verified by simulations. Verification should consist of performance comparison using simulations with the obtained equivalent models and with the complete machine models.
- Analysis of the impact of the charging process on the machines that are being integrated. This includes a multitude of aspects, such as heating, vibrations, aging, acoustic noise and loss analysis. These aspects should be assessed through FEM simulations.
- Optimization of multiphase machines for both charging and propulsion mode. As already stated the main parameter that requires optimization is the stator leakage inductance. However, the optimization has to be performed using the complete machine design.
- Efficiency evaluation of all topologies. Very little work has been done and published on efficiency of integrated charging topologies in general. Since it is an important aspect of any charger, efficiency analysis should be performed for all the topologies that are considered in the Thesis. This should be followed by their comparison.
- Investigation of an asymmetrical nine-phase topology based on the use of a PM machine instead of an induction machine. All the experimental results provided in the Thesis consider integration of machines of induction type. However, the same is applicable to synchronous machines in general and PM machines in particular. Their performance in the charging process is yet to be assessed.

## REFERENCES

- Ahmed, S.M., Iqbal, A., Abu-Rub, H., (2011a), Generalized duty-ratio-based pulsewidth modulation technique for a three-to- k phase matrix converter, *IEEE Transactions on Industrial Electronics*, vol. 58, no. 9, pp. 3925-3937.
- Ahmed, S.M., Iqbal, A., Abu-Rub, H., Rodriguez, J., Rojas, C.A., Saleh, M., (2011b), Simple carrier-based PWM technique for a three-to-nine-phase direct ac-ac converter, *IEEE Transactions on Industrial Electronics*, vol. 58, no. 11, pp. 5014-5023.
- Bai, S., Lukic, S., (2011), Design considerations for dc charging station for plug-in vehicles, *Proc. IEEE Vehicle Power and Propulsion Conf. VPPC*, Chicago, Illinois, CD-ROM.
- Bodo, N., Subotic, I., Levi, E., Jones, M., (2014), Single-phase on-board integrated battery charger based on a nine-phase machine, *Proc. IEEE Industrial Electronics Society Conf. IECON*, Dallas, Texas, pp. 3210-3216.
- Bruyère, A., De Sousa, L., Bouchez, B., Sandulescu, P., Kestelyn, X., Semail, E., (2010), A multiphase traction/fast-battery-charger drive for electric or plug-in hybrid vehicles: Solutions for control in traction mode, *Proc. IEEE Vehicle Power and Propulsion Conf. VPPC*, Lille, France, CD-ROM.
- Capece, S.L., Cecati, C., Rotondale, N., (2003), A new control technique for harmonics elimination in six-switch active rectifiers, *Proc. IEEE Power Tech Conf.*, Bologna, Italy, CD-ROM.
- Chang-Yu, H., Boys, J.T., Covic, G.A., Budhia, M., (2009), Practical considerations for designing IPT system for EV battery charging, *Proc. IEEE Vehicle Power and Propulsion Conf. VPPC*, Dearborn, Michigan, pp. 402-407.
- Che, H.S., Levi, E., Jones, M., Hew, W.P., Rahim, N.A., (2014), Current control methods for an asymmetrical six-phase induction motor drive, *IEEE Transactions on Power Electronics*, vol. 29, no. 1, pp. 407-417.
- Cocconi, A.G., (1994), Combined motor drive and battery recharge system, *US Patent 5,341,075*.
- de Santiago, J., Bernhoff, H., Ekergard, B., Eriksson, S., Ferhatovic, S., Waters, R., Leijon, M., (2012), Electrical motor drivelines in commercial all-electric vehicles: a review, *IEEE Transactions on Vehicular Technology*, vol. 61, no. 2, pp. 475-484.
- De Sousa, L., Bouchez, B., (2010a), Method and electric combined device for powering and charging with compensation means, *Int. Patent WO 2010/057893 A1*
- De Sousa, L., Bouchez, B., (2010b), Combined electric device for powering and charging, *Int. Patent WO 2010/057892 A1*
- De Sousa, L., Dogan, H., (2011), Method of evaluating the zero-sequence inductance ratio for electrical machines, *Proc. European Power Electronics and Applications Conf. EPE*, Birmingham, UK, CD-ROM.
- De Sousa, L., Silvestre, B., Bouchez, B., (2010), A combined multiphase electric drive and fast battery charger for electric vehicles, *Proc. IEEE Vehicle Power and Propulsion Conf. VPPC*, Lille, France, CD-ROM.
- Dong-Gyun, W., Gyu-Yeong, C., Jong-Soo, K., Byoung-Kuk, L., Jin, H., Gu-Bae, K., (2011), Comparison of integrated battery chargers for plug-in hybrid electric vehicles: Topology and control, *Proc. IEEE Int. Electric Machines and Drives Conf. IEMDC*, Niagara Falls, Ontario, pp. 1294-1299.
- Dujic, D., Levi, E., Jones, M., (2010), Dc bus utilisation in multiphase VSI supplied drives with a composite stator phase number, *Proc. IEEE Int. Conf. on Industrial Technology ICIT*, Viña del Mar, Chile, pp.1495-1500.
- Dusmez, S., Cook, A., Khaligh, A., (2011), Comprehensive analysis of high quality power converters for level 3 off-board chargers, *Proc. IEEE Vehicle Power and Propulsion Conf. VPPC*, Chicago, Illinois, CD-ROM.
- Electromagnetic compatibility EMC, (1995), Part 3: Limits - Section 2: Limits for harmonic current emission, IEC 1000-3-2.
- Erb, D.C., Onar, O.C., Khaligh, A., (2010), Bi-directional charging topologies for plug-in hybrid electric vehicles, *Proc. IEEE Applied Power Electronics Conf. APEC*, Palm Springs, California, pp. 2066-2072.
- Gallardo-Lozano, J., Milanés-Montero, M.I., Guerrero-Martinez, M.A., Romero-Cadaval, E., (2011), Three-phase bidirectional battery charger for smart electric vehicles, *Proc. Int. Workshop on Compatibility in Power Electronics CPE*, Tallinn, Estonia, pp. 371-376.
- Gallardo-Lozano, J., Milanés-Montero, I., Guerrero-Martínez, M., Romero-Cadaval, E., (2012), Electric vehicle battery charger for smart grids, *Electric Power Systems Research*, vol. 90, pp. 18-29.
- Garcia, O., Zumel, P., de Castro, A., Cobos, A., (2006), Automotive dc-dc bidirectional converter made with many interleaved buck stages, *IEEE Transactions on Power Electronics*, vol. 21, no. 3, pp. 578-586.
- Gopiyani, A., Patel, V., Shah, M.T., (2010), A novel half-bridge LLC resonant converter for high power dc power supply, *Proc. Int. Power Engineering Conf. IPEC*, Singapore, Singapore, pp. 34-39.
- Greul, R., Drofenik, U., Kolar, J.W., (2003), Analysis and comparative evaluation of a three-phase three-level unity power factor  $\gamma$ -rectifier, *Proc. IEEE Int. Telecommunications Energy Conf. INTELEC*, Yokohama, Japan, pp. 421-428.
- Greul, R., Round, S.D., Kolar, J.W., (2006), The delta-rectifier: analysis, control and operation, *IEEE Transactions on Power Electronics*, vol. 21, no. 6, pp. 1637-1648.
- Gui-Jia, S., Lixin, T., (2010), Control of plug-in hybrid electric vehicles for mobile power generation and grid support applications, *Proc. IEEE Applied Power Electronics Conf. APEC*, Palm Springs, California, pp. 1152-1157.

- Haghbin, S., (2011), Electrical apparatus comprising drive system and electrical machine with reconnectable stator winding, *European Patent* 159,241.
- Haghbin, S., Alakula, M., (2010), Elektrisk Apparat, *Swedish Patent* 1,050,607-9.
- Haghbin, S., Alakula, M., Khan, K., Lundmark, S., Leksell, M., Wallmark, O., Carlson, O., (2010a), An integrated charger for plug-in hybrid electric vehicles based on a special interior permanent magnet motor, *Proc. IEEE Vehicle Power and Propulsion Conf. VPPC*, Lille, France, CD-ROM.
- Haghbin, S., Lundmark, S., Alakula, M., Carlson, O., (2011), An isolated high-power integrated charger in electrified-vehicle applications, *IEEE Transactions on Vehicular Technology*, vol. 60, no. 9, pp. 4115-4126.
- Haghbin, S., Lundmark, S., Alakula, M., Carlson, O., (2013), Grid-connected integrated battery chargers in vehicle applications: review and new solution, *IEEE Transactions on Industrial Electronics*, , vol. 60, no. 2, pp. 459-473, 2013.
- Haghbin, S., Khan, K., Lundmark, S., Alakula, M., Carlson, O., Leksell, M., Wallmark, O., (2010b), Integrated chargers for EV's and PHEV's: examples and new solutions, *Proc. Int. Conf. on Electrical Machines ICEM*, Rome, Italy, CD-ROM.
- Harikumar, J., Vereczki, G., Farkas, C., Bauer, P. (2012), Comparison of quick charge technologies for electric vehicle introduction in Netherlands, *Proc. IEEE Industrial Electronics Society Conf. IECON*, Montreal, Canada, pp. 2889-2895.
- Holmes, D.G., Lipo, T.A., (2003), Pulse width modulation for power converters: principles and practice, *IEEE Press*, Piscataway, NJ.
- Hung-Chun, C., Chang-Ming, L., (2009), Development of a compact switched-reluctance motor drive for EV propulsion with voltage-boosting and PFC charging capabilities, *IEEE Transactions on Vehicular Technology*, vol. 58, no. 7, pp. 3198-3215.
- Hung-Chun, C., Chang-Ming, L., (2011), An integrated driving/charging switched reluctance motor drive using three-phase power module, *IEEE Transactions on Industrial Electronics*, vol. 58, no. 5, pp. 1763-1775.
- Inoa, E., Jin, W., (2011), PHEV charging strategies for maximized energy saving, *IEEE Transactions on Vehicular Technology*, vol. 60, no. 7, pp. 2978-2986.
- Iqbal, A., Ahmed, S.M., Abu-Rub, H., (2012), Space vector PWM technique for a three-to-five-phase matrix converter, *IEEE Transactions on Industry Applications*, vol. 48, no. 2, pp. 697-707.
- Iqbal, A., Moinuddin, S., Khan, M.R., Ahmed, S.M., Abu-Rub, H., (2010), A novel three-phase to five-phase transformation using a special transformer connection, *IEEE Transactions on Power Delivery*, vol. 25, no. 3, pp. 1637-1644.
- Jasinski, M., (2005), Direct power and torque control of ac/dc/ac converter-fed induction motor drives, *PhD thesis*, Warsaw University of Technology, Warsaw, Poland.
- Jasinski, M., Kazmierkowski, M.P., (2011), Fundamentals of ac-dc-ac converters control and applications, in *The Industrial Electronics Handbook – Power Electronics and Motor Drives* (Chapter 16), edited by B.M. Willamowski and J.D. Irwin, CRC Press.
- Jianing, L., Guoqing, X., Linni, J., Liu, L., (2011), Electric air conditioner system with on-board charger for PHEV, *Proc. IEEE Int. Conf. on Information and Automation ICIA*, Shenzhen, China, pp. 421-426.
- Jinrong, Q., Lee, F.C., (2000), Charge pump power-factor-correction technologies. I. Concept and principle, *IEEE Transactions on Power Electronics*, vol. 15, no. 1, pp. 121-129.
- Josefsson, O., Lindskog, A., Lundmark, S., Thiringer, T., (2010), Assessment of a multilevel converter for a PHEV charge and traction application, *Proc. Int. Conf. on Electrical Machines ICEM*, Rome, Italy, CD-ROM.
- Khan, K., Haghbin, S., Leksell, M., Wallmark, O., (2010), Design and performance analysis of a permanent-magnet assisted synchronous reluctance machine for an integrated charger application, *Proc. Int. Conf. on Electrical Machines ICEM*, Rome, Italy, CD-ROM.
- Kinoshita, S., (1997), Electric system of electric vehicle, *US Patent* 5,629,603.
- Kisacikoglu, M.C., Ozpineci, B., Tolbert, L.M., (2010), Examination of a PHEV bidirectional charger system for V2G reactive power compensation, *Proc. IEEE Applied Power Electronics Conf. APEC*, Palm Springs, California, pp. 458-465.
- Kolar, J.W., Friedli, T., (2011), The essence of three-phase PFC rectifier systems, *Proc. IEEE Int. Telecommunications Energy Conf. INTELEC*, Amsterdam, The Netherlands, pp. 1-27.
- Kuperman, A., Levy, U., Goren, J., Zafranski, A., Savernin, A., Peled, I., (2010), Modeling and control of a 50kW electric vehicle fast charger, *Proc. IEEE Convention of Electrical and Electronics Engineers*, Eilat, Israel, pp. 188-192.
- Lacressonniere, F., Cassoret, B., (2005), Converter used as a battery charger and a motor speed controller in an industrial truck, *Proc. European Power Electronics and Applications Conf. EPE*, Dresden, Germany, CD-ROM.
- Lacroix, S., Laboure, E., Hilairret, M., (2010), An integrated fast battery charger for electric vehicle, *Proc. IEEE Vehicle Power and Propulsion Conf. VPPC*, Lille, France, CD-ROM.

- Lascu, C., Asiminoaei, L., Boldea, I., Blaabjerg, F., (2007), High performance current controller for selective harmonic compensation in active power filters, *IEEE Transactions on Power Electronics*, vol. 22, no. 5, pp. 1826-1835.
- Levi, E., (2008), Multiphase electric machines for variable-speed applications, *IEEE Transactions on Industrial Electronics*, vol.55, no.5, pp.1893-1909.
- Levi, E., Bojoi, R., Profumo, F., Toliyat, H.A., Williamson, S., (2007), Multiphase induction motor drives – a technology status review, *IET Electric Power Applications*, vol. 1, no. 4, pp. 489-516.
- Levi, E., Jones, M., Vukosavic, S.N., Toliyat, H.A., (2004), A novel concept of a multiphase, multimotor vector controlled drive system supplied from a single voltage source inverter, *IEEE Transactions on Power Electronics*, vol.19, no. 2, pp. 320- 335.
- Levi, E., Vukosavic, S.N., Jones, M., (2005), Vector control schemes for series-connected six-phase two-motor drive systems, *IEE Proc. – Electric Power Applications*, vol. 152, no. 2, pp. 226-238.
- Limongi, L.R., Bojoi, R., Pica, C., Profumo, F., Tenconi, A., (2007), Analysis and comparison of phase locked loop techniques for grid utility applications, *Proc. Power Conversion Conf. PCC*, Nagoya, Japan, pp. 674-681.
- Lisheng, S., Meintz, A., Ferdowski, M., (2008), Single-phase bidirectional ac-dc converters for plug-in hybrid electric vehicle applications, *Proc. IEEE Vehicle Power and Propulsion Conf. VPPC*, Harbin, China, CD-ROM.
- Liu, S., Hahlbeck, S., Schoenen, T., Hameyer, K., (2012), An integrated on-board charger with direct grid connection for battery electrical vehicle, *Proc. Int. Symposium on Power Electronics, Electric Drives, Automation and Motion SPEEDAM*, Sorrento, Italy, pp. 335–340.
- Lixin, T., Gui-Jia, S., (2009), A low-cost, digitally-controlled charger for plug-in hybrid electric vehicles, *Proc. IEEE Energy Conversion Congress and Exposition ECCE*, San Jose, California, pp. 3923-3929.
- Lixin, T., Gui-Jia, S., (2010), Control scheme optimization for a low-cost, digitally-controlled charger for plug-in hybrid electric vehicles, *Proc. IEEE Energy Conversion Congress and Exposition ECCE*, Atlanta, Georgia, pp. 3604-3610.
- Malinowski, M., (2001), Sensorless control strategies for three-phase PWM rectifiers, *PhD thesis*, Warsaw University of Technology, Warsaw, Poland.
- Ming, Z., Bin, L., Lijun, H., Tolbert, L.M., Zhengyu, L., (2012), Performance study for high power density three-phase Vienna PFC rectifier by using SVPWM control method, *Proc. IEEE Applied Power Electronics Conf. APEC*, Orlando, Florida, pp. 1187-1191.
- Moinoddin, S., Iqbal, A., Abu-Rub, H., Rizwan Khan, M., Ahmed, S.M., (2012), Three-phase to seven-phase power converting transformer, *IEEE Transactions on Energy Conversion*, vol. 27, no. 3, pp. 757-766.
- Nagatsuka, Y., Ehara, N., Kaneko, Y., Abe, S., Yasuda, T., (2010), Compact contactless power transfer system for electric vehicles, *Proc. Int. Power Engineering Conf. IPEC*, Singapore, Singapore, pp. 807-813.
- Neacsu, D.O., (1999), Vectorial current control techniques for three-phase ac/dc boost converters, *Proc. IEEE Industrial Electronics Symposium ISIE*, Bled, Slovenia, pp.527-532.
- Neves, A., Sousa, D.M., Roque, A., Terras, J.M., (2011), Analysis of an inductive charging system for a commercial electric vehicle, *Proc. European Power Electronics and Applications Conf. EPE*, Birmingham, UK, CD-ROM.
- Pellegrino, G., Armando, E., Guglielmi, P., (2009a), An integral battery charger with power factor correction for electric scooter, *Proc. IEEE Int. Electric Machines and Drives Conf. IEMDC*, Miami, Florida, pp. 661-668.
- Pellegrino, G., Armando, E., Guglielmi, P., (2009b), Integrated battery charger for electric scooter, *Proc. European Power Electronics and Applications Conf. EPE*, Barcelona, Spain, CD-ROM.
- Pellegrino, G., Armando, E., Guglielmi, P., (2010), An integral battery charger with power factor correction for electric scooter, *IEEE Transactions on Power Electronics*, vol. 25, no. 3, pp. 751-759.
- Pillai, J.R., Bak-Jensen, B., (2011), Integration of vehicle-to-grid in the western Danish power system, *IEEE Transactions on Sustainable Energy*, vol.2, no.1, pp.12-19.
- Prasad, A.R., Ziogas, P.D., Manias, S., (1991), An active power factor correction technique for three-phase diode rectifiers, *IEEE Transactions on Power Electronics*, vol. 6, no. 1, pp. 83-92.
- Rawson, M., Kateley, S., (1998), Electric vehicle charging equipment design and health and safety codes, *California Energy Commission*.
- Rippel, W.E., (1990), Integrated traction inverter and battery charger apparatus, *US Patent 4,920,475*.
- Rippel, W.E., Cocconi, A.G., (1992), Integrated motor drive and recharge system, *US Patent 5,099,186*.
- Rockhill, A.A., Lipo, T.A., (2010), A simplified model of a nine-phase synchronous machine using vector space decomposition, *Electric Power Components and Systems*, vol. 38, no. 4, pp. 477-489.
- Saber, A.Y., Venayagamoorthy, G.K., (2009), One million plug-in electric vehicles on the road by 2015, *Proc. IEEE Int. Intelligent Transportation Systems Conf. ITSC*, St. Louis, Missouri, CD-ROM.
- SAE international standards, (2011), Power quality requirements for plug-in vehicle chargers, standard J2894/1.
- Salmon, J.C., (1994), Comparative evaluation of circuit topologies for 1-phase and 3-phase boost rectifiers operated with a low current distortion, *Proc. IEEE Canadian Conf. on Electrical and Computer Engineering CCECE*, Vancouver, Canada, pp. 30-33

- Sandulescu A., Meinguet F., Kestelyn X., Semail E., and Bruyere A., (2013), Flux-weakening operation of open-end winding drive integrating a cost-effective high-power charger, *IET Electrical Systems in Transportation*, vol. 3, no. 1, pp. 10-21.
- Sandulescu, P., Idkhajine, L., Cense, S., Colas, F., Kestelyn, X., Semail, E., Bruyere, A., (2011), FPGA implementation of a general space vector approach on a 6-leg voltage source inverter, *Proc. IEEE Industrial Electronics Annual Conf. IECON*, Melbourne, Australia, pp. 3482-3487.
- Sang Joon, L., Seung Ki, S., (1994), An integral battery charger for 4 wheel drive electric vehicle, *Proc. IEEE Industry Applications Society Annual Meeting*, Denver, Colorado, pp. 448-452.
- Seung-Ki, S., Sang-Joon, L., (1995), An integral battery charger for four-wheel drive electric vehicle, *IEEE Transactions on Industry Applications*, vol. 31, no. 5, pp. 1096-1099.
- Shuang, Z., Haghbin, S., Wallmark, O., Leksell, M., Lundmark, S., Carlson, O., (2011), Transient modeling of an integrated charger for a plug-in hybrid electric vehicle, *Proc. European Power Electronics and Applications Conf. EPE*, Birmingham, UK, CD-ROM.
- Slicker, J.M., (1985), Pulse width modulation inverter with battery charger, *US Patent* 4,491,768.
- Soeiro, T.B., Friedli, T., Hartmann, M., Kolar, J.W., (2011), New unidirectional hybrid delta-switch rectifier, *Proc. IEEE Industrial Electronics Annual Conf. IECON*, Melbourne, Australia, pp. 1474-1479.
- Soeiro, T.B., Friedli, T., Kolar, J.W., (2012), Swiss rectifier - a novel three-phase buck-type PFC topology for electric vehicle battery charging, *Proc. IEEE Applied Power Electronics Conf. APEC*, Orlando, Florida, pp. 2617-2624.
- Solero, L., (2001), Nonconventional on-board charger for electric vehicle propulsion batteries, *IEEE Transactions on Vehicular Technology*, vol. 50, no. 1, pp. 144-149.
- Stancu, C., Hiti, S., Mundt, E., (2004), Mobile electric power for medium and heavy duty hybrid electric vehicles, *Proc. IEEE Power Electronics Specialists Conf. PESC*, Aachen, Germany, pp. 228-234.
- Stupar, A., Friedli, T., Minibock, J., Schweizer, M., Kolar, J.W., (2011), Towards a 99% efficient three-phase buck-type PFC rectifier for 400 V dc distribution systems, *Proc. IEEE Applied Power Electronics Conf. APEC*, Fort Worth, Texas, pp. 505-512.
- Subotic, I., Bodo, N., Levi, E., (2015c), An EV drive-train with integrated fast charging capability, *IEEE Transactions on Power Electronics*, accepted, doi: 10.1109/TPEL.2015.2424592.
- Subotic, I., Bodo, N., Levi, E., Jones, M., (2015a) On-board integrated battery charger for EVs using an asymmetrical nine-phase machine, *IEEE Transactions on Industrial Electronics*, vol. 62, no. 5, pp. 3285-3295.
- Subotic, I., Bodo, N., Levi, E., Jones, M., Levi V., (2015b) , Isolated chargers for EVs incorporating six-phase machines, *IEEE Transactions on Industrial Electronics*, accepted, doi: 10.1109/TIE.2015.2412516.
- Subotic, I., Jones, M., Levi, E., (2014b), A fast on-board integrated battery charger for four-motor EVs, *Proc. Int. Conf. on Electrical Machines ICEM*, Berlin, Germany, pp. 2066-2072.
- Subotic, I., Levi, E., (2014a), An integrated battery charger for EVs based on a symmetrical six-phase machine, *IEEE Int. Symposium on Industrial Electronics ISIE*, Istanbul, Turkey, pp. 2074-2079.
- Subotic, I., Levi, E., (2015d), A review of single-phase on-board integrated charging topologies for electric vehicles, *Proc. IEEE Workshop on Electrical Machines Design, Control and Diagnosis WEMDCD*, Torino, Italy, pp. 136-145.
- Subotic, I., Levi, E., Bodo, N., (2014c) A fast on-board integrated battery charger for EVs using an asymmetrical six-phase machine, *Proc. Vehicle Power and Propulsion Conf. VPPC*, Coimbra, Portugal, CD-ROM.
- Subotic, I., Levi, E., Jones, M., Graovac, D., (2013a), On-board integrated battery chargers for electric vehicles using nine-phase machines, *Proc. IEEE Int. Electric Machines and Drives Conf. IEMDC*, Chicago, Illinois, pp. 226-233.
- Subotic, I., Levi, E., Jones, M., Graovac, D., (2013b), Multiphase integrated on-board battery chargers for electrical vehicles, *Proc. Eur. Conf. on Power Electronics and Applications EPE*, Lille, France, CD-ROM.
- Subotic, I., Levi, E., Jones, M., Graovac, D., (2013c), An integrated battery charger for EVs based on an asymmetrical six-phase machine, *Proc. IEEE Industrial Electronics Society Conf. IECON*, Vienna, Austria, pp. 7244-7249.
- Surada, R., Khaligh, A., (2010), A novel approach towards integration of propulsion machine inverter with energy storage charger in plug-in hybrid electric vehicles, *Proc. IEEE Industrial Electronics Annual Conf. IECON*, Glendale, Arizona, pp. 2493-2498.
- Tae-Hoon, K., Seung-Jun, L., Woojin, C., (2011), Design and control of the phase shift full bridge converter for the on-board battery charger of the electric forklift, *Proc. IEEE Int. Conf. on Power Electronics ICPE & ECCE*, Jeju, Korea, pp. 2709-2716.
- Tesla Roadster Specifications, (2009), [http://www.teslamotors.com/display\\_data/teslaroadster\\_specsheet.pdf](http://www.teslamotors.com/display_data/teslaroadster_specsheet.pdf)
- Thimmesch, D., (1985), An SCR inverter with an integral battery charger for electric vehicles, *IEEE Transactions on Industry Applications*, vol. IA-21, no. 4, pp. 1023-1029.
- Wang, Y., Che, Y., Cheng, K.W.E., (2009), Research on control strategy for three-phase PWM voltage source rectifier, *Proc. IEEE Power Electronics Systems and Applications Conf. PESA*, Hong Kong, CD-ROM.

- Wu, H.H., Gilchrist, A., Sealy, K., Israelsen, P., Muhs, J., (2011), A review on inductive charging for electric vehicles, *Proc. IEEE Int. Electric Machines and Drives Conf. IEMDC*, Niagara Falls, Ontario, pp. 143-147.
- Yepes, A.G., (2011), Digital resonant current controllers for voltage source converters, *PhD Thesis*, University of Vigo, Vigo, Spain.
- Yilmaz, M., Krein, P.T., (2011), Review of battery charger topologies, charging power levels and infrastructure for plug-in electric and hybrid vehicles, *IEEE Transactions on Power Electronics*, vol. 28, no. 5, pp. 2151 – 2169.
- Yu, D., Xiaohu, Z., Sanzhong, B., Lukic, S., Huang, A., (2010), Review of non-isolated bi-directional dc-dc converters for plug-in hybrid electric vehicle charge station application at municipal parking decks, *Proc. IEEE Applied Power Electronics Conf. APEC*, Palm Springs, California, pp. 1145-1151.
- Yu-Kang, L., Chung-Yi, L., Min-Tsong, H., Chien-Yu, L., (2011), Phase-shifted full-bridge series-resonant dc-dc converters for wide load variations, *IEEE Transactions on Industrial Electronics*, vol. 58, no. 6, pp. 2572-2575.
- Zhang, S., Zhang, K., Jiang, Z., Lu, F., (2010), Modeling and simulation of three-phase rectifier based on SVPWM, *Proc. Int. Conf. Information and Computing ICIC*, Wuxi, China, vol. 3, pp. 318-321.

## APPENDIX A: EXPERIMENTAL RIG DATA

**Dc sink/source:** “Spitzenberger & Spies” - two DM 2500/PAS single-phase mains emulation systems are connected in series. Each provides half of the dc-bus voltage. An additional resistive load (RL 4000) is connected to the supply, enabling power sinking of up to 4kW.

**Controller:** dSPACE DS1006 processor board. DS2004 high-speed A/D board is used for the A/D conversion of the measured machine phase currents and grid voltages. DS5101 Digital Waveform Output Board is used for the PWM signal generation and the machine speed is read by a DS3002 Incremental Encoder Interface Board. In order to facilitate routing of various measurement signals and to connect them to dSPACE, a “junction box” is made. It also provides filtering for various measurements.

**Converters:** Two two-level eight-phase inverters. IGBTs used are EUPEC FS50R12KE3. Using the heat-sink data, it is estimated that the rated continuous output rms current is 14A, which gives for a 240V rms phase voltage overall nine-phase inverter continuous rating of approximately 32kVA.

**Induction machines:** Obtained by rewinding of three-phase machines, except for the five-phase machine where new stator laminations were also manufactured (with 40 slots). Data are given in Table A1.

The configuration of the experimental rig is shown in Fig. A1.

**Table A1:** Machines' data.

Machine	Pole pairs	Power [kW]	$R_s$ [ $\Omega$ ]	$R_r$ [ $\Omega$ ]	$L_{\gamma s(d-q)}$ [mH]	$L_{\gamma s(x-y)}$ [mH]	$L_{\gamma r}$ [mH]	$L_m$ [mH]
5-phase	2	no data	2.9	2.2	43	$\sim L_{\gamma s(d-q)}$	17	500
asymmetrical 6-phase	3	1.1	12.5	6	36	5.4	36	600
symmetrical 6-phase	3	1.1	3.6	1.8	8	$\sim L_{\gamma s(d-q)}$	11	200
asymmetrical 9-phase	1	2.2	6.5	1.3	25	$\sim L_{\gamma s(d-q)}$	9	1300

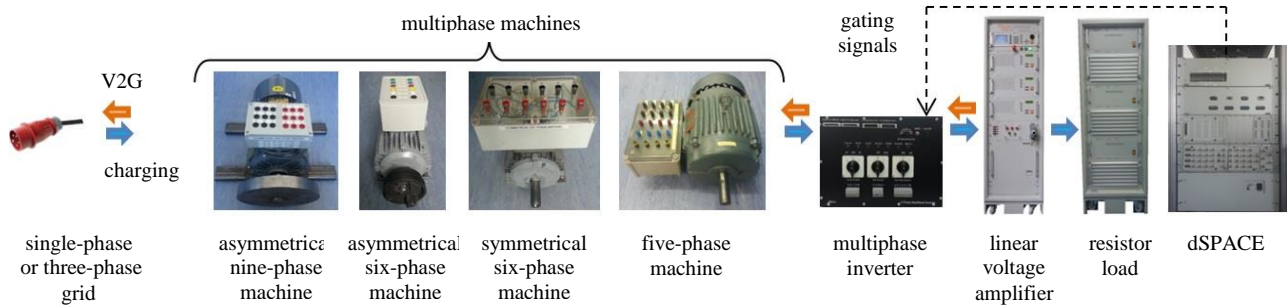


**Fig. A1:** Experimental rig.

**APPENDIX B: PUBLICATIONS FROM THE THESIS****Journal papers:**

- [Subotic, I., Bodo, N., Levi, E., Jones, M., \(2015a\) On-board integrated battery charger for EVs using an asymmetrical nine-phase machine, \*IEEE Transactions on Industrial Electronics\*, vol. 62, no. 5, pp. 3285-3295.](#)
- [Subotic, I., Bodo, N., Levi, E., Jones, M., Levi V., \(2015b\) , Isolated chargers for EVs incorporating six-phase machines, \*IEEE Transactions on Industrial Electronics\*, accepted, doi: 10.1109/TIE.2015.2412516.](#)
- [Subotic, I., Bodo, N., Levi, E., \(2015c\), An EV drive-train with integrated fast charging capability, \*IEEE Transactions on Power Electronics\*, accepted, doi: 10.1109/TPEL.2015.2424592.](#)

**Conference papers:**

- [Subotic, I., Levi, E., Jones, M., Graovac, D., \(2013a\), On-board integrated battery chargers for electric vehicles using nine-phase machines, \*Proc. IEEE Int. Electric Machines and Drives Conf. IEMDC\*, Chicago, Illinois, pp. 226-233.](#)
- [Subotic, I., Levi, E., Jones, M., Graovac, D., \(2013b\), Multiphase integrated on-board battery chargers for electrical vehicles, \*Proc. Eur. Conf. on Power Electronics and Applications EPE\*, Lille, France, CD-ROM.](#)
- [Subotic, I., Levi, E., Jones, M., Graovac, D., \(2013c\), An integrated battery charger for EVs based on an asymmetrical six-phase machine, \*Proc. IEEE Industrial Electronics Society Conf. IECON\*, Vienna, Austria, pp. 7244-7249.](#)
- [Subotic, I., Levi, E., \(2014a\), An integrated battery charger for EVs based on a symmetrical six-phase machine, \*IEEE Int. Symposium on Industrial Electronics ISIE\*, Istanbul, Turkey, pp. 2074-2079.](#)
- [Subotic, I., Jones, M., Levi, E., \(2014b\), A fast on-board integrated battery charger for four-motor EVs, \*Proc. Int. Conf. on Electrical Machines ICEM\*, Berlin, Germany, pp. 2066-2072.](#)
- [Bodo, N., Subotic, I., Levi, E., Jones, M., \(2014\), Single-phase on-board integrated battery charger based on a nine-phase machine, \*Proc. IEEE Industrial Electronics Society Conf. IECON\*, Dallas, Texas, pp. 3210-3216.](#)
- [Subotic, I., Levi, E., Bodo, N., \(2014c\) A fast on-board integrated battery charger for EVs using an asymmetrical six-phase machine, \*Proc. IEEE Vehicle Power and Propulsion Conf. VPPC\*, Coimbra, Portugal, CD-ROM.](#)
- [Subotic, I., Levi, E., \(2015d\), A review of single-phase on-board integrated charging topologies for electric vehicles, \*Proc. IEEE Workshop on Electrical Machines Design, Control and Diagnosis WEMDCD\*, Torino, Italy, pp. 136-145.](#)